

# ISGMA 2014

International Symposium on  
Green Manufacturing and Applications

# PROCEEDINGS



ISSN 2383-4684

June 24 (Tue) - 28 (Sat), 2014

Paradise Hotel, Busan, Korea

# **International Symposium on Green Manufacturing and Applications ISGMA 2014 Proceedings**

The Korean Society for Precision Engineering (KSPE)  
Pusan National University (PNU) Engineering Research Center of Innovative Technology on Advanced  
Forming (ERC/ITAF) Seoul National  
University (SNU) Institute of Advanced Machinery and Design  
Korea Institute of Industrial Technology (KITECH)  
Korea Institute of Machinery and Materials (KIMM)  
Manufacturing Institute for Research on Advanced Initiatives (Pan-Pacific MIRAI)

*This work was supported by the Korean Federation of Science and Technology Societies(KOFST) grant  
funded by the Korean Government.*

# International Symposium on Green Manufacturing and Applications

## ISGMA 2014 Proceedings

---

▪ ISSN 2383-4684

---

### CONTENTS

---

- 1 Influence of Spark Gap in EDM based on Buckingham's  $\pi$  Theorem  
**S.H. Yeo and J. Y. Toh**
- 4 Selective Micropattern Replications using Ultrasonic Imprint Lithography  
**Keun Park, Hyun-Joong Lee and Woosin Jung**
- 7 Design of Signal Processing System for 3D Printing-based Flexible Tactile Sensor terephthalate  
**JuKyoung Lee, Suk Lee, and KyungChang Lee**
- 10 Slip Detection of Robot Gripper using 3D Printing-based Flexible Tactile Sensor  
**HyeongJun Kim, Suk Lee and KyungChang Lee**
- 13 Investigations of a Bistable Energy Harvester by Harmonic Balance Method  
**Huu-Tu Nguyen and Dung-An Wang**
- 17 Prediction of Acceleration of Power-Train based on Rigid Body Motion Analysis  
**Tae-Jin Shin and Sang-Kwon Lee**
- 21 Active Noise Control for Interior Noise of Passenger Car Based on Pre-Processing Using Order Filter  
**Seung-Min Lee, In-Deuk Kang, Tae-Jin Shin and Sang-Kwon Lee**
- 27 The Correlation of Surface Roughness and Pressure Drop for a U-tube of the Heat Exchanger in a Steam Generator  
**Jeong-Hoo Park, Se-Myong Chang, Shin-Young Lee and Gyun-Ho Gim**
- 30 Study on Secondary Combustion Thermo-impact of Gas and Air in Confined Vessel  
**Xiao-lei Hu, Gui-gao Le, Da-wei Ma and Jiayi Guo**
- 35 Active Back Pressure Mechanism for Electric Scroll Compressor  
**Jongbo Won, Ilyoung Park, Jeongsik Shin, Yongnam Ahn and Kweonsoo Lim**
- 40 Performance of Biocomposites Reinforced by Cellulose Nanofiber Obtained from Paper Wastes  
**Hitoshi Takagi, Antonio N. Nakagaito, Satoshi Sugano, Yuya Muneta and Jitendra K. Pandey**
- 44 A Study on the Heat Transfer Characteristics for the Shape of the Heat Sink  
**E. C. Jeon, S. G. Kim, J. H. Sung and Y. H. Kim**
- 48 A Fuzzy AHP Framework for Multi Criteria Decision Making of a Sustainable Product Design  
**Zahari Taha, H.A. Salaam, T. M. Y. S Tuan Ya and Mohd Razali Mohamad**
- 55 An Optimal Ordering and Pricing Policy for Deteriorating Item under the Two-echelon Inventory System in Reverse Logistics  
**Yufang Chiu, He-Hsuan Hsu and Jia-Rong Hong**
- 60 Energy-Efficient Hybrid Flow Shop Scheduling With Lot Streaming  
**Tzu-Li Chen, Yi-Han Chou, I-Chin Wu, Yen-Ming Chen and Tzu-Chi Liu**

- 66 Design of Energy Efficient Distillation Columns Systems  
**Mohd Faris Mustafa, Noor Asma Fazli Abdul Samad, Kamarul 'Asri Ibrahim, Norazana Ibrahim and Mohd Kamaruddin Abd. Hamid**
- 70 A Study on Enhancing Flame Retardant Performance of Building Materials using Carbon materials  
**Hyun Jeong Seo, Su-Gwang Jeong, Jeong-Hun Lee, Sumin Kim, Dong Won Son and Sang-Bum Park**
- 77 Numerical Investigation of Heating Mechanism in Ultrasonic Imprinting  
**Jong Han Park, Ki Yeon Lee and Keun Park**
- 80 Experimental Study of Friction Reduction of Surface Texturing on Cylindrical Surface  
**Rendi Kurniawan and Tae Jo Ko**
- 83 Objective Quantification and Subjective Evaluation for the Fastening Force of Seat Belt in a Vehicle Using Seat Belt in a Vehicle using Force Measurement Robot  
**Hye-young Cho and Sang-kwon Lee**
- 90 Effect of  $Mg_3AlNi_2$  Content on the Cycling Stability of  $Mg_2Ni-Mg_3AlNi_2$  Hydrogen Storage Alloy Electrodes  
**Sheng-Long Lee, Yu-Chih Tzeng and Hui-Yun Bor**
- 95 Test Planning for a Large Wind Turbine Blade Full Scale Static Test Considering the Test Set-up  
**Jin Bum Moon, Hak Gu Lee and Seung-Un Yang**
- 99 A Study on the Recycling of Food -Salt Reduction Plan for Compositing of Food Waste  
**Doo Hee Han**
- 101 Steering Characteristics of AWS(All Wheel Steering) System using Virtual Rigid Axles  
**Kyung-Ho Moon and Jai-Kyun Mok**
- 103 Analyze the Ride Comport Characteristics of Railway Vehicles in the Segment of Rail Corrugation  
**Chan-Woo Lee**
- 106 Investigation of the Effect of Tool Wear and Surface Roughness in Ultrasonic-assisted Milling  
**Chang Ping Li, Min Yeop Kim, Tae Jo Ko and Jong Kweon Park**
- 109 Supercapacitor Based on Polypyrrole and TEMPO-oxidized Bacterial Cellulose Nanofibers (TOBCN) Nanocomposite Films  
**Fan Wang, Jong Yun Kim, Deok-Hyu Lee and Chang-Doo Kee**
- 111 Development of an Advanced Suturing Mechanism for an Endoscopic Surgery Using Successive Suturing Device  
**Byung Gon Kim, Kyung Tae Jun, Kyungnam Kim and Daehie Hong**
- 117 An Experimental Study on the Multiple Layer Perforated Panel Sound Absorbing System for Railroad Noise Reduction  
**Yoon-Sang Yang, Du-San Baek, Dong-Hoon Lee, Jae-Chul Kim and Choon-Keun Park**
- 120 Complete Recycling Method for Lungfishes Waste  
**Doo Hee Han**
- 123 A New Energy Efficiency Index for the German Manufacturing Sector  
**Jörg Mandel and Alexander Sauer**

- 131 Overview of Mechanical and Electrical Products Low Carbon Design  
**Zhifeng Liu, Mengdi Gao , Huanbo Cheng, Qingyang Wang and Xuan Zhou**
- 140 Standardized Hazardous Materials Management for Global Environmental Compliance in Industrial Enterprises  
**Markus Hornberger, Robert Mieke and Thomas Bauernhansl**
- 152 High Income Return and Safe Investments through Financing of Energy Efficient Measures in the Industry  
**Robert Kasprowicz, Siegfried Stender and Thomas Bauernhansl**

# Influence of Spark Gap in EDM based on Buckingham's $\pi$ Theorem

S. H. Yeo<sup>1#</sup> and J. Y. Toh<sup>1</sup>

<sup>1</sup> School of Mechanical and Aerospace Engineering, Nanyang Technological University, 50 Nanyang Avenue, Singapore 639798  
# Corresponding Author / E-mail: mshyeo@ntu.edu.sg

KEYWORDS : EDM, Spark Gap, Surface Roughness

*This project aims to highlight the importance of spark gap in EDM in relations to surface roughness. Two output, spark gap and surface roughness were examined through Buckingham's  $\pi$  theorem, a form of dimensional analysis tool, being the most important part of the project. This tool was utilized to denote on the most influential parameters and sub parameters that influence spark gap and further elaborate on the influence of spark gap in surface roughness. EDM experiments conducted using SKD-11 steel work piece and copper rod electrode. These experiments were used to compare with the formulated equation from Buckingham's  $\pi$  theorem to determine the accuracy of these equations in relation with the experimented data. From the observations, spark gap has a significant impact in surface roughness which is a basic parameter of length in dimension, created by variation of discharge voltage, current and time. Discharge voltage being the most influential parameter. This observation may further enhance the surface finish in EDM relevant to precision engineering.*

## 1. Introduction

Electro discharge machining (EDM) is an operation made possible by erosive action. Two electrodes are held in close proximity in a dielectric fluid during the sparking process. The dielectric fluid continuously filled the spark gap throughout the process and to serve as an insulator and subsequently deionizes in a cyclical manner. With the spark formation, plasma channel will be formed, anode and cathode will erode in this process which creates debris to be flushed away to maintain a stable process repeatedly. In conventional EDM, input parameters such as discharge current (I), voltage (V) and time or pulse on time ( $t_{on}$ ) which are functions of discharge energy are the key parameters that influence the output product such as surface roughness and spark gap. Several studies have reported that have shown that an increase in discharge current, duration and energy would result in a larger spark gap [1, 2]. The discharge current is found to have a larger influence on the spark gap as compared to that of the discharge duration. The spark gap is inversely proportional to the discharge duration which infers, an increase in discharge duration will result in a decrease in spark gap. Klocke [3] observed that spark gap is most influenced by voltage. The influence of discharge time with spark gap is somewhat unclear as the discharge energy is dependent on several other parameters. The effects of spark gap on surface roughness is not well described quantitatively [4].

The objectives of this work are based on Buckingham's  $\pi$  theorem are:

- To investigate discharge voltage, current and time in relations to spark gap
- To investigate spark gap in relations to surface roughness

## 2. Methodology

The approach based on Buckingham's  $\pi$  theorem is used to study the parametric effects [5].

### 2.1 Derivation of Spark Gap Equation

The spark gap condition may be influenced by the parameters as shown in Table 1. These parameters have their own dimensions in mass, length, time, current and absolute temperature (M, L, T, I and  $\theta$ ). Table 1 shows the tabulation of each parameter according to the dimension units. From this tabulation, equation (1 -5) can be obtained by grouping them in its unique dimensions. The dimension mass (M) in equation (1) can be formed. Similar steps were to be applied for other dimensions (L, T,  $\theta$  and I).

$$K_4 + K_6 - K_7 + K_8 = 0 \quad (1)$$

$$K_1 - 3K_4 + 2K_5 + K_6 - 3K_7 + 2K_8 = 0 \quad (2)$$

$$K_3 - 2K_5 - 3K_6 + 3K_7 + 3K_8 = 0 \quad (3)$$

$$K_5 + K_6 = 0 \quad (4)$$

$$K_2 + 2K_7 - K_8 = 0 \quad (5)$$

Solving the simultaneous equations as shown in equation (6) to (8) and grouping the parameters in equation (9), the discharge current, voltage and time is derived for the spark gap given in equation (10).

$$\pi_1 = \frac{G \rho^{0.32} C_p^{0.26}}{\sqrt{0.11} k^{0.26} \sigma^{0.05}} \quad (6)$$

$$\pi_2 = \frac{I \rho^{1.75} k^{5.25} V^{1.8}}{C_p^{5.25} \sigma^{0.25}} \quad (7)$$

$$\pi_3 = \frac{t k^{0.18}}{\sqrt{0.18} \rho^{0.09} C_p^{0.18} \sigma^{0.09}} \quad (8)$$

$$\pi_1 = \alpha [\pi_2, \pi_3] \quad (9)$$

Table 1 Parameters of influence to spark gap

	Properties	Symbol	Dimensions
K <sub>1</sub>	Spark gap	G	L
K <sub>2</sub>	Discharge current	I	I
K <sub>3</sub>	Discharge time	t	T
K <sub>4</sub>	Density	$\rho$	ML <sup>-3</sup>
K <sub>5</sub>	Specific heat	C <sub>p</sub>	L <sup>2</sup> T <sup>-2</sup> $\theta$ <sup>-1</sup>
K <sub>6</sub>	Thermal coefficient	k	MLT <sup>-3</sup> $\theta$ <sup>-1</sup>
K <sub>7</sub>	Electric conductivity	$\sigma$	M <sup>-1</sup> L <sup>-3</sup> T <sup>3</sup> I <sup>2</sup>
K <sub>8</sub>	Voltage	V	ML <sup>2</sup> T <sup>3</sup> I <sup>-1</sup>

Solving the simultaneous equations and grouping the parameters for discharge current, voltage and time, the derived equation for spark gap yields in equation (10). The properties,  $\rho$ ,  $C_p$ ,  $k$ , and  $\sigma$ , that are grouped and denoted as  $\beta$ , which is kept constant throughout the experiments. This will allow the spark gap to be solely based on the relations between discharge current, voltage and time.

$$\text{Spark gap, } G = \beta [ITV^{1.42}] \quad (10)$$

Similar steps that were used for the derivation of spark gap are to be applied in the surface roughness equation (11).

$$\text{Surface roughness, } R_a = \gamma [GI] \quad (12)$$

where  $\gamma$  represents the constant value.

## 2.2 Experimental Procedure

Makino Edge I EDM machine were used to conduct the EDM experiment. This system will be incorporating with kerosene dielectric fluid and two electrodes. One will be diameter 5mm copper tool electrode; the other will be (37x21x20mm) SKD-11 steel work piece. The influence of voltage, current and time on spark gap were conducted with various machine settings, E-1023, E-1025, E-1026 and E-1027. Each machine setting is incorporated with a unique values of voltage, current and time.

Talyscan 150 were used to measure the surface roughness and total depth. This spark gap is measured by using the difference between the total depth measured by the Talyscan 150 and the machining depth of 180  $\mu$ m.

Table 2 Experimental Set up

Electrode tool	Cu, $\varnothing$ 5mm
Workpiece material	Steel, Skd-11
Dielectric powder	Silicon carbide , 50microns
Dielectric fluid	Kerosene
EDM machine	Makino Edge I
Topography scanning system	Talyscan 150
Scanning electron microscope	JEOL-JSM-5600LV
EDM depth	80 microns
Machine settings	E-1023;E-1025;E-1026; E-1027
Powder Concentrations	0g/l, 3g/l, 5g/l and 7g/l

Fig. 1 shows the machined surface for various settings and a typical voltage and current waveforms captured by an oscilloscope are shown Fig. 2 are recorded.

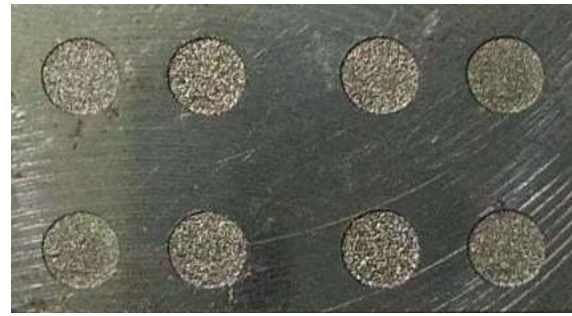


Figure 1 Machined component of various settings

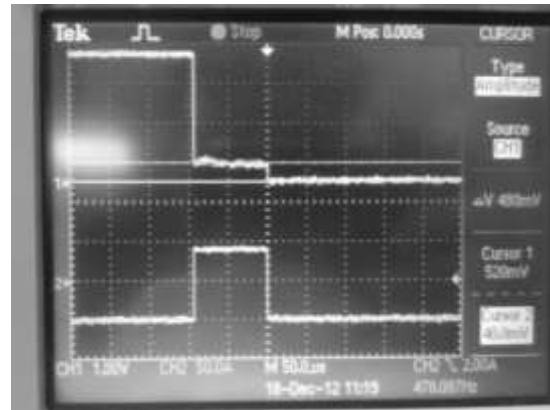


Fig 2: A typical pulse waveform for voltage and current

## 3. Results and Discussion

Buckingham's  $\pi$  equation (10) shows that spark gap is a function between  $ITV^{1.42}$  and material properties of steel, SKD11. Material properties ( $\beta$ ) were kept at constant throughout all the experiments; hence spark gap is a fully dependent on  $ITV^{1.42}$  variations.

The best-fit curve shown in Figure 3 gives an equation, Spark gap =  $53.56(ITV^{1.42})^{0.1691}$ , may be used to formulate a predicted spark gap by equating the basic input parameters into equation (10). This will result in a predicted spark gap can then be used to compare with the experimental spark gap. The difference between both will be used to calculate the accuracy of spark gap derived from Buckingham's  $\pi$  theorem. From Figure 3, it shows that with an increase in  $ITV^{1.42}$  will result in an increase in spark gap. The equation obtained in equation (6), shows that discharge voltage which has a 1.42 times higher power value is more influential in spark gap as compared to current and time, which defers from Gostimirovic et al. [1] in which current has a larger influence in spark gap. From the formulated equation (10), the results shows that an increase in discharge time will result in an increase in spark gap, which defers from Son[2] observations stating that discharge time is inversely proportional to the spark gap.

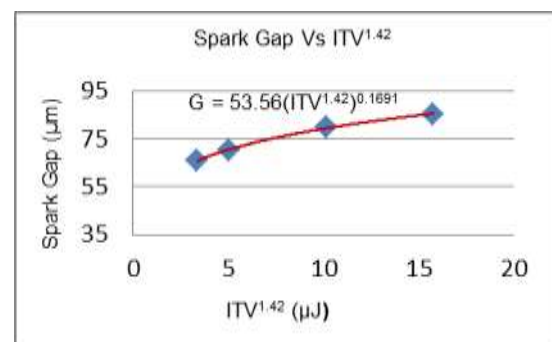
Fig. 3 Influence of "ITV<sup>1.42</sup>" on spark gap

Table 3 shows the various machine settings on the spark gap. The

percentage error is not more than 0.85% suggesting a high degree of accuracy.

Table 3: Error percentage of spark gap

Machine Setting	ITV <sup>1.42</sup> (mJ)	Calculated	Experiment	Error (%)
E -1023	3.36	65.85	65.9	0.08
E -1025	5.07	70.59	70	0.85
E -1026	10.18	79.42	80	0.72
E -1027	15.77	85.53	85	0.63

Under constant current setting, the surface roughness is found to increase linearly with spark gap, as shown Fig. 4. The predicted value can be compared with the data obtained from the experiment, which gives a relationship with R<sup>2</sup> of 0.9194. The result clearly matches the Buckingham's π theorem. The trend line is similar for the other machine settings.

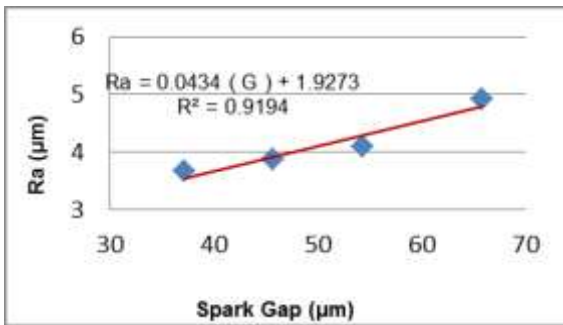


Fig. 4 Surface roughness versus spark gap

### 3. Conclusions

Spark gap which often seen as function of discharge current, time and voltage, can alter the surface roughness. The changes to the spark gap will affect the plasma channel. Discharge current, time and voltage have been commonly used to investigate on spark gap and surface roughness. This work has shown how this parameter spark gap may be influenced by these primary parameters, discharge current, time and voltage (I, T V), and to further show the spark gap as a primary parameter, dimension of length (L), and the relations between spark gap and surface roughness through the help of Buckingham's π theorem, a form of dimensional analysis tool. The major findings of this project are as follows:

- Buckingham's π theorem formulated spark gap equation,  $G = \beta [ITV^{1.42}]$ . This indicates that discharge voltage as basic primary parameters is the most influential parameter with a power index of 1.42 higher than discharge current and time. An increase in  $ITV^{1.42}$  will result in an increase in spark gap.
- Buckingham's π theorem formulated surface roughness,  $R_a = \gamma [GI]$  roughness change based on the variation of spark gap solely. Increase in spark gap will cause the surface roughness to increase hence resulting in a poorer surface roughness.

It is well known that high discharge energy will result in larger

spark gap. However, high energy may also result in a smaller spark gap, if discharge time is inversely proportional to spark gap [3], suggesting that it is more influential than other parameters. However, from the Buckingham theorem, the spark gap is a function of  $ITV^{1.42}$ , which clearly eliminates the possibility of higher energy producing a smaller spark gap. This is so because the influential parameters of discharge voltage and discharge time are not inversely proportional to spark gap.

### ACKNOWLEDGEMENT

The support rendered by the School of Mechanical and Aerospace Engineering, Nanyang Technological University is acknowledged.

### REFERENCES

1. Gostimirovic, M., Kavac, P., Sekulic, M. and Skoric, B., *Influence of discharge energy on machining characteristics in EDM*. Journal of Mechanical Science and Technology, 2012. **26**(1): p. 173-179.
2. Son, S., Lim, H, Kumar, A.S., and Rahman, M., *Influences of pulsed power condition on the machining properties in micro EDM*. Journal of Materials Processing Technology, 2007. **190**(1-3): p. 73-76
3. Klocke, F., Lung, D., Antonoglou, G. and Thomaidis, D., *The effects of powder suspended dielectrics on the thermal influenced zone by electrodischarge machining with small discharge energies*. Journal of Materials Processing Technology, 2004. **149**(1-3): p. 191-197
4. Kiyak, M. and O. Cakir, *Examination of machining parameters on surface roughness in EDM of tool steel*, Journal of Materials Processing Technology, 2007, **191** (1-3): p.141-144
5. Mistic, T.M., Najdanovic, L, and Nestic, L, *Dimensional Analysis in Physics and the Buckingham Theorem*, European Journal of Physics, 2010, **31** (4), p.893-906

# Selective Micropattern Replications using Ultrasonic Imprint Lithography

Keun Park<sup>1#</sup>, Hyun-Joong Lee<sup>1</sup> and Woosin Jung<sup>2</sup>

<sup>1</sup> Graduate Sch. Mechanical System Design Eng., Seoul Nat'l Univ. Sci. Tech., 232 Gongneung-gil, Nowon-gu, Seoul, 139-743, Republic of Korea

<sup>2</sup> Dept. Mechanical System Design Eng., Seoul Nat'l Univ. Sci. Tech., 232 Gongneung-gil, Nowon-gu, Seoul, 139-743, Republic of Korea

# Corresponding Author / E-mail: Second@abc.edu.hk, TEL: +852-1234-5678, FAX: +852-1234-5678

KEYWORDS : Ultrasonic Imprinting Lithography, Micropattern Replication, Selective Patterning, Mask Film

---

*Ultrasonic imprint lithography is a novel process in which micro/nanoscale patterns can be replicated on thermoplastic polymer films with short processing time and low energy consumption. In this study, a selective ultrasonic imprinting process is developed to replicate micropatterns with arbitrary profiles. To replicate micropatterns on selected areas, the conventional imprinting process is modified by placing a profiled metal mask between the horn tip and target film. Ultrasonic waves are then selectively transferred to the target film through the mask film, from which micropatterns can be replicated onto the predefined areas. Experimental observations clearly indicate that the temperature increase and the resulting material softening are concentrated in the masked region, so that micropatterns can be selectively replicated. The proposed selective imprinting process is then applied to micropattern replications on arbitrarily profiled areas. In these applications, the effect of imprinting conditions is discussed in terms of the replication quality in both the masked and the unmasked regions. Through these experimental investigations, it is founded that moderate imprinting conditions are required not only to improve the replication quality in the masked region, but also to prevent excessive replication in the unmasked region.*

---

## 1. Introduction

Nanoimprint lithography (NIL) is a micro/nanoscale patterning technology for polymer substrates, which ensures productivity sufficient for mass production.<sup>1</sup> NIL can generally be categorized into two processes: hot embossing and UV imprinting. The hot embossing uses preheated molds to replicate micro/nano-patterns on thermoplastic polymer substrates,<sup>2</sup> and has the advantages of simple and economical setup as well as the disadvantages of long cycle times.<sup>3</sup> In contrast, UV imprinting uses transparent molds and UV-curable resins to transfer nanoscale patterns at room temperature and low pressure.<sup>4</sup>

Recently, ultrasonic vibration energy has been used to improve the moldability in polymer processing such as hot embossing<sup>5</sup> and injection molding<sup>6</sup>. The use of ultrasonic vibration energy was further developed to ultrasonic imprint lithography (U-NIL) that replicates micro/nano patterns on thermoplastic polymer.<sup>7-8</sup> U-NIL was also applied to the fabrication of superhydrophobic surfaces by forming micro/nano hierarchical structures on thermoplastic polymer substrates.<sup>9</sup>

In NIL processes, micro/nano patterns are fabricated directly on

the surfaces of mold inserts. These patterned regions usually have a rectangular shape for easier manufacturability. In this study, an efficient fabrication method is proposed to develop micropatterns on predefined areas. The proposed process is based on U-NIL, and a profiled mask film is placed between the horn surface and the target film. Thus, the regions in contact with the mask film are softened locally, and micropatterns can then be selectively replicated. The validity of the proposed selective U-NIL is investigated through several experiments.

## 2. Selective U-NIL using Mask Film

U-NIL process uses ultrasonic vibration energy to soften the surface of thermoplastic polymer for micropattern replication. Figure 1 (a) shows a configuration of the U-NIL process. A number of micropatterns are engraved on the mold surface, and the horn vibration is transferred to the mold surface through the polymer film (target film). This ultrasonic vibration causes repetitive deformation and the resulting frictional heat on the polymer surfaces. Thus, the surface region of the target film is sufficiently softened that the

micropatterns engraved on the mold can be replicated. Figure 1 (b) shows a configuration the selective U-NIL process [10]. A mask film with an arbitrary profile is located between the horn and the target film. Ultrasonic wave is then transferred from the horn to the target film through the mask film. Thus, only the regions contacted with the mask film are affected by the ultrasonic excitation. Micropatterns can then be selectively replicated in these regions.

Experiments were performed to verify the feasibility of the selective U-NIL. A prism-patterned mold of which pitch and depth are 48.6 and 16.5  $\mu\text{m}$  was used. As a target film, 30 x 30 x 0.3  $\text{mm}^3$  amorphous polyethylene terephthalate (APET) films were used. An AA-1050 film was used as the mask film. The size of the mask film was 14.1 x 14.1 x 0.4  $\text{mm}^3$ , of which area (200  $\text{mm}^2$ ) was smaller than the area of target film (900  $\text{mm}^2$ ). U-NIL experiments were performed under the condition of 2.0 s vibration time and 0.45 MPa pressure. Figure 2 shows the photograph of the replicated film with an enlarged view for the inside region (A) and the boundary region (B). It can be seen that the micropatterns were successfully replicated in the masked region while they were not replicated in the unmasked region.

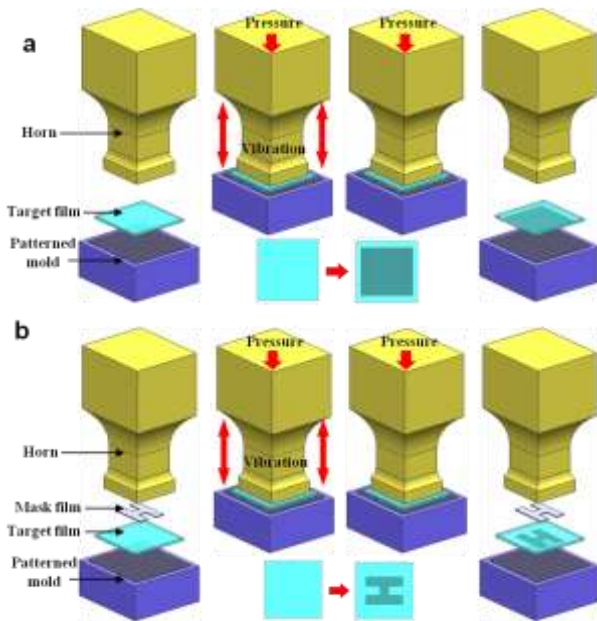


Fig. 1 Configurations of the ultrasonic imprinting process: (a) conventional imprinting, and (b) selective imprinting [10]

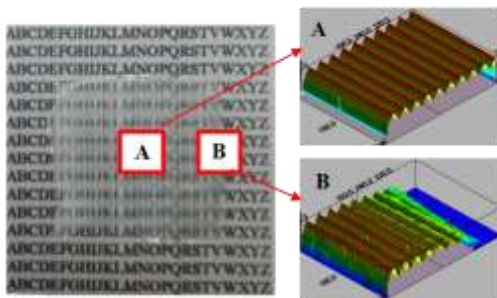


Fig. 2 Replicated polymer film using a rectangular mask and the measured surface profiles for the inside and boundary regions

### 3. Micropattern Replications on Arbitrary Regions

Based on the preliminary results of the previous section, the selective U-NIL process was applied to micropattern replications on arbitrarily profiled regions. Figure 3 (a) shows a negative type mask where the logo for *SeoulTech* is inscribed. The outer diameter of the mask was 32 mm, and the resulting mask area was 605.3  $\text{mm}^2$ . Since this area is much larger than those of the previously used ones, the vibration time was set in the higher range, from 3.0 s to 5.0 s. The mold temperature and imprinting pressure were set to 70  $^{\circ}\text{C}$  and 0.6 MPa, respectively.

Figure 3 (b) shows the replicated APET film under 4.0 s ultrasonic vibration. It is observed that the film transparency was diminished in the masked region, due to surface scattering on the replicated micropatterns. For quantitative comparison of the transparency, transmittance profiles across the section D-D' were measured for the replicated samples under the three imprinting conditions, and plotted in Figure 3 (c). It can be seen that the transmittance in the masked region was higher than 25% when the vibration time was set to 3.0 s, which means that the micropatterns were not sufficiently replicated. On the other hand, the cases of 4.0 and 5.0 s imprinting show low transmittance values (less than 10%) in the masked region. However, at a vibration time of 5.0 s, transmittance reductions were also observed near the mask boundary, even in the unmasked region. This can also be explained by the flash generated near the mask boundary when excessive imprinting conditions were implemented.

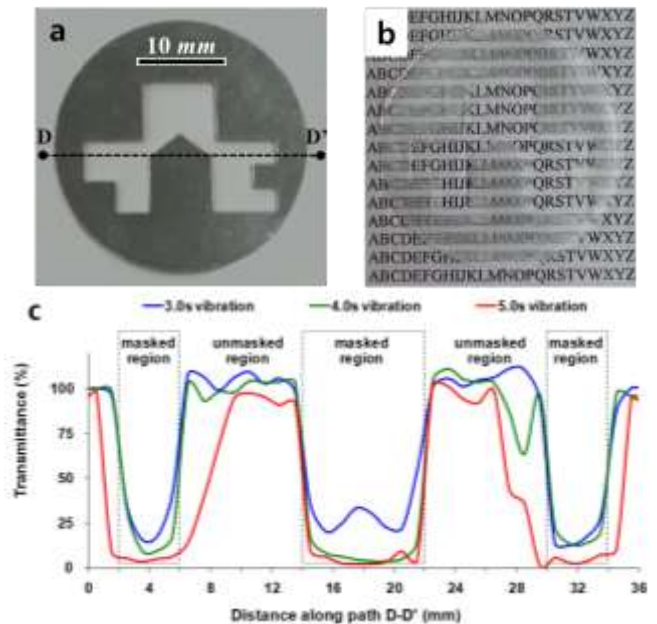


Fig. 3 Selective imprinting using a mask of arbitrary shape: (a) a mask film with a negative logo profile, (b) a replicated polymer film and (c) transmittance comparison along the path D-D' for various vibration time.

Figure 4 shows measured surface profiles at various locations of micropatterns when the 4.0 s vibration was applied. It can be seen that micropatterns were successfully replicated in the masked region without a flash generation. Considering that the replication quality shows apparent differences across the mask boundaries, it can be

concluded that the proposed selective imprinting enables the micropattern replication on arbitrarily-shaped regions under appropriate imprinting conditions.

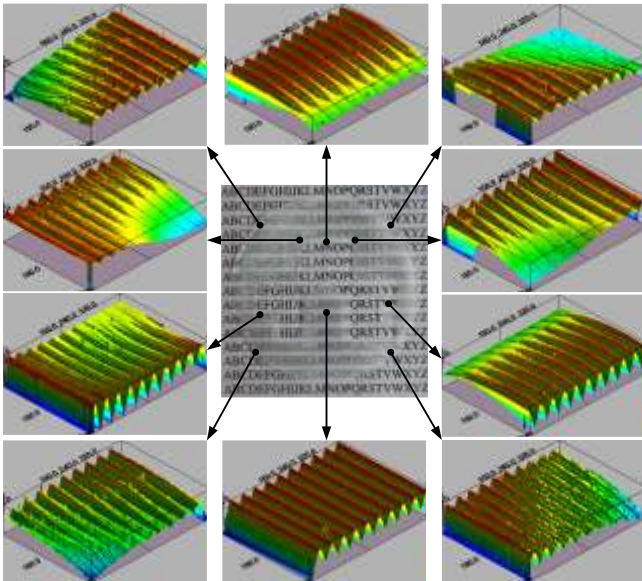


Fig. 4 Surface profiles of the replicated micropatterns at various locations on the logo.

#### 4. Conclusion

In this study, a selective U-NIL process was developed to replicate micropatterns on arbitrarily-profiled regions. The proposed process uses an arbitrarily-profiled mask film to focus ultrasonic waves selectively on the target regions where micropatterns are to be replicated. Experimental observations clearly indicated that the material softening was concentrated in the masked region, so that micropatterns could be selectively replicated. Micropattern replication experiments were further performed using arbitrarily profiled mask films. The effectiveness of the proposed selective U-NIL was evaluated by comparing the optical transmittance between the masked and unmasked regions. Through experimental investigations under various imprinting conditions, it was founded that moderate imprinting conditions were required not only to improve the replication characteristics in the masked region, but also to prevent excessive replication in the unmasked region.

#### ACKNOWLEDGEMENT

This research was financially supported by National Research Foundation of Korea (NRF) grants funded by the Ministry of Education and MSIP, Republic of Korea (Grant number: NRF-2013R1A1A2A10004709 and NRF-2013M2B2A4040973).

#### REFERENCES

1. Lan, H., Ding, Y., Liu, H. and Lu, B., "Review of the wafer stage for nanoimprint lithography," *Microelec. Engng.* Vol. 84, No. 4, pp. 684-688, 2007.
2. Chou, S. Y., Krauss, P. R. and Renstrom, P. J., "Nanoimprint lithography," *J. Vac. Sci. Technol. B*, Vol. 14, No. 6, pp. 4129-4133, 1996.
3. Hecke, M. and Schomburg, W. K., "Review on micro molding of thermoplastic polymers," *J. Micromech. Microeng.*, Vol. 14, No. 3, pp. R1-14, 2004.
4. Yang, Z. H., Chien, F. C., Kuo, C. W., Chueh, D. Y., Tung, Y. C. and Chen, P., "Interfacial adhesion and superhydrophobicity modulated with polymeric nanopillars using integrated nanolithography," *J. Micromech. Microeng.*, Vol. 22, No. 12, 125026, 2012.
5. Mekar, H., Goto, H. and Takahashi, M., "Development of ultrasonic micro hot embossing technology," *Microelec. Engng.* Vol. 84, No. 5-8, pp. 1282-1287, 2007.
6. Michaeli, W., Kamps, T., and Hopmann, C., "Manufacturing of polymer micro parts by ultrasonic plasticization and direct injection," *Microsyst. Technol.*, Vol. 51, No. 2, pp. 243-249, 2011.
7. Khuntontong, P., Blaser, T. and Schomburg, W. K., "Fabrication of molded interconnection devices by ultrasonic hot embossing on thin polymer films," *IEEE Trans. Electr. Pack. Manufact.*, Vol. 32, No. 3, pp. 152-156, 2009.
8. Seo, Y. S. and Park, K., "Direct patterning of micro-features on a polymer substrate using ultrasonic vibration," *Microsyst. Technol.*, Vol. 18, No. 12, pp. 2053-2061, 2012.
9. Cho, Y. H., Seo, Y. S., Moon, I. Y., Kim, B. H. and Park, K., "Facile fabrication of superhydrophobic poly (methyl methacrylate) substrates using ultrasonic imprinting," *J. Micromech. Microeng.*, Vol. 23, No. 5, 055019, 2013.
10. Jung, W. S. and Park, K., "Selective Ultrasonic Imprinting for Micropattern Replication on Predefined Areas," *Ultrasonics*, Vol. 54, No. 6, pp. 1495-1503, 2014.

# Design of Signal Processing System for 3D Printing-based Flexible Tactile Sensor

JuKyoung Lee<sup>1</sup>, Suk Lee<sup>1</sup> and KyungChang Lee<sup>2#</sup>

<sup>1</sup> School of Mechanical Engineering, Pusan National University, San 30, Changjeon-dong, Kumjeong-ku, Busan, Korea, 609-735

<sup>2</sup> Department of Control and Instrumentation Engineering, Pukyong National University, 559-1, Daeyeon-3 dong, Num-gu, Busan, Korea, 608-737

# Corresponding Author / E-mail: gclee@pknu.ac.kr, TEL: +82-51-629-6332

KEYWORDS : Tactile Sensor, Piezoresistive, Signal Processign, Sensor System, Pressure Sensitive

---

*In this paper, flexible tactile sensors can provide valuable feedback to intelligent robots about the environment. This is especially important when the robots, e.g., service robots, are sharing the workspace with human. This paper presents a flexible tactile sensor that was manufactured by direct writing technique, which is one of 3D printing method with multi-walled carbon nano-tubes. The signal processing system consists of three parts: analog circuits to amplify and filter the sensor output, digital signal processing algorithms to reduce undesired noise, and detection algorithm for contact initiation and termination. Finally, experimental setup is implemented and evaluated to identify the characteristics of the flexible tactile sensor system. This paper showed that this type of sensors can detect the initiation and termination of contacts with appropriate signal processing.*

---

## 1. Introduction

Today, robots are used not only on industrial sites but in various other fields, too. The boundaries between human life and robots are being reduced, and robots and humans come into physical contact under a variety of different circumstances. For several years, robots have operated around humans within industrial and scientific settings, but their presence within the home and general society is becoming ever more common nowadays. During a robot's operation, physical contact with a human might be expected or unexpected, and can enhance or interfere with the execution of a robot's behavior.

The movement of robots and the stability of their systems are being researched with particular attention on ways to avoid collision, which is an important issue that must be addressed. There are ways to prevent accidents and techniques for avoiding potential collisions that could occur when driving a robot. The method for measuring the torque value of the robot actuator is one of them. However, torque-based collision avoidance systems that enable a robot to detect the size of a shock are very restrictive. Therefore, regardless of the external environment, sensors for a robot's shock protection system are required.<sup>1</sup>

This paper describes the development of signal processing systems for use in a flexible tactile sensor. The entire configuration of

a signal processing system consists of the analog signal processing and digital signal processing parts and the main control part. This paper is focused only on the signal analysis of the measured data from sensor devices and provides the early stages of research for the improvement and enhancement of signals. In this paper, part of the research focuses on the implementation of a flexible tactile sensor that can be applied in robot signal processing. The purpose of the implementation of the analog signal processing unit is to remove the external disturbance when an input signal is detected in a sensor. The performance of the implemented signal processing unit was tested by measuring and analyzing the pressure using a pressure gauge sensor and assessing whether or not the measured data was correct.

This paper is organized into five sections including this introduction. Section 2 gives a brief overview of flexible tactile sensors and analog signal processing, and Section 3 presents the application of the system, while the experimental results of our system are given in Section 4. Finally, the summary and conclusions are presented in Section 5.

## 2. Tactile sensor

Tactile sensing is a field that is rapidly progressing and the concomitant developments are becoming more valuable. One major

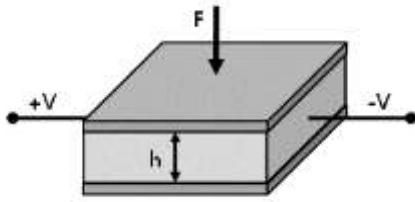


Fig. 1 The structure of a tactile sensor

use of tactile sensing is minimally invasive surgery. This technology allows surgeons to make smaller incisions and use sensors to virtually feel and look at the internal organs of a patient. A highly developed tactile sensor could potentially even discern cancerous cells from healthy cells in a person's body.

Tactile sensors can be classified as force/torque sensors, dynamic sensors, and thermal sensors.<sup>2-4</sup>

**2.1 Force/Torque sensors**

Force/torque sensors are often used in combination with tactile arrays to provide information for force control. A single sensor can sense loads anywhere on the distal link of a manipulator and, not being subject to the same packaging constraints as a "skin" sensor, can generally provide more precise force measurements at a higher bandwidth. If the geometry of the manipulator link is defined, and if single-point contact can be assumed (as in the case of a robot finger with a hemispherical tip contacting locally convex surfaces), then a sensor can provide information about the contact location by ratios of forces and moments in a technique called "intrinsic tactile sensing."

**2.2 Dynamic tactile sensor**

The most common dynamic tactile sensors are small accelerometers at the fingertips or in the skin of a robotic finger. They function roughly like pacinian corpuscles in humans and have a correspondingly large receptive field so that one or two skin accelerometers suffice for an entire finger. These sensors are particularly effective for detecting an object, making and breaking contact, and detecting the onset of slip and the vibrations associated with sliding over textured surfaces.

A second type of dynamic tactile sensor is the stress rate sensor. If a fingertip is sliding at a speed of a few centimeters per second over small asperities in a surface, the transient changes in stresses in the skin will be significant. A piezoelectric polymer, such as polyvinylidene fluoride (PVDF), which produces a charge in response to strain, can be used to produce currents proportional to the range of change of stress.

**2.3 Thermal sensor**

Thermal sensors are an important component in the human ability to identify the materials of which objects are made (think of how metal feels cool to the touch compared to wood) but are not used frequently in robotics. Human thermal sensing involves detecting thermal gradients in the skin, which correspond to both the temperature and thermal conductivity of an object. Robotic thermal

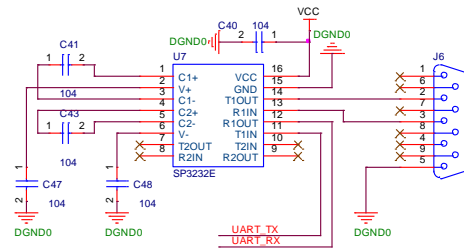
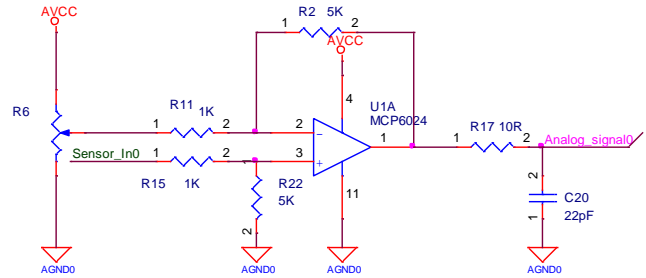


Fig. 2 Signal processing schematic



Fig. 3 Signal processing and filter controller

sensors involve peltier junctions in combination with thermocouples or thermistors. Difficulties have been encountered in obtaining sufficient resolution and time responses when using them to distinguish between different materials.

Laboratories use tactile sensors, as shown in Fig. 1, on force/torque-based sensors. The tactile-sensing sensor employed in our research is commercially available and can be used on all robots. This tactile sensor designed pressure-sensitive materials that use mixture of conductive material and rubber like human skin. Hence our tactile sensor has excellent flexibility and elasticity by the material surrounding the sensor for copying human skin.

**3. Sensing device system**

In the proposed tactile signal processing device for detecting disturbances of tactile sensor analog data, circuitries were implemented to correct the data in the sensor signals and signal processing algorithms. A signal processing circuit is proposed, and this structure could be applied in more than one sensor devices as it works in the measurement environment of the analog signal.

The signal processing system in the tactile sensor is configured by the control processor part responsible for the processing of the signals,

which are in turn obtained with the signal processing part responsible for acquiring the signal and transmission, as well as management, determination, and control. The configuration of the signal processing part, an analog signal processing circuit, comprises an I/V converter, signal amplifier, and signal filter. The tactile sensor consists of the sensor values for the disturbance rejection filter circuit, as shown in Fig. 2 In the signal processing part, the input data gets to be the analog-digital converter (ADC) of the controller process part. This signal processing controller has 16 channel analog input signal(Fig. 3).

#### 4. Experimental results

The tactile sensor signal processing systems for the signal processing of the sensor data gained by the input analog signal pressure. For smooth functioning of the tactile sensing system, the following signal processing experiments were needed:<sup>5-6</sup>

- i. Flexible tactile sensor signal processing operations for the prevention of data element errors due to the pressure of the tactile sensor.
- ii. Reliable pressure measurement comparison experiments for the validation of the proven pressure measuring system.

Measuring tactile sensor system is configured and measure up to 500N, resolution of 0.1N. Measure pressure distribution the human body and support surfaces such as skin, fore, and backrests. This signal used removing noise to curve fitting. Curve fitting can involve either interpolation, where an exact fit to the data is required, or smoothing, in which a “smooth” function is constructed that approximately fits the data.<sup>7</sup>

The tactile sensors used a resistive-based technology. The application of a force to the active sensing area of the sensor resulted in a change in the resistance of the sensing element in inverse proportion to the force applied.

Once the analog signal processing determined the sensor value, the digital signal processing of the main controller was executed. First, it had to go through the ADC process by converting into a digital signal to a given sampling period, and quantization was required to process the main controller input value of the analog signal. The digital signal required filtering that selected and was designed to digitally filter the signal according to the application system.

#### 4. Experimental results

In this paper, we focused on the development of tactile sensor signal processing devices. The result constitutes a signal processing system that reduces the errors between the accuracy of the analog signal. The experiment was carried out using signal processing devices that have already been developed. Tactile sensing is likely to significantly impact overall robotics research. For instance, the incorporation of tactile information would require conventional data processing techniques and algorithms to be revisited. In this context, whole body tactile sensing will be of particular interest as most of the

existing tactile data handling techniques take into account tactile information from the fingers and hands or end-effectors of a robot. The results of the study are as follows:

The tactile sensor used in the experiment was appropriate for signal processing board design. The circuit schematic reduces the disturbances that occur in the tactile sensor characteristic analysis. The change of the output is different depending on the nature of the parts. In particular, the characteristics of the filter part significantly impacted the system errors. The tactile sensor can be applied to platform and component analysis. Tactile sensors are applicable for robot platform research and analysis. The research methods are applicable to finger and gripper robots

#### ACKNOWLEDGEMENT

This work was supported by Components and Materials International Collaborative R&D Program funded by the Ministry of Trade, Industry and Energy (MOTIE) of Korea)

#### REFERENCES

1. Jin, S. H., Lee, J. K., Lee, S., Lee, K. C., “Output Characteristic of a Flexible Tactile Sensor Manufactured by 3D Printing Technique”, *J.of KSPE*, Vol. 31, No. 2, pp. 149-156, 2014.
2. Howe, R. D., Popp, N., Akella, P., Kao, I., and Cutkosky, M. R., “Grasping, manipulation, and control with tactile sensing,” *International Conference on Robotics and Automation*, 1990.
3. Yussof, H., Ohka, M., Suzuki, H., Morisawa, N., and Takata, J., “Tactile sensing-based control architecture in multi-fingered arm for object manipulation,” *Engineering Letters*, vol. 16, no. 2, 2009.
4. Lee, M. H., Nicholls, H. R., “Tactile sensing for mechatronics: a state of the art survey,” *Mechatronics*, vol. 9, no. 1, 1999.
5. Dahiya, R., Metta, G., Valle, M., and Sandini, G., “Tactile sensing—from humans to humanoids,” *IEEE Trans. Robot. Autom.* vol. 26, no. 1, 2010.
6. Wikipedia. Tactile Sensors. Available: [http://en.wikipedia.org/wiki/Tactile\\_sensor](http://en.wikipedia.org/wiki/Tactile_sensor).

# Slip Detection of Robot Gripper using 3D Printing-based Flexible Tactile Sensor

HyeongJun Kim<sup>1</sup>, Suk Lee<sup>1</sup> and KyungChang Lee<sup>2#</sup>

<sup>1</sup> School of Mechanical Engineering, Pusan National University, San 30, Changjeon-dong, Kumjeong-ku, Busan, Korea, 609-735

<sup>2</sup> Department of Control and Instrumentation Engineering, Pukyong National University, 559-1, Daeyeon-3 dong, Num-gu, Busan, Korea, 608-737

# Corresponding Author / E-mail: gcleee@pknu.ac.kr, TEL: +82-51-629-6332

KEYWORDS : Tactile Sensor, Robot Gripper, Force Feedback Control, Slip Detection

---

*In this paper, we design a gripping force control system using tactile sensor to prevent slip when gripper tries to grasp and lift an object. We use a flexible tactile sensor for measuring uniplanar pressure on gripper's finger and develop an algorithm to detect the onset of slip using the sensor output. Those patients were able to view and recognize an object with their eyes and figure out the location for grasping, but were unable to figure out the strength to hold the object, without tactile feedback. We also use a flexible pressure sensor to measure the normal force. In addition, various signal processing techniques are used to reduce noise included in the sensor output. A 3-finger gripper is used to grasp and lift up a cylindrical object. The tactile sensor is attached on one of fingers, and sends output signals to detect slip. Whenever the sensor signal is similar to the slip pattern, gripper force is increased. In conclusion, this research shows that slip can be detected using the tactile sensor and we can control gripping force to eliminate slip between gripper and object.*

---

## 1. Introduction

Though robots can already perform human roles to improve quality of life, with the advancement of industrialization, people have attempted to research and develop robots that can autonomously respond to fluid, changing, and more complicated environment.<sup>1-4</sup> It is impossible for the existing commercial robots to respond to changes in the environment because they only process user's commands upon receipt. To overcome such circumstance and create a robot that responds to a changing environment, a sensor that transforms external stimulus into electrical signal can be used in combination with user's command. The sensors applied to robot include, but are not limited to, infrared or ultrasound sensor, which can measure distance between the sensor and object, gas sensor, which detects certain gases, acceleration sensor and gyro sensor, which detect acceleration and inertia, respectively, and strain gauge and pressure sensor, which detects force and pressure, respectively.

The output of the pressure sensor changes with respect to the pressure applied to the sensor. However, since a single pressure sensor only detects the pressure applied within a narrow range, it cannot be used to measure pressure applied to broader area. For this reason, an array of multiple pressure sensors, also referred to as tactile sensor, is used to partially measure the pressure applied to a wide

range. Attaching this tactile sensor to the surface of gripper provides information similar to the pressure applied when a person holds an object.

In the current study, a system was designed to detect the slip using tactile sensor feedback and control the gripper force to prevent the slip. The organization of the paper is as follows. In chapter 2, the flexible tactile sensor made of pressure sensitive material and signal process board, which processes feedback signals, are explained, followed by the explanation about slip detection mechanism using gripper, in which tactile sensor is attached. Then in chapter 3, gripper control system, which prevents slip, is verified through experiment, and lastly in chapter 4, the conclusion is drawn.

## 2. Flexible tactile sensors and signal processing system

### 2.1 Flexible tactile sensors

Tactile sensor based on pressure sensitive material uses mixture of conductive material and rubber like material for the sensing part, thus it has excellent flexibility and is able to create elasticity similar to that of human skin depending on the material surrounding the sensor. Another advantage is that it has easier manufacturing process. In addition, sensor needs to be flexible enough to be mounted at the end-point of gripper, and since the amount of output is smaller than

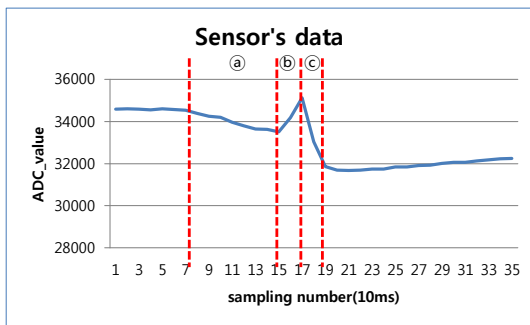
that of other tactile sensors, the composition is more simple.<sup>5-6</sup> Since this sensor used pressure sensitive material mixed with conductive material, it is very sensitive to pressure change and creates sensor noise, thus requiring the noise reduction filter. In addition, very low level of output caused by a wide range of resistance change ( $M\Omega \sim k\Omega$ ) calls for the need of signal amplification circuit.

**2.2 Signal processing for tactile sensors**

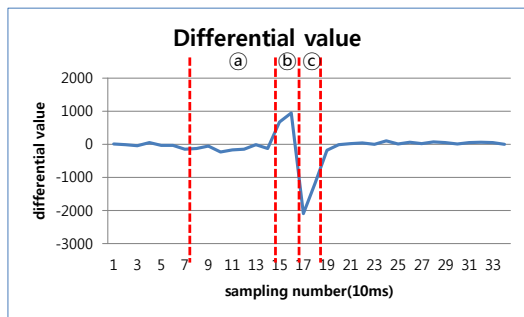
In the current paper, amplification-filter-filter-amplification circuit was composed by using four OP-AMP, and the amplification circuit used non-inverting amplification circuit. Both of the amplification circuits were set to have 5 times of amplification factor, or 25 times in total. The reason for having two separate amplifying circuits is because noise is amplified as well as the signal, decreasing the stability of the circuit. Therefore, noise can be reduced by going through two filters before the filtered signal is amplified again. The low pass filter allows signals with frequencies lower than the cut-off frequency to pass through but filters those with higher frequencies. The signals that have passed through this filter have the cut-off frequency of 100khz. A proper signal setting is obtained through many trials and errors

**3. Slip detection using tactile sensors**

The maximum static friction force between an object and gripper increases in relation to the grasping force of gripper, and slip can be prevented by controlling the gripper force. Fig. 1 shows derivatives of the sensor slip data produced during grasping of gripper and the input data. Fig. 1(a) shows the real-time data of the sensor that produced slip. Force was applied from the beginning of section (a), where the



(a) Sensor data



(b) Differential value

Fig. 1 Data and differential value of flexible tactile sensor

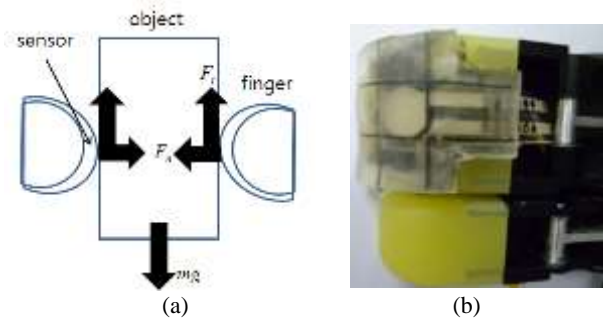
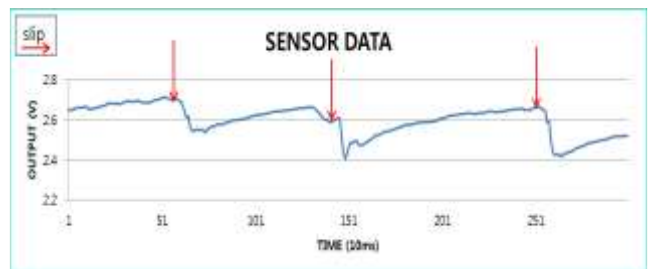


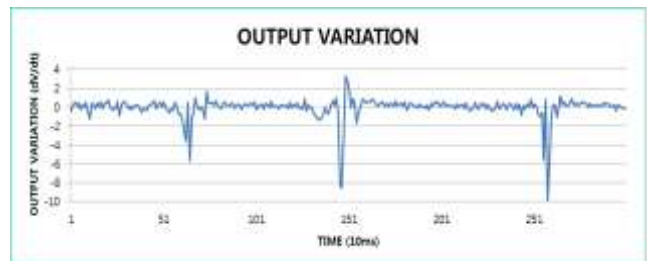
Fig. 2 Gripper's finger with tactile sensor

flexibility of the tactile sensor and static friction force seem to have produced distortion in the sensor. The actual point of occurrence of slip is at the beginning of section (b), where the friction force applied to transform sensor is changed from static friction to kinetic friction. As the elasticity of sensor is recovered, the output of sensor is considered to have increased due to the impact. However, since this section appears for a very short time, it can be confused with the sensor noise. For this reason, the author identifies the slip in section (c). In this section, the kinetic friction is relatively low compared to the impact from the previous section, so the output of sensor is considered to decrease rapidly. In order to distinguish this phenomenon, derivatives of sensor data are used. As shown in Fig. 6(b), the derivative of section (c) is very low.

To detect force and slip, tactile sensor-based robot gripper control system experiment was conducted, in which an object is grasped while moving the gripper up and down to find whether or not slip occurs between the object and the contact surface. Slip pattern detect function was used to detect occurrence of slip. When slip is detected, the grasping force is increased and when slip is not detected, the force is used to lift the object. Through this experiment, the minimum force required for the gripper to lift an object is determined. Fig. 3(a) shows consecutive output signal values at the sensor from Fig. 2 expressed

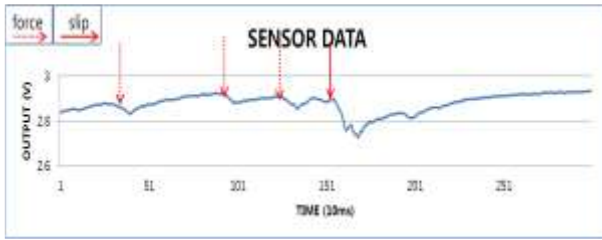


(a) Sensor data

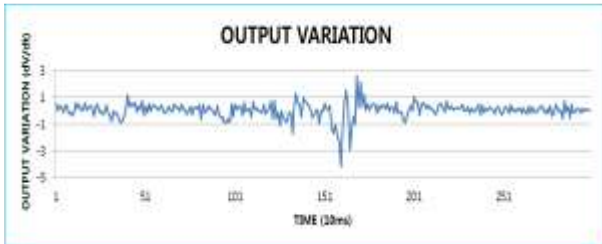


(b) Sensor output voltage variation

Fig. 3 Slip detecting signal



(a) Sensor data



(b) Output voltage variation with not enough force for slip

Figure 4. Compare slip signal with non-slip signal

as moving average. The arrow in the graph shows the change values of sensor in case of slip and Fig. 3(b) shows derived values of input signal values to the sensor to detect slip in gripper.

When it was not sufficient for slip to occur, resulting values were as shown in Fig. 4. Similarly, the occurrence of slip was measured with the last input signal. The output values after moving average decreases when the object does not slip, but the sections do not fall under the threshold, except for when slip occurs in derivatives.

#### 4. Conclusion

In the current paper, slip, which occurs when a robot gripper performs grasping, was detected by using feedback signals of flexible tactile sensors. Based on the input values of sensor, robot gripper drive system was composed and the performance of the system was verified by conducting experiment. In order to do so, when slip occurs during grasping of object, the feedback pattern of tactile sensor was analyzed. The slip preventive algorithm used slip detection to control force applied by gripper. In particular, it proposed force control mechanism that distinguishes between insufficient and sufficient force for the occurrence of slip, and as a result, the minimum force to prevent slip was found. In the future, studies shall be done in areas such as the weight and texture of the target object, as well as the linkage to parallel robot and structural change of conductive material for tactile sensor.

#### ACKNOWLEDGEMENT

This work was supported by Components and Materials International Collaborative R&D Program funded by the Ministry of Trade, Industry and Energy (MOTIE) of Korea)

#### REFERENCES

1. Yussof, H., Ohka, M., Suzuki, H., and Morisawa, N., "Tactile Sensing-based Control Algorithm for Real-Time Grasp Synthesis in Object Manipulation Tasks of Humanoid Robot Fingers," The 17th IEEE International Symposium on In Robot and Human Interactive Communication(RO-MAN), pp. 377-382, 2008.
2. Romano, J. M., Hsiao, K., Niemeyer, G., Chitta, S., and Kuchenbecker, K. J., "Human-Inspired Robotic Grasp Control with Tactile Sensing," IEEE Transactions on Robotics, Vol. 27, No. 6, pp. 1067-1079, 2011.
3. Weiss, L. E., Sanderson, A. C., and Neuman, C. P., "Dynamic Sensor-based Control of Robots with Visual Feedback," Robotics and Automation, IEEE Journal, Vol. RA-3, No. 5, pp. 404-417, 1987.
4. Kim, G. S., Shin, H. J., and Kim, H. M., "Development of Intelligent Robot' Hand with Three Finger Force Sensors," Journal of the Korean Society for Precision Engineering, Vol. 26, No. 1, pp. 89-96, 2009.
5. Kim, J. H., Lee, J. I., Park, Y. K., Kim, M. S., and Kang, D. I., "Development of Tactile Sensor and Its Application," Journal of the Korean Society of Precision Engineering, Vol. 21, No. 9, pp. 20-25, 2004.
6. Kim, M. S., Park, Y. K., and Kwon, S. Y., "Tactile Devices that Mimics Human's Sensory System," Physics and High Technology, pp. 15-22, 2010.

# Investigations of a Bistable Energy Harvester by Harmonic Balance Method

Huu-Tu Nguyen and Dung-An Wang<sup>#</sup>

Graduate Institute of Precision Engineering, National Chung Hsing University, 250 Kuo Kuang Rd, Taichung, Taiwan, ROC, 40227  
<sup>#</sup> Corresponding Author / E-mail: daw@dragon.nchu.edu.tw, TEL: +886-4-2285-2127, FAX: +886-4-2285-8362

KEYWORDS : Bistable, Energy Harvesting, Harmonic Balance Method, Duffing Oscillator

*A bistable mechanism for broadband energy harvesting is analyzed using the harmonic balance method. The bistable mechanism is a chevron-type mechanism consisting of springs and sliders. Interwell, high-energy oscillations of the bistable energy harvester are investigated. High speed during snap-through of the bistable mechanism contributes to large bandwidth of the bistable energy harvester. The bistable energy harvester has much larger bandwidth than a corresponding Duffing oscillator with similar force-displacement characteristics.*

## 1. Introduction

Traditional vibration energy harvesters, such as the cantilever type [1] or spring-supported proof mass type [2], are designed to harvest vibration energy at single resonant frequency. There is a growing need of harvesting broadband, low frequency, ambient vibration energy for wireless sensor node applications. Bistable mechanisms (BMs) have been shown to have a high potential for broadband vibration energy harvesting [3]. Bistable energy harvesters can be devised to harvest broadband, low frequency ambient vibration energy due to their nonlinear spring softening behaviors [4].

Nonlinearity has been exploited to increase the power output of the monostable, Duffing oscillators or impact type vibration energy harvesters. Due to the interwell oscillations of the BMs, the high velocity of the proof mass of the bistable energy harvesters may generate more electrical power than the monostable energy harvesters. The interwell oscillations can occur given the amplitude of the vibration source is large enough to excite the snap-through behaviors of bistable energy harvesters, so that they can efficiently capture more low-frequency vibration energy than the linear, resonant oscillators.

In this paper, a BM for broadband vibration energy harvesting is analyzed. Approximate analytical solutions are obtained by the harmonic balance method. Frequency response of the system is examined. Given the interwell oscillations, the BM is shown to have a much larger bandwidth than the monostable, Duffing oscillator. Experiments are carried out to verify the key features of the bistable energy harvesters.

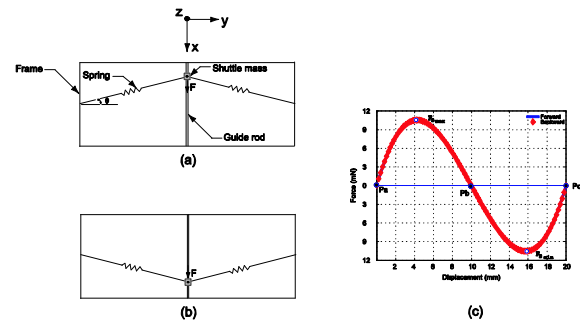


Fig. 1 (a-b) Principle. (c) A typical reaction force versus displacement curve of the BM.

## 2. Design

### 2.1 Principle

Fig. 1(a) is a schematic of a bistable energy harvester. A Cartesian coordinate system is also shown in the figure. Two springs are joined by a slider, which can move along a guide rod. The BM is symmetric with respect to the  $x$  axis. The spring has an inclination angle  $\theta$ . A permanent magnet can be glued to the slider and placed under a conducting coil to facilitate electromagnetic induction for energy harvesting. The assembly of the magnet and the slider is termed as the shuttle mass of the BM.

Schematics of the BM at two stable equilibrium positions,  $P_a$  and  $P_c$ , are shown in Fig. 1(a) and (b), respectively. The BM is initially at the first equilibrium position  $P_a$  (see Fig. 1(a)). Upon the application of a force  $F$  to the shuttle mass in the  $x$  direction, the

springs are compressed. When the compressive force in the spring increases to a maximum at a certain displacement of the shuttle mass, the mechanism snaps towards its second stable position  $Pc$  (see Fig. 1(b)). When the direction of the force  $F$  is reversed, the shuttle mass is moved along the  $-x$  direction. As the compression of the spring reaches its maximum, the mechanism snaps towards its first stable position  $Pa$ . The unstable equilibrium positions,  $Pb$  of the BM is indicated in Fig. 1(c).

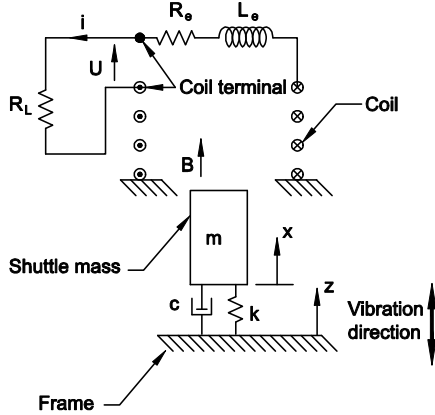


Fig. 2 A model of the bistable energy harvester

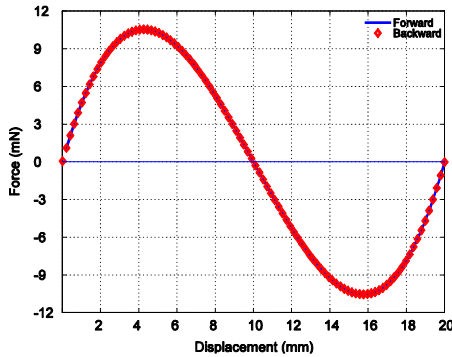


Fig. 3 f-d curves of forward and backward motions of the BM

## 2.2 Lumped model

Fig. 2 is a schematic of a lumped model of the BM and an equivalent electrical circuit for a coil and a load resistor. The motion of the shuttle mass is described by the coordinate  $x$ , and the movement of the support frame is described by the coordinate  $z$ .  $x$  is measured from the support frame. The shuttle mass  $m$  is connected to the support frame via a spring  $k$ . Mechanical damping of the BM is represented by a dashpot with damping coefficient  $c$ .  $i$  is the current through a resistive load  $R_L$  and the coil.  $R_e$  and  $L_e$  are the resistance and self inductance of the coil, respectively.

As the shuttle mass moves relative to the coil, a voltage  $U$  is induced in the loop of the coil, and the electrical energy is delivered to  $R_L$ . Equations of motion of the harvester are

$$m\ddot{x} + d\dot{x} + f(x) + \psi i = F \cos(\Omega t) \quad (1a)$$

$$L\dot{i} + (R_e + R_L)i - \psi\dot{x} = 0 \quad (1b)$$

where the overdot denotes the derivative with respect to time  $t$ . In this investigation, the value of the spring constant of the springs is taken as 100 mN/mm. The original length of the springs is 60.83 mm. The inclination angle  $\theta$  is  $9.46^\circ$ . Fig. 3 shows f-d curves of the forward motion, shown in the sequence of Fig. 2(a-b), and

backward motion, shown in the sequence of Fig. 2(b-a), of the BM based on finite element analyses. As seen in Fig. 3, positions  $x = 0$  and  $x = 10$  are the first and the second stable equilibrium positions of the BM, respectively. The reaction forces for the forward and backward motions can be fitted by a 4th order function,  $f(x)$ , as

$$f(x) = k_4 x^4 + k_3 x^3 + k_2 x^2 + k_1 x \quad (2)$$

where  $k_4 = 0.000007$ ,  $k_3 = 0.027171$ ,  $k_2 = -0.819697$ , and  $k_1 = 5.473274$ . These equations can be non-dimensionalized by defining

$$\omega = \frac{\Omega}{\sqrt{\frac{k_1}{m}}}, \quad \tau = \omega_1 t \quad (3)$$

$$\bar{x} = x \sqrt{\frac{k_3}{k_1}}, \quad \bar{i} = \frac{i}{k_1} \sqrt{L_e k_3}$$

Substituting the dimensionless frequency  $\omega$ , dimensionless time  $\tau$ , dimensionless displacement  $\bar{x}$ , and dimensionless current  $\bar{i}$  into Eq. (1) and using Eq. (2), we obtain the dimensionless equations as

$$\bar{x}'' + \mu \bar{x}' + k_4 k_1^{\frac{1}{2}} k_3^{\frac{3}{2}} \bar{x}^4 + \bar{x}^3 + k_2 k_1^{-\frac{1}{2}} k_3^{-\frac{1}{2}} \bar{x}^2 + \bar{x} + \bar{\zeta} \bar{i} = A \cos(\omega \tau) \quad (4a)$$

$$\bar{i}' + \mu_e \bar{i} - \bar{\zeta} \bar{x}' = 0 \quad (4b)$$

where  $\mu = d / \sqrt{m k_1}$  is the dimensionless mechanical damping,

$\bar{\zeta} = \psi / \sqrt{L_e k_1}$  is the dimensionless transducer constant,

$A = F k_1^{\frac{3}{2}} k_3^{\frac{1}{2}}$  is the dimensionless, and  $\mu_e = (R_L + R_e) \sqrt{m / k_1} / L_e$  is the dimensionless electrical damping. The prime denotes a derivative with respect to dimensionless time  $\tau$ .

## 3. Analysis

In this investigation, a Duffing oscillator (DO) is selected as a representative of a monostable energy harvester to be compared with the BM. The purpose is to demonstrate that the bandwidth of the BM is much higher than that of a DO with the same footprint. The frequency response of the bistable energy harvester and the Duffing-type energy harvester to a harmonic loading is analyzed by the method of harmonic balance. The analysis follows a procedure reported by Stanton et al. [5]. The dimensionless equations of motion for the DO-type energy harvester can be expressed as

$$\bar{x}'' + \mu \bar{x}' + \alpha \bar{x}^3 + \beta \bar{x} + \bar{\zeta} \bar{i} = A \cos(\omega \tau) \quad (5a)$$

$$\bar{i}' + \mu_e \bar{i} - \bar{\zeta} \bar{x}' = 0 \quad (5b)$$

For fair comparison, the BM and the DO have similar normalized f-d curves. When the spring of the mechanism shown in Fig. 1(a) has a f-d relation of Fig. 4, an original length of 863.31 mm and an inclination angle  $\theta$  of  $9.46^\circ$ , the mechanism behaves similar to a DO. The mechanism with the above f-d relation, original length and inclination angle is considered as a DO, hereafter. Fig. 5 shows the normalized f-d curves of the BM and the DO. They have approximately the same value of maximum force in the same displacement range. When the values of and of Eq. 5(a) are taken as 0.037983 and 0.027203, respectively, the DO has the normalized f-d curve shown in Fig. 5.

ISGMA2014-B-7-4

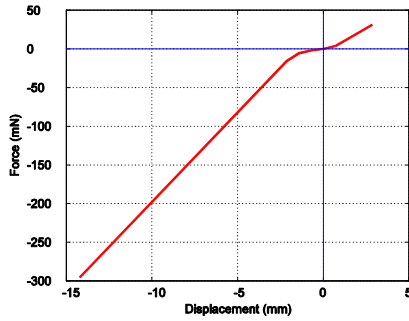


Fig. 4 f-d curve of the nonlinear spring of the Duffing oscillator

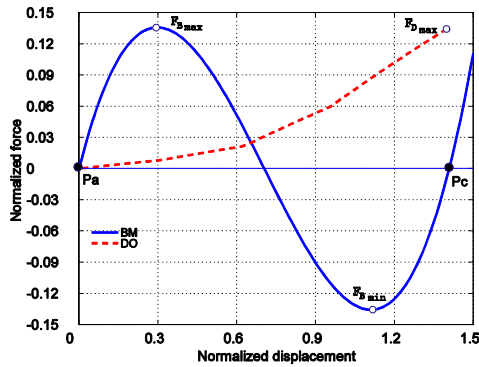


Fig. 5 Normalized f-d curves of the BM and the Duffing oscillator

The oscillation amplitude of the nonlinear systems of Eqs. (4) and (5) may vary in a wide range. Therefore, the classical harmonic balance method can be used to solve the nonlinear oscillation systems. A solution to Eq. (4) can be assumed as

$$\bar{x} = c_1(\tau) + a_1(\tau) \sin \omega\tau + b_1(\tau) \cos \omega\tau \tag{6a}$$

$$\bar{i} = a_3(\tau) \sin \omega\tau + b_3(\tau) \cos \omega\tau \tag{6b}$$

Assuming slowly varying coefficients, i.e.  $\ddot{c}_1 = \ddot{a}_1 = \ddot{b}_1 = \ddot{a}_3 = \ddot{b}_3 = 0$ , substituting the necessary derivatives of  $\bar{x}'$ ,  $\bar{x}''$  and  $\bar{i}'$  into Eq. (4), neglecting higher harmonics and balancing the constant terms and the coefficients of  $\sin \omega\tau$  and  $\cos \omega\tau$ , the steady state equations for the bistable energy harvester are obtained. Solutions of the Duffing-type energy harvester can be obtained similarly. The frequency response can be determined by finding the real roots of the steady state equations. The steady state amplitude of current,  $I$ , is given as

$$I = \sqrt{a_3^2 + b_3^2} \tag{7}$$

The average power through the electrical impedance can be written as

$$P_{ave} = \frac{I^2}{2\mu_e} \tag{8}$$

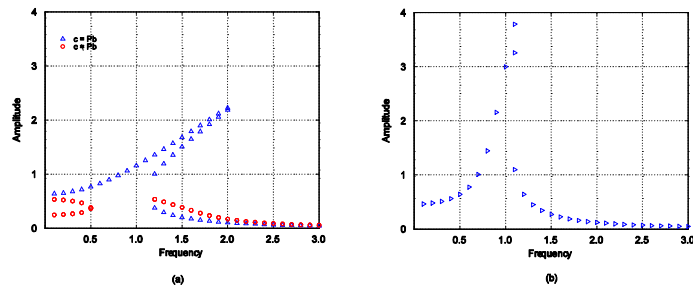


Fig. 6 Amplitude of the response of the (a) BM, (b) DO for the excitation amplitude of  $A = 0.39$

**4. Results**

Depending on the level of the excitation amplitude  $A$ , the BM can exhibit intrawell, low-energy oscillations, or interwell, high-energy oscillations. When undergoing interwell, high-energy oscillations, the BM may exhibit a larger bandwidth than the DO. In order to excite the interwell response of the BM at the frequencies near its fundamental vibration modes, the value of  $A$  is taken as 0.39.

To determine the fundamental system response, the roots of the steady state equations were computed for the parameters  $\mu = 0.08$ ,  $\mu_e = 0.01$ ,  $\zeta = 0.9$  and  $A = 0.39$  for both the BM and the DO. At each excitation frequency  $\omega$ , the real roots of the steady state equations were solved numerically. Fig. 6 is the response amplitudes of the BM and the DO. Fig. 6(a) shows the response amplitude of the BM. The response curves of  $c_1 = P_b$  and  $c_1 \neq P_b$  correspond to the oscillations around the unstable equilibrium position of the BM and otherwise, respectively. As shown in Fig. 6(a), the BM can sustain high-energy oscillations in the frequency range of approximately 0.8 to 2.0 where the response amplitude is higher than 1. The high-energy oscillations of the DO persist in the frequency range of approximately 0.7 to 1.1 where the response amplitude is higher than 1. The BM exhibits a threefold increase in the frequency range of high-energy oscillations compared to the DO. Under the considered excitation level, the BM is capable of sustaining high-energy oscillations in a wide frequency range. Broadband vibration energy harvesting can be achieved by the interwell, high-energy oscillations of the BM.

**5. Summary**

The bandwidth of the BM for vibration energy harvesting is shown to be much larger than the DO by harmonic balance analysis. With similar f-d characteristics, the BM has a threefold increase in the frequency range of high-energy oscillations compared to the DO.

**ACKNOWLEDGEMENT**

The authors are thankful for financial support from the Ministry of Science and Technology, R.O.C., under Grant No. NSC 99-2221-E-005-075.

**REFERENCES**

1. Goldschmidtboeing, F., Woias, P., "Characterization of different beam shapes for piezoelectric energy harvesting," Journal of Micromechanics and Microengineering, vol. 18, 104013, 2008.
2. Mitcheson, P.D., Green, T.C., Yeatman, E.M., Holmes, A.S., "Architectures for vibration-driven micropower generators," Journal of Microelectromechanical Systems, vol. 13, pp. 429-440, 2004.
3. Pellegrini, S.P., Tolou, N., Schenk, M., Herder, J.L., "Bistable vibration energy harvesters: A review," Journal of Intelligent Material Systems and Structures, vol. 24, pp. 1303-1312, 2012.

4. Harne, R.L., Wang, K.W., "A review of the recent research on vibration energy harvesting via bistable systems," *Smart Materials and Structures*, vol. 22, 023001, 2013.
5. Stanton, S.C., Owens, B.A.M., Mann, B.P., "Harmonic balance analysis of the bistable piezoelectric inertial generator," *Journal of Sound and Vibration*, vol. 331, pp. 3617-3627, 2012.

# Prediction of Acceleration of Power-Train based on Rigid Body Motion Analysis

Tae-Jin Shin<sup>1</sup> and Sang-Kwon Lee<sup>1#</sup>

<sup>1</sup> Mechanical Engineering, Inha University, 100 Inharo, Nam-gu, Incheon, South Korea, 402-751  
# Corresponding Author / E-mail: sangkwon@inha.ac.kr, TEL: +82-32-860-8650, FAX: +82-32-868-1716

KEYWORDS : Transfer Matrix, Rigid Body Motion, Inertia Restraint Method, Power-Train

*In low-frequency, a structure show the rigid body motion which includes of translation and rotation. These motions are predicted by analyzing the rigid body transfer matrix. It is impossible to measure acceleration at center of gravity of the power-train in a passenger car because the center of gravity of power-train is located at inside of in power-train. In this paper the acceleration at center of gravity in power-train is estimated during acceleration base on the rigid body analysis of power-train and the measurement of accelerations on the surface of power-train. The test car is operated on roller of the chassis dynameters. In order to validate the method, the acceleration on the surface of power-train is measured at a reference point. The surface acceleration at reference is also predicted using the estimated acceleration at the center of gravity. Both of accelerations are compared each other. The difference of both accelerations is error value. The error value is less than 3%. The method is successfully developed.*

## 1. Introduction

Customers have continuously requested the high quality performance of noise, vibration and harshness (NVH) in a passenger car. Automotive engineers have also tried to enhance the NVH performance of a passenger car. In a vehicle, the vibration of the powertrain is one of major vibration sources. This vibration is transferred to the car body and passengers feel the vibration of car body. Therefore, in order to analysis the vibration of a passenger car, it is important to understand the vibration of a powertrain in a vehicle. Especially, the low frequency vibration of the powertrain influences on the ride comfort of passengers. In low-frequency, a powertrain shows the rigid body motion which includes of translation and rotation. These motions are predicted by analyzing the rigid body transfer matrix [1,2]. It is impossible to measure acceleration at center of gravity of the power-train in a passenger car because the center of gravity (CG) of power-train is located at inside of in power-train. In this paper the acceleration at center of gravity in power-train is estimated during acceleration base on the rigid body analysis of power-train and the measurement of accelerations on the surface of power-train. The test car is operated on roller of the chassis dynameters. In order to validate the method, the acceleration on the surface of power-train is measured at a reference point. The surface acceleration at reference is also predicted using the estimated acceleration at the center of gravity. Both of accelerations are compared each other. The difference of both accelerations is error

value. The error value is less than 3%. The method is successfully developed.

## 2. Theorem and Experiment

### 2.1 Rigid body motion and transfer matrix

The rigid body motion of a powertrain includes of translation and rotation likely to Fig.1.

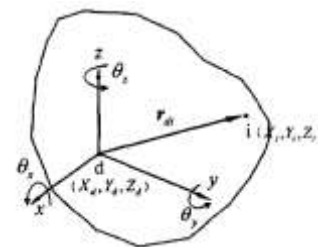


Fig. 1 Expression of rigid body motion

The acceleration of an arbitrary point at the surface of powertrain can be expressed by the translational acceleration and the product of rotational acceleration at the CG point and the space vector from the CG point to an arbitrary point. It is given by Eq. (1)

$$\ddot{X}_p = \ddot{X}_{CG} + \ddot{\theta}_{CG} \times d_{cp} \quad (1)$$

where  $\ddot{x}_p$  is acceleration at the arbitrary point  $p$ ,  $\ddot{x}_{CG}$  and  $\ddot{\theta}_{CG}$  are the translational acceleration at the CG point and the rotational acceleration of the rigid powertrain respectively. The  $d_{cp}$  is a distance from the CG point to the arbitrary point  $p$ . The acceleration vector at an arbitrary point  $p$  is obtained by multiplying the transfer matrix by the acceleration vector at the CG point and given by Eq. (2)

$$\begin{Bmatrix} \ddot{x} \\ \ddot{y} \\ \ddot{z} \end{Bmatrix}_p = \begin{bmatrix} 1 & 0 & 0 & 0 & Z_p - Z_{CG} & -(Y_p - Y_{CG}) \\ 0 & 1 & 0 & -(Z_p - Z_{CG}) & 0 & X_p - X_{CG} \\ 0 & 0 & 1 & Y_p - Y_{CG} & -(X_p - X_{CG}) & 0 \end{bmatrix} \begin{Bmatrix} \ddot{x} \\ \ddot{y} \\ \ddot{z} \\ \ddot{\theta}_x \\ \ddot{\theta}_y \\ \ddot{\theta}_z \end{Bmatrix}_{CG} \quad (2)$$

Similarly, the acceleration vectors at the two points 1, and 2, are expressed in Eq. (3)

$$\begin{Bmatrix} \ddot{x}_1 \\ \ddot{y}_1 \\ \ddot{z}_1 \\ \ddot{x}_2 \\ \ddot{y}_2 \\ \ddot{z}_2 \end{Bmatrix} = \begin{bmatrix} 1 & 0 & 0 & 0 & Z_{p1} - Z_{CG} & -(Y_{p1} - Y_{CG}) \\ 0 & 1 & 0 & -(Z_{p1} - Z_{CG}) & 0 & X_{p1} - X_{CG} \\ 0 & 0 & 1 & Y_{p1} - Y_{CG} & -(X_{p1} - X_{CG}) & 0 \\ 1 & 0 & 0 & 0 & Z_{p2} - Z_{CG} & -(Y_{p2} - Y_{CG}) \\ 0 & 1 & 0 & -(Z_{p2} - Z_{CG}) & 0 & X_{p2} - X_{CG} \\ 0 & 0 & 1 & Y_{p2} - Y_{CG} & -(X_{p2} - X_{CG}) & 0 \end{bmatrix} \begin{Bmatrix} \ddot{x} \\ \ddot{y} \\ \ddot{z} \\ \ddot{\theta}_x \\ \ddot{\theta}_y \\ \ddot{\theta}_z \end{Bmatrix}_{CG} \quad (3)$$

From Eq. (3), the acceleration vector at the CG point can be obtained by the inversion of transfer matrix. However, since the transfer matrix in Eq.(3) is singular form [3-5], in order to solve this singular problem, at least, the acceleration vectors of three response points are requested. Therefore, the acceleration vector at the response points is generally expressed by the product of the transfer matrix and the acceleration vector at the CG and is given by Eq. (4)

$$\begin{Bmatrix} \ddot{x}_1 \\ \ddot{y}_1 \\ \ddot{z}_1 \\ \vdots \\ \ddot{x}_n \\ \ddot{y}_n \\ \ddot{z}_n \end{Bmatrix} = \begin{bmatrix} 1 & 0 & 0 & 0 & Z_{p1} - Z_{CG} & -(Y_{p1} - Y_{CG}) \\ 0 & 1 & 0 & -(Z_{p1} - Z_{CG}) & 0 & X_{p1} - X_{CG} \\ 0 & 0 & 1 & Y_{p1} - Y_{CG} & -(X_{p1} - X_{CG}) & 0 \\ \vdots & \vdots & \vdots & \vdots & \vdots & \vdots \\ 1 & 0 & 0 & 0 & Z_{p,n} - Z_{CG} & -(Y_{p,n} - Y_{CG}) \\ 0 & 1 & 0 & -(Z_{p,n} - Z_{CG}) & 0 & X_{p,n} - X_{CG} \\ 0 & 0 & 1 & Y_{p,n} - Y_{CG} & -(X_{p,n} - X_{CG}) & 0 \end{bmatrix} \begin{Bmatrix} \ddot{x} \\ \ddot{y} \\ \ddot{z} \\ \ddot{\theta}_x \\ \ddot{\theta}_y \\ \ddot{\theta}_z \end{Bmatrix}_c \quad (4)$$

The notation  $n$  is number of response points. In general case, transfer matrix is  $3 \times n$ . The number of points  $n$  should be larger than 3, the transfer matrix is a rectangular matrix. To inverse a rectangular matrix, the pseudo inversion method should be used. The acceleration vector at the CG point is obtained by the pseudo inversion and given by Eq.(5).

$$\begin{Bmatrix} \ddot{x} \\ \ddot{y} \\ \ddot{z} \\ \ddot{\theta}_x \\ \ddot{\theta}_y \\ \ddot{\theta}_z \end{Bmatrix}_{CG} = \begin{bmatrix} 1 & 0 & 0 & 0 & Z_{p1} - Z_{CG} & -(Y_{p1} - Y_{CG}) \\ 0 & 1 & 0 & -(Z_{p1} - Z_{CG}) & 0 & X_{p1} - X_{CG} \\ 0 & 0 & 1 & Y_{p1} - Y_{CG} & -(X_{p1} - X_{CG}) & 0 \\ \vdots & \vdots & \vdots & \vdots & \vdots & \vdots \\ 1 & 0 & 0 & 0 & Z_{p,n} - Z_{CG} & -(Y_{p,n} - Y_{CG}) \\ 0 & 1 & 0 & -(Z_{p,n} - Z_{CG}) & 0 & X_{p,n} - X_{CG} \\ 0 & 0 & 1 & Y_{p,n} - Y_{CG} & -(X_{p,n} - X_{CG}) & 0 \end{bmatrix}^{-1} \begin{Bmatrix} \ddot{x}_1 \\ \ddot{y}_1 \\ \ddot{z}_1 \\ \vdots \\ \ddot{x}_n \\ \ddot{y}_n \\ \ddot{z}_n \end{Bmatrix}_p \quad (5)$$

The pseudo inversion of the transfer matrix is given by Eq. (6)

$$\ddot{X}_c = \left( T_{cp}^T T_{cp} \right)^{-1} T_{cp}^T \ddot{X}_p \quad (6)$$

where  $T_{cp}$  is transfer matrix of general form. The acceleration at any arbitrary internal or external point of the power-train can be derived from estimated acceleration at the CG point. If coordinate of any arbitrary point is obtained, the acceleration at that point expressed in Eq. (7).

$$\ddot{X}_q = T_{cq} \left( T_{cp}^T T_{cp} \right)^{-1} T_{cp}^T \ddot{X}_p \quad (7)$$

where  $\ddot{X}_q$  is acceleration at arbitrary point a,  $T_{cq}$  is transfer matrix from the CG point to the point q.

## 2.2 Measuring acceleration at surface of the power-train

The inverse theory explained in the section 2.1 is applied to the prediction of the practical powertrain with in-line 4 cylinder engine. At the first, the acceleration is measured at 8 point of the surface of the test powertrain. Figure.2 shows the attachment position of 8 accelerometers. The one of accelerometers is reference point and this data is used for validation of the method. The acceleration at the CG point is estimated by using 7 measured data and the acceleration at the reference position is estimated by using the acceleration of the CG point to validate the suggested method in the paper.

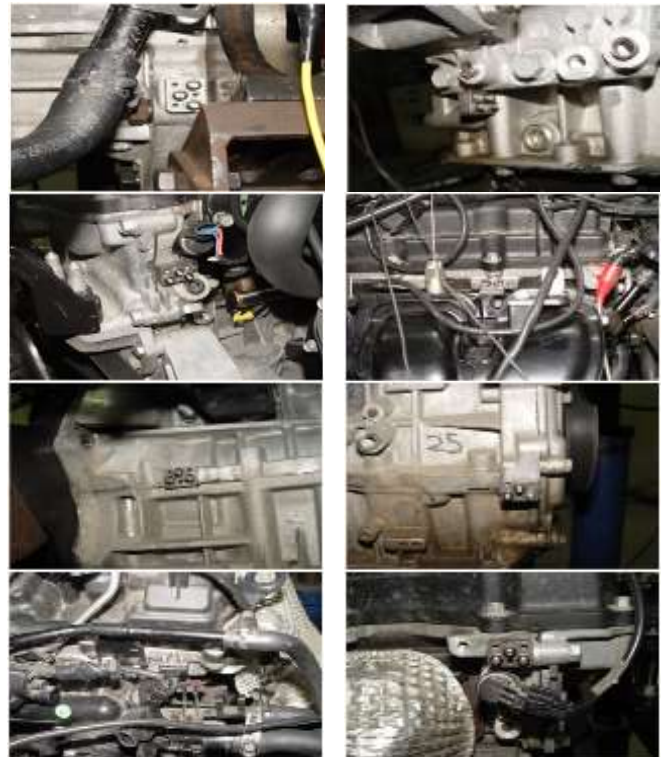


Fig. 2 Attached 8 accelerometers on the surface of the test powertrain for the measurement of acceleration.

Four accelerometers are attached to the front of power-train and others accelerometers are placed at the back of power-train. All

measured data are transferred to the signal conditioner ( LMS mobile, 32 Channel, LMS Co.) which is controlled by the control computer. The operation condition of the test power-train is idle. The sampling frequency is 4096 Hz and the data is measured for 10 second. The transfer matrix is calculated by using the coordinated positions which is obtained by 3D modeler of the power-train. The coordinate point of each measuring point is listed in Table 1. The zero point of this coordinate is the CG point of the test power-train.

Table 1 Coordinate of measuring point

Measuring Point	Coordinate (m / center is CG)		
	X axis	Y axis	Z axis
1	-0.2166	0.1231	-0.1610
2	0.1679	0.0917	-0.1512
3	0.2023	0.1019	0.1957
4	-0.1195	0.0776	0.2319
5	-0.1596	-0.1683	-0.1032
6	0.1945	-0.1865	-0.1030
7	-0.2370	-0.1213	0.2420
8	0.1942	-0.1914	0.2413

The 8th point is reference position. Accelerations from 1 to 7 are used to estimate acceleration of the CG point. Fig. 3 shows the translational and rotational acceleration at the CG point.

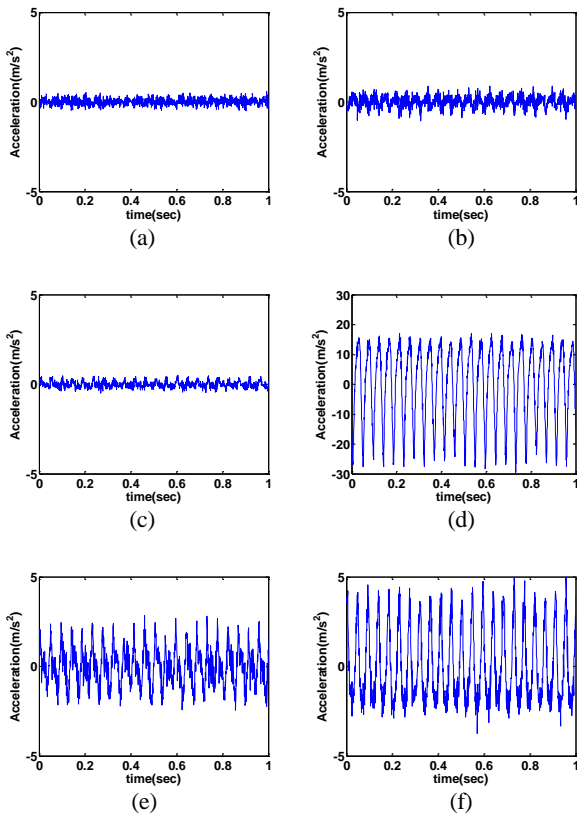


Fig. 3 Estimated acceleration at center of gravity. (a) x-axis, (b) y-axis, (c) z-axis, (d) rx-axis, (e) ry-axis, (f) rz-axis.

The powertrain used in the experiment is an in-line 4 cylinder

engine with the balance shaft. The rolling motion of this kind of engine induces high level of rolling acceleration as shown in Fig.3 (d). The amplitude of rolling acceleration is much bigger than other cancelations. The translation acceleration in the z-axis is very low since the test engine includes the balance shaft which is used for the reduction of the acceleration in the z-direction. From the estimated acceleration at the CG point, the acceleration at the reference point can be calculated. The estimated acceleration of the reference point is compared with the direct measured three translation acceleration at the reference point as shown in Fig. 4.

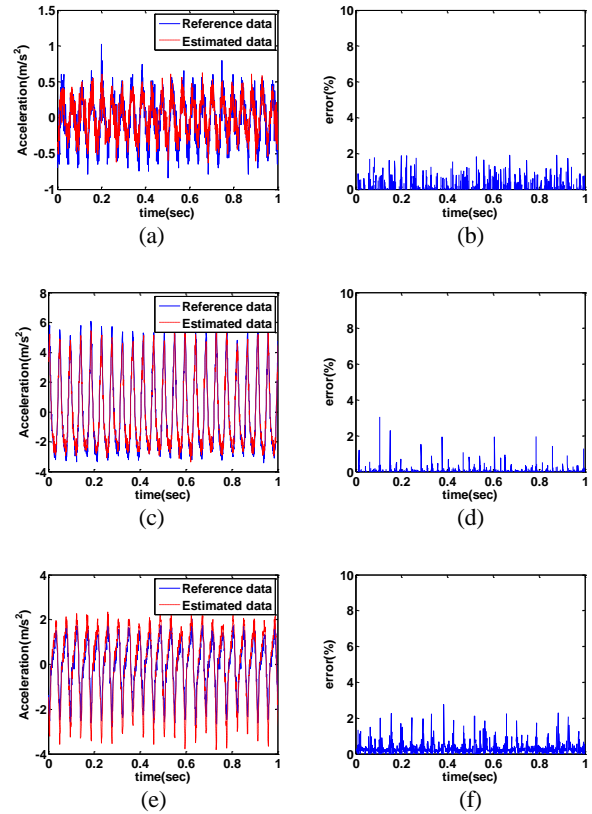


Fig. 4 Comparison between estimation and measurement at reference point. (a) x-axis, (b) error at x-axis, (c) y-axis, (d) error at y-axis, (e) z-axis, (f) error at z-axis.

Fig.4 (a) (c) and (e) show the comparison between the estimated acceleration and direct measured acceleration at reference point. Fig.4 (b) (d) and (f) show the errors between two accelerations. The level of error is less than 3%.

### 3. Conclusions

In order to estimate the acceleration at any point of the running powertrain, the rigid body motion of the running powertrain is analyzed based on matrix inversion method. The matrix inversion theory is discussed. The theory is applied to the estimation of the acceleration at the CG point of the test powertrain. In order to estimate the acceleration, the acceleration is measured at the 8 positions of the surface of the running powertrain. The measured seven accelerations are used to calculation of the CG point. The one measured acceleration at the reference point is used for the validation

of the suggested method. The acceleration at the reference point is estimated by using the coordinate and the acceleration of CG point. The direct measured acceleration and the estimated acceleration at the reference are compared for the validation. The deference error is less than 3%. Therefore, the suggested method can be used for the estimation of the acceleration at any point of the running powertrain.

## ACKNOWLEDGEMENT

This work was supported by Mid-career Researcher Program through NRF grant funded by the MEST (No. 2010-0014260).

## REFERENCES

1. Ko. K. H and Kook H. S. Improving Accuracy of Measurement of Rigid Body Motion by Using Transfer Matrix, Transactions of the Korean Society for Noise and Vibration Engineering, pp. 253-259, 2002,
2. Lee. H. and Lee. Y. B and Park. Y. S., Response and Excitation Point Selection for Accurate Rigid-Body Inertia Properties Identification, Mechanical systems and Signal Processing. Vol. 13, No. 4, pp. 571-592, 1999
3. Pandit, S. M. and Hu. Z. Q., Determination of Rigid Body Characteristics from Time Domain Medal Test Data, Journal of Sound and Vibration, Vol. 177, No. 1, pp. 31-41, 1994
4. Yoon. K. R and Kwak. B.C., Improvement Techniques for Low Frequency Boom Noise of Sports Utility Vehicles, The Korean Society of Automotive Engineers, pp. 977-982, 2006
5. 5. Crouch. T, Matrix Methods Applied to Engineering Rigid Body Mechanics, Pergamon Press, pp. 45-57, 1985

# Active Noise Control for Interior Noise of Passenger Car Based on Pre-Processing Using Order Filter

Seung-Min Lee<sup>1</sup>, In-Deuk Kang<sup>1</sup>, Tae-Jin Shin<sup>1</sup> and Sang-Kwon Lee<sup>1,\*</sup>

<sup>1</sup> Department of Mechanical Engineering, Inha University, 100, Inha-ro, Nam-gu, Incheon, South Korea, 402-751  
\* Corresponding Author / E-mail: sangkwon@inha.ac.kr, TEL: +82-32-860-7305, FAX: +82-32-868-1716

KEYWORDS : Active Noise Control, FXLMS Algorithm, Order Filter

---

*Active noise control is a technique to decrease unwanted noise using secondary sound. Active noise control (ANC) can be used for improving sound quality in a passenger car, for example, by decreasing the engine booming noise or modifying the engine noise inside the car. A conventional algorithm having used for active noise control is the leaky filtered X\_LMS algorithm. This algorithm is an extension of the famous filtered X\_LMS algorithm widely used in active noise control. In the paper, the filtered X\_LMS with adaptive order filter is suggested for the effective control of the engine noise inside of a car. In order to control the interior noise, 2 speakers and 2 error microphones are used. DS1104 of dSPACE is used as the controller of the ANC. For active noise control, RPM signal is needed to make reference signal. RPM signal is normally obtained from CAN (Controller Area Network) signal. But in this paper, instead of using CAN signal, TTL signal from engine was used. Therefore, RPM signal is made using TTL signal and in this process to make RPM signal, order filter is used. The 2nd order components of engine rotation speed that cause booming noise can be reduced by using the ANC system with pre-processing adaptive order filter.*

---

## 1. Introduction

Recently the fuel efficiency of cars has become a world widely major theme. Most of traditional technologies, such as vibration isolators, acoustical absorbing materials, enclosures, barriers, and vibration damping materials, to solve a noise and vibration problem in the car generally require an increase in mass [1]. This method badly influences the fuel consumption rate. A new noise and vibration technology is needed to improve the fuel economy. Therefore, the electronic control technology using active noise reduction has emerged as a new alternative. The idea behind active noise control (ANC) is to generate opposite phase sound that destructively interferes with the existing sound field. The concept of ANC was patented for the first time in the 1930s, but not until the 1990s did practical implementations become available [2]. In the 1990s, control algorithms and the computing power of digital signal processors were developed to a sufficient level to make practical control systems possible [3]. This idea is applied to the automotive industry 1988 [4]. An almost identical system with the previous one implemented and mass produced by Nissan for Bluebird model in 1992 to cancel the second order engine boom. The system was separated from the car audio system and was relatively expensive. The car was available for

a short time in the Japanese market only and did not find any direct successors [4]. Although active control has been experimentally demonstrated in vehicles for over 20 years, it is only recently that the levels of integration within the vehicle's electronic systems have allowed the cost to become affordable. Active control may now allow a reduction in the weight of conventional passive methods of low frequency noise control, helping the push towards lighter, more fuel efficient, vehicles [4-9]. In this paper, we consider the active noise control (ANC) system for a passenger car to control the interior noise. Most of algorithm used for the ANC of the interior noise in a car is the filtered-X LMS algorithm (FXLMS) [3]. In order to control the engine noise inside of car, such as booming and rumbling [10], the reference signal is required in the FXLMS algorithm [11]. The reference signal should be synchronized with engine speed. The engine speed is calculated by using the pulse signal detected at engine speed sensor such as cam shaft position sensor (CSPS) or engine ignition position sensor (EIPS). Nowadays, the pulse signal of engine speed is delivered to the engine management control unit (ECU) system. The ECU supplies the engine speed data to the display throughout a high speed gateway. The ANC system can also use this data for the generation of reference signal. Most of reference signals used for the noise control of an engine are the sine wave at the instant

frequency (rpm/60). This sine wave is discretely changed with the increment of engine speed but not continuous. Therefore, the ANC system using this reference cannot work when the engine speed is changed rapidly from 1000rpm to 6000rpm but work well at the fixed rpm. In this paper a new adaptive order filter (AOF) for the ANC system of interior noise of a car is proposed. The new algorithm uses the continuous reference signal instead of the sine wave.

## 2. New Adaptive Order Filter for Active Noise Control

### 2.1 FXLMS Algorithm

The LMS algorithm cannot be used in active noise control as such, however. The adaptive filter is followed by the secondary path from the secondary source to the error sensor. The output signal is thus modified by the secondary-path transfer function before it reaches the cancellation point at the error sensor. In active noise control, the error signal becomes

$$e(n) = d(n) + y'(n) = d(n) + s(n) * y(n) = d(n) + s(n) * [\mathbf{w}^T(x)\mathbf{x}(n)] \quad (1)$$

where  $s(n)$  is the impulse response of the secondary path. The gradient term in the LMS algorithm is then expressed as

$$\nabla \hat{\xi}(n) = 2[\nabla e(n)]e(n) = 2[s(n) * \mathbf{x}(n)]e(n) = 2\mathbf{x}'e(n) \quad (2)$$

where  $\mathbf{x}'(n)$  is called the filtered reference signal vector. Substituting the gradient term into the equation of the steepest descent algorithm gives

$$\mathbf{w}[n+1] = \mathbf{w}[n] - \mu e[n]\mathbf{x}'[n] \quad (3)$$

which is the filtered-reference (or filtered-x) LMS (FXLMS) algorithm [3].

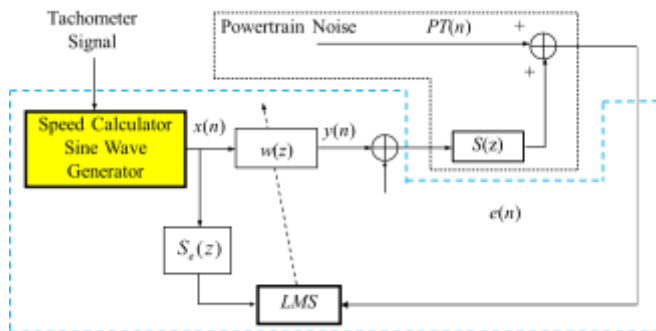


Fig. 1 Block diagram of the filtered-x LMS algorithm.

The block diagram of the FXLMS algorithm is given in Fig. 1. The secondary path is denoted as  $S(z)$  and the secondary-path estimate as  $S_e(z)$ . It has been empirically found that the maximum step size for the FXLMS algorithm is approximately

$$\mu_{max} = \frac{1}{P_x(L_w + \Delta)} \quad (4)$$

where  $P_x = E[x'(n)]$  is the power of the filtered reference signal,  $L_w$  is the length of the adaptive filter and  $\Delta$  is the overall delay in the secondary path in samples [3]. The delay in the secondary path is the

most significant factor influencing the dynamic response of the feed forward active noise control system. Therefore, the delay should be kept small by decreasing the distance between the secondary source and the error sensor and reducing the delay of the control system components. In practice, the FXLMS algorithm is stable even if the adaptive filter coefficients change significantly on a timescale associated with the dynamic response of the secondary path. In the block diagram of the FXLMS algorithm as shown in Fig.1,  $x(n)$  is the reference signal and the input vector for the adaptive filter  $\mathbf{w}(n)$ . The reference  $x(n)$  is a sine wave with instantaneous frequency  $f_i(Hz) = rpm / 60$ .

### 2.2 FXLMS Algorithm with Adaptive Notch Filter (ANF)

When the multiple sinusoidal waves should be controlled, FXLMS Algorithm with notch adaptive filter (ANF) becomes one of solutions. This ANC system is used for the control of multiple sinusoidal waves such as engine noise, muffler noise since it deliver multiple narrow band sinusoidal waves  $y(n)$  to actuator such as a speaker without interference between multiple sinusoidal waves. An adaptive notch filter uses a sinusoidal reference signal and two adaptive weights to cancel narrowband noise. The advantages of the adaptive notch filter are easy control of bandwidth and the capability to adaptively track the exact frequency of the disturbance. Fig. 2 shows the ANC system together with ANF.

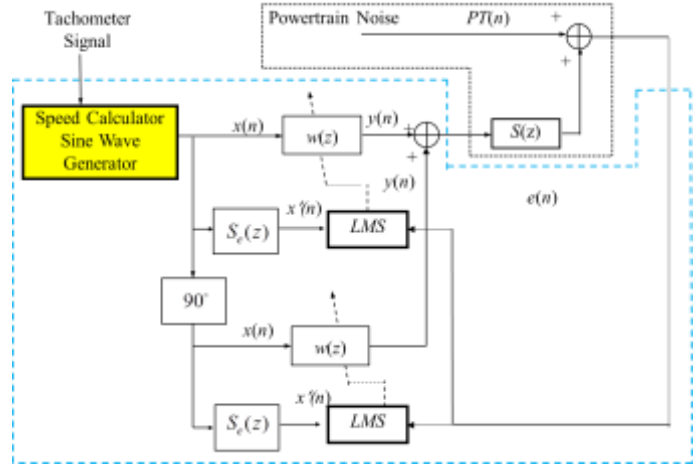


Fig. 2 Block diagram of the filtered-x LMS algorithm with ANF.

However, the frequency of reference signal is changed rapidly, this ANC system with ANF does not work very well since the rotation frequency of the powertrain is changed and the plant noise also changed. ANF cannot find the optimal point for the cost function and generate a large value of least squared error. Especially the number of eigenvalue in the reference signal is large then the least squared error also increases [13]. In order to reduce the least squared error, the leaky LMS algorithm is used to reduce the control speed [14]. This algorithm is given by

$$\mathbf{w}[n+1] = (1 - \mu\alpha)\mathbf{w}[n] + \mu e[n]\mathbf{x}'[n] \quad (5)$$

where  $\alpha$  is a positive control parameter and satisfies the condition,

$$0 \leq \alpha < 1 / \mu \quad (6)$$

This increases the algorithm robust but decreases the adaptation

speed.

### 2.3 FXLMS Algorithm with Adaptive Order Adaptive Filter (AOF)

In order to control the multiple order noises of engine rotation speed, a new ANC system is required with an adaptive filter based on the harmonic orders of the engine rotating speed. For this novel work, the reference signal should be generated the frequency modulated signal continuously synchronized with the engine rotating speed. The reference signal should be given by

$$x(n) = \sum_{i=1}^N a_i(n)x_i(n-1) + a_2(n)x_i(n-2) \quad (7)$$

where  $i$  is 1, 2, 3, ... $N$  and  $N$  is the number of harmonic components to be controlled.  $a_i(n)$  is the amplitude of  $i$ -th order frequency modulated wave at the  $i$ -th order rotating frequency of the engine speed.  $x(n)$  is the 2<sup>nd</sup> order moving averaged parametric model and it is called "adaptive order filter". Eq. (7) is the adaptive order filter. Fig. 3 shows Block diagram of the filtered-x LMS algorithm with AOF.

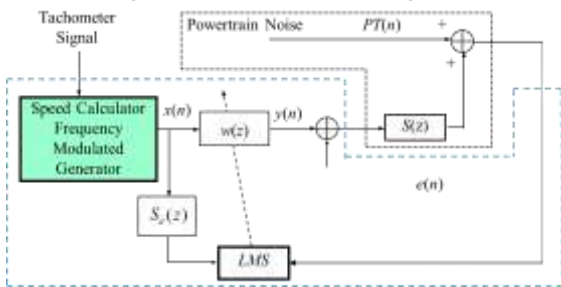


Fig. 3 Block diagram of the filtered-x LMS algorithm with AOF.

## 3. Active Noise Control in the Cabin of a Passenger Car

### 3.1 Experimental Setup and Procedure

A sport utility car is used for the interior noise control. The 2.2L diesel engine is used for powertrain of this car. The instrument of the active noise control is loaded inside a car. Fig. 4 shows the block diagram for active control of interior noise of this car.

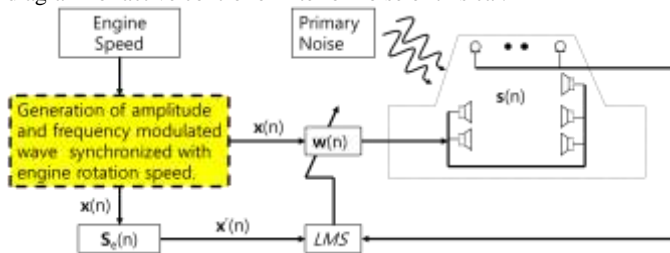


Fig. 4 Block diagram for active control of interior noise of a test vehicle.

The equipment for ANC is illustrated as shown in Fig. 5. Four microphones are used for the measurement of error signal and are attached to the roof of a test car. Five speakers are used to generate the secondary sound sources to cancel the primary noise sources inside of car. The error signals are transferred to the input channels of

dSPACE control board via the ICP amplifier (PCB Company). The pulse signal including the information of speed of engine is detected by the cam shaft position sensor and transferred to the input channels of dSPACE control board. Both input data are transferred to the control computer via A/D converter inside of dSPACE control board. The pulse signal is used for the calculation of the instantaneous frequency and the reference signal  $x(n)$  which is the frequency modulated signal and presented in Eq. (7). The reference signal is convolved by the estimated impulse response of the secondary path. The signal is the input  $x'(n)$  of LMS algorithm in Eq. (3). The adaptive filter  $w(n)$  is updated by using error data  $e(n)$  and input data  $x'(n)$ .

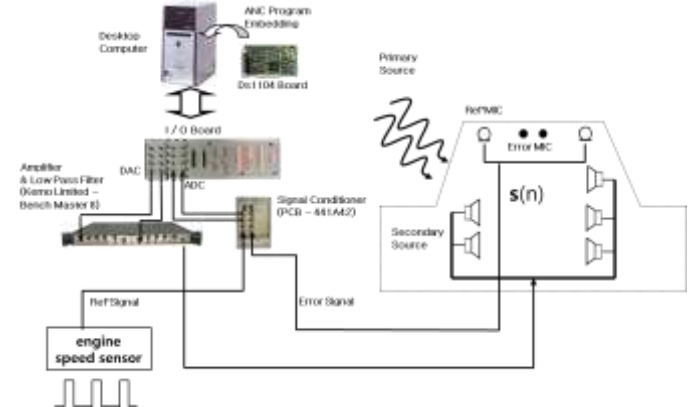


Fig. 5 Equipment for ANC system for active control of interior noise of a test vehicle

### 3.2 Measurement of Impulse Response of the Secondary Path

The impulse response of the secondary path is estimated using the LMS algorithm. Block diagram for the estimation of impulse response of the secondary path is shown in Fig. 6.

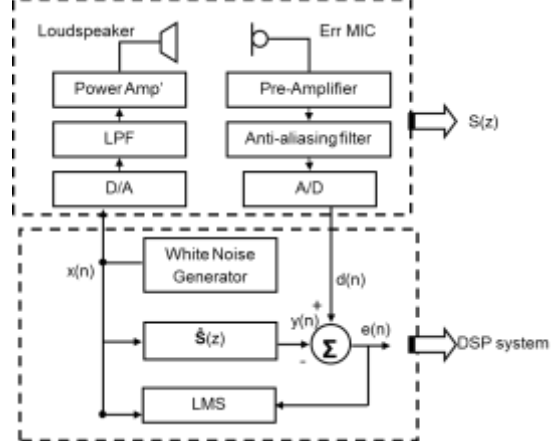


Fig. 6 Block diagram for the estimation of impulse response of the secondary path

The random white signal is used for the input data of the loudspeaker. The impulse response of the secondary path is obtained after enough convergence. The transfer function  $S(z)$  of the secondary path is obtained by taking the z-transform for the impulse response. The results are plotted as shown in Fig. 7.

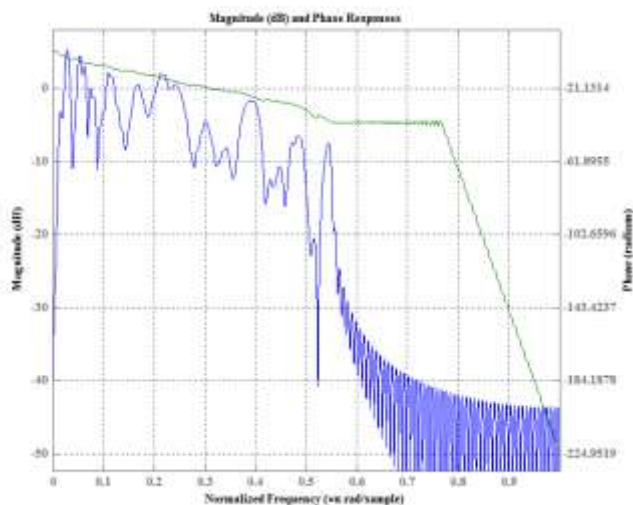


Fig. 7 Transfer function  $S(z)$  of the secondary path and Impulse response  $s(n)$  of the secondary path

### 3.3 Comparison of the Algorithms

For the comparison of the conventional FXLMS algorithm, the FXLMS algorithm with ANF, Leaky LMS algorithm and the FXLMS algorithm with AOF are tested. When the engine speed increased under the no load condition of the engine, the ANC system is operated and the interior noise is measured. The engine speed is increased from 1000 rpm to 4500rpm. The sound pressure levels are compared when three different algorithms are applied. Fig. 8 shows the test results. The new algorithm, it is called as the FXLMS algorithm with AOF, shows the best performance among three algorithms. The new algorithm shows the significant reduction of the interior noise.

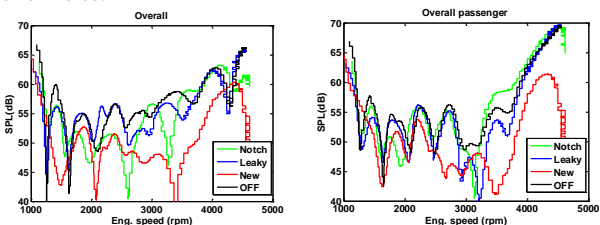


Fig. 8 comparison of sound pressure level among the FXLMS algorithm with ANF, the leaky FXLMS algorithm and the FXLMS algorithm with AOF

### 3.4 Performance of the ANC System with AOF

In order to drive the vehicle with ANC system, the speaker, control computer, monitor and dSPACE channel board are loaded in the test vehicle and the microphone is also attached to the roof of test vehicle. Fig. 9 shows this all systems.

Fig. 10 shows the comparison of sound pressure level between before the ANC system works and after the ANC system does not work. Fig. 10(a) shows the time history for the both data and Fig. 10(b) shows the spectrum of both data. The sound pressure level of interior noise is reduced to 15 dB above 80Hz. The engine condition is no load for this test and the engine speed is increased rapidly from 1000 rpm to 4500rpm during 11second.



Fig. 9 Equipment for the active noise control of interior noise in the test vehicle.

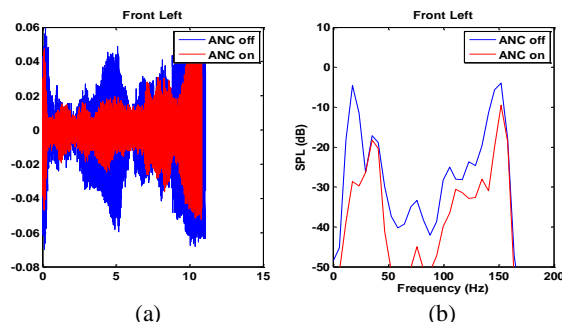


Fig. 10 Performance of the ANC system with new algorithm (a) time history and (b) spectrum analysis of the sound pressure of interior noise.

Fig. 11 shows the sound pressure of interior noise of the test vehicle. The upper solid line is the sound pressure level of interior noise and the low solid line is the actively controlled sound pressure level. Fig. 11(a) present the overall sound pressure and Fig. 11(b) shows sound pressure of the 2nd order component of the engine rotating frequency. The 2nd order is generally related the booming noise [10]. The engine condition is full load d for this test and the engine speed is increased rapidly from 1000 rpm to 4500rpm during 10second. In the case, the other higher orders are not controlled since the calculation speed of ANC system is over the capacity of the dSPACE.

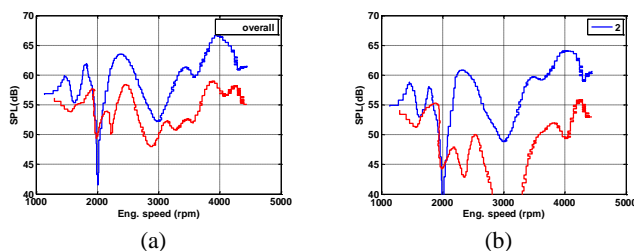


Fig. 11 Performance of the ANC system with new algorithm (a) overall level (b) the 2nd order.

Fig. 12(a) shows the color map for the sound pressure level of interior noise when the ANC system turns off. It can be seen that the sound pressure level of the 2nd order is high along the increased engine speed. The low frequency noise is related to the background noise. The noise under 20Hz is not hearing sound. In this vehicle, the sound pressure level of higher order component is not lower than that of 2nd order component. Therefore, the 2nd order component of the engine speed is controlled. Fig. 13 shows the sound pressure level

of the interior noise which is actively controlled by the ANC system with AOF.

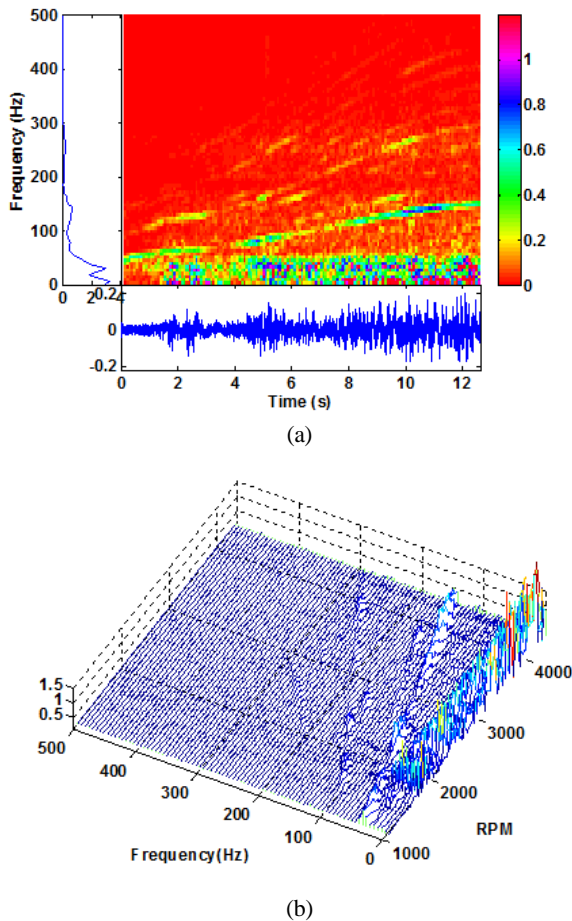


Fig. 12 Color map and waterfall plot of the interior noise in the test vehicle when the ANC is turns off. The load of engine is full (WOT condition) and its speed increase from 1000rpm to 4500 rpm during 11second. (a) color map (b) waterfall plot.

From these results, the new developed ANC system with AOF is work very well and its performance is excellent to reduce the sound pressure of the interior noise related to the harmonic components of engine rotating speed.

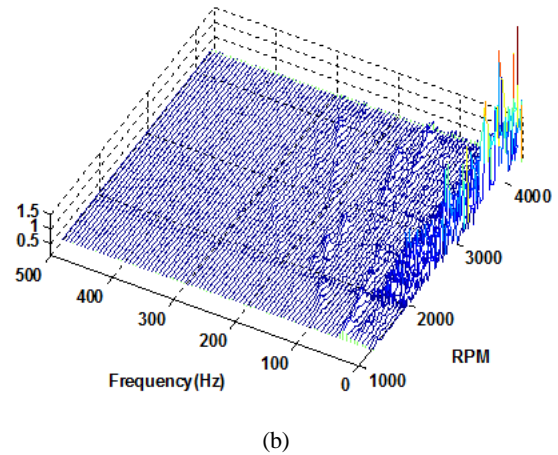
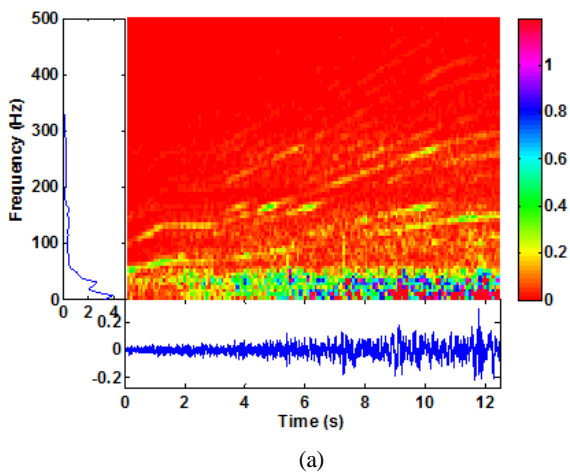


Fig. 13 Color map and waterfall plot of the interior noise in the test vehicle when the ANC is turns on. The load of engine is full (WOT condition) and its speed increase from 1000rpm to 4500 rpm during 11second. (a) color map (b) waterfall plot

### 3. Conclusions

In the paper, the new FXLMS algorithm with AOF is developed. This is developed based on the generation of the reference wave associated with the harmonic orders of the engine rotating speed. The performance of this algorithm is compared with that of the traditional FXLMS algorithms and its family. A SUV is used for the test of the ANC system with this algorithm. The sound pressure level of interior noise actively controlled by this algorithm is reduced to 15dB while the reduction of the sound pressure is reduce to 2-3dB by the traditional FXLMS algorithm and its family. Finally the ANC system with new algorithm is used for the control of the interior noise during driving the road. At the full load condition of the engine, the sound pressure level of the interior noise of the test car is extremely reduced. The performance of the new developed ANC system is very excellent. This can be used for active sound design

### ACKNOWLEDGEMENT

This work was supported by Mid-career Researcher Program through NRF grant funded by the MEST (No. 2010-0014260)

### REFERENCES

1. Crocker, M. J., "Noise Control," Volume 2, New York, John Wiley & Sons, Inc. 1997.
2. Hansen, C. H., "Understanding Active Noise Cancellation," London, Spon Press, 2001.
3. Kuo, S. M. and Morgan, D. R., "Active Noise Control Systems Algorithms and DSP Implementations," New York, John Wiley & Sons, Inc. 1996.
4. Elliott, S. J., "A Review of Active Noise and Vibration Control in Road Vehicles," ISVR Technical Memorandum No. 981, Dec.

- 2008.
5. Schirmacher, R., "Active Noise Control and Active Sound Design – Enabling Factors for New Powertrain Technologies," Proc. 6th International Styrian Noise, Vibration & Harshness Congress, Graz, Austria, Jun. 2010.
  6. Reese, L., "Active Sound-profiling for Automobiles," Doctoral thesis, ISVR, Southampton, UK, 2004.
  7. <http://paultan.org/2008/07/24/toyota-crown-hybrid-features-active-noisecontrol/>. Checked 27th May 2011.
  8. Nikkei Electronics Asia, <http://techon.nikkeibp.co.jp/article/HONSHI/20080428/151147/?P=2>. Checked 27th May 2011.
  9. <http://ophelia.sdsu.edu:8080/ford/09-29-2013/news-center/press-releases-detail/pr-2013-ford-fusion-hybrid2658-active-37160.html>
  10. Lee, S. K., "Objective Evaluation of Interior Sound Quality in Passenger Cars during Acceleration", *Journal of Sound and Vibration*, Vol.310, No. 1, pp. 149-168, 2008.
  11. Kim, H. W., Park, H. S., Lee, S. K. and Shin, K. H. "Modified-Filtered-u LMS Algorithm for Active Noise Control and Its Application to a Short Acoustic Duct," *Mechanical Systems and Signal Processing*, Vol.25, pp. 475–484, 2011.
  12. Kim, E. Y., Kim, B. H. and Lee, S. K., "Active Noise Control in a Duct System Based on a Frequency-estimation Algorithm and The FX-LMS Algorithm," *International Journal of Automotive Technology*, Vol.14, No.2, pp.291-299, 2013.
  13. Lee, S. K. "Adaptive Signal Processing and Higher Order Time Frequency Analysis for Acoustic and Vibration Signatures in Condition Monitoring," Ph. D thesis, ISVR, University of Southampton, 1998.
  14. Haykin, S., "Adaptive Filter Theory," Prentice Hall, 2nd Edition, 1991.

# The Correlation of Surface Roughness and Pressure Drop for a U-tube of the Heat Exchanger in a Steam Generator

Jeong-Hoo Park<sup>1</sup>, Se-Myong Chang<sup>1,#</sup>, Shin-Young Lee<sup>1</sup> and Gyun-Ho Gim<sup>2</sup>

<sup>1</sup> School of Mechanical Engineering, Kunsan University, 558 Daehak-ro, Gunsan-shi, Jeonbuk, South Korea, 573-701  
<sup>2</sup> Soosan Heavy Industry Co., Ltd., 260 Jeongmunsongsan-ro, Yanggam-myeon, Hwaseong-shi, Gyeonggi, South Korea, 445-933  
 # Corresponding Author / E-mail: smchang@kunsan.ac.kr, TEL: +82-63-469-4724

KEYWORDS : Surface Roughness, Pressure Drop, U-shaped Tube, Steam Generator, Inconel 690, FLUENT, CFD

*In this research, we studied the pressure drop affecting on the internal surface roughness of a tube which is used cooling system of Pressurized-Water Reactor(PWR). We studied a range of various surface roughness of the tube as well as a full scale U-shape tube model using ANSYS-FLUENT, commercial codes based on Computational Fluid Dynamics(CFD). The material of the tube is cut from the real heat transfer tube of Inconel 690 now used in the steam generator. We studied the effect of internal surface roughness of the heat transfer tube on the pressure drop in the tube system. The roughness is correlated with the pressure drop to be presented as a single equation for the modeled U-shape tube from the numerical simulation.*

## 1. Introduction

Since the first nuclear power plant built in 1978, 22 plants have been running in Korea, playing an important role by generating about 23% of total domestic electric power. For the case of steam generator of Gori-1 exchanged in 1989, various types of corrosion have been experienced such as pitting, SCC(stress corrosion cracking), and wear, etc. The succeeding plants also have various types of corrosion problems though they are managed better for corrosion [1].

The vibration generated by fluid causes from three kinds: fluid-elastic instability, the forced vibration with unsteady pressure fluctuation originated from turbulence, and the periodic vibration with vortex shedding on the heat pipe around which in the steam generator these causes can bring about the wear or the fatigue fracture, finally resulting in the failure of SG [2]. Cracks of heat pipe and TSP(tube support plate) causes from various microscopic factors like chemistry and sludge deposit [3], but one of the primary factors to consider is fretting wear in the combination of tube and TSP.

## 2. Methods and Result

### 2.1 Numerical Method

The pressure drop is directly related with surface roughness, which is a function of Reynolds number and roughness ratio defined as the

ratio between roughness and tube diameter. For the analysis of primary water, three-dimensional unsteady incompressible Navier-Stokes equations are used:

$$\nabla \cdot \mathbf{V} = 0 \quad (1)$$

$$\rho \left( \frac{\partial \mathbf{V}}{\partial t} + \mathbf{V} \cdot \nabla \mathbf{V} \right) = -\nabla p + \mu \nabla^2 \mathbf{V} \quad (2)$$

In Eqs. (1~2),  $\mathbf{V}$  is velocity vector;  $p$  is pressure;  $\rho$  and  $\mu$  are density and viscosity, respectively. No-slip boundary condition is applied at the tube wall; the inlet condition is specified as a mean flow rate and a given fluctuation; the outlet boundary is set as the ambient pressure. Additionally,  $k-\omega$  SST turbulence model is used for the turbulent intensity of 5% for the incident flow [4].

### 2.2 Result and Discussion

For a straight tube, the correlation of Darcy friction factor,  $f$  with Reynolds number and roughness ratio,  $\varepsilon/d$  [5].

$$\frac{1}{\sqrt{f}} = -2.0 \log_{10} \left( \frac{\varepsilon/d}{3.7} + \frac{2.51}{\text{Re}_d \sqrt{f}} \right) \quad (3)$$

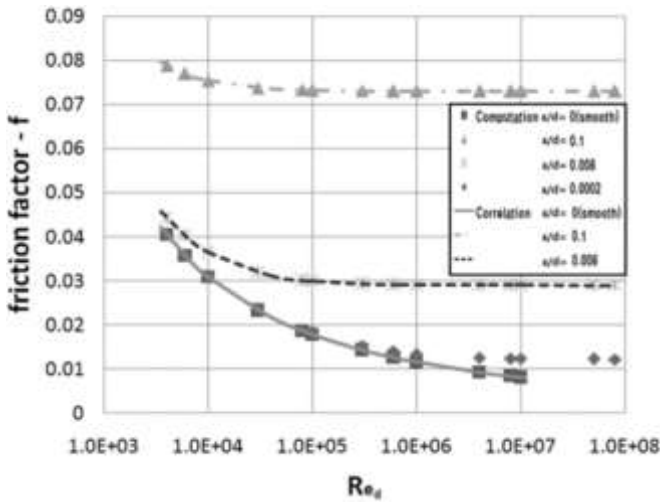


Fig. 1 Darcy Friction Factor vs. Reynolds number

The plot of Eq. (3) is given in Fig. 1, and this graph is called Moody chart. By changing the parameters, we can obtain the numerical values of Fig. 1 where ANSYS-FLUENT is used for numerical computation.

The result is very sensitive to the grid scale, especially the vertical size of the first grid,  $\Delta y$ , which is expressed with a dimensionless parameter:

$$y^+ = \Delta y \sqrt{\frac{\rho}{\mu} \frac{du}{dy}} \Big|_{y=y_w} \quad (4)$$

where  $u$  is the transformed velocity component to the tangential direction of the wall. To get the proper values coinciding with Eq. (3) in the parametric plane of Fig. 1, the dimensionless wall distance should be  $y^+ < 1$  in the whole computational domain.

For example, when the computational domain is a pipe of 20 mm diameter and 2 m length, 1,023,678 tetrahedral elements with smooth

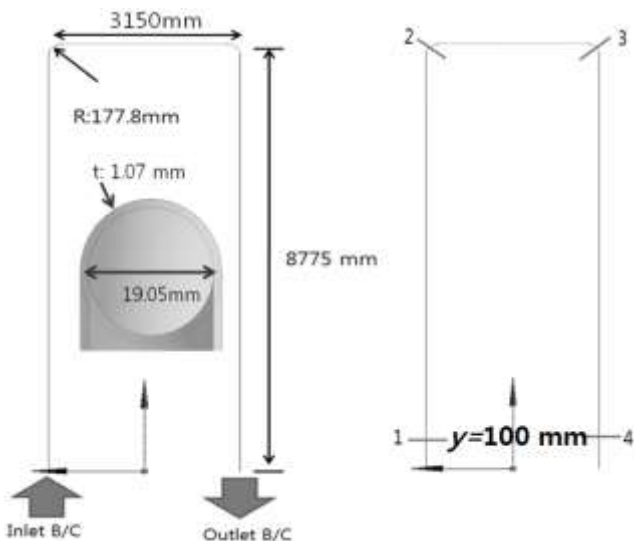


Fig. 2 Full scale model

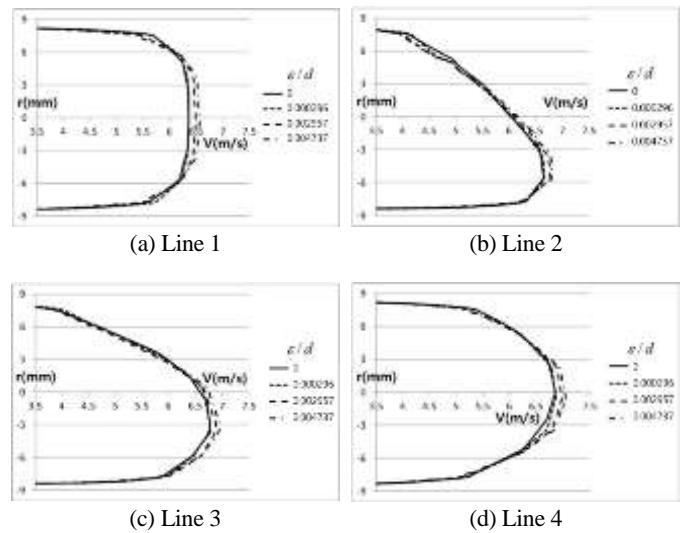


Fig. 3 Flow velocity distribution

inflation at the wall should be used for each computation of Fig. 1 at least  $y^+ \approx 0.3$ .

The performance of U-tubes usually used in steam generators are listed in Table 1.

Table 1 General performance of u-tube

Material	Inconel Alloy 690 (Ni 60%, Cr 30%, Fe 10%)
Size and surface roughness	External diameter : 19.05mm ( $\pm 0.1$ mm), Thickness : 1.07 mm Length : max 27.4 m, min 15.4 m (mean 20.7 m) Surface roughness: inside 0.5 $\mu\text{mRa}$ , outside 1.6 $\mu\text{mRa}$
Tube shape	U-shaped dune (bending radius R:76.2~279.4 mm)
Mechanical Properties	Density: 8,190 kg/m <sup>3</sup> Young's modulus: 211 GPa Poisson's ratio: 0.289

From the geometry data, we composed a standard full-scale model for the computation of fluid: Fig. 2. In the classical theory, the pressure drop directly depends on the Darcy friction factor,  $f$ :

$$\Delta p = \rho g h_f = f \frac{L}{d} \left( \frac{1}{2} \rho V^2 \right) \quad (5)$$

Where  $V = \|\mathbf{V}\|_2$  in the radial mean;  $L$  and  $d$  are length and diameter of pipe, respectively [5]. However, the additional pressure loss should be generated in the bended corner of pipe.

Fig. 3 (a)~(d) shows the velocity distributions at four cross sections marked in Fig. 3. The roughness ratio,  $\epsilon/d$  lies in the range from 10 to 200 times of the regular value in Table 1. As the roughness increases, the maximum velocity at the center increases because the boundary layer becomes thicker. The centrifugal force at corners deforms velocity ( $\mathbf{V}$ , vertical to lines) profile to ones asymmetric, and the positive sign of  $r$  means the inner direction. To obtain these

results, 4,191,063 tetrahedral elements are used for computation each other. The mean value of flow velocity is 6 m/s under the operating condition.

In Fig. 4, the correlation for pressure drop that means the difference of static pressure between inlet and outlet is a function of roughness ratio for the present system, in a linear regression form, such as

$$\frac{\Delta p}{\frac{1}{2}\rho V^2} = 2435\left(\frac{\varepsilon}{d}\right) + 15.76 \quad (6)$$

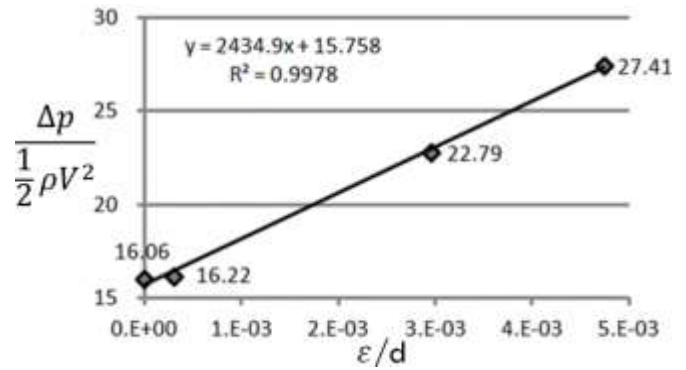


Fig. 4 Pressure Drop vs. Surface Roughness

### 3. Summary

Surface roughness is studied for the system of U-tube used for the heat pipe in the steam generator for the PWR, which is suspected as the key cause for pressure drop in pipes. To consider surface roughness and pressure drop, ANSYS-FLUENT code was tuned for the proper grid level with empirical correlations such as Moody chart. For the full-scale model, a correlation of pressure drop for the surface roughness ratio has been derived from the result of flow analysis. The larger the roughness ratio is, the larger Friction factor is, and the slower velocity at wall is as Fig. 3. Therefore, pressure drop is affected on the roughness ratio. If the roughness ratio is increased, pressure drop is expressed in a correlation form such as Eq. (6) and Fig. 4. However, the surface roughness is increased, because of friction around the wall, so we should try to decrease the roughness ratio for the improvement of the performance for U-tubes in the steam generator of hydro-thermal system for a nuclear power plant.

### ACKNOWLEDGEMENT

This research has been supported by 1) the Energy Technology Development program (Grant No. 20111510100060) and 2) the Human Resources Development program (Grant No. 20124010203240) of the Korea Institute of Energy Technology Evaluation and Planning (KETEP) grants funded by the Korea government Ministry of Trade, Industry, and Energy.

### REFERENCES

- [1] S. S. Hwang, "Corrosion and Corrosion Prevention of Steam Generator Tubes in PWRs-1," *Corrosion and Protection*, Vol.6, pp. 59-67, 2007.
- [2] K. W. Ryu, C. Y. Park, "Analysis of Fluid-elastic Instability in the CE-type Steam Generator Tube," *J. Korean Soc. for Noise and Vibration Eng.*, Vol. 12, pp. 261-271, 2002.
- [3] H. Chung, et al., "A Review on The ODS-CC of Steam Generator Tubes in Korean NPPS," *Nuclear Engineering and Technology*, Vol. 45, pp. 513-522, 2012.

- [4] F. R. Menter, "Two-Equation Eddy-Viscosity Turbulence Models for Engineering Application," *AIAA Journal*, Vol. 32, pp.1598-1605, 1994.
- [5] F. M. White, *Fluid Mechanics*, 7th ed., McGraw-Hill, New York, 2010.

# Study on Secondary Combustion Thermo-impact of Gas and Air in Confined Vessel

Xiao-lei Hu<sup>1</sup>, Gui-gao Le<sup>1,#</sup>, Da-wei Ma<sup>1</sup> and Jiayi Guo<sup>2</sup>

<sup>1</sup> School of Mechanical Engineering, Nanjing University of Science and Technology, 200, Xiaolingwei Street, Nanjing, China, 210094  
<sup>2</sup> Engineering Practice and Innovation Education Center, Anhui University of Technology, Ma'anshan 243032, China  
 # Guigao Le / E-mail: leguigao@mail.njust.edu.cn , TEL: +8625-8431-5125, FAX: +8625-8431-5125

KEYWORDS : Confined Vessel, Secondary Combustion, Moving Boundary, Numerical Simulation

*The present study deals with the simulation investigations of thermo-impact obtained as a result of the secondary combustion of gas and air in a confined space. To study the secondary combustion with dynamic zone in confined space, a three-order accurate MUSCL scheme was employed to solve 10-step reaction and 9 species chemical reactions of H<sub>2</sub>/CO and dynamic laying methods was adopted to simulate boundary motion. The comparison between numerical and experimental results of free jet flow impacting on plat proved that the method was reliable. The secondary combustion can increase the fluid temperature. The impact tendency of mobile boundary accords with the inlet boundary trend; whereas the wall of vessel is in condition of high temperature. The research results can be applied in high pressure vessel design.*

## NOMENCLATURE

$Q(t)$  = variable control volume;  
 $\Gamma(t)$  = outside surface of control volume,  $i = 1, \dots, N$  ;  
 $N$  = number of chemical species in mixture gas;  
 $\rho_i$  = the  $i$  th species density  
 $\rho$  = mixture density  
 $p$  = pressure of mixture species  
 $T$  = temperature of mixture species  
 $u$  = velocity of  $x$  vector  
 $v$  = velocity of  $y$  vector  
 $u_w$  = velocity of  $x$  mobile mesh  
 $v_w$  = velocity of  $y$  mobile mesh  
 $h_i$  = he enthalpy of species  $i$   
 $\tau$  = viscous stress tensor,  
 $k$  = thermal conductivity  
 $D_i$  = diffusion coefficient of species  $i$   
 $\dot{\omega}_i$  = the mass of production rate  
 $E$  = total energy of per mixture  
 $v'_{i,r}$  = stoichiometric coefficient for reaction  $i$  in reaction  $r$   
 $v''_{i,r}$  = stoichiometric coefficient for reaction  $i$  in reaction  $r$   
 $M_i$  = symbol denoting species  $i$   
 $k_{f,r}$  = forward rate constant for reaction  
 $k_{b,r}$  = backward rate constant for reaction  $r$

$C_{j,r}$  = molar concentration of species  $j$  in reaction  $r$  (kgmol/m<sup>3</sup>)  
 $\eta'_{j,r}$  = rate exponent for reaction species  $j$  in reaction  $r$   
 $A_r$  = pre-exponential factor (consistent units)  
 $\beta_r$  = temperature exponent (dimensionless)  
 $E_r$  = activation energy for the reaction (J/kgmol)  
 $R$  = universal gas constant (J/kgmol K)  
 $p_{atm}$  = atmospheric pressure (101325Pa)  
 $S_i^0$  = standard-state entropy of the mixture material  
 $h_i^0$  = standard-state enthalpy of the mixture material

## 1. Introduction

Many practical systems, such as gas generator, ramjet combustors, furnaces, rocket combustors, integrated ramjet combustors (IRR), involve secondary combustion phenomenon. The combustion phenomena involve a tremendous number of complexities which are related to the mixture of fuel and air streams in confined space of combustion chamber. The flow field involves regions of secondary combustion, reverse flow, separation and reattachment along with turbulent mixing. Modern launcher utilize injection gases generated by burning a fuel rich solid propellant whose primary combustion products are H<sub>2</sub>, CO, CO<sub>2</sub>, N<sub>2</sub>, O<sub>2</sub>, H, OH and other noncombustible gases. These injection gases exit the gas generator can lead distortion in open and confined space<sup>[1]</sup>.

Many researchers have investigated secondary combustion in open space by experiment and simulation. Hong [2] adopted 9 species and 10 steps H<sub>2</sub>/CO reaction model to simulated Atlas rocket secondary combustion plume. The result showed that the fluid structure is agreed with the experiment photos. Candle [3] used finite rate method to study Atlas-II temperature and OH distribution. The simulation result of OH distribution is agreed with experiment. LI [4] adopted TVD scheme and finite rate method simulated secondary combustion of solid rocket plume, and got the fluid structure and axis temperature distribution. Jiang [5] used RNG k-ε two equations turbulent model and finite rate to simulate the impact effect of solid rocket motor exhaust plume to launching platform. The situational values of temperature and pressure are agreed with experiment.

The above researches of secondary combustion were focusing on open region. The secondary combustion in confined vessel has not yet been reported. The objective of this paper is to gain the influence of secondary combustion to fluid temperature and the thermo-impact regularity. The three-order accurate MUSCL scheme, RNG k-ε two-equation turbulent model, finite rate method and dynamic laying methods was employed to solve 10-step reaction and 9 species Navier-Stokes equation. The validation of the established numerical method is compared with reference experiment [5]. After tested and verified, the secondary combustion fluid model in confined space was investigated.

## 2. Computation method and calculation model

### 2.1 Governing equation

The present numerical method solves a set of governing equations describing the conservation of mass, momentum (Navier-Stokes equations), energy, species concentration and turbulence quantities. The governing equations are written as follows:

$$\frac{\partial}{\partial t} \int_{\Omega(t)} Q d\Omega + \oint_{\Gamma(t)} F d\Gamma + \oint_{\Gamma(t)} G d\Gamma + \frac{v}{y} \int_{\Omega(t)} S d\Omega = \int_{\Omega(t)} W d\Omega \quad (1)$$

where

$$Q = \begin{bmatrix} \rho_i \\ \rho u \\ \rho v \\ \rho E \end{bmatrix} \quad S = \begin{bmatrix} \rho_i \\ \rho u \\ \rho v \\ \rho E + p \end{bmatrix} \quad W = \begin{bmatrix} \dot{\omega}_i \\ 0 \\ 0 \\ q \end{bmatrix}$$

$$F = \begin{bmatrix} \rho_i(u - u_w) - D_i \frac{\partial \rho_i}{\partial x} \\ \rho u(u - u_w) + p - \tau_{xx} \\ \rho v(u - u_w) - \tau_{xy} \\ (\rho E + p)(u - u_w) - [(u - u_w)\tau_{xx} + (v - v_w)\tau_{xy} - q_x] \end{bmatrix}$$

$$G = \begin{bmatrix} \rho_i(v - v_w) - D_i \frac{\partial \rho_i}{\partial y} \\ \rho u(v - v_w) - \tau_{yx} \\ \rho v(v - v_w) + p - \tau_{yy} \\ (\rho E + p)(v - v_w) - [(u - u_w)\tau_{yx} + (v - v_w)\tau_{yy} - q_y] \end{bmatrix}$$

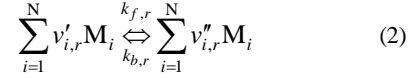
$$q_x = k \frac{\partial T}{\partial x} + \left( \sum_{i=1}^N D_i h_i \frac{\partial \rho_i}{\partial x} \right), \quad q_y = k \frac{\partial T}{\partial y} + \left( \sum_{i=1}^N D_i h_i \frac{\partial \rho_i}{\partial y} \right)$$

The finite volume and explicit scheme are adopted to solve the governing equation. The three-order MUSCL scheme is adopted to solve convective term. The Runge-kutta method is adopted to solve time term. Turbulent model uses RNG k-ε two equations. The standard wall function is adopted.

### 2.2 Calculation method

Arrhenius Law is adopted to describe detail chemical reactions of secondary combustion in confined region, and turbulent fluctuation of secondary combustion is neglected.

Consider the  $r$  th reaction written in general form as follows:



where

The molar rate of creation/destruction of species  $i$  in reaction  $r$  is given by:

$$\hat{R}_{i,r} = \Gamma(v''_{i,r} - v'_{i,r}) \left( k_{f,r} \prod_{j=1}^{N_r} [C_{j,r}]^{\eta_{j,r}} - k_{b,r} \prod_{j=1}^{N_r} [C_{j,r}]^{v''_{j,r}} \right) \quad (3)$$

The third-body effect in this paper is not included.

The forward rate constant  $k_{f,r}$  is computed using the Arrhenius expression as follows:

$$k_{f,r} = A_r T^{\beta_r} e^{-E_r/RT} \quad (4)$$

The backward rate constant for reaction  $r$ ,  $k_{b,r}$  is computed from the forward rate constant using the following relation:

$$k_{b,r} = \frac{k_{f,r}}{K_r} \quad (5)$$

where  $K_r$  is the equilibrium constant for the  $r$  th reaction, computed from:

$$K_r = \exp\left(\frac{\Delta S_r^0}{R} - \frac{\Delta H_r^0}{RT}\right) \left(\frac{P_{atm}}{RT}\right)^{\sum_{i=1}^N (v''_{i,r} - v'_{i,r})} \quad (6)$$

The term within the exponential function represents the change in Gibbs free energy, and its components are computed as follows:

$$\frac{\Delta S_r^0}{R} = \sum_{i=0}^N (v''_{i,r} - v'_{i,r}) \frac{S_i^0}{R} \quad (7)$$

$$\frac{\Delta H_r^0}{RT} = \sum_{i=0}^N (v''_{i,r} - v'_{i,r}) \frac{h_i^0}{RT} \quad (8)$$

The 9 species and 10 steps chemical reaction model<sup>[10]</sup> is adopted. The reaction mechanism is shown in Table 1. M is the third-body, such as HCl.

Tab.1 Chemical reaction mechanism

Reaction formula	Chemistry rate constant
CO+OH=CO <sub>2</sub> +H	2.8×10 <sup>-17</sup> T <sup>1.3</sup> exp(330/T)
H <sub>2</sub> +OH=H <sub>2</sub> O+H	1.9×10 <sup>-15</sup> T <sup>1.3</sup> exp(-1825/T)
H <sub>2</sub> +O=OH+H	3.0×10 <sup>-14</sup> Texp(-4480/T)
H+O <sub>2</sub> =OH+O	2.4×10 <sup>-10</sup> exp(-8250/T)
OH+OH=H <sub>2</sub> O+O	1×10 <sup>-11</sup> exp(-550/T)
CO+O+M=CO <sub>2</sub> +M	7×10 <sup>-33</sup> exp(-2200/T)
H+H+M=H <sub>2</sub> +M	3×10 <sup>-30</sup> T <sup>-1</sup>
O+O+M=O <sub>2</sub> +M	3.0×10 <sup>-34</sup> exp(900/T)
O+H+M=OH+M	1×10 <sup>-29</sup> T <sup>-1</sup>
H+OH+M=H <sub>2</sub> O+M	1×10 <sup>-25</sup> T <sup>-2</sup>

### 2.3 Dynamic mesh update methods

According to the mobile boundary motion, the structure grid is adopted to disperse spatial zone of computing model. The spring-based smoothing method and dynamic laying method are employed to simulate the missile motion in Ref [9].

### 2.4 Calculation model and boundary condition

The calculation model is component of gas generator, tube and mobile boundary, as (a) in Fig.1. The mobile boundary's moving is by jet flow injected from gas generator. The nozzle expansion ratio of gas generator is 2, throat radius is 40 mm, the volume of confined region is 39.25 m<sup>3</sup>. Considering the axial symmetry, two-dimensional axisymmetric calculation model is adopted to analysis the fluid. Calculation mesh is shown in (b) in Fig.1. During the computing time, the missile has not moved out of tube.

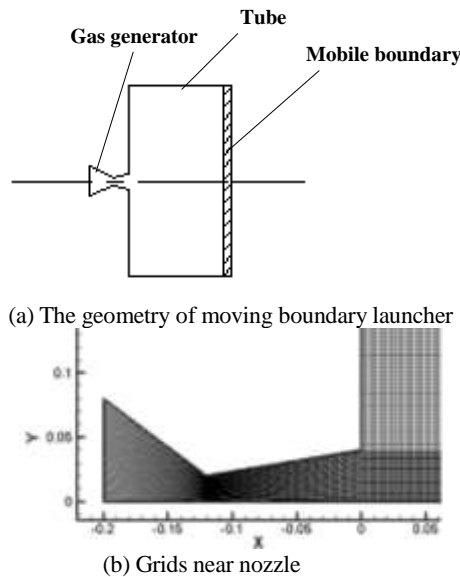


Fig.1 Calculation model

The inlet boundary type of gas generator is pressure inlet and the pressure variation tendency over time is shown in Fig.2. The total temperature is 1500K. The wall boundary of tube and nozzle is no-slip walls. The minimum free energy method<sup>[9]</sup> is adopted to compute the propellant combustion products. The species and mass fraction of gas generator inlet is shown in Tab.2. The pressure in tube is 101 325 Pa, and the temperature is 300 K, and the mass of N<sub>2</sub> and O<sub>2</sub> is 0.79 and 0.21, separately.

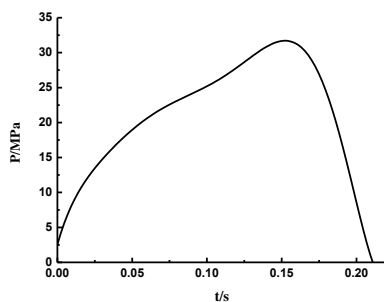


Fig.2 Pressure profiles of inlet nozzle

Tab.2 Species and mass fraction of inlet

species	H <sub>2</sub> O	CO	H <sub>2</sub>	CO <sub>2</sub>	N <sub>2</sub>
mass fraction	0.16	0.27	0.004	0.26	0.305

### 3 Numerical method validation

According to the experimental geometry and data of secondary combustion of rocket motor exhaust plume<sup>[6]</sup>, we established the free jet impact model, and set four temperature monitor on the ground. The detail description on the nozzle character was shown in Ref.6. The distance of A, B, C, D points on the ground are 0.2 m, 0.3 m, 0.4 m, 0.5 m from the projection of nozzle center. It is 1.75m from the nozzle exit to the ground. The inlet boundary type of nozzle is pressure inlet, and the chamber pressure is 7 MPa. The total temperature is 3000 K. The pressure out boundary with general non-reflecting boundary condition<sup>[7]</sup> is adopted at the pressure outlet is 101325 Pa, and outlet temperature is 300 K. The acceleration of gravity is 9.8 m/s<sup>2</sup>. Nine species are considered (H<sub>2</sub>O, CO, CO<sub>2</sub>, H<sub>2</sub>, N<sub>2</sub>, O<sub>2</sub>, OH, H and O). The detail description of mass fraction was shown in Ref.6. Tab.3 lists the simulation and experimental temperature measured by the temperature sensors on points A, B, C and D. The biggest relative error is 5.7%. Tab.3 proves reliability of simulation models. The biggest relative error of temperature between the simulation and experiment is It proves reliability of simulation models.

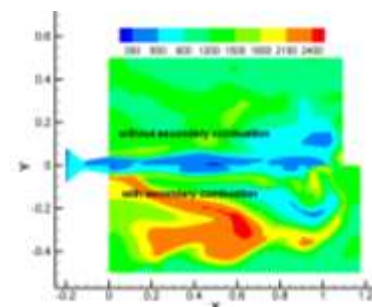
Table.3 Comparison between numerical and experimental results

monitor objects	A	B	C	D
Simulation / K	1030	976	867	712
Experiment / K	1000	940	820	681
Relative error / %	2.9	3.7	5.7	4.4

### 4 Results and discussion

Fig.3 separately shows the temperature distribution comparison with and without secondary combustion at 0.1 s and 0.2 s. Fig. 4 presents the axis temperature comparison with and without secondary combustion at 0.1 s and 0.2 s. From the temperature distribution and axis temperature comparison, we can see that the secondary combustion can improve the flow temperature. The reason why the secondary combustion has higher temperature lies in a large amount of heat are produced through series of chemical reactions in confined tube with secondary combustion. In Fig.3, we can see the maximum temperature with secondary combustion is about 2500 K, whereas without secondary combustion is about 1900 K, which means flow maximum temperature with secondary combustion is 600 K higher than without.

High temperature in the flow field with secondary combustion distributes near nozzle. The reason is that the jet flow rebounded from mobile boundary joined with the exit jet from nozzle formats an irregular region, where inner is air and round is gas. In the irregular region, the air and gas occur chemical reaction again and release energy to promote the flow temperature and the boundary move more quickly, which can be proved in Fig.4. So the place near nozzle is higher than any other regions.



(a) 0.1s

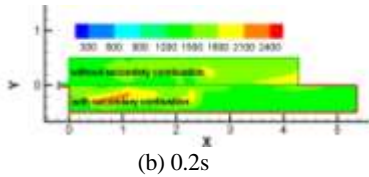


Fig.3 Comparison flow of temperature distribution (the unit of temperature is K)

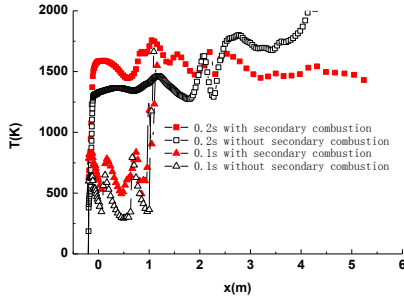
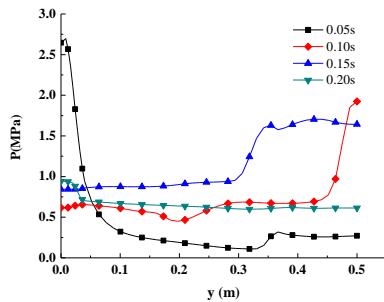


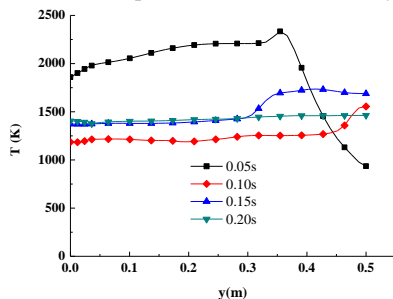
Fig.4 Axis temperature comparison

Fig.5 Presents the thermo-impact profiles of mobile boundary with secondary combustion. Seen from the figures, the pressure tendency is increasing from 0.1s to 0.15s and decreasing over the period from 0.15s to 0.2s, which rise and falls with the tendency of nozzle pressure. By contract, the temperature of fluctuates during the launch time and remain at about 1400K at 0.20s. In the pressure profiles of mobile boundary, we can see that the center of moving boundary is the maximum point at firstly, which is 2.7 MPa. After the flow field is stable, the pressure difference on the edge is unobvious and maintain 0.75 MPa.

According to the ideal gas state equation, the temperature's fluctuate is inversely proportional to pressure tendency, which other parameters is constant. Whereas in this paper, the boundary is moving. So at the comprehensive action of pressure and volume, the temperature is fluctuate in Fig.5.



(a) Pressure profiles of mobile boundary

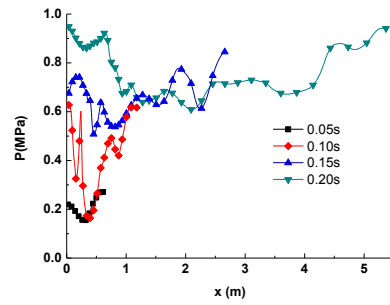


(b) Temperature profiles of mobile boundary

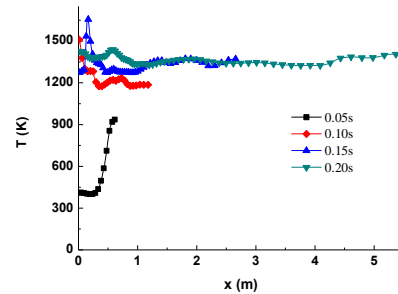
Fig.5 Thermo-impact profiles of mobile boundary

Fig.6 are thermo-impact profiles of tube during the computer time. Seen from the profiles, the pressure and temperature goes up during the period from 0.05s to 0.2s. The maximum pressure and temperature points over the tube wall are the two endpoints near nozzle and the moving boundary after the flow field is state. The reason is the endpoints easily gather gas and is hard to spread out. The

temperature on the tube is 1450K after 0.1s, which is close to the nozzle total temperature. The tube need considering thermal protection during working time.



(a) Pressure profiles of tube



(b) Temperature profiles of tube

Fig.6 Thermo-impact profiles of tube

### 5 Conclusions

(1) By inducing the energy source terms caused by the chemical reaction in energy equation, the secondary combustion flow field with moving boundary is calculated in a coupling way. The calculation results accord well with the experimental results, which indicate that the coupling solution is reliable.

(2) The temperature of region with secondary combustion is higher than without combustion and the high temperature region is mainly around the exit of nozzle, indicating that chemical reaction can increase the temperature and mainly occurs in that region.

(3) The center of moving boundary is the maximum pressure point during impacting. Two endpoints are both in the condition of high pressure and temperature.

### ACKNOWLEDGEMENT

Thank you for Doctor Hu Ma for helping in simulation.

### REFERENCES

1. ZHANG Guang-xi, ZHOU Wei-min, ZHANG Gang-chui, et al. Study on characteristics of flow field in exhaust plume for SRM. Journal of Solid Rocket Technology. Vol.31 No.1, pp. 19-23, 2008.
2. Hong J S, Levin D A, Collins, Emery J, et al. Comparison of Atlas ground based plume imagery with chemically reacting flow solutions, AIAA-1997-2537, 1997
3. Candler G V, Rao R M, Sinha K, Levin D A. Numerical simulations of Atlas- II rocket motor plumes. AIAA-99- 31103, 1999.
4. Li Jun. TVD scheme with chemical reaction flow and application in combustion gas jetting flow. Transactions of Nanjing

- University of Aeronautics and Astronautics, Vol.22 No.1, pp. 64-70, 2005.
5. Jiang Yi, Ma Yanli, Wang Weichen, Shao Liwu. Inhibition Effect of Water Injection on Afterburning of Rocket Motor Exhaust Plume. Chinese Journal of Aeronautics, Vol.23 No.6, pp. 653-659, 2010.
  6. Shu C W, Osher S. Efficient implementation of essentially non-oscillatory shock capturing schemes II. Journal of Computational Physics. Vol.83 No.6, pp. 32-78, 1989
  7. Thompson K W. Time dependent boundary conditions for hyperbolic systems. Journal of Computational Physics. Vol.68 No.6, pp. 1-24, 1987
  8. Shi T H. A new  $k-\varepsilon$  Eddy-viscosity model for high Reynolds number turbulent flows-model development and validation[J]. Computers Fluids, Vol.24 No.3, pp. 227-238, 1995
  9. JIANG Yi, Hao Ji-guang. Study on theory and test of a new type "concentric canister with jet flow" vertical launcher[J]. Journal of Astronautics, Vol.29 No.1, pp.236-241, 2008.
  10. Zhang Ping, Sun Weisheng, Sui Ying. Principle of Solid Rocket Technology, Beijing institute of technology press, 1992.
  11. Jensen D E, Jones G A. Reaction rate coefficients for Flame calculations. Combustion and Flame, Vol.32 No.1, pp. 1-34, 1978.
  12. Jiang Yi, Fu Debing. Numerical simulation for non equilibrium chemically reacting fluid field of the solid rocket motor exhaust plume [J]. Journal of Astronautics, Vol.29 No.2, pp. 615-620, 2008.
  13. You Guo-zhao, Xu Houqian, Yang Qiren. Intermediate Ballistics [M]. Beijing national defense industry press, 2003.

# Active Back Pressure Mechanism for Electric Scroll Compressor

Jongbo Won<sup>1#</sup>, Ilyoung Park<sup>1</sup>, Jeongsik Shin<sup>1</sup>, Yongnam Ahn<sup>1</sup> and Kweonsoo Lim<sup>1</sup>

<sup>1</sup> Halla Visteon Climate Control Corp., 95, Sinilseo-ro, Daedeok-gu, Daejeon, South Korea, 306-230  
# Corresponding Author / E-mail: jwon@hvcglobal.com, TEL: +82-42-930-5926, FAX: +82-42-930-6992

KEYWORDS : Back Pressure, Control Valve, Scroll, Electric Compressor

*Eco-friendly vehicles such as EV and FCEV require more efficient parts to increase mileage without charging. Active back pressure mechanism for e-Comp. (Electric Scroll Compressor) was developed to meet the requirement. As the first step, we found out the optimal back pressure under the conditions that e-Comp. operates. And then we made the control valve to control and hold back pressure level in accordance with discharge pressure level against the internal leakage and excess friction occurred between orbiting and fixed scroll. For exact comparison between current back pressure mechanism and active back pressure mechanism, we designed modified e-Comp. that could eliminate the influence caused by scroll machining deviation. As a result, active back pressure mechanism showed that it improved COP up to 5.7% when compared to current back pressure mechanism.*

## NOMENCLATURE

$F_a$  = compressed refrigerant force (N)  
 $F_b$  = back pressure force (N)  
 $P_d$  = discharge pressure (kPaG)  
 $P_b$  = back pressure (kPaG)  
 $P_s$  = suction pressure (kPaG)

## 1. Introduction

The core-technology trend of current industry focuses on environment and efficiency. In terms of environment, the era that mass-production is impossible if they aren't eco-friendly products is entering because restrictions and standards such as GWP(Global Warming Potential), TEWI(Total Equivalent Warming Impact) and LCCP(Life Cycle Climate Performance) are tightened under major premise of environmental protection. In terms of efficiency, all the manufactures are conducting research for high-efficiency products because customers are accustomed to the concept of consumption power reduction.

Automotive industry is developing hybrid, electric and fuel cell vehicles to reduce and eliminate CO<sub>2</sub> occurred by fossil-fuel ignition. All the power come from electric battery especially in electric and fuel cell vehicles, so engine-driven parts should be changed to electric

parts. For this reason, electric compressors are needed instead of engine-driven compressor.

It is possible for electric compressors to control displacement by the fact that electric compressor speed is independent from vehicle engine speed and can have their own speed. Among electric compressors, electric scroll compressors have high volume efficiency, low efficiency deviation and compact package due to narrow compression space. Also they have low pulsation owing to sequential compression process. But leakage path is so complicated and long that internal leakage occurs during compression process. Major internal leakages are divided into axial and radial internal leakage occurred between orbiting and fixed scroll, and it is necessary that these internal leakages are minimized for improved efficiency of electric scroll compressor.

In this paper, we are introducing new back pressure mechanism to minimize axial internal leakage for improved efficiency of electric scroll compressor.

## 2. Design of active back pressure mechanism

### 2.1 Problem definition and Concept

The back pressure in electric scroll compressor pushes orbiting scroll against the compressed refrigerant generated between orbiting and fixed scroll. Fig. 1 shows compressed refrigerant force ( $F_a$ ) and back pressure force ( $F_b$ ) occurred during compressing process. It is ideal back pressure mechanism that back pressure force increases as

compressed refrigerant force increases and on the contrary to that, back pressure force decreases as compressed refrigerant force decreases.

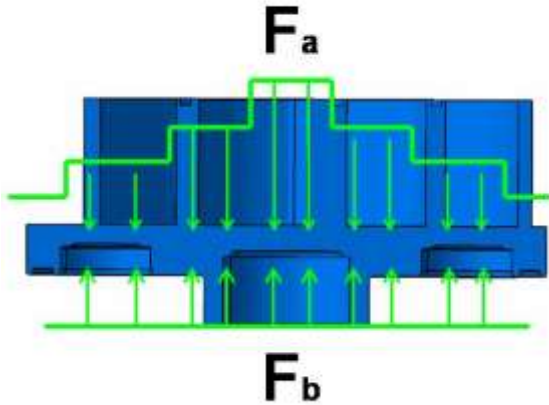


Fig. 1 Force balance on orbiting scroll

Fig. 2(a) shows current back pressure mechanism for electric scroll compressor. Discharge refrigerant gas with high pressure is passed through orifice and narrow path and back pressure level is determined by the status of relief valve located between back pressure chamber and suction chamber. Relief valve would open if the pressure difference between back pressure and suction pressure is more than setting pressure of relief valve, otherwise it would close. For this reason, back pressure level is determined as suction pressure plus setting pressure of relief valve. Therefore, back pressure level wouldn't be enough to hold orbiting scroll against compressed refrigerant force because back pressure force is maintained while compressed refrigerant force increases under high discharge pressure condition such as idle. The active back pressure mechanism that controls back pressure level in connection with compressed refrigerant force was designed to solve that like Fig. 2(b). Discharge pressure has strong influence on compressed refrigerant force, so back pressure level is determined as the function of discharge pressure in active back pressure mechanism.

Discharge pressure is equal to suction pressure when A/C mode is off. It causes control valve closed. When A/C turn on, the pressure difference between discharge and suction side increases as electric scroll compressor operates. If the pressure difference between discharge and suction side is less than the setting pressure of control valve, control valve keeps closing so back pressure level is still equal to suction pressure level. It means that suction pressure doesn't reach main A/C usage condition at which evaporator temperature is enough low. To meet target suction pressure faster, entire discharge refrigerant is guided to condenser by blocking the refrigerant moving to back pressure chamber through control valve. When the pressure difference between discharge and suction side is more than the setting pressure of control valve after meeting target suction pressure, control valve opens and some discharge refrigerant gas gets to move to back pressure chamber. Simultaneously refrigerant moves from back pressure chamber to suction chamber through orifice but back pressure can be increased up to a certain level because of the orifice

with high fluid resistance. If back pressure level reaches a certain level, back pressure level can be hold because the refrigerant amount moving from discharge chamber to back pressure chamber would be equal to that moving from back pressure chamber to suction chamber.

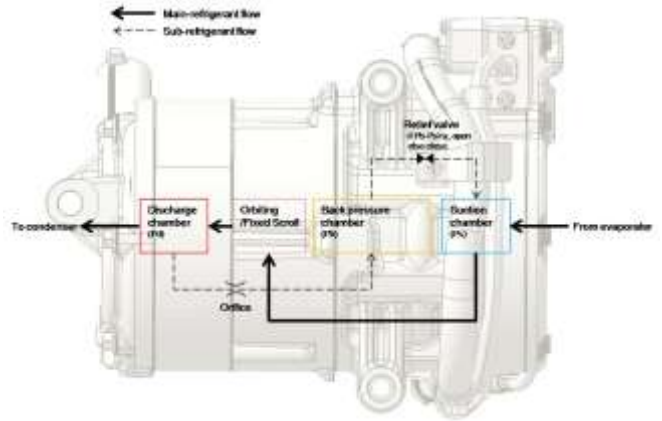


Fig. 2(a) Schematic diagram of current back pressure mechanism

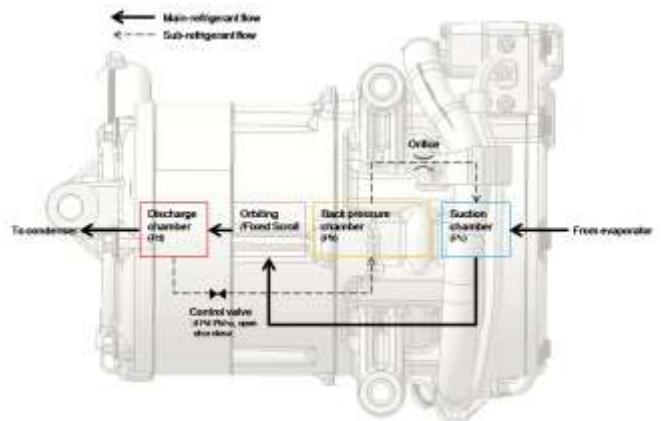


Fig. 2(b) Schematic diagram of active back pressure mechanism

2.2 Target back pressure level



Fig. 3 Modified e-Comp. to determine target back pressure

The sample like Fig. 3 was build to select the optimal back pressure in accordance with discharge pressure for maximum COP. The refrigerant amount moving to back pressure chamber could be controlled by connecting hose and needle valve externally between discharge chamber and back pressure chamber. Cooling capacity, consumption power and discharge refrigerant temperature were measured as back pressure level increased under each test conditions.

Fig. 4 shows that COP increased as back pressure level increased and COP decreased after back pressure level reached up to a certain level. That means decreased axial internal leakage led to increased COP and friction loss between orbiting and fixed scroll led to decreased COP. After selecting the optimal back pressure level for maximum COP under each test conditions, target back pressure level was determined by fitting the optimal back pressure levels linearly.

No.	Discharge pressure [kPaG]	Suction pressure [kPaG]	Comp speed [RPM]
1	1400	200	5000
2	1700	215	5000
3	2000	230	5000
4	2400	250	5000

Table 1 Test condition for target back pressure

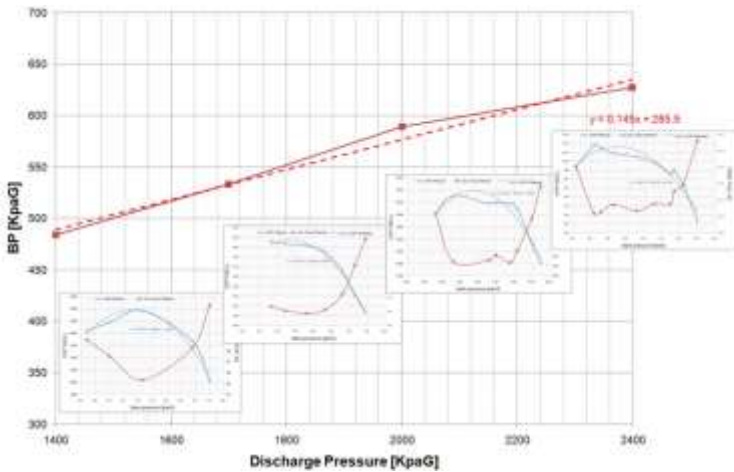


Fig. 4 Target back pressure

### 2.3 Control valve design

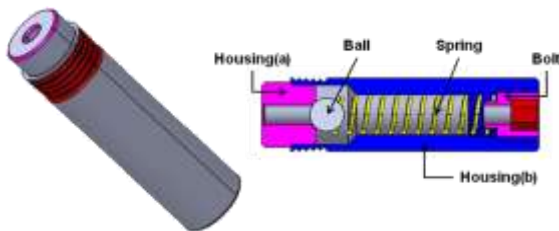


Fig. 5 Structure of control valve

Fig. 5 shows the structure of control valve located between discharge chamber and back pressure chamber and controlling the refrigerant amount moving to back pressure chamber. Control valve consists of valve housing(a), valve housing(b), ball, spring and bolt. The setting pressure of control valve is controlled by axial length of spring and bolt tightening, and the fluid resistance of control valve is controlled by hole size in valve housing(a). Also, the assembly structure that valve housing(a) is inserted into housing(b) when control valve is assembled inside electric scroll compressor prevents external leakage.

### 2.4 Control valve test set-up and results

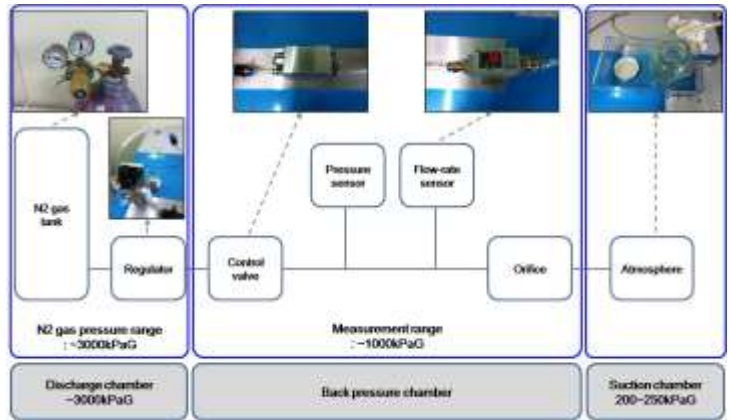


Fig. 6 Test set-up for control valve

The test set-up to confirm the function of control valve was established as Fig. 6. It was described the internal structure of electric scroll compressor related to back pressure. High pressure environment such as discharge chamber was formed with high pressure nitrogen gas and regulator. Back pressure chamber was formed by putting control valve and orifice. Also suction chamber was described as the atmosphere. In advance, the function of control valve inside electric scroll compressor was checked, measuring the pressure between control valve and orifice as nitrogen pressure increased slowly.

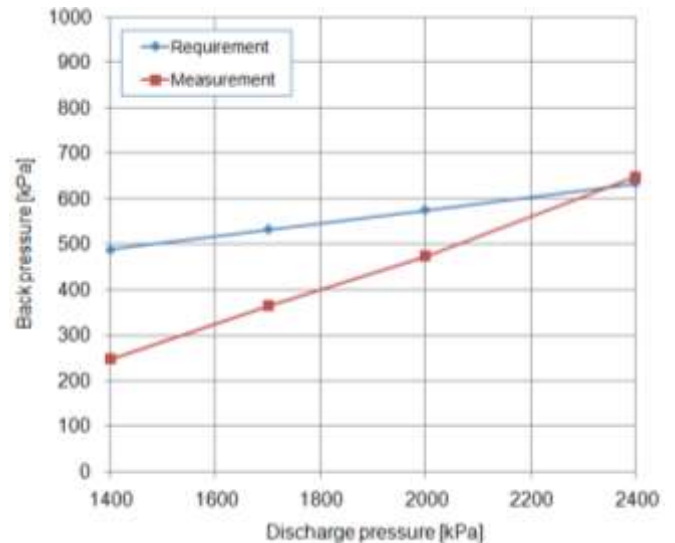


Fig. 7 Test result of control valve

Fig. 7 shows the back pressure level trend in accordance with nitrogen pressure. Even though measured back pressure was about 240kPa lower than target back pressure at 1400kPaG nitrogen pressure, measured back pressure reached target back pressure at 2400kPaG nitrogen pressure. Considering that suction chamber was described as the atmosphere, about 200kPa lower than the suction pressure of electric scroll compressor, test result was concluded as satisfaction level.

### 3. Effectiveness of active back pressure mechanism

**3.1 Test sample for active back pressure mechanism**

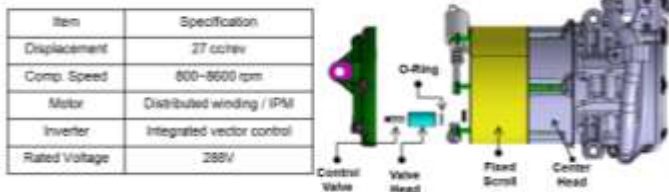


Fig. 8 Sample specification for active back pressure mechanism

The electric scroll compressor used in this study was built as Fig. 8. To assemble control valve into fixed scroll, control valve was inserted into valve head with interference and then valve head was assembled into fixed scroll by using the screw tap on the surface of valve head. The o-ring located between valve head and fixed scroll prevented the leakage that could occur between them. Also, back pressure was measured through the hole penetrating center head.

**3.2 Test result of active back pressure mechanism**

Test was conducted under test condition as table 1 to confirm the back pressure level generated by active back pressure mechanism. As a result, the back pressure generated by active back pressure mechanism was about 26~38kPa lower than target back pressure but was judged as target back pressure because the back pressure range corresponding to  $\Delta COP$  0.01 is target back pressure  $\pm 50$ kPa.

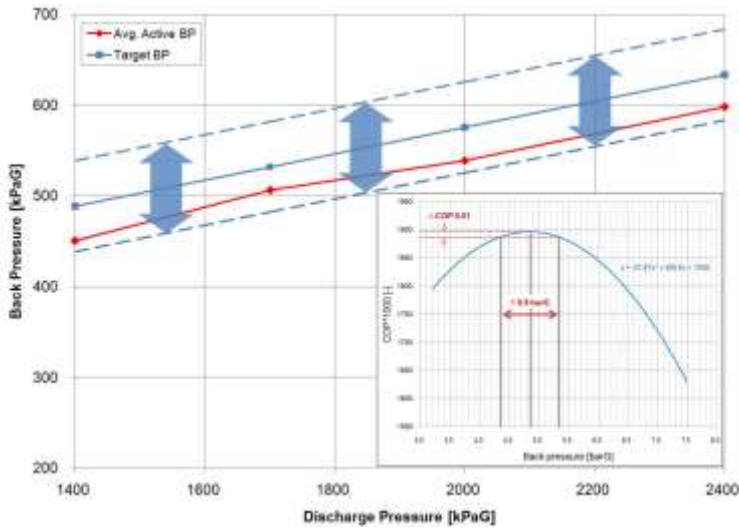


Fig. 9 Back pressure level of active back pressure mechanism

Fig. 10 shows that the comparison of back pressure level generated in current back pressure mechanism and active back pressure mechanism. The back pressure difference between current back pressure mechanism and active back pressure mechanism increased as discharge pressure increased. There was about 20~30kPa difference between them at 1400kPaG discharge pressure and the back pressure difference increased up to 100kPa at 2400kPaG discharge pressure. When compared to current back pressure mechanism, the COP of active back pressure mechanism was improved under all the conditions except one. Especially, it showed high COP improvement in high discharge pressure environment. That

was proportional to the back pressure difference between current back pressure mechanism and active back pressure mechanism. It was difficult to confirm improved COP at low discharge pressure environment as the back pressure difference generated from two mechanisms was small.

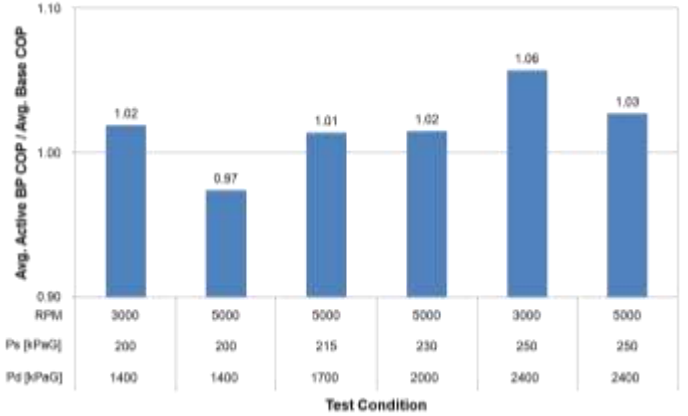
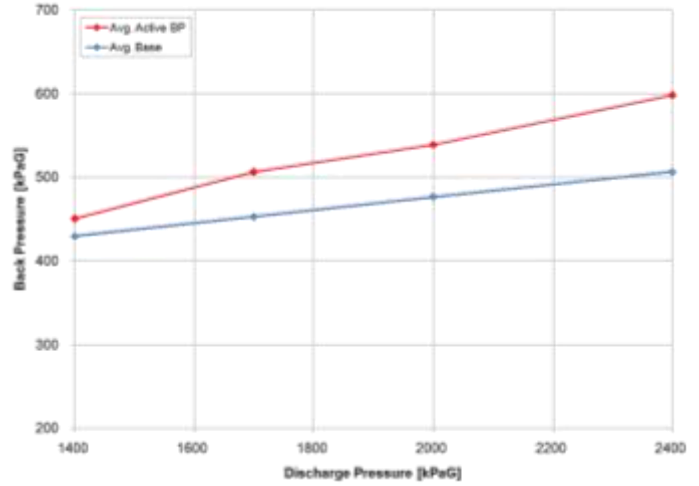


Fig. 10 Comparison between active back pressure mechanism and current back pressure mechanism

**4. Conclusions**

Below conclusion can be obtained by this study about active back pressure mechanism of electric scroll compressor.

- 1) The forces having influences on orbiting scroll are compressed refrigerant force and back pressure force, and back pressure force was realized as the function of discharge pressure.
- 2) The optimal back pressure level for maximum COP was selected at each discharge pressure, and target back pressure level and range were determined considering product deviation.
- 3) It was confirmed that target back pressure level was achievable by control valve test.
- 4) The back pressure levels of current back pressure mechanism and active back pressure mechanism were compared, and active back pressure mechanism improved COP up to 5.7%.

**ACKNOWLEDGEMENT**

This work was supported and sponsored by Halla Visteon Climate Control Corp.

## REFERENCES

1. Kim, H. J., Lee, W. H., "Stability of the axially compliant fixed scroll in scroll compressors," Korean Journal of Air-Conditioning and Refrigeration Engineering, Vol. 9, No. 2, pp. 93-103
2. Fushiki T., et, al., "Development of scroll compressor with new compliant mechanism," Sixteenth International Compressor Engineering Conference at Purdue, C18-3
3. Koo, I. H., Nam, B. Y., Lee, G. H., "Design of Back Pressure Control Valve for Automotive Scroll Compressor," International Compressor Engineering Conference at Purdue, July 14-17, 2008

# Performance of Biocomposites Reinforced by Cellulose Nanofiber Obtained from Paper Wastes

Hitoshi Takagi<sup>1#</sup>, Antonio N. Nakagaito<sup>1</sup>, Satoshi Sugano<sup>1</sup>, Yuya Muneta<sup>2</sup> and Jitendra K. Pandey<sup>3</sup>

<sup>1</sup> Institute of Technology and Science, The University of Tokushima, 2-1 Minamijosanjima-cho, Tokushima Japan

<sup>2</sup> Graduate School of Advanced Technology and Science, The University of Tokushima, 2-1 Minamijosanjima-cho, Tokushima Japan

<sup>3</sup> University of Petroleum and Energy Studies, Dehradun, India

# Corresponding Author / E-mail: takagi@tokushima-u.ac.jp, TEL: +81-88-656-7359, FAX: +81-88-656-9082

KEYWORDS : Cellulose, Extraction, Biocomposites, Green Composites, Nanofiber, Inorganic Compound

---

*A large amount of paper sludge has been discharged in the world, because paper is an important material for our daily life. The physical properties of paper sludge are not sufficient to make new papers, but its dimension is much larger than cellulose nanofibers. The cellulose nanofibers have been showing greater potential to improve mechanical performance of polymer composites. The objectives of this study are to extract the cellulose nanofibers from waste paper sludge, and to check the applicability of the extracted cellulose nanofiber as a reinforcing phase in biocomposites. The cellulosic nanofibers were extracted by chemical and physical treatments. In order to examine the reinforcing effect of the extracted cellulose nanofiber, biocomposites were fabricated by combining this nanofiber with poly vinyl alcohol, and then the tensile tests were conducted to evaluate the enhancement in mechanical properties of the resultant biocomposites.*

---

## 1. Introduction

Cellulose is one of the typical biomass material and the utilization of the cellulose in various fields has spread broadly considering the mass production of cellulose. In plant cell walls, stiff semi-crystalline cellulose nanofibers are embedded in complex and amorphous matrix of lignin and hemicellulose where the size and shape of the cellulose nanofibers are controlled by the dimensions of the crystalline regions. This crystalline cellulose is a main source of unique structural and physical functionalities to be applied in various applications [1-3]. The crystalline region has high modulus and high strength estimated to be 150 GPa and 10 GPa, respectively [4-7].

Although there are various cellulosic waste resources, the utilization of different cellulosic wastes for extraction of crystalline cellulose requires more exploration for yield optimization. The research on the crystalline cellulose has two serious challenges. The first one is the efficient extraction of crystalline cellulose, namely the process is long and needs more energy for the extraction. The second one is the difficulty in dispersion of the crystalline cellulose in many organic solvents and polymers, which severely limits their application to water-based polymer matrices [1].

Recently the crystalline cellulose nanofiber can be extracted using many types of methods and each method provides different scale of

crystalline cellulose region [5, 9]. In this study, both mechanical and chemical treatments were used to extract crystalline cellulose nanofiber from waste bio-resources. Waste newspaper and paper sludge were used as a low-cost source for cellulose nanofiber. The reinforcing effect of the obtained cellulose nanofibers was also examined by composing with water-soluble biodegradable resin (PVA).

## 2. Experimental Method

### 2.1 Extraction of Cellulose Nanofibers

In fiber extraction processes, a series of alkaline treatment, bleaching treatment, acid hydrolysis treatment, and mechanical treatment were used. Alkaline treatment by an aqueous solution of 5wt% sodium hydroxide (NaOH) is necessary to remove hemicellulose in the pulp of the newspaper. This treatment was continued for 3 hours at 80 °C, followed by several washing cycles until pH became neutral. Crystalline cellulose is embedded in hemicellulose and by applying the alkaline treatment, an expansion of the hemicellulose matrix occur, resulting in the reduction of intermolecular hydrogen bonding.

The bleaching treatment was conducted by mixing 25 g of sodium

chloride ( $\text{NaClO}_2$ ) and 200 ml of acetic acid ( $\text{CH}_3\text{COOH}$ ) in 1000 ml of water at  $80^\circ\text{C}$ , until colored substances were removed. Some remaining grey color gradually changed to white after several continuous washing. The other objective of bleaching process was to leach the lignin out completely. Then, the samples were subjected to acid hydrolysis treatment with an aqueous solution of 64% sulphuric acid ( $\text{H}_2\text{SO}_4$ ) for 1 hour at  $70^\circ\text{C}$ . After completion of acid hydrolysis treatment, the samples were quenched into cold water followed by several washing cycles until pH became neutral. Then, the sample was kept in water swollen state during the whole chemical process to avoid generating strong hydrogen bonding among crystalline cellulose after matrix removal.

After the completion of chemical treatments, the physical treatment was conducted in order to isolate and disperse crystalline cellulose nanofiber in water suspension solution. The highly purified crystalline cellulose nanofiber suspension was then placed in an ultrasonic homogenizer (model UH-150; SMT Co., Ltd., Japan). The subsequent ultrasonication treatment was conducted for 1 hour to isolate the crystalline cellulose nanofibers from their cellulosic bundle fibers. The ultrasonication treatment was carefully carried out in cold water bath to absorb the heat generated during the ultrasonication treatment.

## 2.2 Characterization of Cellulose Nanofiber

Scanning electron microscopy (SEM) (model S-4700; Hitachi Ltd., Japan) was used for structural analysis of crystalline cellulose nanofiber extracted by acid hydrolysis treatment. The samples were dried at  $70^\circ\text{C}$  in a drying oven for about 12 hours. The obtained sheets were mounted on a metallic stub and platinum coated by sputter coating technique for 20 seconds to avoid charging-up the SEM images. Images of crystalline cellulose nanofiber were taken at low accelerating voltage (1.5 kV) at different magnifications.

## 2.3 Fabrication and Mechanical Characterization of Cellulose Nanofiber Reinforced Composites

In order to prepare polyvinyl alcohol (PVA) solution (RS-2817, Kuraray Co. Ltd., Japan), 500 ml of water in a beaker was heated to  $90^\circ\text{C}$  using a mantle heater. When the water temperature reached  $90^\circ\text{C}$ , PVA powder was gradually added in the hot water, and the PVA powder was dissolved in the hot water by stirring. The final PVA concentration of the cellulose nanofiber suspension was calculated by the ratio of the weights of cellulose nanofiber added and resultant cellulose nanofiber suspension. In this study, the weight content of the cellulose nanofiber was fixed to be 10wt.%. The cellulose nanofiber/PVA suspension was cast into the plastic shallow tray having the dimension of about  $200 \times 150 \times 15$  mm, and then dried at  $30^\circ\text{C}$  for 48 hours. After drying, the cellulose nanofiber/PVA composite sheet was cut into  $100 \times 10$  mm to prepare tensile specimens. The typical specimen thickness was 60-80  $\mu\text{m}$ .

Then tensile tests were carried out using a universal testing machine (model 5567; Instron Corp., USA) to evaluate the mechanical properties of cellulose nanofiber/PVA biocomposites. The specimen dimension was  $100 \times 10$  mm. The gauge length was 30 mm, and the crosshead speed was 1.0 mm/min.

## 3. Results and Discussion

### 3.1 Morphology of Cellulose Nanofiber

Figure 1 shows the SEM photomicrographs of the cellulose nanofibers extracted from waste newspaper, toilet paper, paper sludge A, and paper sludge B. These samples were all undergone by alkali treatment, bleach treatment, sulphuric acid treatment, and ultrasonication treatment. It can be seen from these SEM photomicrographs that the pulps of the waste newspaper was changed its shape and morphology, and the pulps were actually fibrillated into cellulose nanofibers.

### 3.2 Mechanical Properties of the PVA/cellulose Nanofiber Biocomposites

The tensile strength and Young's modulus of cellulose nanofiber/PVA biocomposites increased as indicated in Table 1. As expected, we can see a significant enhancement in mechanical performance of cellulose nanofiber-reinforced biocomposites as compared to that of neat PVA resin. High Young's modulus was obtained for the biocomposites reinforced by cellulose nanofiber extracted from paper sludge. Thin increases may be responsible for a fine dispersion of inorganic compounds, which were added during paper making.

Table 1 Tensile properties of cellulose nanofiber-reinforced biocomposites and neat PVA resin

Samples	Tensile strength (MPa)	Young's modulus (GPa)
Neat PVA resin	78	4.7
PVA-10wt.% cellulose nanofiber biocomposites (waste newspaper)	92	6.0
PVA-10wt.% cellulose nanofiber biocomposites (toilet paper)	112	7.4
PVA-10wt.% cellulose nanofiber biocomposites (sludge A)	115	8.2
PVA-10wt.% cellulose nanofiber biocomposites (sludge B)	125	8.4

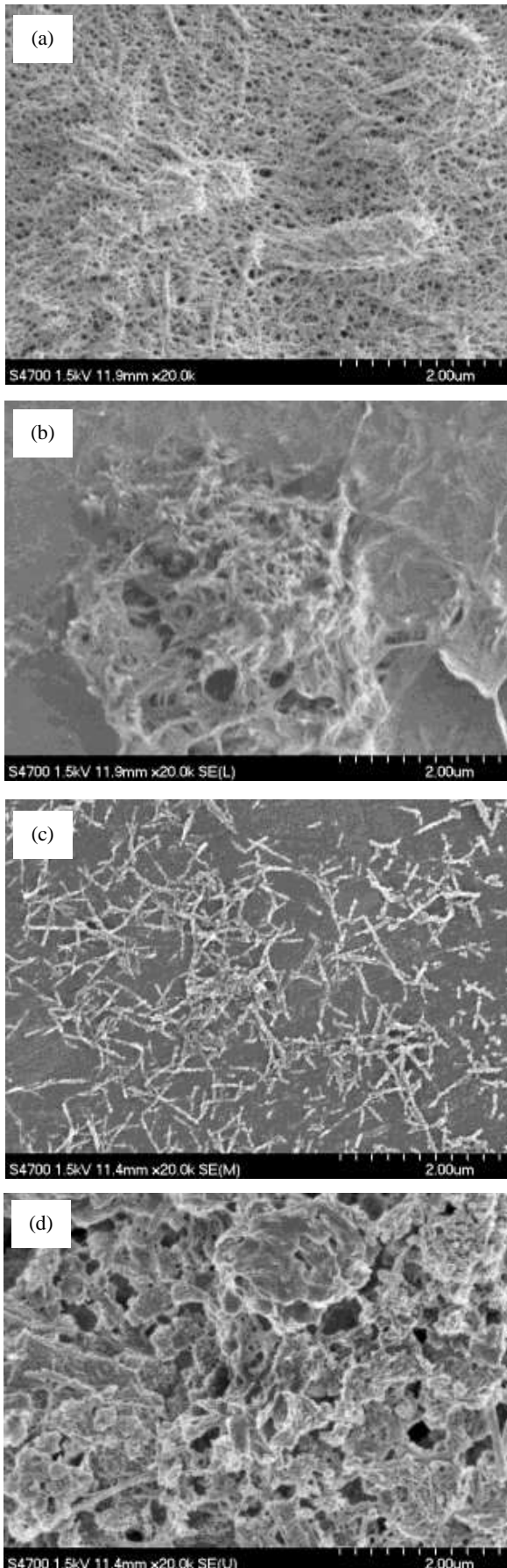


Fig. 1 SEM photomicrographs of cellulose nanofibers extracted from (a) waste newspaper, (b) toilet paper, (c) paper sludge A, and (d) paper sludge B.

### 3. Conclusions

1. Cellulose nanofibers having a nano-meter scale diameter can be extracted from cellulosic waste materials using the combination of acid hydrolysis and ultrasonication treatments.
2. Cellulose nanofiber-reinforced biocomposites were fabricated from PVA resin and cellulose nanofiber extracted from the waste materials.
3. Enhancement in mechanical properties of cellulose nanofiber-reinforced PVA biocomposites was clearly indicated. Especially enhanced Young's modulus was clearly obtained for biocomposites reinforced by paper sludge-derived cellulose nanofibers.

### ACKNOWLEDGEMENT

This work was partially supported by Japan Society for the Promotion of Science (JSPS) KAKENHI Grant Number 24656394.

### REFERENCES

1. Beck-Candanedo, S., Roman, M., and Gray, D. G., "Effect of reaction conditions on the properties and behavior of wood cellulose nanocrystal suspensions", *Biomacromolecules*, Vol. 6, No. 2, pp. 1048–1054, 2005.
2. Wang, B. and Sain, M., "Coated nanofibers in composites", *BioResources*, Vol. 2, No. 3, pp. 371–288, 2007.
3. Cordeiro, N., Mendonca, C., Pothan, L. A., and Varma, A., "Monitoring surface properties evolution of thermochemically modified cellulose nanofibres from banana pseudo-stem", *Carbohydrate Polymers*, Vol. 88, No. 1, pp. 125–131, 2012.
4. Helbert, W., Cavaille, J. Y. and Dufresne, A., "Thermoplastic nanocomposites filled with wheat straw cellulose whiskers. Part I: Processing and mechanical behavior", *Polymer Composite*, Vol. 17, No. 4, pp. 604–611, 1996.
5. Frone, A. N., Panaitescu, D. M., Donescu, D., Spataru, C. I., Radovici, C., Trusca, R., and Somoghi, R., "Preparation and characterization of PVA composites with cellulose nanofibers obtained by ultrasonication", *Bioresources*, Vol. 6, No. 1, pp. 487–512, 2011.
6. Sakurada, I., Nukushima, Y., and Ito, T., "Experimental determination of the elastic modulus of crystalline regions in oriented polymers", *Journal of Polymer Science*, Vol. 57, No. 165, pp. 651–660, 1962.
7. Page, D. H. and EL-Hosseiny, F., "The mechanical properties of single wood pulp fibres. Part VI. Fibril angle and the shape of the

- stress-strain curve”, *Journal of Pulp and Paper Science*, Vol. 9, No. 4, pp. 99–100, 1983.
8. Nakagaito, A. N. and Yano, H., “The effect of morphological changes from pulp fiber towards nano-scale fibrillated cellulose on the mechanical properties of high-strength plant fiber based composites”, *Applied Physics A-Materials Science & Processing*, Vol. 78, No. 4, pp. 547–552, 2004.
  9. Souza Lima, M. M. D. and Borsali, R., “Rodlike cellulose microcrystals: structure, properties, and applications ” , *Macromolecular Rapid Communications*, Vol. 25, No. 7, pp.771–787, 2004.

# A Study on the Heat Transfer Characteristics for the Shape of the Heat Sink

E. C. Jeon<sup>1</sup>, S. G. Kim<sup>2,#</sup>, J. H. Sung<sup>3</sup> and Y. H. Kim<sup>3</sup>

<sup>1</sup> Department of Mechanical Engineering, Dong A Univ.

<sup>2#</sup> Corresponding Author / Graduate School of Mechanical Engineering,

Dong A UNIV.E-mail : smartkim123@naver.com

<sup>3</sup> Department of New Materials Engineering, Dong A Univ.

KEYWORDS : Heat Sink, FEM(Finite Elements Method), Optimization, Heat Performance, Heat Resistance, Infrared Camera, Blower, Computational Fluid Dynamics

---

*Currently, electronic goods including smart phones are getting thinner and smaller. As a result, the caloric value per unit area of electronic equipment has improved and cooling technology comes to the fore to maintain ideal temperature inside the electronic goods. Among them, deciding the shape of the heat sink which maximally performs cooling function is important since the cooling performance of the heat sink which is the representative of cooling system depends on how to design the shape. Therefore, in this study, by using the modeling shape of each heat sink, this study confirms the optimization result according to the change of height of the tip clearance after analyzing thermal performance in accordance to the shape of the heat sink which is the object model by using ANSYS CFX which is the commercial finite element analysis program. Also, using infrared ray camera which is the thermal uncooled sensor type, this study confirms the tip clearance, shape and flux for improving thermal performance of the heat sink by comparing analysis and experimental value. ..*

---

## 1. Introduction

Currently, as many industries are developed, advanced equipment including a laptop computer becomes higher specifications and smaller in size by consumers' demand. As a result, the problem of heat value of electronic equipment stands out. As an alternative of the problem, the cooling technology becomes important to maintain proper temperature of the main parts of electronic equipment. Generally, the heating problem is related to the size and durability of the products. Therefore, the operation temperature importantly influences the products in terms of reliability.

Thus, cooling effectively components is regarded as the important problem. As the representative device to solve the heating problem of small products which are high performance and intensive effectively, the heat sink which raises the cooling performance by increasing the area of heat transfer per unit volume is widely used. According to the shape, the cooling performance of the heat sink is different. Therefore, the shape design is important for optimal cooling performance. In accordance with the shape, the heat sink is generally divided into Plate-fin heat sink and Pin-fin heat sink.

Plate-fin heat sink is easy to process and design. Therefore, it is widely used as the cooling device of the electronic device. Pin-fin heat sink can be used regardless of the flow direction. Since fins are separated, this heat sink raises the heat performance by blocking forming a boundary layer. With Plate-fin heat sink, it is widely used

as the cooling solution of an electronic device. To figure out which heat sink is advantageous and which heat sink has better heat performance between two heat sinks which have different characteristics, the study in comparing the heat performance among various heat sinks has been conducted since old times.

If we look at the recent studies among them, Kim and Webb<sup>1)</sup> optimized the heat sink by using experimental interaction equations which can predict the heat resistance and the falling pressure of the heat sink.

Kim<sup>2)</sup> investigated experimentally each radiant heat characteristic according to the shape and the way of heat transfer of the heat sink, conducted the analysis on numerical value regarding the layered heat sink which is thought to be the outstanding radiant heat characteristic and compared to the experiment result. .

Kang et al.<sup>3)</sup> sat up the arrangement of elements, the wind speed and the shape of the heat sink when cooling nature and forced convection and invented the program which predicts the temperature rise of the elements. However, since generally, the heat sink which applies to the electronic equipment and a machine product has the severe limitation of area and use environment, the simple shape of the heat sink has the limitation for improving the heat performance. . Lau. El-Sayed et al., O. N. Sara evaluated the heat performance in accordance with the size variation of tip clearance.<sup>4)-(7)</sup>, and Min et al.<sup>8)</sup> defined that in the condition of constant pumping power, tip clearance can improve the heat performance of the heat sink and the

optimal value exists by the analysis of numerical value and experiments. Also, E.A.M Elshafei<sup>(9)</sup> experimentally confirmed that in the condition of the same Reynolds number, the optimal value of tip clearance which can maximize the heat performance of straight-fin heat sink exists.

Also, because of the development and research of computer hardware and analysis on numerical value, the reliability of common floating analysis program which uses finite element method has been increased and by using this, numerical value research has been continuously conducted. In this study, with some heat sink modeling, after analyzing the heat performance according to the shape by using CFX which is the floating analysis program, the objective is to confirm the result in accordance with the change of height of tip clearance.

Also, by using the infrared camera of thermal type uncooled sensor and comparing the analysis value and experimental value, the study suggests the condition of the optimal flux and shape to improve the heat performance of the heat sink.

## 2. Method

In this study, the purpose is to figure out the cooling performance according to the difference of tip clearance which is cooling distance and the shape of the heat sink and its goal is to find the optimal cooling condition according to the flux.

As the object model, it applies to the optimal heat sink through the result by selecting the shape of the aluminum heat sink of the same base plate size. First, through SolidWorks, each heat sink conducted 3D modeling. In this study, the material of the heat sink is Aluminum. Base plate is 40mm, the thickness of the base plate is 1 to 5mm and height is 10 to 40mm.

Also, the consumption of electrical power of the heat rays is 30W and the rage of shooting of the thermo-graphic camera is 140x140mm. Fig. 7(a) indicates 3D modeling of the object shape by using SolidWorks. Then, the information of the heat sink which is used in the experiment is like Tale 1.

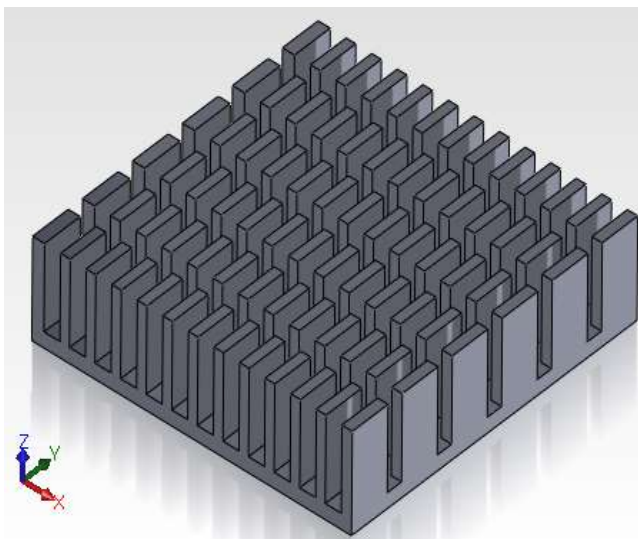


Fig. 1 3D modeling of heat sink

Table. 1 Information of Heat sink

Case Number of Heat sink	Parameter	
1	Base Plate height	4mm
	Fin height	6mm
2	Base Plate height	2mm
	Fin height	11mm
3	Base Plate height	1mm
	Fin height	14mm
4	Base Plate height	5mm
	Fin height	15mm
5	Base Plate height	3mm
	Fin height	21mm
6	Base Plate height	2mm
	Fin height	28mm
7	Base Plate height	5mm
	Fin height	35mm

In this study, after figuring out the heat performance by using FEM program, it confirmed the temperature distribution through the thermo-graphic camera to check the reliability of the program. Also, for forced convection, a blower was used and to measure the flux of the blower, the pitot tube way was used. Besides, when the diameter of the blower is (D) and the distance between the edge of the pin and the blower is (H) through 3, 8 and 12 times 25mm, the diameter and change of height of the blower is H/D. Also, based on the values of ratio which the height of fin (F) and the height of the base plate (L) is F/L and the gap distance of fin (W) and the height of the base plate (L) is W/L, the shape and ratio of the heat sink which has optimal cooling condition was figured out.

## 3. Result

After confirming the radiant heat effect in the condition of nature through the basic analysis, the floating analysis was conducted. The program for the floating analysis is Ansys CFX. Then, the reliability of the program was confirmed through the actual experiment. Like the experiment of natural convection, after forced convention by using the blower, this experiment got the result value by using the thermo-graphic camera. First, the height of the experimental equipment was adjusted for the ratio H/D (the diameter of the blower (D) and the distance between the edge of the pin and the blower,) to be 3, 8 and 12 and each radiant heat effect was confirmed. Also, the experimental equipment which can adjust the height was manufactured. This equipment was made of transparent acrylic and the thickness was 5mm. The ratio of 3 is first experiment and each height is 72, 192 and 288mm.

In this study, although the simple blower diameter was analyzed by conducting experiment as the ratio of height between the blower and the pin of edge, in the bad condition of use environment, by using the ration in the study, the radiant heat effect seems to be better

Table. 2 Experiment and FEM result about temperature parameter

Case number	FEM		Experiment		Error(%)
1	Max	41.65 °C	Max	40.9 °C	1.8
	Min	41.61 °C	Min	40.6 °C	2.43
2	Max	33.1 °C	Max	32.51 °C	1.78
	Min	32.49 °C	Min	29.6 °C	8.9
3	Max	39.56 °C	Max	39.6 °C	0.5
	Min	39.51 °C	Min	39.1 °C	1.04
4	Max	39.61 °C	Max	36.4 °C	8.1
	Min	39.34 °C	Min	35.3 °C	10.3
5	Max	36.82 °C	Max	36.4 °C	1.14
	Min	35.7 °C	Min	34.7 °C	2.8
6	Max	37.33 °C	Max	37.2 °C	0.35
	Min	36.25 °C	Min	35.1 °C	3.17
7	Max	33.45 °C	Max	33 °C	1.35
	Min	33.09 °C	Min	30.6 °C	7.52

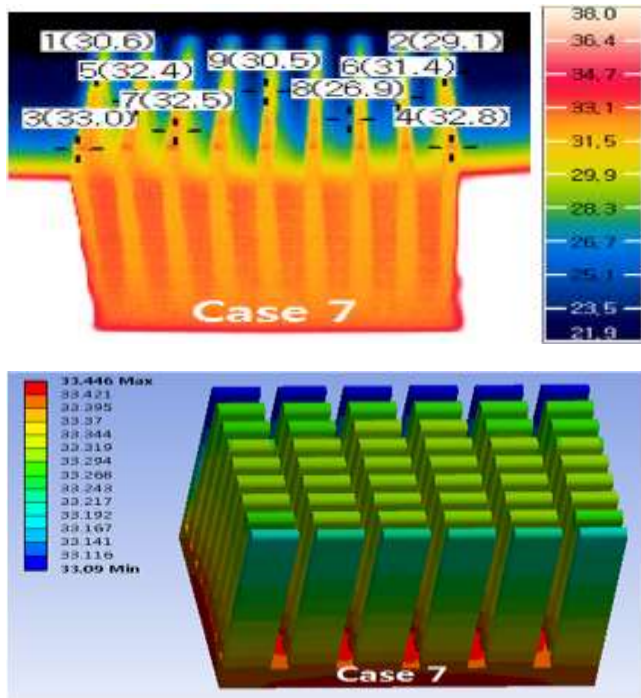


Fig. 2 Compare result about FEM and Experiment

Fig.2 compared the analyzed result and the data which the thermographic camera shot and Table 2 indicates the whole data and the compared result. When analyzing the result, it was confirmed that plate-fin heat sink which has the pin of tetragonal height has not only high reliability and but also high radiant heat performance. After that, to check the optimal shape and radiant heat condition of the heat sink, after fixing base plate to 3mm, Reynolds number altered from 10,000 to 30,000 by changing the shape in accordance with each height. At this time, the height between the edge of the heat sink and the blower is maintained 72, 192 and 288mm like the former experiment. Fig.3 and Fig. 4 indicate the heat resistance according to Reynolds number.

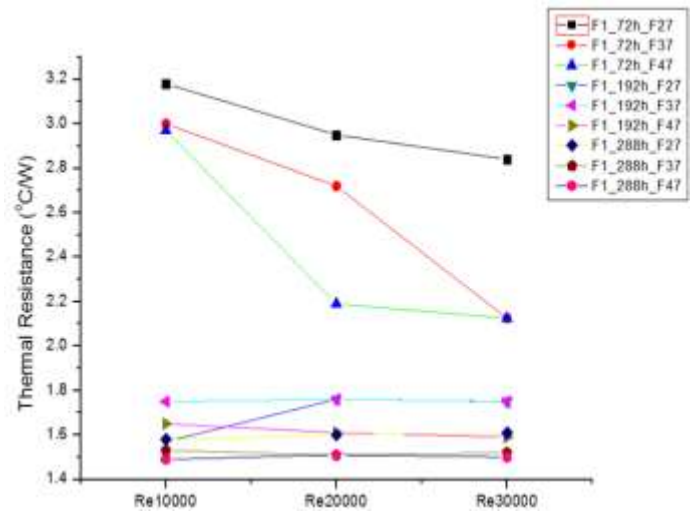


Fig. 3 Graph of thermal resistance about Function 1

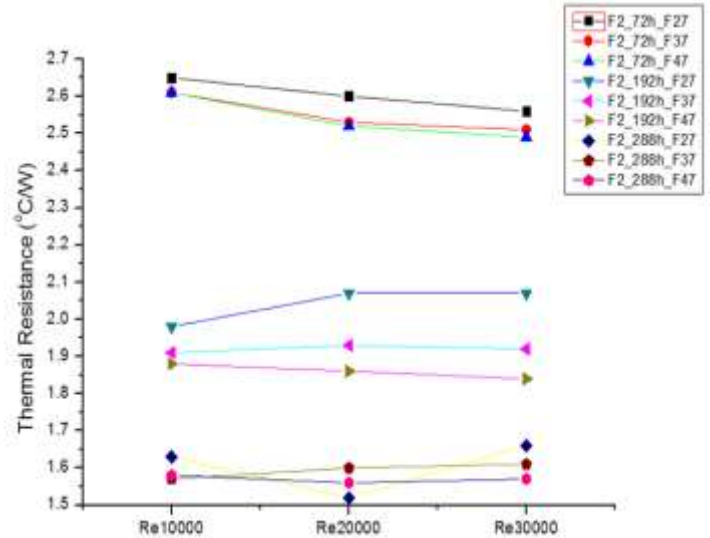


Fig. 4 Graph of thermal resistance about Function 2

### ACKNOWLEDGEMENT

This work was supported by grant No. RT104-01-03 from the Regional Technology Innovation Program of the Ministry of Knowledge Economy (MKE).

### REFERENCES

- 1) S. Y. KIM, R. L. Webb, "Thermal Performance Analysis of Fan-Heat Sink for CPU Cooling", Journal of IMECE, Vol. 42172, (2003)
- 2) J. H. KIM, "A Study on the heat transfer characteristics for layered heat sink", Ph. D. Thesis of HanYang University, pp. 1~106, (2004).
- 3) S. W. KANG, H. S. PARK, Y. K. KLim., C. S. JEON,

- C. D. LEE, "thermal design for electrical devices using heat sink", Journal of KSME, B, pp. 207~212, (1998).
- 4) KEI. S. LAU, Roop. L. MAHAJAN, "Effects of tip clearance and fin destiny on the performance of heat sink for VLSI packages", IEEE Transaction on Components, Hybrids and Manufacturing Technology, Vol. 12, No. 4, pp. 757~765, (1989).
  - 5) Saad. A. El-Sayed, Shamloul. M. MOHAMED, Ahmed M. Abdel-latif, Abdel-hamid. E. Abouda, "Inverstigation of turbulent heat transfer and fluid flow in longitudinal rectangular fin-arrays of different geometries and shrouded fin array", Experimental Thermal and Fluid Science, Vol. 26, pp. 879~900, (2002).
  - 6) O. N. SARA, "Performance analysis of rectangular ducts with staggered square pin fin", Energy Conversion and Management, Vol. 44, pp. 1787~1803, (2003).
  - 7) Y. J. MIN, S. P. JANG, S. J. KIM, "Effect of Tip clearance on the cooling performance of a micro channel heat sink", Journal of Heat and Mass Transfer, pp. 1099~1103, (2003).
  - 8) J. W. KIM, "Experimental Study on the Effect of Tip Clearance for a Straight Fin Heat Sink", Master degree thesis, pp. 23~24, (2004).
  - 9) E.A.M. Elshafei, "Effect of flow bypass on the performance of a shrouded longitudinal fin array", Applied thermal engineering. pp. 2233~2242, (2007).

# A Fuzzy AHP Framework for Multi Criteria Decision Making of a Sustainable Product Design

Zahari Taha<sup>1</sup>, H.A. Salaam<sup>2#</sup>, T.M.Y.S Tuan Ya<sup>3</sup> and Mohd Razali Mohamad<sup>4</sup>

<sup>1</sup> Faculty of Manufacturing Engineering, Universiti Malaysia Pahang (UMP), Pekan, Pahang, Malaysia. 26600

<sup>2</sup> Faculty of Mechanical Engineering, Universiti Malaysia Pahang (UMP), Pekan, Pahang, Malaysia. 26600

<sup>3</sup> Department of Mechanical Engineering, Faculty of Engineering, Universiti Teknologi PETRONAS (UTP), Bandar Sri Iskandar, Tronoh, Perak, Malaysia. 31750

<sup>4</sup> Faculty of Manufacturing Engineering, Universiti Teknikal Malaysia Melaka (UTEM), Hang Tuah Jaya, Durian Tunggal, Melaka, Malaysia. 71600

# Corresponding Author / E-mail: hadisalaam@ump.edu.my, TEL: +609-4246220, FAX: +609-4246222

KEYWORDS : Fuzzy AHP, Multi-Criteria Decision Making (MCDM) and Sustainable Product Design

---

*Three main criteria have been identified for a sustainable product namely manufacturing cost, environmental cost and social cost. Consideration of the manufacturing cost is critical in ensuring the economic sustainability of the manufacturer. Environmental considerations have become very crucial as the world communities have realized the necessity to meet the needs of the present generations without compromising the ability of future generations to meet their own needs. Social costs are difficult to identify but at a factory floor level it implies the effect of manufacturing a product on the workers and it's users, and in this case is equated to ergonomics consideration. These criteria are considered in the early stages of product design and as such decision for the final design involves multi criteria decision making in the presence of multiple objectives. The objectives are usually conflicting and therefore, the proposed solution is highly dependent on the preferences of groups of decision makers and is developed within an understanding framework and mutual compromise. There are many examples of MCDM methods such as Weight Summed Method (WSM), Analytical Process Hierarchy (AHP) and Fuzzy Analytical Process Hierarchy (FAHP). This paper presents a brief review of multi-criteria decision making (MCDM), analytical hierarchy process (AHP), fuzzy analytical hierarchy process (FAHP) theory and previous research associated with AHP and FAHP. It also proposes a Fuzzy AHP framework for a sustainability assessment tool development which will help a designer to choose a design that will satisfy the sustainability criteria of economics, environmental and ergonomics.*

---

---

## NOMENCLATURE

$n$  = number of criteria

$w_i$  = weight value of criteria  $i$

$w_j$  = weight value of criteria  $j$

$\tilde{M}$  = triangular fuzzy number symbol

$l$  = the smallest possible value

$m$  = the most promising value

$u$  = the largest possible value

$l(y)$  = the left side of Fuzzy Number

$r(y)$  = the right side of Fuzzy Number

$\tilde{w}$  = fuzzy priority vector

---

## 1. Introduction

The broad definition of a 'sustainable product' is a product that has minimum impact on the environment at each phase of its life cycle. However the word sustainable has a wider implication on environmental, social and economic aspects of the design. In addition to fulfilling the technical performance and costs demanded by the client, a product designer needs to consider the various stakeholders or interested parties in the product. However to take into consideration the whole gamut of stakeholders as depicted by Howarth et al 2006 is complex where it involves customer, client, user, manufacturers, local council, employers, professional institutions, material supplier, environment agency, trade associations, contractors, community, planning officer, energy and water supplier as shown in Figure 1.

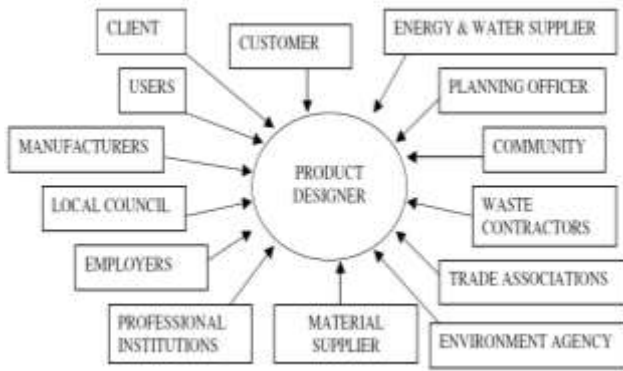


Fig. 1 Typical range of stakeholders

In this paper we proposed an approach that takes into consideration only several major stake holders interested in the economics, environmental and ergonomic aspects of the product. The client and the user can be considered as one major stake holder who is both interested in the economics aspects. The trade associations will be interested in the social aspects of the workers and in this case we have focused on the ergonomics implications as it would have a long term effect on the quality of life of the workers. The environmental aspects would be of interest to the environmental agency and the community. However making decisions taking into consideration these three aspects is still a difficult task as it involves multiple objectives.

Multi-criteria decision making (MCDM) methods such as Weight Summed Method (WSM), Analytical Process Hierarchy (AHP) and Fuzzy Analytical Process Hierarchy (FAHP) are some of the methods that can be used.

In this paper we present a brief review of analytical hierarchy process (AHP), fuzzy analytical hierarchy process (FAHP) theory and previous research associated with AHP and FAHP and consequently propose a Fuzzy AHP framework for a sustainability assessment tool which will help a designer to choose a design that will satisfy the sustainability criteria of economics, environmental and ergonomics.

## 2. Analytic Hierarchy Process (AHP)

Analytical Hierarchy Process (AHP) was developed by Thomas L. Saaty in the year 1970's. It is a flexible quantitative method used for selecting decision among alternatives based on criteria performance with respect to one or more criteria (Rouyendegh and Erkan, 2012). In this method, a group of expert individuals are asked to make pairwise comparisons to derive a priority scale. The evaluation process involves seven steps which starts with describing the unstructured problem; detailing the related criteria and possible alternatives; arranging the problem goals, criteria and alternatives into a hierarchy; recruiting pair wise comparisons among decision elements; using the Eigen value method to predict the relative weights of the decision elements; computing the consistency properties of the matrix; and collecting the weighted decision elements.

The problem need to be described in detail in particular the knowledge required for ease of solving the problem and also detailing

the criteria and possible alternatives. A mutually independent hierarchical structure is then established, where at the top of the hierarchy structure is the goal of the decision, followed by the objectives or criterion from a broad perspective, through the intermediate levels and at the bottom of the hierarchical structure is all possible alternative solutions to the goal such as shown in Figure 2.

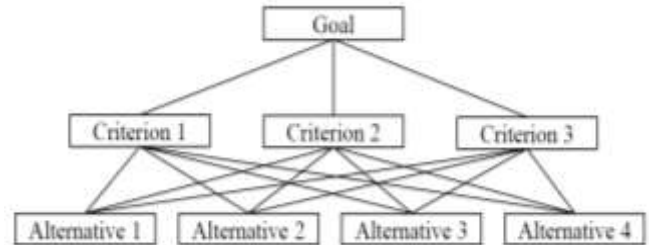


Fig. 2 Analytic Hierarchy Process of a three level decision making problem

The next step is to perform a pairwise comparison by a group of expert people in the targeted research area. Each element is compared between the same level element and with different level element. The number of comparison can be determined by using equation (1) where  $n$  is the number of criteria involved in the evaluation.

$$\text{Number of Comparison} = (n(n-1))/2 \quad (1)$$

Let the alternatives be denoted by  $\{A_1, A_2, \dots, A_n\}$  and their weights as  $\{w_1, w_2, \dots, w_n\}$ . The pairwise comparison matrix  $W$ , can then be written in matrix form as

$$W = \frac{w_i}{w_j} = \begin{pmatrix} w_1/w_1 & w_1/w_2 & \dots & w_1/w_n \\ w_2/w_1 & w_2/w_2 & \dots & w_2/w_n \\ \vdots & \vdots & \ddots & \vdots \\ w_n/w_1 & w_n/w_2 & \dots & w_n/w_n \end{pmatrix} \quad (2)$$

The pairwise comparison matrix,  $A$  which represents the expert judgment can be written as

$$A = [a_{ij}] = \begin{pmatrix} 1 & a_{12} & \dots & a_{1j} & \dots & a_{1n} \\ 1/a_{12} & 1 & \dots & a_{2j} & \dots & a_{2n} \\ \vdots & \vdots & \ddots & \vdots & \ddots & \vdots \\ 1/a_{1j} & 1/a_{2j} & \dots & a_{ij} & \dots & a_{in} \\ \vdots & \vdots & \ddots & \vdots & \ddots & \vdots \\ 1/a_{1n} & 1/a_{2n} & \dots & 1/a_{in} & \dots & 1 \end{pmatrix} \quad (3)$$

The relative importance of the pairwise comparison judgments can be conducted by referring to the AHP fundamental rating scale table as shown in Table 1.

Table 1: The AHP fundamental rating scale (Saaty, 2008)

Intensity of preference (Numerical Value)	Definition (Verbal Scale)	Explanation
1	Equally preferred; equal preference	Two elements contribute equally to the objective
3	Moderately preferred; weak preference of one over other	Experience and judgement slightly favour one element over another
5	Strongly preferred; essential or strong preference	Experience and judgement favour one element over another
7	Very strongly preferred; demonstrated preference	An element is very strongly favoured and its dominance is demonstrated in practice
9	Extremely preferred; absolute preference	The evidence favouring one element over another is of the highest possible order of affirmation
2, 4, 6, 8	Intermediate values between the two adjacent judgements	When compromise is needed
Reciprocals of above nonzero	If an element <i>j</i> has one of the above numbers assigned to it when compared with element <i>i</i> , then <i>i</i> has the reciprocal value when compared with <i>j</i>	
Ratios	Ratios arising from the scale	If consistency were to be forced by obtaining <i>n</i> numerical values to span the matrix.

The next step is to determine the eigenvector. According to Saaty (2008), a simple way to obtain the eigenvector is to raise the pairwise matrix to powers that are successively squared each time. Then, the row sums are calculated and normalized. This step is repeated until the difference between these sums in two consecutive calculations is smaller than a prescribed value.

According to Saaty, the next step is to calculate the consistency index and consistency ratio by using equations (4) and (5).

$$Consistency\ Index\ (CI) = (\lambda_{max} - n)/(n - 1) \quad (4)$$

$$Consistency\ Ratio\ (CR) = CI/RI \quad (5)$$

Where  $\lambda_{max}$  represent the principle eigenvalue; CI represent consistency index and RI represent the average value of CI for random matrices using the Saaty scale which only accept a matrix as a consistent one if  $CR < 0.1$  (Saaty, 2008).

The conventional AHP method has been used to solve problems in many applications such as selecting the machining process to fabricate a knife blade (Zhang, 2012); selection of port location (Bian, 2011) and selection of a method to dispose health care waste (Karsak et al 2011).

Although the AHP method is commonly used to solve multi-criteria decision making problems, this method also have a disadvantage such as the inconsistency being large; which have been criticize by many researchers (Srdjevic, 2005). The AHP method uses a scale between 1-9 and cannot handle uncertainty in judgments.

In order to overcome this shortcoming, many researchers have developed new techniques and methods to replace the eigenvector prioritization method in AHP (Srdjevic, 2005). These methods include the Weighted Sum Method (WSM), Weighted Product Method (WPM), The Preference Ranking Organization Method for Enrichment Evaluation (PROMETHEE), The Technique for Order Preference by Similarity to Ideal Solutions (TOPSIS), Multi-Attribute Utility Theory (MAUT) and Simple Multi Attribute Rating Technique (SMART) (Pohekar and Ramachandran 2004)

There are researchers who have modified the eigen vector method, but a study has shown that it is ineffective across the different error

criteria and can be singled out (Srdjevic, 2005). The priorities assessment also can be solved by using direct least squares (DLS) method, weighted least squares (WLS) method, logarithmic least absolute values (LLAV) method, logarithmic goal programming (LGP) method and fuzzy preference programming (FPP) method (Srdjevic, 2005); triangular fuzzy numbers (TFN),  $\alpha$ -cut, trapezoidal fuzzy numbers and synthetic extend analysis (Mikhailov, 2003). Today, one of the most widely used MCDM methods to replace the conventional AHP application is Fuzzy Analytic Hierarchy Process (FAHP) which adopts the fuzzy set and fuzzy number theory (Rouyendegh and Erkan, 2012).

### 3. Fuzzy Set and Fuzzy Set Number

Fuzzy set theory (FST) was first introduced by Zadeh in the year 1965 to deal with data uncertainty and vagueness. It also allows mathematical operators and programming to be performed in a fuzzy domain. Fuzzy set (FS) is a class of objects with a range of grades of membership. Such a set is characterized by a membership function which assigns to each object a grade of membership value between zero to one value (Rouyendegh and Erkan, 2012).

The symbol ‘ $\sim$ ’ is usually place above a symbol to indicate it is FST. Symbol  $\tilde{M}$  represents the triangular fuzzy number (TFN) as shown in Figure 3.

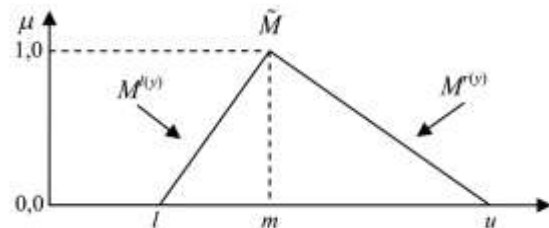


Fig. 3 A TFNs of  $\tilde{M}$

Triangular Fuzzy Number (TFN) is denoted as  $l, m, u$  ( $l \leq m \leq u$ ) where  $l$  is the smallest possible value,  $m$  is the most promising value and  $u$  is the largest possible value that describe the fuzzy event. The membership function of TFN can be described as

$$\mu\left(\frac{x}{\tilde{M}}\right) = \begin{cases} 0 & x < l \\ \frac{x-l}{m-l} & l \leq x \leq m \\ \frac{u-x}{u-m} & m \leq x \leq u \\ 0 & x > u \end{cases} \quad (6)$$

Fuzzy number can always be given by its corresponding left and right representation of each degree of membership as shown in Equation (7) where  $l(y)$  represent the left side of Fuzzy Number (FN) and  $r(y)$  represent the right side of Fuzzy Number (FN).

$$\tilde{M} = M^{l(y)}, M^{r(y)} = [l + (m - l)y, u + (m - u)y], y \in [0, 1] \quad (7)$$

There are four operations involved in determining fuzzy number which is additional, subtraction, multiplication and division of fuzzy number.

$$(a_1, b_1, c_1) + (a_2, b_2, c_2) = (a_1 + a_2, b_1 + b_2, c_1 + c_2) \quad (8)$$

$$(a_1, b_1, c_1) - (a_2, b_2, c_2) = (a_1 - a_2, b_1 - b_2, c_1 - c_2) \quad (9)$$

$$(a_1, b_1, c_1) \times (a_2, b_2, c_2) = (a_1 \times a_2, b_1 \times b_2, c_1 \times c_2) \quad (10)$$

$$(a_1, b_1, c_1) / (a_2, b_2, c_2) = (a_1 / c_2, b_1 / b_2, c_1 / a_2) \quad (11)$$

**4. Fuzzy Analytic Hierarchy Process (FAHP)**

The disadvantage of AHP in dealing with domain expert judgment is the use of the scale 1-9 and their Eigen values. This means that it doesn't handle the uncertainty in these judgments. In order to overcome this, Fuzzy Environment Approach (FEA) can be used within AHP calculations to determine the most optimum alternative (Ho et al 2010); (Ali et al 2012). Fuzzy AHP (FAHP) mimics human thinking as it sometimes uses misleading information and ambiguity to generate decision in addition to the advantages of AHP; ease of handling qualitative and quantitative data, use of hierarchical structure, pair wise comparison, reduce inconsistency, and generates priority vectors (Noor et al 2012).

Today, more and more real life problems uses linguistic environment to make decisions by human (Ali et al 2012); (Noor et al 2012). Classical decision making method works only with exact and ordinary data. For example, when evaluating a car speed linguistic terms like “very slow”, “slow”, “fast”, “very fast” can be used. Here, fuzzy method can be used for vague and qualitative assessment of human beings (Ali et al 2012). The theory of fuzzy sets has extended traditional mathematical decision theories so that it can cope with any vagueness problems.

FAHP is an extension of the AHP method. The assessment of different criteria is done using fuzzy number compared to AHP using crisp numbers. FAHP is an enhancement of AHP and was developed to overcome the defect in AHP. According to Rouyendegh and Erkan (2012), Fuzzy AHP have been applied in many applications such as in staff selection, selecting partnerships and minimally biased weight method in staff selection, economics of government size (Mirsepassi and Mehrara, 2012; Fahp3), weapon selection (Dagdeviren et al, 2009) and sustainability assessment (Starkl and Burner, 2004); (Damghani and Nezhad, 2013).

According to Rouyendegh and Erkan (2012), there are 9 steps to in Fuzzy AHP. The first step is to select a group of expert people for decision making evaluation. The next step is to ask the expert group to make a pairwise comparison of the decision criteria and rate it with relative scores. Rouyendegh and Erkan (2012) have employed the fuzzy conversion scale as shown in Table 2 to replace Saaty preference scale.

Table 2: Fuzzy AHP conversion scale.

Importance Intensity	Triangular Fuzzy Scale	Importance Intensity	Triangular Fuzzy Scale
1	(1, 1, 1)	1/1	(1/1, 1/1, 1/1)
2	(1, 2, 4)	1/2	(1/4, 1/2, 1/1)
3	(1, 3, 5)	1/3	(1/5, 1/3, 1/1)
5	(3, 5, 7)	1/5	(1/7, 1/5, 1/3)

7	(5, 7, 9)	1/7	(1/9, 1/7, 1/5)
9	(7, 9, 11)	1/9	(1/11, 1/9, 1/7)

The third steps is to calculate the value of  $\tilde{G}_i(l_i, m_i, u_i)$ . After each expert makes a pairwise comparison decision, the relative scores of  $\tilde{G}_i$  can be calculated as follows:

$$l_i = (l_{i1} \otimes l_{i2} \otimes \dots \otimes l_{ik})^{\frac{1}{k}}, i = 1, 2, \dots, k \quad (12)$$

$$m_i = (m_{i1} \otimes m_{i2} \otimes \dots \otimes m_{ik})^{\frac{1}{k}}, i = 1, 2, \dots, k \quad (13)$$

$$u_i = (u_{i1} \otimes u_{i2} \otimes \dots \otimes u_{ik})^{\frac{1}{k}}, i = 1, 2, \dots, k \quad (14)$$

Next, the fourth step is to calculate the value of  $\tilde{G}_T$  by establishing the geometric fuzzy mean of the total row using equation (15). This is followed by the determination of fuzzy priorities for each candidate based on sub-factors using linguistic variables which are defined for the TFN as shown in Table 3.

$$\tilde{G}_T = (\sum_{i=1}^k l_i, \sum_{i=1}^k m_i, \sum_{i=1}^k u_i) \quad (15)$$

Table 3: Fuzzy numbers

Importance Intensity	Triangular Fuzzy Scale
Very good	(3, 5, 5)
Good	(1, 3, 5)
Moderate	(1, 1, 1)
Poor	(1/5, 1/3, 1/1)
Very poor	(1/5, 1/5, 1/3)

The sixth step is to calculate the fuzzy geometric mean of the fuzzy priority value ( $\tilde{w}$ ) with normalization priorities for factors using Equation (16).

$$\tilde{w} = \frac{\tilde{G}_i}{\tilde{G}_T} = \frac{(l_i, m_i, u_i)}{(\sum_{i=1}^k l_i, \sum_{i=1}^k m_i, \sum_{i=1}^k u_i)} = \left[ \frac{l_i}{\sum_{i=1}^k l_i}, \frac{m_i}{\sum_{i=1}^k m_i}, \frac{u_i}{\sum_{i=1}^k u_i} \right] \quad (16)$$

The seventh step is to calculate fuzzy priorities for the lower and upper limits for each  $\alpha$  value as shown in Equation (17).

$$w_{il} = (w_{il\alpha}, w_{iu\alpha}); i = 1, 2, \dots, k; l = 1, 2, \dots, l \quad (17)$$

Where:

$$W_{il} = \frac{\sum_{i=1}^l \alpha(w_{ii})_l}{\sum_{i=1}^l \alpha_i}; i = 1, 2, \dots, k; l = 1, 2, \dots, l \quad (18)$$

$$W_{iu} = \frac{\sum_{i=1}^l \alpha(w_{ii})_l}{\sum_{i=1}^l \alpha_i}; i = 1, 2, \dots, k; l = 1, 2, \dots, l \quad (19)$$

The eight step is to defuzzify the value by combining the upper limit and lower limit values by using the optimism index ( $\lambda$ ) using Equation (20).

$$w_{id} = \lambda . w_{iu} + (1 - \lambda) . w_{il}; \lambda \in [0, 1]; i = 1, 2, \dots, k \quad (20)$$

Lastly, the final step is to defuzzify values priorities by normalizing using Equation (21).

$$W_{in} = \frac{w_{id}}{\sum_{i=1}^k w_{id}}; i = 1, 2, \dots, k \quad (21)$$

### 5. Sustainability Product Design Framework

Sustainability concept first appeared in The Brundtland Report in the late 1980's which can be defined as development that meets the needs of the present without compromising the ability of future generations to meet their own needs (Hao, 2012). The U.S. Department of Commerce (Ziout et al 2013) defines sustainable manufacturing as “the creation of manufactured products that use processes that minimize negative environmental impacts, conserve energy and natural resources, are safe for employees, communities, and consumers and are economically sound.”

Realizing this, the proposed product design framework of this project follows Rouyendegh and Erkan (2012) which starts with describing the unstructured problem for a better understanding of the problem. The next step is detailing the related criteria for evaluation purposes and possible alternatives to solve the problem. After undergo various previous research papers, there are three suitable criteria for this project such as proposed by Zahari Taha et. al, (2013). They are economic cost assessment, environmental impact assessment and ergonomic assessment with limited to 4 solutions.

For economic cost assessment criteria, the total manufacturing cost will be considered as shown is Equation (22).

$$\text{Total Manufacturing Cost} = \text{Material Cost} + \text{Tool Cost} + \text{Coolant and Lubricant Cost} + \text{Energy Cost} + \text{Labour Cost} \quad (22)$$

Where:

$$\text{Material Cost} = \text{Standard size price (RM / Volume)} \times \text{Required size (Volume)} \quad (23)$$

$$\text{Tool Cost} = \frac{\text{Number of cutting tool (n)} \times \text{tool cost / unit (RM)}}{\text{number of unit produced}} \quad (24)$$

$$\text{Energy Cost} = \text{Energy used to fabricate a product (kWh)} \times \text{Commercial electrical tariff (RM/kWh)} \quad (25)$$

$$\text{Labour Cost} = \text{Total time to fabricate a product (hour)} \times \text{Salary (RM/hour)} \quad (26)$$

If the machining process involves more than one type of cutting tools, each types of cutting tool cost must be considered.

$$\text{Coolant or Lubricant Cost} = \text{Coolant or lubricant volume} \times \text{Coolant or lubricant cost rate} \quad (27)$$

For Coolant or Lubricant Volume and Makeup volume, the detail calculation is shown in Equation (28) and (29).

$$\text{Coolant or Lubricant Volume} = \frac{\text{Coolant or Lubricant tank capacity} + \text{makeup volume}}{\text{month used} \times \text{actual output}} \quad (28)$$

$$\text{Makeup volume} = \frac{\text{Coolant or Lubricant tank capacity} \times \text{Coolant or Lubricant loss rate}}{1 - \text{Coolant or Lubricant loss rate}} \quad (29)$$

The ergonomic assessment used in this project is motion economic checklist because of its nature which considers the tasks involved in producing the product. Then, the problem goals, criteria and alternatives are arranged into a hierarchy such as shown in Figure 4.



Fig 4 Proposed of three levels Fuzzy Analytic Hierarchy Process arrangement

The proposed framework proceeds with the forming of a group of experts to make pair wise comparisons of the decision elements. Here, the number of representatives proposed is more than one for each criteria and the number of people for each criteria is equally distributed. The fuzzy preferences scale use for pairwise comparison in this framework is adopted from Rouyendegh and Erkan (2012) as shown in Table 2.

After the group of experts have finished making pairwise comparisons, the relative score value of  $\tilde{G}_i(l_i, m_i, u_i)$  can be calculated using equation (12) – (14).

Then, the overall relative score value of  $\tilde{G}_T$  is calculated by establishing the geometric fuzzy mean of the total row using equation (15). Since the criteria used in this frame work is specific to three and no other sub-criteria to be considered, the next steps is to calculate the fuzzy geometric mean of the fuzzy priority value ( $\tilde{w}$ ) with normalization priorities for factors using Equation (16); followed by determining fuzzy priorities for the lower and upper limits for each  $\alpha$  value using Equation (17); defuzzify the value by combining the upper limit and lower limit values by using the optimism index ( $\lambda$ ) using Equation (20) and lastly defuzzify values priorities by normalizing using Equation (21). The proposed sustainability product design framework summary process flow is shown in Figure 5.

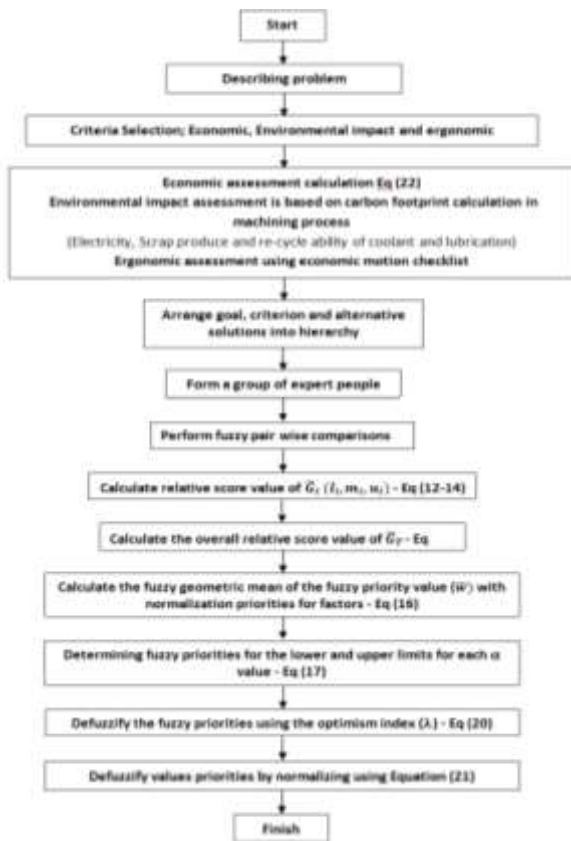


Fig. 5 Summary of proposed product design framework

The selected product design for this case study is based on the calculated results, where the highest score is then selected as the most optimum results.

### 3. Conclusions

As a conclusion, this paper has presented a review of the conventional analytic hierarchy process proposed by Saaty and its enhancement using fuzzy logic known as fuzzy analytic hierarchy process. The application of both methods is then reviewed in general. The fuzzy AHP method is used to evaluate the multiple objectives in sustainability product design problems. The expected output from this case study is an evaluation method which will help the manufacturing industry especially in Malaysia to evaluate their products at the design stage.

### ACKNOWLEDGEMENT

The authors would like to thank the MTUN secretariat under MTUN CoE grant and Ministry of Education Malaysia for the financial support for this project.

### REFERENCES

1. Howarth, G. and Hadfield, M., "A Sustainable Product Design

model," *Material and Design* Vol 27, pp. 1128-1133, 2006.

2. Rouyendegh, B. D and Erkan, T. E., "Selection of Academic Staff using the Fuzzy Analytic Hierarchy Process (FAHP): A Pilot Study," *Technical Gazette* 19, 4, pp. 923-929, 2012.
3. Saaty, T. L., "Decision Making with the Analytic Hierarchy Process," *Int. J. Services Sciences*, Vol. 1, No. 1, 2008.
4. Hao, Z., "Integrating Sustainable Manufacturing Assessment Into Decision Making for a Production Work Cell", Master Thesis, Oregon State University, 2012.
5. Bian, K. A., "Application of Fuzzy AHP and ELECTRE to China Dry Port Location Selection," *The Asian Journal of Shipping and Logistic*. Vol 2 pp 331-354, 2011.
6. Karsak, E. E., Dursun, M., Karadayi, M. A., "A Fuzzy Multi-Criteria Group Decision Making Framework for Evaluating Health-Care Waste Disposal Alternatives," *Expert Systems with Applications* 38, pp 11453-11462, 2011.
7. Srdjevic, B., "Combining Different Prioritization Methods in Analytic Hierarchy Process Synthesis," *Computers & Operations* 32, pp. 1897-1919, 2005.
8. Pohekar, S. D. and Ramachandran, M., "Application of Multi-Criteria Decision Making to Sustainable Energy Planning – A Review," *Renewable & Sustainable Energy Reviews* 8, pp 365-381, 2004.
9. Mikhailov, L., "Deriving Priorities from Fuzzy Wise Comparison Judgments," *J. of Fuzzy Set and Systems*, Vol. 134, pp. 365-385, 2003.
10. Ho, W., Xu, X., and Dey, P. K., "Multi-Criteria Decision Making Approaches for Supplier Evaluation and Selection: A Literature Review," *European Journal of Operational Research* 202. pp 16-24, 2010.
11. Ali, N.H., Sabri, I.A.A., Noor, N. M.M, Ismail, F., "Rating and Ranking Criteria for Selected Islands Using Fuzzy Analytic Hierarchy Process (FAHP)," *Int. J. Applied Mathematics and Informatics* 1, Vol 6, 2012.
12. Noor, N. M.M., Sabri, I.A.A., Hitam, M.S., Ali, N.H., Ismail, F., "Fuzzy Analytic Hierarchy Process (FAHP) Approach for Evaluating Tourism Islands in Terengganu, Malaysia," *ICCIT* 2012.
13. Mirsepassi, N., and Mehrara, A., "Using FAHP with the Objective of Selecting the Most Efficient Indicator for Determining the Economic Size of Government," *J. Basic. Appl. Sci. Res.* Vol 2, No. 2, pp. 1308-1316, 2012.
14. Dagdeviren, M., Yavuz, S., Kilinc, N., "Weapon Selection Using the AHP and TOPSIS Methods Under Fuzzy Environment," *Expert Systems with Applications* 36, pp 8143-8151, 2009.
15. Brunner, N., and Starkl, M., "Decision Aid System for Evaluating Sustainability: A critical Survey," *Env. Imp. Ass. Rev.*, 24, pp. 441-469, 2004.

16. Damghani, K. K., and Nezhad, S. S., "A Hybrid Fuzzy Multiple Criteria Group Decision Making Approach for Sustainable Project Selection," *J. of Appl. Soft. Comp.*, Vol. 13, pp. 339-352, 2013.
17. Zahari Taha, Salaam, H.A., Phoon, S.Y. and Tuan Ya, T.Y.M., "Integrated Sustainability Assessment: A Case Study of Screw Design," *17th International Conference on Industrial Engineering Theory, Applications and Practice 2013*, pp 1121-1127.
18. Ziout, A., Azab, A., Altarazi, S., ElMaraghy, W. H., "Multi-Criteria Decision Support for Sustainability Assessment of Manufacturing System Reuse," *J. Mfg. Sc. and Tech.* 6, pp 59-69, 2013.

# An Optimal Ordering and Pricing Policy for Deteriorating Item under the Two-echelon Inventory System in Reverse Logistics

Yufang Chiu #, He-Hsuan Hsu and Jia-Rong Hong

Department of Industrial & Systems Engineering, Chung Yuan Christian University  
200 Chung Pei Rd., Chung-Li, Taiwan

# Corresponding Author / E-mail: davidchiu@cycu.edu.tw, TEL: +886-3-265-4422, FAX: +886-265-4499

KEYWORDS : Inventory System, Reverse Logistics, Deterioration, Backlogging

---

*Inventory management in reverse logistics is different from that in logistics, and it should take the returned products into consideration. Most of the previous papers related to two-echelon inventory system in reverse logistics only discussed the usability of electronic components and the consumption of products when demand occurs. However, the variation of inventory level not only would be affected by customer demand, but also by the deterioration of electronic components. This study focused on the two-echelon inventory system in reverse logistics and the deterioration of electronic components. Therefore, this study combined the consideration of deterioration and two-echelon inventory system in reverse logistics, and derived the optimal lot-size and selling price of new product. Moreover, this study added the consideration of backlogging in the model, and then tested whether there is a significant difference for joint total inventory costs between the two models. The results of numerical example and sensitivity analysis revealed that considering the deteriorating products in two-echelon inventory system in reverse logistics, the profit of choosing the strategy of the backlogging would be more than that of choosing the prohibition of the backlogging.*

---

## 1. Introduction

Because of the shortened life cycle of product and the increasing environmental consciousness, many enterprises focused on reverse logistics to increase customer service level, save cost and confirm laws and decrees. Jayaraman (2003) discussed that recycling goods can be reused for decreasing material costs and influences on environment. Here the reverse logistics include the inspection, storing, sorting and remanufacturing of products.

In traditional inventory model, the assumptions have no limitation on time, which means that the products and quantity of inventory will not change when time goes by. But the function of partial products will degenerate and perish gradually in increasing time. The products are called deteriorating or perishable products.

Ghare and Schrader (1963) mentioned the value of raw material will degenerate with time which follows the exponential distribution to derive EOQ of deteriorating products. The regular products and deteriorating products have differences in initial inventory, and it means that the order quantity of deteriorating products is more than

that of regular products. Jaggi *et al.* (2006) shortened the cycle time of production and increased the number of replenishment to decrease the order quantity and discarding cost of deteriorating products.

Dubois *et al.* (2004) mentioned that logistics is the process of delivered goods which includes raw material, work in process (WIP), finished goods, salvage stores and design and management of control system. Shang and Peter (2009) mentioned that observing 1200 manufacturers in Taiwan and applying mathematic model to inspect logistic ability, performance and economic performance, the result shows that the efficient managerial inventory and sharing information is able to promote logistic performance.

Due to pollution, consumed resources and limitation of environmental regulations, enterprises must manage life cycle of products in order to confirm environmental regulations. Kim *et al.* (2006) defined reverse logistics as "products which are unable to use are recovered through the remanufacturing process for a series activities that salvage products are sold again." Lu (2007) indicated remanufacturing is a recovering method that used products, defective products and parts of component on product can be remanufactured

goods through remanufacturing process. Mitra (2007) thought that although remanufacturing is a mechanism of reuse and recovered salvage products, it must be based on the degree of disassembled products and the quantity level of recovered products. Salvage products which were collected must be inspected in detail before remanufacturing.

Nahmias (1982) assumed in original inventory model products do not possess the limitation of time, and it means that the products and quantity on inventory do not change value due to following time. But the function in practice deteriorates and spoils slowly following time, and it is called deterioration or perishable products. Ferguson *et al.* (2007) mentioned EOQ of deteriorating products including the parameters of deteriorating products. When the parameters of deteriorating products are bigger, it causes the entire cost increases. Rau *et al.* (2003) indicated the critical parameters are influenced by cost which includes inspective cost, carrying cost, deteriorating cost and the cost of decreased price. So the parameters number in ordering deteriorating products is more than initial EOQ.

Liang *et al.* (2009), Kim *et al.* (2006), Van der laan and Trunter (2006) and Chung *et al.* (2008) discussed remanufacturing issue with recovered items of electronic components in inventory model of recovered salvage goods. Raafat (1991) indicated the electronic components are like deteriorating goods, and deteriorating rate follows exponential distribution. But in the reference of reverse logistics scholars usually inspected whether recovered goods can be repaired or not. Instead, few scholars considered the deteriorating of recovered goods. Therefore, this study added the deteriorating to inventory system of recovered products of two stages and discussed the problem what kind of influence for entire inventory level and total inventory cost. The Conceptual graph of reverse logistics is:

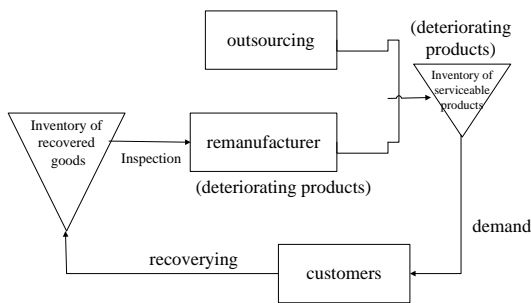


Fig. 1 Conceptual graph of reverse logistics

## 2. Model Construction

### 2.1 Assumptions

This study has a number of assumptions so that the objectives of this study would be clarified.

1. The main products are electronic components.
2. The volume of inventory and capacity are limited .
3. The rate of demand is a linear function of unit sales price, that is  $D(p) = a - bp$ , where  $a, b > 0$  and  $p < a / b$ .
4. The price of refurbished goods is lower than the new products, and  $P_2 = P_1r$ ,  $0 < r < 1$ .
5. The deteriorating rate of inventory of electronic components is

continuous and exponentially distributed.

6. Only consider the situation of inventory within a single cycle time.
7. Returned products of electronic components must go through the process of disassembling and test.
8. When a certain amount of returned products achieved, the returned products will be dismantled and tested, while tested returned products would be refurbished and provided to the retailers.

### 2.2 Notation

- R: Product recycle rate (number / time).  
 $D_1$ : The new product demand rate of Retailer (number / time).  
 $D_2$ : The refurbished demand rate of Retailers (number / time).  
 $Re$ : The refurbished rate of returned products (number / time).  
 $x$ : The dismantled inspection rate of returned products (number / time).  
 $\theta_m$ : The deteriorating rate of new electronic components.  
 $\theta_r$ : The deteriorating rate of recovered electronic components.  
 $q$ : The refurbished fraction of recovered products.  
 $Q_m$ : The order number of each batch of new products (number / sales cycle).  
 $Q_r$ : The number of each batch of returned products (number / sales cycle).  
 $I_{ri}(t)$ : The level of inventory at the business of recovery during time  $t$ . ( $i = 1, 2$ )  
 $I_{mi}(t)$ : The level of inventory at the manufacturer during time  $t$ . ( $i = 3, 4, 5$ ).  
 $M$ : the number of orders for new products.  
 $h$ : Holding cost of per unit new products of unit time (cost / (number of products \* time)).  
 $H$ : Holding costs of per unit refurbished goods of unit time (cost / (product number \* time)).  
 $K_s$ : Setup cost of order new products (cost / setup times).  
 $K_r$ : Setup cost of refurbished returned products (cost / setup times).  
 $P_1$ : Unit retail price of new products.  
 $P_2$ : Unit retail price of refurbished goods.  
 $c_m$ : Order cost of unit new products.  
 $c_r$ : Refurbished cost of unit returned products.  
 $c_t$ : Test cost of unit returned products.  
 $c_d$ : Disposal cost of unit waste goods.  
 $c_b$ : Cost of shortage of unit new products.

### 2.3 Formulation of Model 1

In model 1, both degradation and demand of considered electronic components with the price function are constructed in the two stages reverse logistics inventory system, and shortages are not allowed. This study has been calculated in connection with related cost and joint total cost of inventory of returned products and manufacturer, and then given the prices of new and refurbished products of deteriorating electronic components. The conceptual diagram of a two stage inventory system is shown as in figure 2.

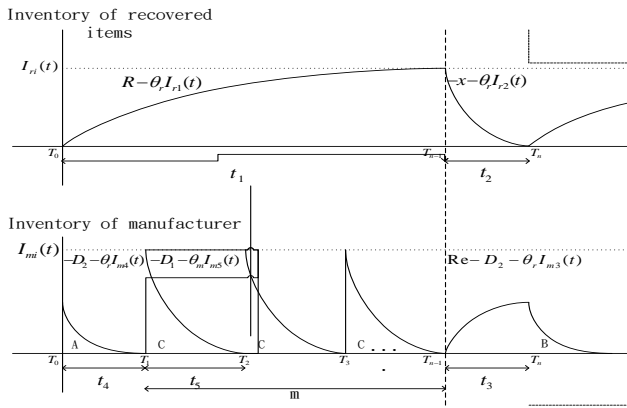


Fig. 2 The two-stage inventory system diagram of model 1

This study recognizes that the variation of inventory level not only caused by decrease in demand but also deterioration. Therefore, the instant of inventory level at all stages in the deteriorating rate, recovery rate, demand rate and the refurbished rates under the influence of the differential equation can be derived.

From related costs of the second inventory system of figure 2, the total costs include setup cost, ordering cost, inspection costs, refurbished costs, the cost of disposal, and holding costs.

The related profit of two stage inventory form figure 2 is separated into profit of new products and refurbished products.

Total profit of all cycle is equal to subtracting total joint cost  $TC_1$  from total revenue  $TR_1$  of entire cycle. The purpose of this study is to obtain the length of recycle and sales cycle within different stage ( $t_1$ ) and sales price of product ( $p_1$ ) to maximize total profit during entire cycle. Because there are variables with five period of time and price, this study simplified variables of the model to be two variables through deriving, as shown below:

$$TP_1(t_1, p_1) = TR_1 - TC_1 \quad (1)$$

**2.4 Solutions of Model 1**

Because the model of discussion would find maximum profit, this study must prove that the optimal solution of the model 1 is existed before obtaining the maximum profit.

And, Hessian Matrix of model 1 is:

$$H = \begin{bmatrix} \frac{\partial^2 TP_1(t_1, p_1)}{\partial t_1^2} & \frac{\partial^2 TP_1(t_1, p_1)}{\partial t_1 \partial p_1} \\ \frac{\partial^2 TP_1(t_1, p_1)}{\partial p_1 \partial t_1} & \frac{\partial^2 TP_1(t_1, p_1)}{\partial p_1^2} \end{bmatrix}$$

$$H = \frac{\partial^2 TP_1(t_1, p_1)}{\partial t_1^2} \times \frac{\partial^2 TP_1(t_1, p_1)}{\partial p_1^2} - \left( \frac{\partial^2 TP_1(t_1, p_1)}{\partial t_1 \partial p_1} \right)^2$$

After proving the Hessian Matrix being a negative defined matrix, this study is able to make sure the model of profit  $TP_1(t_1, p_1)$  as a concave function. The result means that the model has optimal solution  $t_1^*$  and  $p_1^*$  as follows:

$$p_1^* = \frac{a}{2b} \quad (2)$$

$$t_1^* = \frac{m \ln \left[ \frac{\theta_r \left( \frac{a}{2b} \theta_m + h \right)}{\theta_m^2 c_m + h \theta_r} \right]}{\theta_r} \quad (3)$$

**2.5 Formulation of Model 2**

Manna and Chaudhuri (2006) discussed production level to minimize total average cost on the situation of no shortage and shortage perspective considering the demand rate as the function of related time. Dye *et al.* (2007) and Hou (2006) developed an inventory model considering the deterioration of product allows backlogging in case of shortage. The backlogging means when shortage occurs, customers will not give up to consume the product of shortage and wait for next replenishment. Therefore this study expanded the structure of model 1 and allows the situation of backlogging, and when the number of shortage reaches certainty quantity, new products are ordered to replenish. The conceptual diagram of inventory system with two stages is shown as follows:

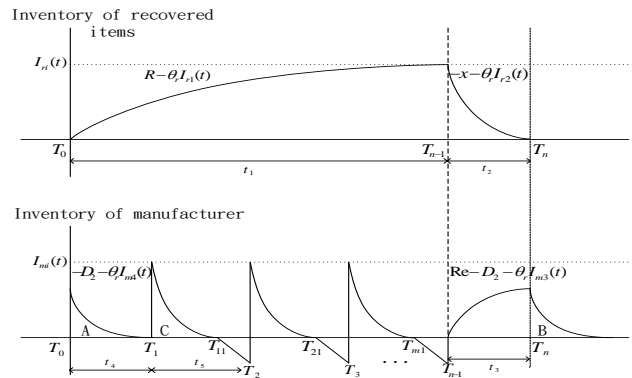


Fig. 3 The two-stage inventory system diagram of model 2

From figure 3, the difference between model 1 and model 2 is that in the fifth stage and new sixth stage where shortage is allowed, every order cycle of new products can be divided into the positive inventory and the negative inventory at time  $T_{j1}$ . From figure 3, the positive inventory decreases in term of demand and deteriorating rate from inventory level of time  $T_1$  to time  $T_{11}$ . Instead of the negative inventory from time  $T_{11}$ , although inventory level already decreases to 0, the demand of new products of retailer still exists. At this movement, the situation of shortage happens until replenishment of time  $T_2$ .

In the sixth stage, after the replenishment of new products has been done, the manufacturer has no inventory of new products on the period and does not order new products. In the allowed situation of shortage, the demand will happen on the stage so that the variation of inventory level is in term of the demand of new products of retailer.

Because model 2 is the extension of model 1, this study only assumes that the shortage is allowed during the sales of manufacturer new products. According to the cost of new products, this study includes the ordering cost, the shortage cost and the carrying cost in the sales cycle of new products of manufacturer.

According to that the Hessian Matrix is greater than 0, this study proved that the model of profit  $TP_2(t_1, p_1)$  is a concave function. The

optimal solution  $t_1^*$  and  $p_1^*$  exist in this model.

$$p_1^* = \frac{a + bc_b(1-k)}{b} \tag{4}$$

$$t_1^* = \frac{m \ln \left[ 1 + \frac{\theta_m \left[ \frac{a + bc_b(1-k)}{b} - c_m - c_b(1-k) \right]}{k(\theta_m c_m + h)} \right]}{\theta_m k} \tag{5}$$

### 3. Verification of Models

This section provides an numerical example that employing data from references into models to obtain  $t_1^*$  and  $p_1^*$ , and the joint total profit  $TP(t_1^*, p_1^*)$ . This section also delivers a sensitive analysis to test factors that influence the total profit  $TP(t_1^*, p_1^*)$  in entire cycle.

#### 3.1 Numerical Examples

The data of the ordering number referred to Konstantaras *et al.* (2010). If  $m$  is a variable, this study will produce the third variable, and Hessian Matrix is too complex. Therefore, this study referred to the numerical data of Konstantaras *et al.* (2010) to obtain the related results as shown in table 1.

Table 1 Parameters of model 1 and model 2

Parameter	Number	remarks
R	400	quantity/time
Re	1000	quantity/time
x	1000	quantity/time
$\theta_m$	0.01	
$\theta_r$	0.01	
q	0.8	
k	0.7	
h	8	cost/(quantity*time)
H	3	cost/(quantity*time)
$K_s$	5	cost/number of setup
$K_r$	10	cost/number of setup
$C_m$	50	cost/quantity
$C_r$	30	cost/quantity
$C_t$	10	cost/quantity
$C_d$	5	cost/quantity
$C_b$	20	cost/quantity
i	0.6	
a	200	
b	0.3	
m	3	

And then the results with maximum total joint profits of model 1 and model 2 are shown in table 2.

Table 2 Comparison of numerical results

	$p_1^*$	$t_1^*$	$Q_{r1}(t)$	$Q_{m5}(t)$	$TP(t_1^*, p_1^*)$
Model 1 (Shortage not allowed)	333.33	21.576	7762.9	1016.9	273514.28
Model 2 (Shortage allowed)	665.94	22.09	7928.2	718.08	485549.14

The result shows that total joint profit of model 2 is greater than that of model 1. When selling new products, the ordering number decreases because of considering the product deterioration, and thus the total joint cost decreases to increases the total joint profit.

#### 3.2 Sensitivity Analysis

From sensitivity analysis, an increasing recycle rate presents that the quantity of recycle goods and the quantity of sales refurbished goods increase to make the total joint cost increases. An increasing refurbished ratio of recycle goods presents that the quantity of sold refurbished products increases to make total joint cost increases. An increasing price of the refurbished goods makes the total joint profit increase. Finally, an increase in order number of new products in model 1 will increase significantly more total joint profit than that in model 2.

### 4. Conclusions & Future Research

#### 4.1 Conclusion

According to above analysis and hypothesis test, there is a significant difference between the joint total profit of model 1 and model 2. Under the inventory system of reverse logistics applying deteriorating feature, together with inspection and refurbished processes, the joint total profit of model 2 is better than joint total profit of model 1 through hypothesis test. One of the reasons is the unit shortage cost in numerical example is too small, and the other reason is that the proportion of length of positive inventory influences the cost of model 2. Another reason is the relation of allowed shortage and backlogging. Therefore, loss sale due to shortages is not significant in this study.

#### 4.2 Further Research

For direction of further research, this study suggested the follows:

1. This study only assumed deteriorating of products follows exponential distribution, but in practice the deteriorating of products can follow other distribution such as Weibull distribution and normal distribution, etc. Therefore, the other deteriorating function can be discussed in the future.
2. In practice, if the time of waiting for replenishment is longer due to shortage, part of buyers would not wait, then the loss sales incur for manufacturer. Therefore, the loss sale and partial backlogging will be able to be discussed in the future.
3. This study assumed both the recovered rate and refurbished rate to be constant. In practice, recovered rate may be influenced by product quality, quantity and other factors. Therefore, random recovered rate needs to be considered in the future.

## ACKNOWLEDGEMENT

The Authors want to express gratitude to the National Science Council, Taiwan (NSC102-2221-E033-059) for its financial support on this research.

## REFERENCES

1. Chung, S. L., Hui, M.W. and Po, C.Y., "Optimal policy for a close-Loop supply chain inventory system with remanufacturing," *The Journal of Mathematical and Computer Modeling*, Vol. 48, pp. 867-881, 2008.
2. Dye, C.Y., Ouyang, L.Y. and Hsieh, T.P., "Inventory and price strategies for deteriorating items with shortage: A discounted cash flow approach," *Computer & Industrial Engineering*, Vol. 52, pp. 29-40, 2007.
3. Ferguson, M., Jayaraman, V. and Souza, G.C., "An application of the EOQ model with nonlinear holding cost to inventory management of perishables," *European Journal of Operational Research*, Vol. 180, pp. 485-490, 2007.
4. Ghare, P.M. and Schrader, G.F., "A model for exponential decaying inventory," *Journal of Industrial Engineering*, Vol. 14, No. 5, pp. 238-243, 1963.
5. Hou, K.L., "An inventory model for deteriorating items with stock-dependent consumption rate and shortages under inflation and time discounting," *European Journal of Operational Research*, Vol. 168, pp. 463-474, 2006.
6. Jaggi, C.K., Aggarwal, K.K. and Goel, S.K., "Optimal order policy for deteriorating items with inflation induced demand," *International of production economics*, Vol. 103, pp. 707-714, 2006.
7. Jayaraman, V., Patterson, R.A. and Rolland, E., "The design of reverse distribution network: Models and solution procedure," *European Journal of Operation Research*, Vol. 150, pp. 128-149, 2003.
8. Kim, J.G., Chatfield, D.C., Harrison, T.P. and Hayya, J.C., "Quantifying the bullwhip effect in a supply chain with stochastic lead time," *European Journal of Operational Research*, Vol. 173, pp. 617-636, 2006.
9. Kim, K., Song, I., Kim, J. and Jeong, B., "Supply planning model for remanufacturing system in reverse logistics environment," *Computers & Industrial Engineering*, Vol. 51, pp. 279-287, 2006.
10. Konstantaras, I., Skouri, K. and Jaber, M.Y., "Lot sizing for a recoverable product with inspection and sorting," *Computers & Industrial Engineering*, Vol. 58, pp. 452-462, 2010.
11. Liang, Y., Pokharel, S. and Lim, G.H., "Pricing used products for remanufacturing," *European Journal of Operation Research*, Vol. 193, pp. 390-395, 2009.
12. Lu, Z. and Bostel, N., "A facility location model for logistics systems including reverse flows: The case of remanufacturing activities," *Computers & Operations Research*, Vol. 34, No. 2, pp. 299-323, 2007.
13. Manna, S.K. and Chaudhuri, K.S., "An EOQ with ramp type demand rate, time dependent deterioration rate, unit production cost and shortage," *European Journal of Operational Research*, Vol. 171, pp. 557-566, 2006.
14. Mitra, S., "Revenue management for remanufactured products," *Omega*, Vol. 35, pp. 553-562, 2007.
15. Nahmias, S., "Perishable inventory theory: A review," *Operations Research*, Vol. 30, No. 4, pp. 680-708, 1982.
16. Raafat, F., "Survey of literature on continuously deteriorating inventory models," *The Journal of the Operational Research Society*, Vol. 42, No. 1, pp. 27-37, 1991.
17. Rau, H. and Wu, M.Y. and Wee, H.M., "Integrated inventory model for deteriorating items under a multi-echelon supply chain environment," *International journal of production economics*, Vol. 86, pp. 155-168, 2003.
18. Shang, K.C. and Peter, B.M., "Logistics capability and performance in Taiwan's major manufacturing firms," *International Journal of Transportation Research Part*, Vol. 41, pp. 217-234, 2009.
19. Van der Laan, E. and Teunter, R.H., "Simple heuristics for push and pull remanufacturing policies," *European Journal of Operational Research*, Vol. 175, pp. 1084-1102, 2006.

# Energy-Efficient Hybrid Flow Shop Scheduling With Lot Streaming

Tzu-Li Chen<sup>1</sup>, Yi-Han Chou<sup>#</sup>, I-Chin Wu<sup>1</sup>, Yen-Ming Chen<sup>2</sup> and Tzu-Chi Liu<sup>2</sup>

<sup>1</sup>Department of Information Management, Fu Jen Catholic University, New Taipei City, 24205, Taiwan, ROC

<sup>2</sup>Industrial Technology Research Institute, Hsinchu, 31040, Taiwan, ROC

# Corresponding Author / E-mail: stevenfriend5566@gmail.com, TEL: +886+2+29052620, FAX: +886+2+29052182

KEYWORDS : Hybrid Flow Shop Scheduling, Lot Streaming, Energy Efficiency, Genetic Algorithm

*The hybrid flow shop scheduling (HFS) problems are commonly encountered in many real-world manufacturing operations such as computer assembly, TFT-LCD module assembly, solar cell manufacturing etc. Most previous work considered the scheduling problem on time requirement to improving production efficiency. However, increasing amount of worldwide carbon emissions are intensifying to cause the global warming problem. Many countries or international organizations start to pay attention to this problem and formulate some mechanisms to reduce the carbon emission. Nowadays, manufacturing enterprises has also been growing interest in the development of energy savings. Thus, this research attempts to reduce energy cost and completion time from manufacturing system level perspectives. The paper first proposed the multi-objective mixed integer programming to address the energy-efficient hybrid flow shop scheduling with lot streaming (EEHFSLS) to simultaneously minimize production makespan and electric power consumption. Due to the trade-off nature of both objectives and the computational complexity of proposed multi-objective mixed integer programming, this study adopts the Non-Dominated Sorting Genetic Algorithm (NSGA-II) to obtain the approximate Pareto solutions efficiently.*

## 1. Introduction

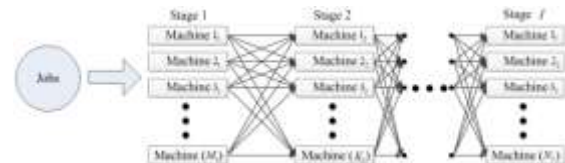
The Hybrid Flow shop Scheduling (HFS) problems are commonly encountered in many real-world manufacturing operations such as computer assembly, TFT-LCD module assembly, solar cell manufacturing, etc. Generally, these frameworks include complex production model of multiple processing stages and each stage contains multiple parallel machines. Machines in each stage can be identical, some related or unrelated at all. Figure 1 illustrates the framework of HFS proposed by (Salvador 1973).

In recent years, the problems of increasing amount of worldwide carbon emissions are intensifying (Solomon et al. 2007). These would cause global warming, rapid exhaustion of various non-renewable resources, and decreasing biodiversity. Current industry accounts about half of total world energy consumption and the energy consumption of these has almost doubled over the last 60 years.

According to statistics, the manufacturing industry is responsible for 31% primary energy consumption and 36% of CO<sub>2</sub> emissions.

Given the above description, manufacturing enterprises are facing pressure to reduce their carbon footprint. Consequently, the energy consumption should be considering optimizing with a holistic approach.

Figure 1 Hybrid flow shop scheduling (HFS) framework



Nowadays, manufacturing enterprises has been growing interest in the development of energy savings. The research on minimizing the power consumption of manufacturing systems has focused on different perspectives: the machine level, the product level and the manufacturing system level. From the machine level perspectives, these studies focus on developing and designing more energy-efficient machines and equipment to reduce the power and energy demand of machine components (Li et al. 2011, Mori et al. 2011, Neugebauer et al. 2011). From the product level perspectives, research on carbon reduction methods in the product design perspective is modeled to support the improvements of product design and operational decisions (Rahimifard et al. 2010, Seow and Rahimifard 2011, Kara et al. 2010, Weinert et al. 2011). However, both the machine and product redesign require enormous financial investments. Most of the manufacturing companies would not use these methods, especially those small and medium sized enterprises.

Therefore, this research attempts to reduce energy cost and completion time in manufacturing system level perspectives. Owing to decision models that support energy savings, it is feasible to achieve a significant reduction in power consumption in manufacturing applications. (Mouzon and Yildirim 2008) first addressed the energy consumption combined with job-based objective (completion time and tardiness) on single machine. They measured the total energy consumption by summation of idle power and machine-dependent setup power.

In real world, it is commonly seen with advanced machines running next to the older ones. In addition, these machines may have different rates of power consumptions. Even each machine would cause different power consumption by adjusting speed status. In general, the faster speed would take the job done faster but it would spend more power consumption. The energy cost saving technique called dynamic voltage or speed scaling and was originally studied by (Yao et al. 1995).

Based on the above description, this paper proposes the multi-objective mixed integer programming to address the Energy-Efficient Hybrid Flow shop Scheduling with Lot Streaming (EEHFSLS) to simultaneously minimize production makespan and electric power consumption. Lot streaming is a technique to split a given job called subplot, each consisting of identical items which is used to reduce production makespan in multi-stage manufacturing systems (Defersha and Chen 2012) (See as figure 2). Due to the trade-off nature for both of objectives and the computational complexity of proposed multi-objective mixed integer programming, our study adopts the genetic algorithm (GA) to obtain the approximate Pareto solutions. In scheduling methods, we developed the multi-objectives energy efficiency scheduling (MOEES) algorithm.

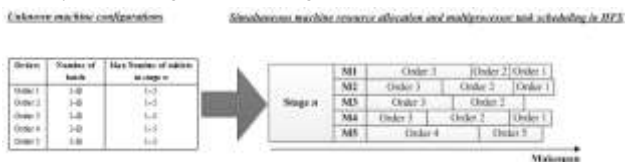


Figure 2 The concept of single order being assigned to multiple machines with variable lot splitting

The purposes of our study are summarized as follows:

1. The problem has to decide the number of sublots and the size for each job.
2. The schedule is computed by processing sequence of these sublots on each machine in each stage.
3. For the EEHFSLS problem considering both production efficiency and electric power consumption, this study modeled the multi-objective mixed integer programming.
4. Due to the computational complexity of multi-objective mixed integer programming, our research adopts NSGA II in order to find the approximate pareto solutions more efficiently.

The rest of the paper is organized as follows: Section 2 defines the problem description of energy-efficient hybrid flow shop scheduling with lot streaming (EEHFSLS) and multi-objective mixed integer programming model. Due to the computational complexity, Section 3 develops the non-dominated sorting genetic algorithm II

(NSGA II) to obtain the approximate Pareto solutions. Section 4 is the experiment study that the example gives an instance about the EEHFSLS model and evaluates the electricity power consumption (EPC) and makespan under different preference vectors within NSGA-II. At last, section 5 described the conclusion about multi-objective mixed integer programming addressing the energy-efficient hybrid flow shop scheduling with lot streaming (EEHFSLS) to simultaneously minimize production makespan and electric power consumption.

## 2. Energy-efficient hybrid flow shop scheduling with lot streaming (EEHFSLS)

In this section, this study presents the problem description of Energy-Efficient Hybrid Flow shop Scheduling with Lot Streaming (EEHFSLS) in section 2.1. In section 2.2, this problem is defined with multi-objective mixed integer programming model.

### 2.1 Problem Statement

The HFS problem under study is as follows.

Figure 3 shows the HFS considered by this study. There are  $N$  jobs to be processed in  $I$  stages. Each stage contains different number of unrelated parallel machines. In the HFS system, every machine includes release dates by its own. The processing and setup time of each machine for each job is not identical.

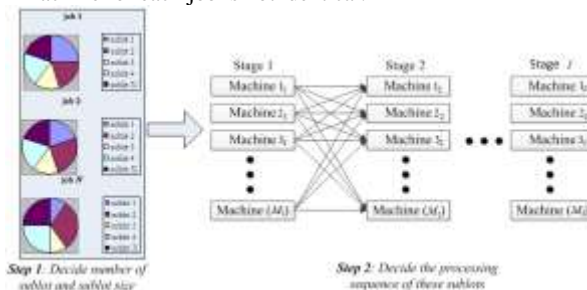


Figure 3 The HFS considered by this study

In real manufacturing environment, not every job would go through all of stages. Some of jobs only processed in some specific machines called machine eligibility. Each job includes  $J$  sublots which the size is not equal to each other. This implies that our proposed using consistent-variable batch method split job into sublots for different sizes by batch splitting model.

However, in real world, these machines may have different rates of power consumptions. Each machine would cause different power consumption and completion time by adjusting speeds. In general, the faster speed would make the job done faster but would spend more electricity cost. Therefore, while the HFS with lot streaming considered the power consumption issue, it would be the problem of Energy-Efficient Hybrid Flow shop Scheduling with Lot Streaming (EEHFSLS).

The problem of EEHFSLS is to minimize the scheduling of make span and power consumption. Makespan means the completion time of the last subplot processed in the system. Power consumption is the value of total machines processing power consumption plus idle time power consumption of each machine. There are two critical decisions that our problem has to decide it. First, this problem has to decide the number of sublots and the size for each job. Then, the schedule is computed by processing sequence of these sublots on each machine in each stage.

The assumptions of this study are as follows:

1. Each subplot can be processed at most on one machine at a time.
2. The minimum number of sublots for each job is equal to one which means the size of subplot is equal to the size of that job.

3. The maximum number of sublots for each job is unlimited. (Note: If each job contained excessive number of sublots. It will cause a lot of extra setup time and extend the makespan of the schedule.
4. If the size of sublots is equal to zero. Then, it is not necessary to process this sublot.
5. A setup is needed before the processing of each sublot of a job on a machine.
6. If the job is needed to be processed on specific machine, other machines are unenforceable to this job.
7. The unit processing time and the setup time are known constants.
8. Sublots of different products can be interleaved.
9. The power consumption between setup time and processing time is independent to each other.
10. Higher speed status would cause more power consumption but reduce the makespan.
11. While processing each job, it is non-priority and non-preemptive.

### 2.1 A multi-objective mixed integer programming model for EEHFSLs

To present a mathematical model for the problem described above, we define several notations. These notations are explained in the following:

#### Indices

- $i, l$  Stage index,  $i$  or  $l = 1, 2, \dots, I$
- $m, k$  Machine index,  $m$  or  $k = 1, 2, \dots, M_i$ , where  $M_i$  is number of machines in stage  $i$
- $n, p$  Jobs (products) index,  $n$  or  $p = 1, 2, \dots, N$
- $j$  Sublot index,  $j = 1, 2, \dots, J_n$ , where  $J_n$  is total number of sublots of job  $n$
- $r, u$  Production runs index,  $r$  or  $u = 1, 2, \dots, R_{m,i}$ , where  $R_{m,i}$  is maximum number of production runs of machine  $m$  in stage  $i$
- $s$  Machine speed index,  $s = 1, 2, \dots, S$

#### Parameters

- $E_n$  A set of pairs of stages ( $l, i$ ) for job  $n$  constrained by precedence relations, i.e., the processing of job  $n$  in stage  $l$  is followed by its processing in stage  $i$ . That job can skip in some stages
- $T_{n,m,i,s}$  Processing time for one unit of job  $n$  on machine  $m$  in stage  $i$  by speed  $s$
- $Q_n$  Batch size/demand quantity of job  $n$
- $S_{m,i,n,p,s}$  Setup time on machine  $m$  in stage  $i$  for processing job  $n$  following the processing of job  $p$  on this machine by speed  $s$ ; if  $n = p$ , the setup may be called minor setup
- $B_{n,i}$   $\begin{cases} 1 = \text{if job } n \text{ needs processing in stage } i \\ 0 = \text{otherwise} \end{cases}$
- $D_{n,m,i}$   $\begin{cases} 1 = \text{if job } n \text{ can be processed on machine } m \text{ in stage } i \\ 0 = \text{otherwise} \end{cases}$   
 $D_{n,m,i} \leq B_{n,i}$  (specified machine)
- $F_{m,i}$  The release time of machine  $m$  in stage  $i$
- $PW_{m,i,s}$  Electric power consumption of machine  $m$  in stage  $i$  by speed  $s$  during the processing status
- $SW_{m,i,s}$  Electric power consumption of machine  $m$  in stage  $i$  by speed  $s$  during the setup status
- $PI_{m,i}$  Electric power consumption of machine  $m$  in stage  $i$  during the idle status
- $\theta$  Large positive number

#### Decision variables

- $c_{max}$  Makespan of the schedule. It is the maximum of the completion times of all the sublots
- $c_{j,n,i}$  Completion time of the  $j^{th}$  sublot of job  $n$  from stage  $i$
- $\hat{c}_{r,m,i}$  Completion time of the  $r^{th}$  run of machine  $m$  in stage  $i$
- $\lambda_{j,n}$  Size of the  $j^{th}$  sublot of job  $n$
- $v_{r,m,i,j,n,s}$   $\begin{cases} 1 = \text{if the } r^{th} \text{ run on machine } m \text{ in stage } i \text{ is for the } j^{th} \text{ sublot of job } n \text{ by speed } s \\ 0 = \text{otherwise} \end{cases}$
- $x_{r,m,i,j,n}$   $\begin{cases} 1 = \text{if the } r^{th} \text{ run on machine } m \text{ in stage } i \text{ is for the } j^{th} \text{ sublot of job } n \\ 0 = \text{otherwise} \end{cases}$
- $y_{r,m,i,n}$   $\begin{cases} 1 = \text{if the } r^{th} \text{ run on machine } m \text{ in stage } i \text{ is for job } n \\ 0 = \text{otherwise} \end{cases}$
- $z_{r,m,i}$   $\begin{cases} 1 = \text{if the } r^{th} \text{ potential run of machine } m \text{ in stage } i \text{ has been assigned a sublot to process} \\ 0 = \text{otherwise} \end{cases}$
- $\gamma_{j,n}$   $\begin{cases} 1 = \text{if sublot } j \text{ is non-zero } (\lambda_{j,n} > 1) \\ 0 = \text{otherwise} \end{cases}$
- $p_{max}$  Maximum of electric power consumption of the schedule

#### Objective Function

$$\text{Minimize } F1 = c_{max} \quad (1)$$

$$\text{Minimize } F2 = p_{max} \quad (2)$$

#### Constraints

- Assignment constraints between production run and sublot

$$\hat{c}_{r,m,i} \geq c_{j,n,i} + \theta \times x_{r,m,i,j,n} - \theta \quad \forall (r, m, i, j, n) \quad (3)$$

$$\hat{c}_{r,m,i} \leq c_{j,n,i} + \theta \times x_{r,m,i,j,n} + \theta \quad \forall (r, m, i, j, n) \quad (4)$$

- Setup time constraint for first run on machine  $m$  in stage  $i$

$$\hat{c}_{1,m,i} - \sum_s v_{1,m,i,j,n,s} \times (\lambda_{j,n} \times T_{n,m,i,s} + S_{m,i,n,0,s}) - \theta \times x_{1,m,i,j,n} + \theta \geq F_{m,i} \quad \forall (m, i, j, n) \quad (5)$$

- Setup time constraint for another run except first run

$$\hat{c}_{r,m,i} - \sum_s v_{r,m,i,j,n,s} \times (\lambda_{j,n} \times T_{n,m,i,s} + S_{m,i,n,p,s}) - \theta (y_{r-1,m,i,p} + x_{r,m,i,j,n}) + 2\theta \geq \hat{c}_{r-1,m,i} \quad \forall (r, m, i, j, n, p) \mid r > 1 \quad (6)$$

- Relation of binary variables constraints

$$\sum_s v_{r,m,i,j,n,s} = x_{r,m,i,j,n} \quad \forall (r, m, i, j, n) \quad (7)$$

$$y_{r,m,i,n} = \sum_{j=1}^{J_n} x_{r,m,i,j,n} \quad \forall (r, m, i, n) \quad (8)$$

$$\sum_{n=1}^N \sum_{j=1}^{J_n} x_{r,m,i,j,n} = z_{r,m,i} \quad \forall (r, m, i) \quad (9)$$

- Assignment constraint between (production) run and next run

$$z_{r+1,m,i} \leq z_{r,m,i} \quad \forall (r, m, i) \mid r < R_{m,i} \quad (10)$$

- Sum of the size of the job constraint

$$\sum_{j=1}^{J_n} \lambda_{j,n} = Q_n \quad \forall n \quad (11)$$

- Sublot existence constraints

$$\lambda_{j,n} \leq \theta \times \gamma_{j,n} \quad \forall (j, n) \quad (12)$$

$$\gamma_{j,n} \leq \lambda_{j,n} \quad \forall (j, n) \quad (13)$$

- Job skip some stage constraint

$$\sum_{m=1}^{M_j} \sum_{r=1}^{R_{m,j}} x_{r,m,i,j,n} = \gamma_{j,n} \times B_{n,i}; \forall (i, j, n) \quad (14)$$

- Specified machine constraint

$$x_{r,m,i,j,n} \leq D_{n,m,i} \quad \forall (r, m, i, j, n) \quad (15)$$

- Makespan constraint

$$c_{\max} \geq c_{j,n,i} \quad \forall (j, n, i) \quad (16)$$

- Electric power consumption constraint

$$P_{\max} \geq \sum_r \sum_m \sum_i \sum_j \sum_n \sum_s PW_{m,i,s} \times v_{r,m,i,j,n,s} \times \lambda_{j,n} \times T_{n,m,i,s} + \sum_r \sum_m \sum_i \sum_j \sum_n \sum_s SW_{m,i,s} \times v_{r,m,i,j,n,s} \times S_{m,i,n,p,s} + \sum_m \sum_i PI_{m,i} \times \left( c_{\max} - \sum_r \sum_j \sum_n \sum_s v_{r,m,i,j,n,s} \times (\lambda_{j,n} \times T_{n,m,i,s} + S_{m,i,n,p,s}) \right) \quad (17)$$

- Domain constraints

$$v_{r,m,i,j,n,s}, x_{r,m,i,j,n}, y_{r,m,i,n}, z_{r,m,i}, \gamma_{j,n} \in \{0, 1\} \quad (18)$$

$$P_{\max}, c_{\max}, c_{j,n,i}, \hat{c}_{r,m,i}, \lambda_{j,n} \geq 0 \quad (19)$$

### 3. Solution Algorithms

Due to the computational complexity, section 3.1 presents Non-Dominated Sorting Genetic Algorithm II (NSGA II) to solve the multi-objective mixed integer programming and obtain the approximate Pareto solutions.

#### 3.1 Non-Dominated Sorting Genetic Algorithm II (NSGA II)

For the NP-hard nature of the proposed multi-objective mixed integer programming model, this study adopts NSGA II to find the approximate Pareto solutions through the evolutionary process.

There are two parts in NSGA II. First, NSGA II using fast non-dominated sorting classify all solutions to different fronts according to the dominate status. Then, the solutions of same front using crowding distance algorithm identify the quality of solution. Thus, NSGA II identifies multi-objective solutions by non-dominated sorting and crowding distance.

##### 3.1.1 Chromosome representation

In hybrid flowshop scheduling (HFS) problems, when lot streaming was considered, the problems need to transform the chromosome format to encoding the subplot size and permutation for each job.

The chromosome in NSGA-II was divided into two segments. Left-hand-side Segment (LHS-Segment) means the decision of subplot size for each job. Right-hand-side Segment (RHS-Segment) represents the sequence of subplot size for each job.

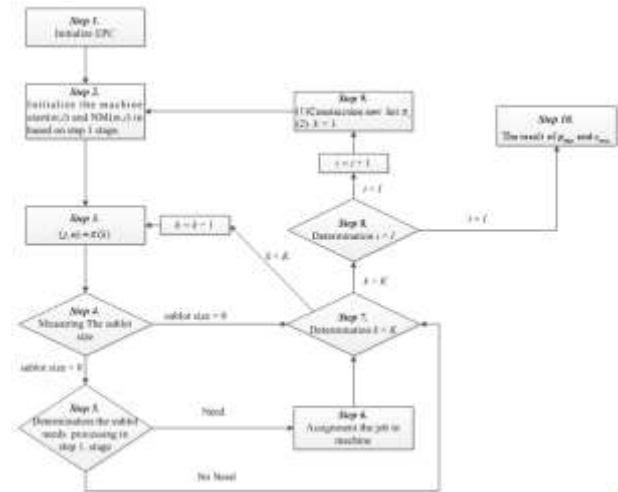
##### 3.1.2 Initialization population generation

In our proposed model, the initialization chromosome of LHS-Segment initial value was generated by random value in the interval [0, 1]. The initial values in RHS-Segment are the random sequence number from 1 to the length of LHS-Segment.

##### 3.1.3 Fitness evaluation

This paper proposed the Multi-objectives energy efficiency scheduling algorithm (MOEES) extended from the LS algorithm is to calculate the minimize makespan and power consumption for each chromosome. The flow chart illustrates in figure 4.

Figure 4 The flow chart of MOEES algorithm



##### 3.1.4 Non-Dominated Sorting

Due to the trade-off nature of between these two solutions of multi-objectives, this study adopts non-dominated sorting to sort each chromosome of population. There are two parts in non-dominated sorting, one is fast non-dominated sorting, and another is crowding distance computation.

###### ■ Fast Non-Dominated Sorting

In fast non-dominated sorting, each solution have to record the number of dominate by some solutions and dominate other solutions, then it found the solutions which number of dominate by some solutions was zero. After found dominate, it would remove just found solutions. Searching number of dominate by some solutions is zero again. More previous front means the solutions dominate the behind front solutions.

###### ■ Crowding Distance Computation

After using fast non-dominated sorting to find the solutions belongs to which front, it was adopting crowding distance to calculate the solution in order to distinguish the solution of same front. Take advantage of sorting the same front of solutions to decide the rank of each solution. Crowding distance used to calculate the distance of before and after solutions called Euclidean distance. Assume that the distance of boundary solutions were infinite due to its lack general distance. Therefore, when the sorting algorithm was finished, the smaller the ranking, the better rank, in the same rank, the greater crowding distance, the better rank.

##### 3.1.5 Selection operation

According to numerous of selection operation, our study used the binary tournament selection. Based on binary tournament selection, it would randomly select two of individuals in populations. Comparing by non-dominated sorting algorithm, the better rank would be selected.

d. Repeat the above step until exceed the required quantities.

### 3.1.6 Crossover operation

This study adopt two crossover operations, one for LHS-Segment: Two-Point Crossover (TPC) and another for RHS-Segment: Single-Point Order Crossover (SePOC) are described as follows, respectively.

■ *LHS-Segment: Two-Point Crossover (TPC):*

Two-point crossover operation chooses two crossover points in two parent chromosome, randomly. The genes between these two points were doing crossover operation.

■ *RHS-Segment: Single-Point Order Crossover (SePOC):*

In RHS-Segment of two parents choose one crossover point, randomly. The left side genes of this crossover point copy its gene to the relative offspring. The remaining of the missing genetic offspring was copying by another parent gene of its relative position to offspring.

### 3.1.7 Mutation operation

This study adopts two Mutation Operation, included LHS-Segment: Partition Randomization Mutation (PRM) and RHS-Segment: Order-Swap Mutation (OSM) are described as follows.

■ *LHS-Segment: Partition Randomization Mutation (PRM):*

LHS-Segment is randomly select two mutations; the gene s between the mutation points would reset the value.

■ *RHS-Segment: Order-Swap Mutation (OSM):*

RHS-Segment is randomly selects two mutation points and exchanges the value of each gene.

### 3.1.8 Replacement operation

In proposed genetic algorithm, our study adopts tournament selection method. The detail step was ranking the chromosome by non-dominated sorting; the better rank of chromosomes would take into the next generation of population until it fills up.

### 3.1.9 Formation of elite population

The initial Pareto set was added into the first generation of elite population. The second generation and later of elite population were merged by the new Pareto set and original elite population, then it using non-dominated sorting algorithm to generate the rank of chromosome and find the new Pareto set then updating to the next generation of elite population.

### 3.1.10 Stopping criteria

This study used specification of a maximum number of generations as stopping criteria. While iteration reaches the specified maximum number of evolution algebra, the algorithm would terminate and find the more convergence Pareto set of scheduling solutions.

## 4. Experiment Study

For example, the instance included two stages. Stage 1 exist three machines and two machines in stage 2. There are three jobs to be processed and all of jobs need to be processed in each stage. Jobs 1, 2 and 3 for each demand quantity are 10, 20 and 20, respectively. Assuming that job 1 was separated into 2 sublots, job 2 and job 3 was separated into 3 sublot (see as table 1). Table 2 shows the value of release date ( $F_{m,i}$ ) and electric power consumption during the idle status ( $PI_{m,i}$ ) of machine  $m$  in stage  $i$ , respectively. The value of electric power consumption

of machine  $m$  in stage  $i$  by speed  $s$  ( $SW_{m,i,s}$ ) were described in table 3. Table 4 presents the data of setup time on machine  $m$  in stage  $i$  for processing job  $n$  following the processing of job  $p$  on this machine by speed  $s$  ( $S_{m,i,p,s}$ ). The data in table 5 are the electric power consumption of machine  $m$  in stage  $i$  by speed  $s$  during the processing status ( $PW_{m,i,s}$ ). Table 6 illustrated the value of processing time for one unit of job  $n$  on machine  $m$  in stage  $i$  by speed  $s$ .

Table 1 Demand quantity ( $Q_n$ ) and number of sublots for each job

	Job 1	Job 2	Job 3
$Q_n$	10	20	20
Sublots	2	3	3

Table 2 Different performance of  $PI_{m,i}$  and  $F_{m,i}$

	m1, i1	m2, i1	m3, i1	m1, i2	m2, i2
$PI_{m,i}$	0.4	0.2	0.2	0.2	0.4
$F_{m,i}$	0	0	0	0	0

Table 3 Different performance of  $SW_{m,i,s}$

	m1, i1	m2, i1	m3, i1	m1, i2	m2, i2
$SW_{m,i,1}$	10	8	10	6	7
$SW_{m,i,2}$	3	2	3	2	2

Table 4 Different performance of  $S_{m,i,p,s}$

		m1, i1	m2, i1	m3, i1	m1, i2	m2, i2
$S_{m,i,1,p,s}$	s=1	2	2	2	2	-
	s=2	4	4	4	4	-
$S_{m,i,2,p,s}$	s=1	3	4	3	3	3
	s=2	6	8	6	6	6
$S_{m,i,3,p,s}$	s=1	3	-	2	3	2
	s=2	6	-	4	6	5

Table 5 Different performance of  $PW_{m,i,s}$

	m1, i1	m2, i1	m3, i1	m1, i2	m2, i2
$PW_{m,i,1}$	20	15	16	18	21
$PW_{m,i,2}$	5	4	5	5	5

Table 6 Different performance of  $T_{n,m,i,s}$

		m1, i1	m2, i1	m3, i1	m1, i2	m2, i2
$T_{1,m,i,s}$	s=1	1	2	1	1	-
	s=2	2	4	2	2	-
$T_{2,m,i,s}$	s=1	1	1	1	1	1
	s=2	3	2	2	3	2
$T_{3,m,i,s}$	s=1	1	-	1	1	2
	s=2	3	-	3	3	4

Based on above data, this experiment evaluates the EPC and makespan under different preference vectors within NSGA-II. The values of  $w_{MK}$  and  $w_{EPC}$  are randomly generated within interval [0, 1]. Decision makers would choose the most appropriate weight in different situations as the practical application. Thus, this study divided the interval of preference vector into five sections which means the  $w_{MK}$  and  $w_{EPC}$  generated in (0,1),(0.2,0.8), (0.5,0.5),(0.8,0.2),(1,0), respectively and the results illustrated in figure 5. From the figure 5, it can be observed that the different weight of these preference vectors would bring about different scheduling. In most case, lower makespan would cause higher el

electric power consumption, vice versa.

## 5. Conclusion

This paper proposed the multi-objective mixed integer programming model to address the energy-efficient hybrid flow shop scheduling with lot streaming (EEHFSLS) for simultaneously minimize production makespan and electric power consumption. Due to the trade-off nature of both objectives and the computational complexity of proposed multi-objective mixed integer programming, this study adopts the NSGA-II to obtain the approximate Pareto solutions. According to the experimental results, NSGA-II can solve the problem effectively.

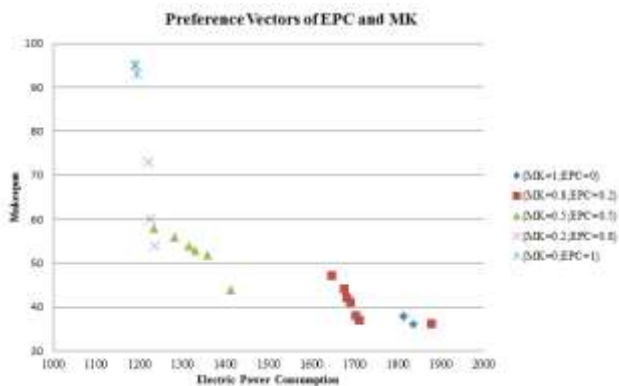


Figure 5 Non-dominated solutions under different preference vector

## ACKNOWLEDGEMENTS

This work was under the auspices of Industrial Technology Research Institute. The financial support provided by Bureau of Energy (Grant No. D455CU4200) is gratefully acknowledged.

## REFERENCES

1. Deb, K., Pratap, A., Agarwal, S., Meyarivan, T., "A fast and elitist multiobjective genetic algorithm: NSGA-II", *Transactions on Evolutionary Computation*, IEEE, Vol. 6, No. 2, 2002.
2. Defersha, F.M., Chen, M., "Mathematical model and parallel genetic algorithm for hybrid flexible flowshop lot streaming problem", *The International Journal of Advanced Manufacturing Technology*, Vol. 62, No. 1-4, pp.249–265, 2012.
3. Kara, S., Manmek, S., Herrmann, C., "Global manufacturing and the embodied energy of products", *CIRP Annals - Manufacturing Technology*, Vol. 59, No. 1, pp.29–32, 2010.
4. Li, W., Zein, A., Kara, S., Herrmann, C., "An Investigation into Fixed Energy Consumption of Machine Tools", *Globalized Solutions for Sustainability in Manufacturing*, pp.268–273, 2011
5. Luo, H., Du, B., Huang, G.Q., Chen, H., Li, X., "Hybrid flow shop scheduling considering machine electricity consumption cost", *International Journal of Production Economics*, Vol. 146, No. 2, pp.423–439, 2013.
6. Mori, M., Fujishima, M., Inamasu, Y., Oda, Y., "A study on energy efficiency improvement for machine tools", *CIRP Annals - Manufacturing Technology*, Vol. 60, No. 1, pp.145–148, 2011.
7. Mouzon, G., Yildirim, M.B., "A framework to minimize total energy consumption and total tardiness on a single machine", *International Journal of Sustainable Engineering*, Vol. 1, No. 2, pp.105–116, 2008.
8. Neugebauer, R., Wabner, M., Rentzsch, H., "Structure principles of energy efficient machine tools", *CIRP Journal of Manufacturing Science and Technology*, Vol. 4, No. 2, pp.136–147, 2011.
9. Rahimifard, S., Seow, Y., Childs, T., "Minimising Embodied Product Energy to support energy efficient manufacturing", *CIRP Annals—Manufacturing Technology*, Vol. 59, No. 1, pp.25–28, 2010.
10. Salvador, M.S., "A solution to a special class of flow shop scheduling problems", *Symposium on the Theory of Scheduling and Its Applications Lecture Notes in Economics and Mathematical Systems*, Vol. 86, pp.83–91, 1973.
11. Seow, Y., Rahimifard, S., "A framework for modelling energy consumption within manufacturing systems", *CIRP Journal of Manufacturing Science and Technology*, Vol. 4, No. 3, pp.258–264, 2011.
12. Solomon, S., D. Qin, M. Manning, Z. Chen, M. Marquis, K.B. Averyt, M. Tignor, H.L. Miller, "Contribution of Working Group I to the Fourth Assessment Report of the Intergovernmental Panel on Climate Change", *IPCC Fourth Assessment Report: Climate Change*, 2007.
13. Weinert, N., Chiotellis, S., Seliger, G., "Methodology for planning and operating energy-efficient production systems", *CIRP Annals - Manufacturing Technology*, Vol. 60, No. 1, 2011, pp.41–44
14. Yao, F., Demers, A., Shenker, S., "A scheduling model for reduced CPU energy", *Proceedings of the 36th annual symposium on foundations of computer science*, pp.374–382, 1995.

# Design of Energy Efficient Distillation Columns Systems

Mohd Faris Mustafa<sup>1</sup>, Noor Asma Fazli Abdul Samad<sup>2</sup>, Kamarul 'Asri Ibrahim<sup>1</sup>,  
Norazana Ibrahim<sup>3</sup> and Mohd Kamaruddin Abd. Hamid<sup>1,#</sup>

<sup>1</sup> Process Systems Engineering Centre, Faculty of Chemical Engineering, Universiti Teknologi Malaysia, 81310 UTM Johor Bahru, Johor, Malaysia.

<sup>2</sup> Faculty of Chemical Engineering and Natural Resources, Universiti Malaysia Pahang, Lebuhraya Tun Razak, 26300 Gambang, Pahang, Malaysia.

<sup>3</sup> UTM-MPRC Institute of Oil & Gas, Faculty of Petroleum and Renewable Energy Engineering, Universiti Teknologi Malaysia, 81310 UTM Johor Bahru, Johor, Malaysia.

# Corresponding Author / E-mail : ekamaruddin@cheme.utm.my

**KEYWORDS:** Energy Efficient Distillation Columns, Driving Force, Pinch Technology

*Distillation is the primary separation process widely used in the industrial chemical processing. Although it has many advantages, the main drawback is its large energy requirement, which can significantly influence the overall plant profitability. However, the large energy requirement of these processes can be systematically reduced by using driving force and energy integration methods. This paper presents a methodology for designing energy efficient distillation columns systems based on those two methods. Accordingly, the proposed methodology consists of four hierarchical steps. In the first step, the system of distillation columns for multicomponent separation is designed based on the conventional distillation column design (shortcut) method. Then, the conventional distillation columns systems design is improved in terms of energy saving by using driving force method in the second step. It is expected in the third step that the distillation columns systems design can be further improved in terms of energy saving by using energy integration method. Finally, the distillation columns systems design is evaluated in terms of economic performance. The simulation results by using Aspen HYSYS have shown that the direct sequence (Benzene and Toluene) for BTX (Benzene, Toluene and p-Xylene) has energy savings with 8% reduction by using driving force method compared to a shortcut method. It can be verified that the proposed methodology has the capability in designing energy efficient distillation columns in an easy, systematic and practical manner.*

## 1. Introduction

The demand for energy has been continuously increasing for years and operation units with large energy demand such as distillation columns have become more difficult to be supplied. The energy efficiency of distillation columns systems becomes an important criterion during retrofitting and design of industrial chemical processes. On the other hand, reducing energy requirements of distillation column systems leads to lower CO<sub>2</sub> emission. This becomes the reason why the plant designer must take the different energy saving solutions into consideration and choose the best distillation columns systems design for the specific separation task.

Reducing product cost in chemical industry has been very effectively used in energy saving method for distillation columns by heat integration columns system. Heat integration by two columns is based on an idea to match utilizing overhead vapour of one column in order to provide heat content for boiling up a second column. Heat integration column is the process of hot streams was heat exchanged with cold streams. In this process the rectifying and stripping sections was designed by internally coupled through heat exchanger. These designs have proven an enormous improvement by reducing the reboiler and condenser duties will lead to energy saving efficiency. Therefore, the development of process and energy integration technique have been developed such as the fully thermally coupled distillation columns (FTCDC or Petlyuk column)

and dividing wall columns (DWCs), which can have greater to reduce energy consumption. The divided wall column allows reversible splits with no part of the separation being used twice and the main source of its superior energy efficiency over other column configurations. However, Petlyuk systems have strong interactions between their columns because of the thermal integration, which can inhibit their design and operation.

Therefore, a new methodology that will enable to design energy efficient distillation columns (EEDCs) is proposed in this paper. Accordingly, the proposed methodology consists of four hierarchical steps. In the first step, the system of distillation column for multicomponent separation is designed based on the conventional distillation column design method. Then, the conventional distillation columns systems design is improved in terms of energy saving by using driving force method in the second step. It is expected in the third step that the distillation columns systems design can be further improved in terms of energy saving by using energy integration method. Finally, the distillation column systems design is evaluated in terms of economic performance. By applying the proposed methodology, it is possible to make an early assumption on sequence of distillation column systems that is the best in terms of energy saving. Significant energy savings can be made with the use of distillation column trains with driving force [1] and energy integration [2] methods.

Bek-Pederson and Gani [1] developed a systematic design and synthesis of distillation systems using a driving force based method.

This method suggested that at the highest driving force, the separation becomes easiest due to the large difference in composition between the phases and therefore, the energy necessary to achieve the separation task at each individual distillation column is at a minimum. In addition, Sobocan et al. [3] developed a systematic synthesis of energy integrated distillation column systems. This method helps in reducing external energy input of the distillation column systems by minimizing the utility consumption and maximizing the heat exchange between the integrated columns.

This paper presents a methodology for designing energy efficient distillation column systems based on driving force and energy integration methods. In the next section, review on energy integrated distillation columns design is discussed followed by a detail of the proposed methodology which consists of four hierarchical steps. The application of this methodology is tested by using a case study and ends with conclusion.

## 2. Overview of Energy Integrated Distillation Columns Design

The design method for energy integrated distillation columns can be summarized into four types which are: 1) conventional type distillation column with multicomponent separation, 2) conventional type distillation column with driving force, 3) conventional type distillation column with pinch technology and 4) conventional type distillation column with driving force combining with pinch technology. The McCabe-Thiele graphical technique has been used as a basic and simple technique to determine the design values of distillation column [4].

In this study, two graphical methods are used to determine the optimal design for energy efficient, which are driving force and pinch technology. Driving force method usually uses in the earliest stage of designing distillation column in order to successfully achieve the desired separation. In distillation column, driving force is the difference between composition in vapour phase and liquid phase which occurs when the difference of properties such as boiling point and vapour pressure [5]. The ideal designs for distillation column is based on the driving force approach to maximum, will lead to energy necessary in maintaining the two phase system in minimum or highly energy efficient design. Therefore, in the second type of distillation column design, the driving force method will be used as an additional step in similar conventional distillation column with the present of driving force diagram.

Meanwhile, pinch technology represent as a simple thermodynamically method that produce minimum energy consumption by using the first key of pinch analysis (setting energy target) as a key part for energy monitoring [6]. Pinch technology method helps to optimize the heat transfer equipment during temperature crossover between hot streams and cold streams according to the first and second law of thermodynamics. Then, the third type of distillation design method is achieved by using pinch technology in the conventional type of distillation column in order to reduce energy consumption in the process which mean more energy saving can be obtained. Lastly, the design of energy efficient distillation column can be created by combining driving force method with pinch technology in the conventional type of distillation column. Theoretically, by combining these two methods with the conventional type of distillation columns can produce more energy efficient.

## 3. Methodology for Designing Energy Efficient Distillation Columns Systems

In this section, we discuss in more details the development of a systematic methodology for designing energy efficient distillation columns systems based on driving force and energy integration methods. Accordingly, the proposed methodology consists of four hierarchical steps as shown in Fig 1.

The first step deals with the conventional distillation columns systems design, which will become the base design used for verification purposes. In this step, the system of distillation column for multicomponent separation is designed based on the conventional distillation column design method. Then, the conventional distillation columns systems design is improved in terms of energy saving by using driving force method in the second step. It is expected in the third step that the distillation columns systems design can be further improved in terms of energy saving by using energy integration method.

Finally, the distillation column systems design is evaluated in terms of economic performance. By applying the proposed methodology, it is possible to make an early assumption on type of distillation column systems design that is the best in terms of energy saving and cost.

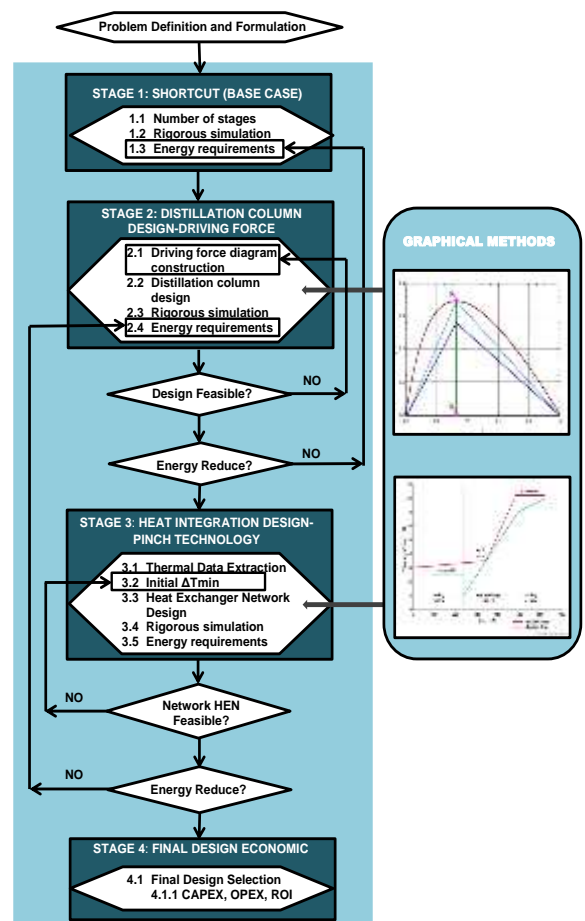


Fig. 1: A new proposed methodology for an energy integrated distillation columns.

The simulation models of the studied distillation columns systems are implemented in the Aspen HYSYS process simulator. In the first step, the number of the theoretical trays, location of the feed trays and the reflux ratio are estimated with shortcut design procedure. The results of the shortcut design are then implemented in rigorous column model. In the second step, by fixing the number of the theoretical trays obtained in the previous step, the location of the feed trays and the reflux ratio are estimated by using driving force method. Then, the results of the driving force design are implemented in rigorous column model, and the total energy consumption is compared with the previous shortcut design. In the

third step, the energy saving of the distillation columns systems designed by driving force method is further improved by implementing energy integration. The design of the heat exchanger network is synthesized by using thermal pinch method. The results of the heat exchanger network design are then implemented in rigorous column model, and the total energy consumption is compared with the two previous designs. Finally, the economic performance is calculated and analyzed.

#### 4. Case Study for Benzene, Toluene and p-Xylene (BTX)

The separation case study of a ternary mixture of benzene, toluene and p-xylene is selected to highlight the application of the proposed methodology as shown in Table 1. The feed flowrate is 100kmol/hr and products consist of three components. In this case study, A, B and C are denoted as light, intermediate and heavy components. The temperature and pressure for feed are selected at 75 ° and 2 atm.

In the first stage, the separation sequence based on the short cut design method is applied. The energy required for this separation sequence is taken as a reference. Then, the energy requirements for the separation is verified or further improved by using driving force method.

Table 1: Case study of flow rate feed and product specification.

Streams	Feed	
	kmol/hr	X
Components		
Benzene (A)	50.00	0.50
Toluene (B)	30.00	0.30
p-xylene(C)	20.00	0.20
Total	100	1.00

Fig 2 shows the driving force diagrams for two different binary separations which are Benzene-Toluene (direct sequence) and Toluene-p-Xylene (indirect sequence). From the figure, it can be seen that the plot of Benzene-Toluene shows the higher point compared to Toluene- p-Xylene. According to the driving force method, at the higher point at the driving force diagram separation becomes easier and the energy required to maintain that separation is at the minimum. Therefore, by just analysing the driving force diagram, we can identified the best distillation columns sequence that will require less energy.

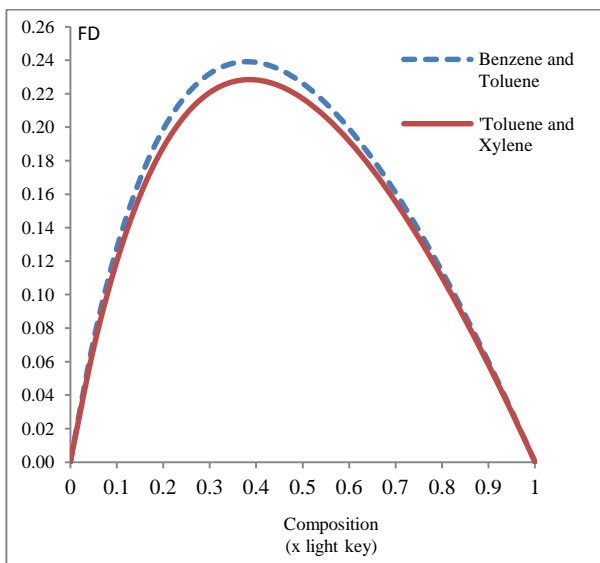


Fig 2: Driving force diagram for BTX separation system.

The sequence obtained from the driving force method will be then verified in terms of energy saving by using Aspen HYSYS process simulator. Tables 2 and 3 show the results for the percentage of energy savings for indirect and direct sequences by using Aspen HYSYS simulations. It is verified that energy saving with 8% reduction can be obtained by using direct sequence as suggested by the driving force method.

#### 5. Summary

The methodology for designing energy efficient distillation column systems based on driving force and heat integrated methods has been presented. Accordingly, the proposed methodology consists of four hierarchical steps. By applying the proposed methodology, it is possible to make an early assumption on the sequence of distillation column systems that is the best in terms of energy saving.

Table 2: Separation of Toluene and p-Xylene (Indirect Sequence)

Design	Shortcut Method	Driving Force Method
No. of stages, N <sub>s</sub>	24	24
No. of feed location, N <sub>F</sub>	10	15
Reflux Ratio	0.628	0.507
Composition at top	Benzene	0.6023
	Toluene	0.3697
	p-xylene	0.0100
Composition at bottom	Benzene	0.0000
	Toluene	0.0100
	p-xylene	0.9900
Energy Condenser, kW	2161	2098
Energy Reboiler, kW	2292	2229
Total Energy, kW	4453	4327
Percentage Energy Saving with Driving Force Method, %	3	

Table 3: Separation of Benzene and Toluene (Direct Sequence)

Design	Shortcut Method	Driving Force Method
No. of stages, N <sub>s</sub>	21	21
No. of feed location, N <sub>F</sub>	10	13
Reflux Ratio	1.421	1.070
Composition at top	Benzene	0.9900
	Toluene	0.0100
	p-xylene	0.0000
Composition at bottom	Benzene	0.0100
	Toluene	0.5900
	p-xylene	0.4000
Energy Condenser, kW	1809	1663
Energy Reboiler, kW	1937	1792
Total Energy, kW	3746	3455
Percentage Energy Saving with Driving Force Method, %	8	

#### Acknowledgement

The financial support from Universiti Teknologi Malaysia is highly acknowledged.

## References

- [1] Bek-Pedersen, E., Gani, R. (2004). Design and Synthesis of Distillation Systems Using a Driving-Force Based Approach. *Chemical Engineering and Processing*, 43, 251-262.
- [2] Kemp, I. C. (2007). *Pinch Analysis and Process Integration. A User Guide on Process Integration for the Efficient Use of Energy*. Elsevier, Amsterdam, the Netherlands.
- [3] Sobocan, G., Glavic, P. (2012). A simple method for systematic synthesis of thermally integrated distillation sequences. *Chemical Engineering Journal*, 89 (1-3), 155-172.
- [4] Wang, J. L., and Mansoori, G. A. (1994). A Revision of the Distillation Theory (Part I). *Scientia Ir.*, 1(3), 267-287.
- [5] Bek-Pedersen, E., and Gani, R. (2004). Design and Synthesis of Distillation Systems Using a Driving-Force Based Approach. *Chemical Engineering and Processing*, 43, 251-262.
- [6] Kemp, I. C. (2007). *Pinch Analysis and Process Integration. A User Guide on Process Integration for the Efficient Use of Energy*. Elsevier, Amsterdam, the Netherlands.

# A Study on Enhancing Flame Retardant Performance of Building Materials using Carbon Materials

Hyun Jeong Seo<sup>1</sup>, Su-Gwang Jeong<sup>1</sup>, Jeong-Hun Lee<sup>1</sup>, Sumin Kim<sup>1#</sup>, Dong Won Son<sup>2</sup> and Sang-Bum Park<sup>2</sup>

<sup>1</sup> Building Environment & Materials Lab, School of Architecture, Soongsil University, Seoul 156-743, Republic of Korea

<sup>2</sup> Department of Wood Processing, Korea Forest Research Institute, Seoul 130-712, Korea

# Corresponding Author / E-mail: skim@ssu.ac.kr, TEL: +82-2-820-0665, FAX: +82-2-816-3354

KEYWORDS : Carbon Materials , Flame Retardant , Wood-based Materials, Exfoliated Graphite Nanoplatelets (xGnP), Cone Calorimeter

---

*In this study, flame retardant was applied to coating materials for improvement of flame retardancy. The coating materials were applied to the surface of wood-based materials used interior materials and furniture, with high flame retardant performance were prepared by the stirring of carbon materials, such as natural graphite(NG), expandable graphite(EG) and exfoliated graphite nanoplatelets (xGnP), in liquid water-based paint, for confirming flame retardant performance of carbon materials. We have conducted experiments of two types. At first, carbon materials were compared with phosphorus flame retardant, which is used of conventional flame retardants, for expression flame retardant performance. Secondary, three types of carbon materials are were compared to each other about expression flame retardant performance. Phosphorus flame retardant and carbon materials were added to liquid water-based paint at same mass fractions (5.0 wt%). And these solutions were painted to building materials which is used to interior. The flame retardant performance of prepared samples was conducted by TGA and cone calorimeter experiment. TGA analysis revealed that Paint/Carbon materials blending composites have good thermal durability in the working temperature ranges. In case of cone calorimeter experiments, and the result of experiment was showed that this result satisfied standard for flame retardant performance standard in ISO 5600-1.*

---

## 1. Introduction

Wood has a beautiful design, superior mechanical strength and easy processing ability. Because of this, plate material of processed timber has been used actively for building interiors and furniture materials [1]. In particular, according to the latest global trends in sustainable timber, it is being used more frequently. However, when used as a building material, wood has a big problem of flammability. In the combustion of wood, wood chemically reacts with the oxygen in air to produce light, heat and the oxidation phenomena of burning. When wood is heated in air, there were reports in the pyrolysis, even after 180 °C [2]. The ignition temperature of the wood is about 350 °C [2]; when compared with other building materials such as stone, cement and concrete, in the event of a fire, wood can be seen as highly flammable. There are two ways to suppress the flammability, and improve the flame retardancy, of wood and wood-based panels. The first method is that wood-based panels are immersed in a solution of flames or are impregnated with flame retardant [3-6]. The second method is that flame retardant resin is coated on the surface of wood-based panels [7-9]. In the first the for retardant performance is expressed according to the charging of flame retardants, such as phosphorus flame retardant, inorganic flame retardants, or carbon-

based flame retardants in the air gap of wood-based panels. In the second case, it is a way to block the flames, by coating the surface of the product with retardant paint or coating film [10]. There is a high level of interest in using nano-size reinforcing fillers for making composite materials with exceptional properties [3-6, 11]. Also, research on the carbon material used in flame-retardant performance improvement among nanomaterials has recently been actively undertaken. Among the carbon materials, the kinds mainly used as flame retardant are Graphite, Amorphous carbons, Carbon nanotubes (CNTs) and they have some differences depending on the type and characteristics [10-13]. However, of these carbon materials, Carbon nanotubes (CNTs) are still expensive due to the difficulty of the manufacturing process. On the other hand, graphite is a natural substance that exists in abundance and are stacked six-sided colon as a carbon layer structure is made of a composite material as a filler has been a growing interest [13]. Expandable graphite (EG) is usually produced by using H<sub>2</sub>SO<sub>4</sub>-graphite intercalation compounds (GICs), through comparatively low-cost acid treatment. H<sub>2</sub>SO<sub>4</sub>-GICs are widely used for the exfoliation process, because they can give a high expansion volume, during thermal treatment [14]. The EG maintains layered structures similar to natural graphite flake, but produces admirably different sizes of pores, and nano-sheets with very high

aspect ratio [14, 18]. If the expression of the performance of carbon materials is to appear properly inside the material, it should be evenly distributed [15]. In addition, during the life cycle of building materials, such as a panel or wall, time passes, so the use of applied carbon materials should not result in degradation of the flame retardant performance. Building materials to which carbon materials are added should be durable, because of being applying to a building [16]. In addition, in order to secure safety at the time of the fire, wood-based panels for the building interior should not only have improved flame-retardant performance, but also have the properties of being environmentally friendly when fires occur, such as smothering the release of toxic gases. By satisfying these chemical characteristics, the resistance to fire in the building is increased, and at the same time, the safety can be secured. It is confirmed from previous studies that carbon materials exhibit flame retardant performance just through a mixture of physical agitation, without chemical treatment [16]. Therefore, in this study, the carbon material is mixed with paint for interior construction using a stirrer, and the flame retardant performance was confirmed through the methods of phosphorus and carbon-based flame retardant paint being applied to the surface of wood-based panels.

The aim of this study was to determine the combustion characteristics of the coating materials applied to the surface according to ISO 5660-1, using a cone calorimeter. The purpose of this study is resolving the combustibility of wood-based panels for use in building interiors and furniture. In order to achieve this goal, we propose utilizing carbon material as an additive. Also, we use thermo-gravimetric analysis (TGA), for measuring thermal behavior.

## 2. Experimental

### 2.1 Materials

In the experiment, we used carbon nanotubes (CNT), natural graphite, expandable graphite, and exfoliated graphite nanoplatelets (xGnP) as carbon-based flame retardant. CNT, EG, and xGnP were confirmed by previous research to have flame retardancy [6, 14, 19]. The xGnP was produced by the method of treatment of the graphite's surface acid treatment with sulfuric acid ( $H_2SO_4$ ) and the infliction of heat.

Table 1 Conditions of mixed flame retardant

Description	Retardant paint A	Retardant paint B	Retardant paint C
Type of retardant	APP	CNT	xGnP
Weight ratio of the components (%)	5.0	5.0	5.0

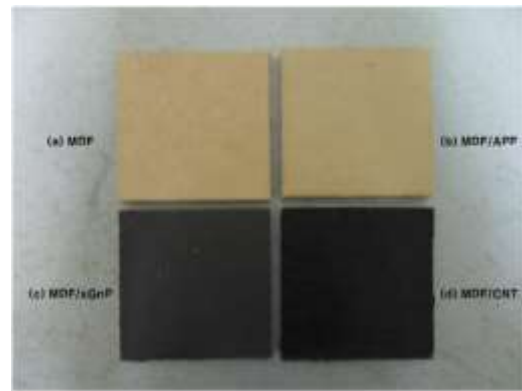


Fig. 1 Experimental specimens

### 2.2 Preparation

According to the standard that is provided by the company preparing paint, they were applied to the coating of the paint. We applied paints on the surface of MDF four times for each specimen. Table 3 shows the condition of the specimens for this experiment.

Table 2 Conditions of mixed carbon-based flame retardant.

Description	carbon-based retardant paint A	carbon-based retardant paint B	carbon-based retardant paint C
Type of retardant	Nature graphite (NG)	Expandable graphite (EG)	Exfoliated graphite nanoplates (xGnP)
Weight ratio of the components (%)	5.0	5.0	5.0

Table 3 Application to the surface of the specimen

Description	Composition of retardant filler	Number of times applied	Applied weight (g)
MDF	No treatment	0	5.5g/times
	MDF / APP	4	5.5g/times
	MDF / CNT	4	5.5g/times
	MDF / xGnP	4	5.5g/times
	Water-based Paint / MDF	4	5.5g/times
	MDF /NG	4	5.5g/times
	MDF / EG	4	5.5g/times

The material was applied to an explosion, and crushed through the process [14]. First, two types of flame retardant were added to the flame-retardant coating material, with the weight ratio of flame-retardant coating material A in the same manner as the ratio of the phosphorus-based flame retardant (Ammonium Polyphosphate; APP), and flame-retardant coating material B was prepared for commercially available flame-retardant phosphorus-based flame retardant based paints A, with the aqueous coating material in a mixture of a carbon-based flame retardant Flame retardant coatings B,

C of the flame retardant performance for comparison (Table 1). The paint used to paint the base was SAMHWA PAINT INDUSTRIAL CO., LTD. designed building built in water-based paint for the main ingredient is a synthetic melanin resin. Specimens were produced by DONGWHA NATURE FLOORING CO., LTD. for furniture materials of medium density fiber board (MDF). For testing by Cone Calorimeter, the foundation was of size 100mm×100mm×10mm. (Fig 1) The second specimen was produced by coating three kinds of carbon-based flame retardant paint. The coating material used in the carbon materials are natural graphite (NG), expandable graphite (EG) and exfoliated graphite nanoplates (xGnP), which were mixed at a weight ratio of 5% in water-based paints.

### 2.3 Characterization technics

#### 2.3.1. Flammability testing

Cone calorimeter tests were carried out according to the procedures indicated in the standard of ISO 5660-1. The MDFs were conditioned to equilibrium at 70% and 28 °C prior to testing. All specimens were measured in the horizontal position and the square specimens were heated with heating intensity (Heat flux) of 50kJ/m<sup>2</sup> for each specimen. Fig. 2 shows the cone calorimeter machine used in this experiment. This machine is located in The Forest Research Institute of South Korea. During the test, the following parameters were determined heat release rate (HRR), peak heat release rate (PHRR), total heat release (THR) and mass loss rate. Additionally, through determining the smoke emission rate (SPR) and CO yield data, we tried to detect the fire hazard for toxic gases.



Fig. 2 Cone calorimeter

#### 2.3.2. Thermo-gravimetric analysis

Thermo-gravimetric analysis (TGA, TA instrument, TGA Q 5000) was carried out to determine the decomposition temperature. Specimens were cut into by approximately 2-4 mg, and fitted to a nitrogen atmosphere consisted of 99.5 % nitrogen and 0.5 % oxygen to prevent oxidation, in the range of 0-600 °C, at a heating rate of 10 °C/min.

## 3. Results and discussion

### 3.1. Heat Release Rate (HRR)

The heat release rate is the size of the calories caused by the

specimen surface area, and is the best element that indicates the risk of burning materials. Fig. 3 shows the results of the first experiment by the cone calorimeter, which are the HRR curves of MDF and coated MDF with flame retardants. The specimens, to which xGnP and APP are applied how improved flame retardant performance.

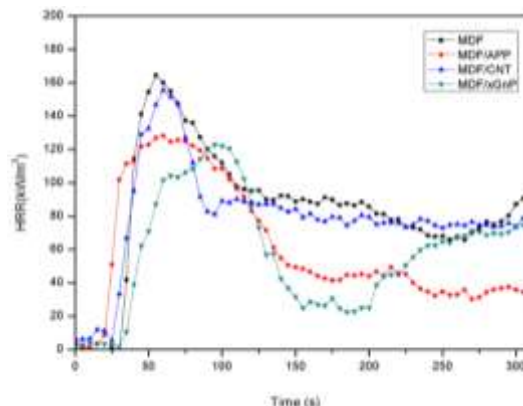


Fig. 3 Heat Release Rate (HRR) of the comparison among the flame retardants

In the case of xGnP/MDF specimen, the peak temperature is the last to appear at the beginning of the experiment. This result is determined as showing benefits of delaying combustion, when fire occurs. After 200 seconds passed, the HRR value of the xGnP is increased. However, it was still a lower value than the value of the non-treated specimens. According to ISO 5660-1 standard, the value of APP/MDF and xGnP/MDF specimens satisfied Level 3 flame retardant criteria. Table 4 shows the ISO 5660-1 standard provisions of the flame retardant performance in Japan.

Table 4 Cone calorimeter test of ISO 5660-1 standard [20]

Class of Flammability	Performance standards		Determination reference
	Heating conditions	Heating time (m)	
First class (non-combustible)	50kW/m <sup>2</sup>	20	<ul style="list-style-type: none"> <li>Total heat release (THR) should be less than 8MJ/m<sup>2</sup>.</li> </ul>
Second class (Semi-noncombustible)	50kW/m <sup>2</sup>	10	<ul style="list-style-type: none"> <li>The peak HRR should not exceed 200kW/m<sup>2</sup> for more than 10 seconds.</li> </ul>
Third class (flame retardant)	50kW/m <sup>2</sup>	5	<ul style="list-style-type: none"> <li>When fire occur, penetration, cracks, holes, etc. that are harmful should not occur.</li> </ul>

Fig. 4 shows secondary data among the graphite. The specimen applied with paint only, resulted in values of over 200kW/m<sup>2</sup>. Overall, graphite-based MDF specimens exhibited low values, compared to the value of the specimen applied with paint only. The EG/MDF showed the lowest value of HRR, because, EG was a blast, while it absorbs heat. The flame retardant performance is improved, even if we have applied other graphite. These results confirmed the greater safety of wood-based panels applied with graphite-based composites,

as building materials for interiors when exposed to fire, compared to untreated wood-based panels.

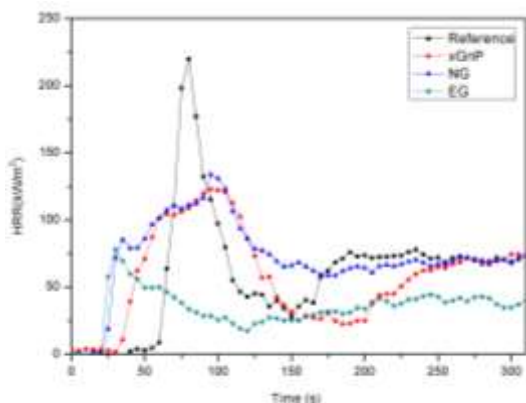


Fig. 4 Heat Release Rate (HRR) of the graphite-based flame retardants

### 3.2 Peak of Heat Release Rate (PHRR) and Total Heat Release (THR)

Tables 5 and 6 show the values of PHRR, THR and mass reduction ratio that are results of all the experiments.

Table 5 The results of the Cone calorimeter test by the comparison among the flame retardants

	$PHRR(kW/m^2)$	$tPHRR (s)$	Mass reduction ratio (%)
MDF	164.35	55	66.25
MDF/APP	128.23	60	47.45
MDF/CNT	155.60	60	66.39
MDF/xGnP	122.89	100	61.87

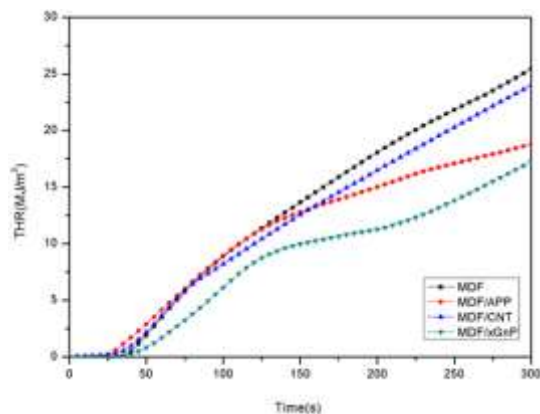
The results of PHRR confirm that, the value of all specimens did not exceed 200kW/m<sup>2</sup>. The value of tPHRR shows that the heat release time was delayed. When compared with the all the other specimens, the value of xGnP/MDF is the lowest; therefore, we can determine that xGnP has thermal stability. As a result, MDFs coated with the surface using graphites showed flame retardant performance. When viewing the results, it is most unique that EG/MDF showed the best value for flame retardant.

Table 6 The results of the Cone calorimeter test by the graphite-based flame retardants

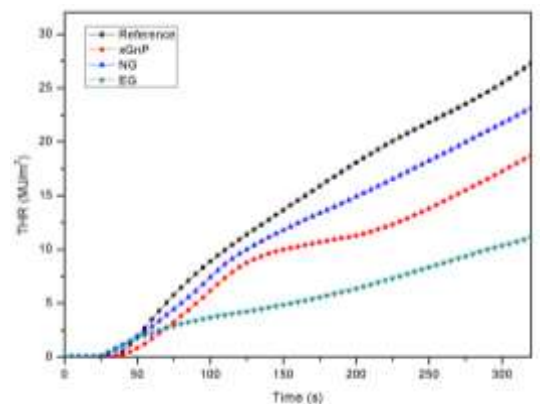
	$PHRR(kW/m^2)$	$tPHRR (s)$	Mass reduction ratio (%)
Reference	213.97	55	77.23
xGnP/MDF	122.89	100	33.61
NG/MDF	128.09	65	29.25
EG/MDF	77.95	30	7.97

Fig. 5 is the THR curve of two types of experiment. The THR curves show the trends of retardant performance of graphite-based coatings. As can be seen from looking at the graphs, all kinds of

graphite have flame retardancy. The mass loss ratio indicated the amount burned, when fire occurred. As shown in the table, MDFs coated with flame retardant showed a lower mass loss rate. In particular, EG/MDF showed a rate that was the lowest, with a value of less than 10 percent. Because EG is treated by acid, it has a high surface area, and lacks a high negative surface charge, so has a good heat absorption capacity [14].



(a) Comparison among the flame retardants



(b) Graphite-based flame retardants

Fig. 5 Total heat release (THR) of flame retardants (a) and (b)

### 3.3 Smoke emission of untreated MDF and coated MDF

Many types of interior materials and furniture release dense smoke that limit visibility, and can cause disorientation for people attempting to escape from a fire situation. The production of smoke and toxic gas along with the HRR play an important role in understanding the risk of fire related to interior materials and furniture [21]. Fig. 6 shows the SPR curves of untreated MDF and coated MDF. The SPR of water-based paints/MDF and EG/MDF was the highest and lowest among the coated MDFs, respectively. This result was attributed to their higher HRR and lowest HRR. The SPR of xGnP/MDF and NG/MDF were lower than that of Water-based paints/MDF, indicating that for the graphite-based coating materials, the coated surface of the MDF reduced the SPR. However, the SPR of CNT/MDF was much higher than that of the other carbon-based coating materials, because CNT has toxicity [22].

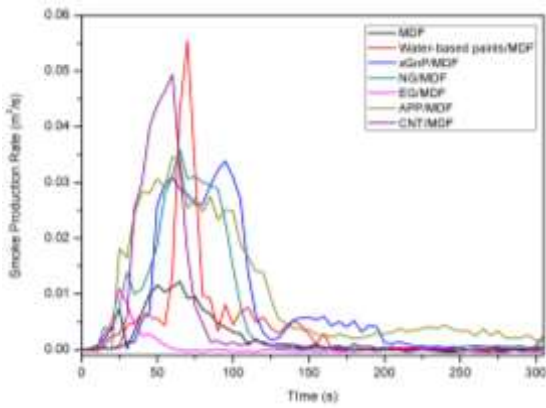


Fig. 6 Smoke production rate (SPR) curves of untreated MDF and coated MDFs

Wood-based panels, such as MDF, are used widely as interior materials and furniture. However, one of the limitations of MDF as an interior material is its flammability [23]. Therefore, the high HRR and SPR of MDF need to be treated with flame retardant and non-toxic materials, to improve the fire safety and behavior. Fig. 7 shows the CO yield of the untreated MDF and coated MDFs. The gas products released by decomposing untreated MDF and coated MDFs depend on the chemical nature of the organic component material, oxygen availability and the temperature of the fire [21].

As shown in the graph, the CO emitted from the MDF treated with different types of flame retardant show various peak points, respectively. Among the results, the CO yield of EG/MDF and NG/MDF showed the unique shape of a curve. EG was produced by acid treatment, so that it was exploded by being intermittently applied to heat. In the case of that of NG/MDF, it showed intensive release of CO gas, early in the combustion. It is apparent that an increase in the value of HRR is almost associated with an increase in the CO yield [21]. However, as shown in Fig. 8, the peak point of the CO yield of NG/MDF exhibited lower value than that of the others.

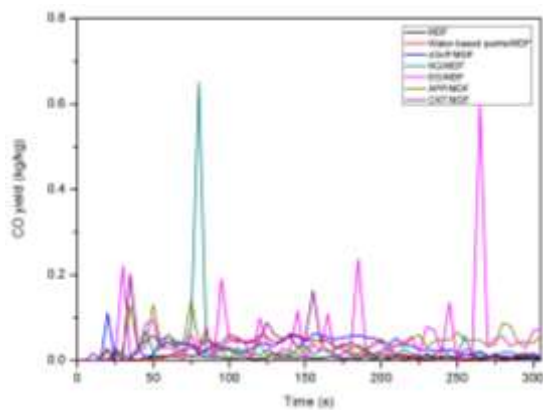


Fig. 7 CO yield of untreated MDF and coated MDFs, as a function of time

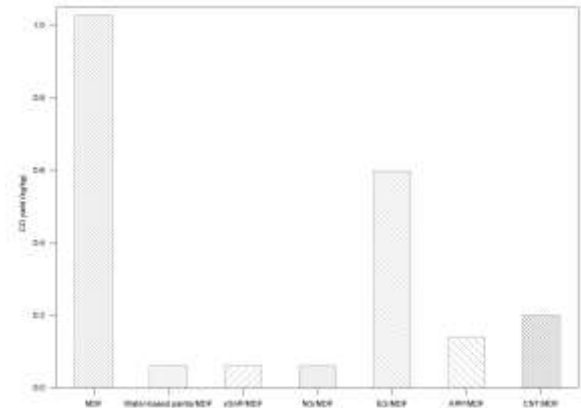


Fig. 8 Peaks of CO yield of of untreated MDF, and coated MDFs

Also, the CO yield of EG/MDF, which showed a unique pattern, exhibited lower value, as compared to untreated MDF. Therefore, graphite-based coating materials have a lower hazard of fire occurring. The importance of reducing smoke to increase human survival in a fire has prompted the characterization of the smoke properties for a wide range of interior and furniture materials. From these results, it was concluded that the HRR and SPR are important factors for evaluating a fire hazard, and that the application of graphite-based coating materials to interior materials as a flame retardant is an effective method for enhancing fire safety, and resisting the fire [23].

### 3.4 Thermal stability of xGnP-based coating materials

The thermal stability of xGnP-based coating materials was evaluated, by means of TGA. TGA is measured by adding the specimens to a temperature program about changing the mass of specimens, utilizing time and temperature as a function. It is a thermal gravimetric analysis of ideal composition, utilized to analyze substances into volatile materials (water, solvents, etc.), polymers, carbon filler and ash, etc. According to the derivative weight curve, all the samples mainly degraded in two steps. In the case of 5wt.% xGnP-based coating materials, the first peak occurred at 358.6 °C, and the second peak occurred at 417.3 °C. On increasing the xGnP contents of xGnP-based coating materials, the peak temperature is highest at 369.0 °C of the first peak, and at 425.5 °C of the second peak. In the case of 7wt.% xGnP-based coating materials, showing a slow peak point, the peak temperature slowly declined by 395.8 °C of the first peak, and a second peak point didn't appear. All the samples showed small weight losses of almost 17%, and the mass loss of the composite is shown in Fig. 9. Comparing the results, 10wt.% xGnP-based coating materials show the lowest weight loss; therefore, the retardant performance is proportional to the weight ratio, to a certain extent. However, the curves of all three are of almost similar shape. The TGA curves show that all kinds of xGnP have thermal stability.

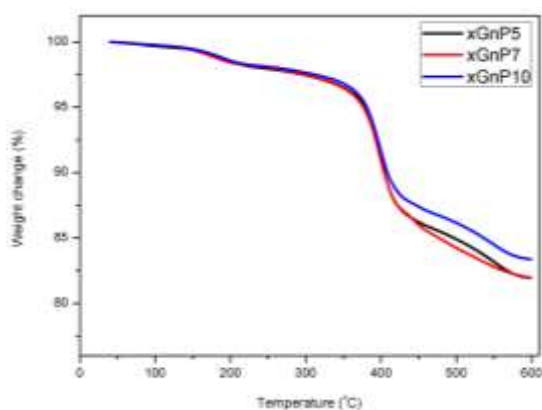


Fig. 9 TGA curves of xGnP-based materials

#### 4. Conclusions

The combustion characteristics of carbon-based materials for coating the surface of MDF were investigated, according to ISO 5660-1, using a cone calorimeter. The kind of flame retardant, applied to the MDF, confirmed the HRR, PHRR, THR and mass reduction ratio. Also, the SPR emission and CO yield were measured, for enhancing the fire safety, and resisting the fire. Among all flame retardants, APP/MDF and xGnP/MDF showed that the application of flame retardant to interior materials is an effective method for enhancing the fire safety. In addition, CNT of the results of previous studies with the different cases confirmed that the flame retardant performance was not well expressed. Although xGnP was physically mixed with an existing water-based paint, it was similar to the performance of a flame retardant shown in APP. Allowing this result, the physical dispersion of the mixture with just xGnP evenly distributed flame retardant performance could have determined this expression. However, in the case of CNT, was not built in a well-distributed so that low-retardant performance could not appear in our evaluation. Also, we compared the various types of graphite on the thermal stability and flame retardant performance. The case of EG/MDF showed the best flame retardant performance of several aspects data. Also, according to the TGA curves, all graphite-based coating materials show thermal stability at occurring fire temperature. As a result, flame retardant coating with carbon materials, like xGnP, NG and EG, can be considered as flame retardant building materials, such as interior construction, and furniture for buildings.

#### ACKNOWLEDGEMENT

This research was supported by the Converging Research Center Program funded by the Ministry of Education, Science and Technology (2013K000390).

#### REFERENCES

- Kim, JI., Park, JY., Kong, YT., Lee, BH., Kim, HJ. and Roh, JK. "Performance on Flame-Retardant Polyurethane Coatings for Wood and Wood-based Materials," MOKCHAE KONGHAK, Vol. 30, No. 2, pp.172-179, 2002.
- Rowell, RM., "Handbook of Wood Chemistry and Wood Composites," 2013.
- Moon, SC. and Emrick, T., "High flame resistant and strong electrospun polyacrylonitrile-carbon nanotubes-ochre nanofibers," Polymer, Vol. 54, No. 7, pp. 1813-1819, 2013.
- Isitman, NA. and Kaynak, C., "Nanoclay and carbon nanotubes as potential synergists of an organophosphorus flame-retardant in poly (methyl methacrylate)," Polym. Degrad. Stabil, Vol. 95, No. 9, pp. 1523-1532, 2010.
- Naumann, A., Seefeldt, H., Stephan, I. and Noll, M., "Material resistance of flame retarded wood-plastic composites against fire and fungal decay," Polym. Degrad. Stabil, Vol. 97, No. 7, pp. 1189-1196, 2012.
- Wang, G and Yang, JY., "Influences of expandable graphite modified by polyethylene glycol on fire protection of waterborne intumescent fire resistive coating," Surf. Coat. Technol, Vol. 204, No. 21-22, pp. 3599-3605, 2010.
- Chou, CS., Lin, SH., Wang, CI. and Liu, KH., "A hybrid intumescent fire retardant coating from cake - and eggshell - type IFRC," Powder. Technol, Vol. 198, No. 1, pp.149-156, 2010.
- Zhang, T., Du, Z, Zou. W, Li, H. and Zhang, C., "The flame retardancy of blob-like multi-walled carbon nanotubes-silica nanospheres hybrids in poly (methyl methacrylate)," Polym. Degrad. Stabil, Vol. 97, No. 9, pp.1716-1723, 2012.
- Chen, G, Yao, K. and Zhao, J., "Montmorillonite Clay/Poly(methyl methacrylate) Hybrid Resin and Its Barrier Property to the Plasticizer Within Poly(vinyl chloride) Composite," J. Appl. Polym. Sci, Vol. 73, No. 3, pp. 425-430, 1999.
- Kashiwagi, T., Grulke, T., Hilding, J., Groth, K., Harris, R., Butler, K., Shields, K., Kharchenko, S. and Douglas, J., "Thermal and flammability properties of polypropylene/carbon nanotube nanocomposites," Polymer, Vol. 45, No. 12, pp.4227-4239, 2004.
- Lu, H. and Wilkie, CA., "Synergistic effect of carbon nanotubes and decabromodiphenyl oxide/Sb<sub>2</sub>O<sub>3</sub> in improving the flame retardancy of polystyrene," Polym. Degrad. Stabil, Vol. 95, No. 4, pp. 564-571, 2010.
- Kamae, T. and Drzal, T. L., "Carbon fiber/epoxy composite property enhancement through incorporation of carbon nanotubes at the fiber matrix interphase – Part I: The development of carbon nanotube coated carbon fibers and the evaluation of their adhesion," Composites: Part A, Vol. 43, No. 9, pp. 1569-1577, 2012.
- Kang, SJ., Kim, KJ., Kim, MS., Kim, BJ. et al coauthor. "Carbon Materials Applications Manual," 2008.
- Kim, S. and Drzal, T. L., "High latent heat storage and high thermal conductive phase change materials using exfoliated graphite nanoplatelets," Sol. Energy. Mater, Sol. Cells, Vol. 93, No. 1, pp.136-142, 2009.

15. Dittrich, B., Wartig, A. K., Hofmann, D., Mlhaupt, R. and Schartel, B., "Flame retardancy through carbon nanomaterials: Carbon black, multiwall nanotubes, expanded graphite, multi-layer graphene and graphene in polypropylene," *Polym. Degrad. Stabil.*, Vol. 98, No. 8, pp.1-11, 2013.
16. Zhao, X., Hayashi, A., Noda, Z., Kimijima, K., Yagie, I. and Sasakia, K., "Evaluation of change in nanostructure through the heat treatment of carbon materials and their durability for the start/stop operation of polymer electrolyte fuel cells," *Electrochim. Acta*, Vol. 97, No. 1, pp.1053–1061, 2013.
17. Przepiński, J., Czyżewski, A., Pietrzak, R., Toyoda, M. and Morawski, W. A., "Porous carbon material containing CaO for acidic gas capture : Preparation and properties," *J. Hazard. Mater.*, Vol. 263, No. 2, 2013.
18. Zhao, Y. F., Xiao, M., Wang, S. J., Ge, X. C. and Meng, Y. Z., "Preparation and properties of electrically conductive PPS/expanded graphite nanocomposites," *Compos. Sci. Technol.*, Vol. 67, No. 11-12, pp.2528–2534, 2007.
19. Stéphane, C., Nguyen, T. P., Chapelle, M. L., Lefrant, S., Journet, C. and Bernier, P., "Characterization of singlewalled carbon nanotubes-PMMA composites," *Synth. Met.*, Vol. 108, No. 2, pp.139–149, 2000.
20. ISO 5660-1, "Reaction to Fire Tests – Heat Release, Smoke Production and Mass Loss Rate – Part1 Heat Release Rate (Cone Calorimeter Method)," 2002.

# Numerical Investigation of Heating Mechanism in Ultrasonic Imprinting

Jong Han Park<sup>1</sup>, Ki Yeon Lee<sup>2</sup> and Keun Park<sup>1#</sup>

<sup>1</sup> Dept. Mechanical System Design Engng., Seoul Nat'l Univ. Sci. Tech., 232 Gongneung-gil, Nowon-gu, Seoul, 139-743, Republic of Korea  
<sup>2</sup> R&D Department, Home Appliance Lab., LG Electronics Co., 372-23 Gasan-dong, Geumcheon-gu, Seoul, 153-802, Republic of Korea  
# Corresponding Author / E-mail: kpark@seoultech.ac.kr, TEL: +82-2-970-6358, FAX: +82-2-974-8270

KEYWORDS : Ultrasonic Imprinting, Micropattern Replication, Finite Element Analysis, Heating Mechanism

---

*Ultrasonic imprinting is a novel process in which micropatterns can be replicated on thermoplastic polymer films with short imprinting time and low energy consumption. The micro-scale vibration of an ultrasonic horn causes repetitive deformation and friction on the polymer surface, which results in heat generation due to viscoelastic dissipation energy. As the ultrasonic vibration repeats in high frequency, the polymer temperature increases to its softening temperature, and the micropatterns engraved on the horn surface can be replicated on the softened surface. In this study, the heating mechanism in the ultrasonic imprinting process is numerically investigated using finite element (FE) analysis. For the simulation of the ultrasonic imprinting process, a coupled FE analysis is performed by connecting structural FE analysis for the vibration stage and thermal FE analysis for the heating stage. For the vibration stage, a nonlinear structural analysis is performed to calculate the ultrasonic wave propagation and the resulting viscoelastic dissipation energy generation inside the polymer. For the heating stage, a transient heat transfer analysis is performed using the obtained dissipation energy data. Through the proposed coupled simulation, heating mechanism of ultrasonic imprinting is investigated numerically and is compared with experimental measurement. Effects of imprinting conditions on the heating characteristics are also discussed through the proposed simulation.*

---

## 1. Introduction

These days, ultrasonic vibration energy has been widely applied in various manufacturing fields such as machining, joining and material processing. Recently, the ultrasonic energy was further applied to ultrasonic imprinting (U-NIL) that replicates micro/nano patterns directly on thermoplastic polymer substrates.<sup>1-2</sup> In this process, ultrasonic energy is converted into heat at the interface between polymer substrates and molds so that polymer surfaces become softened enough to be deformed by external force.<sup>3</sup> The heating mechanism is similar with that of ultrasonic welding while U-NIL uses patterned mold or horn for micro/nano pattern replication. Owing to its simple apparatus setup and high productivity, the U-NIL process has increasingly been applied to the fabrication of functional components such as micro-devices and super-hydrophobic surfaces.<sup>4-6</sup>

Several researches have been performed to investigate the U-NIL process numerically. Lin and Chen<sup>7</sup> analyzed the flow field and temperature distribution during U-NIL using computational fluid dynamics (CFD) simulation. Zhang and Li<sup>8</sup> conducted a coupled

thermal-mechanical numerical analysis to simulate the ultrasonic welding process of aluminum foil. Elangovan et al.<sup>9</sup> solved thermal FEA problems to predict temperature change at weld interface during ultrasonic welding of metallic materials. Rani and Rudramoorthy<sup>10</sup> performed FEA to predict the vibration characteristics and the resulting thermal effects for various horn types in ultrasonic welding of polymer materials.

In this study, a coupled numerical analysis is performed to simulate the ultrasonic imprinting process, by connecting structural FE analysis for the vibration stage and thermal FE analysis for the heating stage. For the vibration stage, a structural analysis is performed to calculate the ultrasonic wave propagation and the resulting deformation energy generation inside the polymer substrate. The estimated deformation energy is then transformed into internal heat generation, from which a transient heat transfer analysis can be performed for the heating stage. Through the proposed coupled simulation, heating mechanism of ultrasonic imprinting could be successfully investigated.

## 2. Overview of the U-NIL process

The U-NIL process uses ultrasonic vibration energy to soften thermoplastic polymer substrates for pattern replication. The micro-scale vibration of the horn causes repetitive deformation of the polymer surface, which results in heat generation due to viscoelastic dissipation energy. As the ultrasonic vibration repeats in high frequency, the polymer temperature increases to its softening temperature. Thus, the micropatterns engraved on the horn surface can be replicated on the softened substrate.

The U-NIL process follows four steps, as illustrated in Fig. 1. The first step is the vibration step where an ultrasonic horn presses a polymer substrate with ultrasonic excitation. The next step is the filling step where the polymer surface is softened by the deformation heat, and microcavities of the horn surface are filled with the molten polymer. After this filling step under ultrasonic vibration, a holding force is maintained for several seconds in order to improve pattern replication until the molten polymer surface is fully solidified (holding step). Finally, the horn recedes and the replicated substrate is ejected from the mold (demolding step).

In the U-NIL process, an ultrasonic horn should vibrate along its longitudinal direction in order to ensure high replication accuracy. A circular horn was designed and fabricated to resonate at the given excitation frequency. Considering that the horn vibration imposes compressive force only during the downward motion, the vibration stage can be divided into loading mode and unloading mode. In the loading mode, the horn moves downward so as to impose a compressive force on the substrate. In contrast, the horn moves upward in the unloading mode so that no external force is applied on the substrate. Figure 2 plots the measured force signal under three cycles of ultrasonic vibration. The frequency of the ultrasonic wave was 28 kHz, and the resulting time period for each cycle was measured to be 35.7  $\mu\text{s}$ . It can be seen that the measured force showed a half sinusoidal signal during the loading mode while no external force was detected during the unloading mode. The force amplitude was measured to 1.861 kgf.

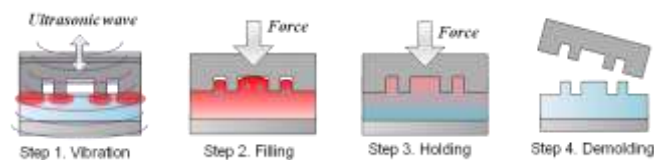


Fig. 1 Stepwise description of the U-NIL process

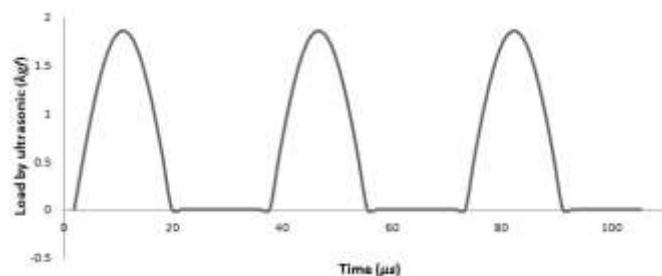


Fig. 2 Measured force signal during the ultrasonic excitation

### 3. Numerical Analysis for the U-NIL Process

#### 3.1 Structural wave propagation analysis

To obtain the repetitive deformation fields during the vibration stage, a transient structural analysis was performed. The analysis domain was simplified using a 2-dimensional plain strain model, and only a half section was taken by considering symmetry. The polymer substrate is an Altuglass PMMA sheet with 0.8 mm thickness. Nine micropatterns were modeled on the horn tip with the following dimensions: 250  $\mu\text{m}$  pitch, 100  $\mu\text{m}$  width and 34  $\mu\text{m}$  depth. The elastic modulus and Poisson's ratio of the substrate are 3.18 GPa and 0.38, respectively. As a boundary condition, compressive forces were applied for the contact regions between 9 micropatterns of the horn and the PMMA surface. ANSYS<sup>TM</sup> was utilized in the transient structural analysis and the relevant wave propagation simulation.

Figure 3 shows the transient deformation results of the PMMA substrate during the first loading cycle ( $0 \sim \lambda/2$ ). The maximum deformation occurred at 8.93  $\mu\text{s}$ , which corresponds to  $\lambda/4$  in wavelength. The resulting strain field at this point was then set to the amplitude of the strain signal, from which the viscoelastic dissipation energy generated in the PMMA substrate can be calculated.

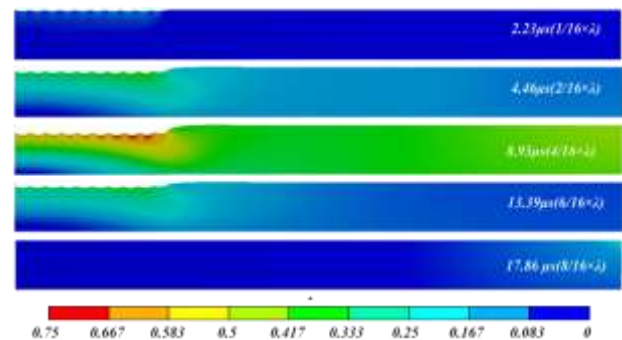


Fig. 3 Transient deformation results during the loading period (unit:  $\mu\text{m}$ , magnification factor: 10)

#### 3.2 Transient heat transfer analysis

For the transient heat transfer analysis, the heat generation rate was calculated using from the obtained strain field of the structural analysis. Figure 4 shows the calculated heat generation distribution. It can be seen that the heat generation was concentrated in the deformed regions contacted with horn micropatterns. In the heat transfer analysis, the mold region was included in the analysis domain in order to consider the heat conduction between the mold and substrate.

Figure 5 shows the change of the temperature distribution of the PMMA substrate from 0.1s to 0.8s with an increment of 0.1s. It can be seen that temperature rises as the vibration time increases, showing that higher temperature than the glass transition temperature ( $T_g$ , 105  $^{\circ}\text{C}$ ) at the 0.6 s of vibration time. After that, further temperature rise proceeds and the entire deformation zone reaches to  $T_g$  at the 0.8s of vibration time while the outside region still remains at the room temperature. These results mean that the polymer substrate can be heated efficiently over a short period while not raising the temperature of the entire part.

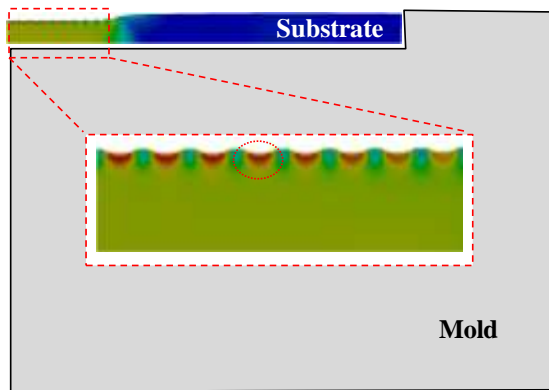


Fig. 4 Heat generation distribution in the PMMA substrate.

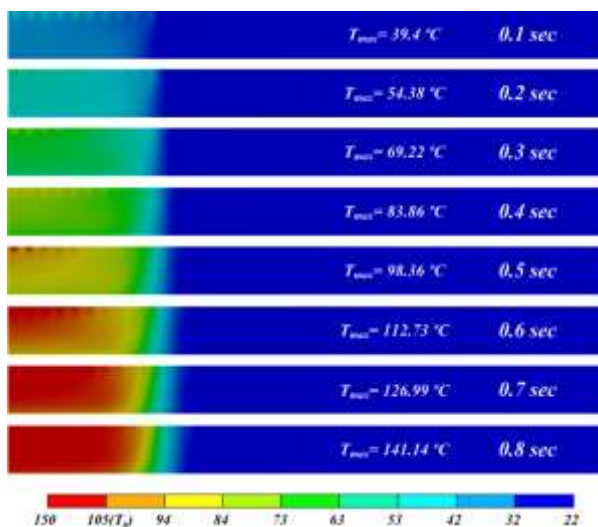


Fig. 5 Transient temperature distributions of the PMMA substrate under ultrasonic vibration.

#### 4. Conclusion

In this study, the heating mechanism in the U-NIL process was numerically investigated. For the simulation of the U-NIL process, a coupled FE analysis was performed by connecting structural FE analysis for the vibration stage and thermal FE analysis for the heating stage. The strain field obtained from the structural FE analysis was used to calculate viscoelastic dissipation energy generated. By imposing this strain energy as equivalent heat generation, the heating mechanism in U-NIL could be simulated from the thermal FE analysis. Through the proposed integrated simulation, heating mechanism of ultrasonic imprinting can be successfully described so as to investigate the effects of various processing conditions in future study.

#### ACKNOWLEDGEMENT

This research was financially supported by National Research Foundation of Korea (NRF) grants funded by the Ministry of Education and MSIP, Republic of Korea (Grant number: NRF-2013R1A1A2A10004709 and NRF-2013M2B2A4040973).

#### REFERENCES

1. Mekar, H., Goto, H. and Takahashi, M., "Development of ultrasonic micro hot embossing technology," *Microelec. Engng.* Vol. 84, No. 5-8, pp. 1282-1287, 2007.
2. Seo, Y. S. and Park, K., "Direct patterning of micro-features on a polymer substrate using ultrasonic vibration," *Microsyst. Technol.*, Vol. 18, No. 12, pp. 2053-2061, 2012.
3. Peng, L., Deng, Y., Yi, P. and Lai, X., "Micro hot embossing of thermoplastic polymers: a review," *J. Micromech. Microeng.*, Vol. 24, No. 1, 013001, 2004.
4. Khuntontong, P., Blaser, T. and Schomburg, W. K., "Fabrication of molded interconnection devices by ultrasonic hot embossing on thin polymer films," *IEEE Trans. Electr. Pack. Manufact.*, Vol. 32, No. 3, pp. 152-156, 2009.
5. Schomburg, W. K., Burlage, K., and Gerhardy, C., "Ultrasonic hot embossing," *Micromachines*, Vol. 2, No. 2, pp. 157-166, 2011.
6. Cho, Y. H., Seo, Y. S., Moon, I. Y., Kim, B. H. and Park, K., "Facile fabrication of superhydrophobic poly (methyl methacrylate) substrates using ultrasonic imprinting," *J. Micromech. Microeng.*, Vol. 23, No. 5, 055019, 2013.
7. Lin, C. H. and Chen, R., "Effects of mold geometries and imprinted polymer resist thickness on ultrasonic nanoimprint lithography," *J. Micromech. Microeng.*, Vol. 17, No. 7, pp. 1220-1231, 2007.
8. Zhang, C. and Li, L., "A coupled thermal-mechanical analysis of ultrasonic bonding mechanism," *Metallurgical Mater. Trans.* Vol. 40B, pp. 196-207, 2009.
9. Elangovan, S., Semeer, S. and Prakasan, K., "Temperature and stress distribution in ultrasonic metal welding – An FEA-based study," *J. Mater. Process. Technol.* Vol. 209, pp. 1143-1150, 2009.
10. Rani, M. R. and Rudramoorthy, R., "Computational modeling and experimental studies of the dynamic performance of ultrasonic horn profiles used in plastic welding," *Ultrasonics*, Vol. 53, No. 3, pp. 763-772, 2013.

# Experimental Study of Friction Reduction of Surface Texturing on Cylindrical Surface

Rendi Kurniawan<sup>1</sup> and Tae Jo Ko<sup>1#</sup>

<sup>1</sup> School of Mechanical Engineering, Yeungnam University, Gyeongsan-si, Gyeongsanbuk-do, South Korea, 712-719  
# Corresponding Author / E-mail: tjko@yu.ac.kr, TEL: +82-53-810-3836, FAX: +82-53-810-4627

KEYWORDS : Friction Reduction, Surface Texture

*This paper presents our recent work of experimental study of friction reduction investigation of surface texture on outer cylindrical surfaces. The surface texture on cylindrical surface has been produced by piezoelectric tool holder actuator (PTHA) which was assembled in conventional two-axis lathe machine. These experiments have been carried out to investigate whether the surface texture is able to improve the lubrication performance of cylindrical contacts planar surface or not. The surface texture was machined using PTHA on Al 6061 and AISI 1045 using vibration frequency ranging 50 Hz to about 260 Hz. The normal loads of 10 N and 50 N were applied and the rotation speeds between 100 rpm and 1000 rpm were applied in the tribology tests. The results show the evidence that the surface texturing reduces the friction coefficient in these trials ranging 20% to 40%.*

## NOMENCLATURE

CoF = Coefficient of Friction

$f_m$  = vibration frequency

## 1. Introduction

Micro dimples in term of a surface texture have gained great attention of tribology scholars due to a benefit to increase energy efficiency. This kind of application can be implemented in engine, ring pistons, cam mechanism, or mechanical bearing seals which need lubrication conditions to the energy efficiency.

Based on various tribology studies, micro dimples improve the frictional performance of sliding contact of planar surfaces under wet lubrication condition.<sup>1</sup> Scientists argued that the micro dimples act as oil reservoir as well as micro-bearing in which the lubricant is supplied into the two sliding contact surfaces producing micro fluid film.<sup>2</sup> As a result, the micro dimples enhance the load carrying capacity of the lubricant film between planar surfaces in term of the hydrodynamic pressure.<sup>3</sup>

The friction reduction depends on the tribological test and the surface texture shapes either its parameters or texture orientations of the sliding contact. Y. Uehara et. al investigated the effect of dimpling on the tribological properties of a silicon nitride ceramic against

hardened bearing steel under lubricated oil, planar to curved surface contact conditions.<sup>4</sup> In this paper, we present our recent experimental work of friction reduction on cylindrical surface with the existence of micro dimples under wet lubrication and validating which one of the surface textures gives a better performance compared to the other textured surfaces.

## 2. Fabrication of Textured Surface

The textured surfaces have been manufactured by using the piezoelectric tool holder actuator (PTHA). The PTHA that is installed in conventional machine lathe as illustrated in Fig. 1, in which the PTHA that was described in the previous work.<sup>5</sup> The PTHA consists of two components, the first is parallel flexure bar and piezo actuator. The cutting tool is able to travel along x-axis about 26  $\mu\text{m}$ . The total stiffness of the parallel bar flexure is approximately 50 N/ $\mu\text{m}$ .

The textured surfaces which have various depths between 8  $\mu\text{m}$  and 15  $\mu\text{m}$  were successfully created. The Fig. 2 shows typically the 3D topography of the textured surfaces with 15  $\mu\text{m}$  and 8  $\mu\text{m}$ , respectively. The textured surfaces with various depths were established by using vibration frequency of 120 Hz at constant spindle speed of 30 rpm. Table 1 shows the detail micro dimple features.

Not only the textured surfaces that have various depths were built but also with various vibration frequencies were established. Fig. 3

shows the textured surfaces were manufactured by various frequencies varying from 50 Hz to 260 Hz. The shape of the micro dimple will vary if the various frequencies are applied.

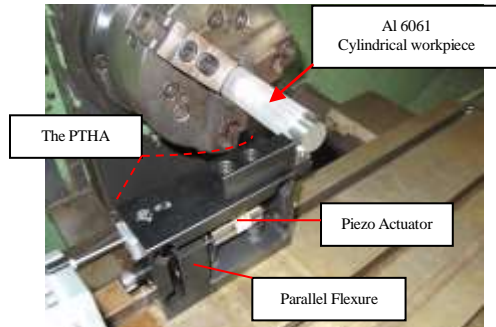


Fig. 1 The PTHA installed in conventional machine lathe

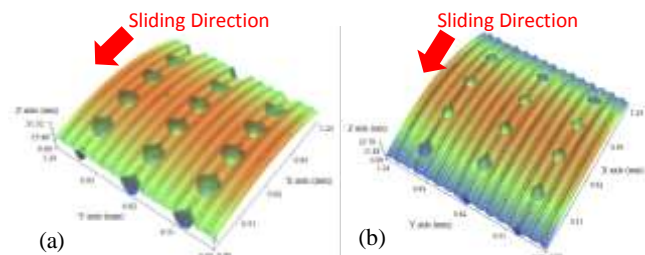


Fig. 2 Topography of cylindrical surfaces with micro dimples pattern, (a) depth of 15  $\mu\text{m}$ , (b) depth of 8  $\mu\text{m}$

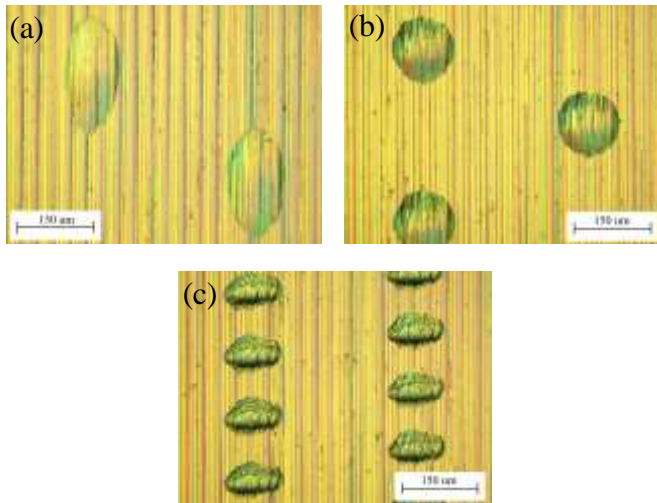


Fig. 3 The textured surfaces are established using various frequencies  $f_m$ , (a) 50 Hz, (b) 100 Hz, and (c) 260 Hz

### 3. Experimental Setup

The friction investigations are based on experimental studies. In these trials, block-on-ring friction test under oil lubrication were carried out over sliding rotation speeds ranging 100 rpm to about 1000 rpm. The constant normal load of 50 N was used. The commercial tribometer made by Hanmi Industries. Corp was used as shown in Fig. 4. The tribometer has limitation of the normal load is about 80 N and maximum rotational speed is 1500 rpm. The tribometer has constant control normal load, so the data of friction is considerably accurate. The detail of the tribology experimental setup

is shown in Table. 1. The engine oil of 5W-30 was used and the trials were conducted in room temperature is about 22°C.

Table 1: Summary description of the experimental setup

Micro dimple fabrication	
Vibration frequencies:	$f_m = 50 \text{ Hz} - 260 \text{ Hz}$ (Al 6061) using PCD tool $f_m = 50 \text{ Hz} - 200 \text{ Hz}$ (AISI 1045) using CBN tool
Sample dimension:	DIA = 25 mm (Al 6061) DIA = 27 mm (AISI 1045) Length = 45 mm Contact Length = 20 mm
Micro dimple dimensions:	Length = 60 $\mu\text{m} - 300 \mu\text{m}$ Width = 80 $\mu\text{m} - 120 \mu\text{m}$ Depth = 8 $\mu\text{m} - 15 \mu\text{m}$ Distribution = 12 dimples ( in 1.25 mm <sup>2</sup> area, depends on ratio vibration frequency and rotational speed) in this case $f_m = 120 \text{ Hz}$ and $N = 30 \text{ rpm}$
Tribology test	
Condition:	Block on ring test (wet lubrication)
Oil:	Engine oil 5W-30 ( $T = 22^\circ\text{C}$ ) ( $\mu = 0.0577 \text{ Pas}$ )
Normal load:	$F_N = 50 \text{ N}$
Sliding distance:	Distance = $\text{rpm} \times 10$
Rotational speed:	$\omega_N = 100 \text{ rpm to } 1000 \text{ rpm}$ (Al 6061) $\omega_N = 100 \text{ rpm to } 1500 \text{ rpm}$ (AISI 1045)

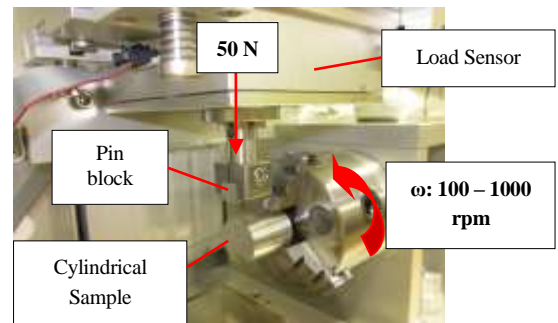


Fig. 4 The block-on-ring tribometer which was utilized in these trials

### 4. Experimental Results

Experiments have been conducted in various rotational speeds with constant load of 50 N. The friction trials of the Al 6061 contacts Al 6061 surface and AISI 1045 contact SKD11 surface are summarized.

The average CoF gradually decreases when the rotational speed increases, as shown in the experimental results. Typically, the friction reduction occurs in the lower speeds on two planar sliding contacts. Fundamentally, in the hydrodynamic lubrication regime occurs at the relative high speeds where the two solid surfaces are separated by the lubrication. Due to the textured surface, the micro dimple acts a micro poor that supplies lubricant so that the two contact surfaces separates and reduces friction. As the speed is increased, the hydrodynamic regime takes place, so the friction reduction becomes effective in this case.

In the Fig. 4, micro dimple whose depth of 8  $\mu\text{m}$  only reduces the friction at lower speeds, instead micro dimple whose depth of 15  $\mu\text{m}$  leads in higher speeds. Fig. 5 shows the average CoF comparison between un-textured and textured surfaces that have been made at various vibration frequencies ranges from 50 Hz to 260 Hz. This investigation shows that the textured surface at  $f_m = 260 \text{ Hz}$  has best performance, resulting up to 40 % efficiency. On the other hand, as shown in Fig. 6, the textured surface on the carbon steel made at  $f_m =$

ISGMA2014-P-A-09

50 Hz does not show any benefit in friction reduction. It is probably caused by the longer dimension (300  $\mu\text{m}$ ) compared to the contact area. In the Fig. 6, the micro dimple at  $f_m = 200$  Hz has no significant friction reduction, because characteristic of the textured shape is totally different compared to Al 6061 built at  $f_m$  260 Hz, the textured is relatively large and the micro dimple is close to each other, due to utilization of the CBN tool.

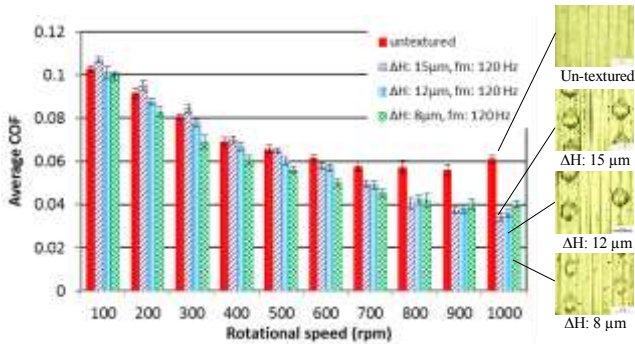


Fig. 4 Average CoF with various depths (Al 6061)

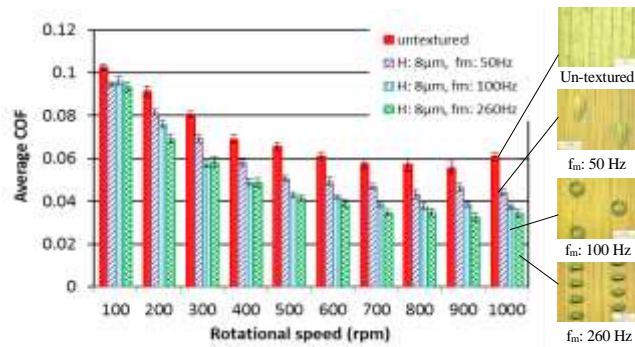


Fig. 5 Average CoF with various vibrational frequencies (Al 6061)

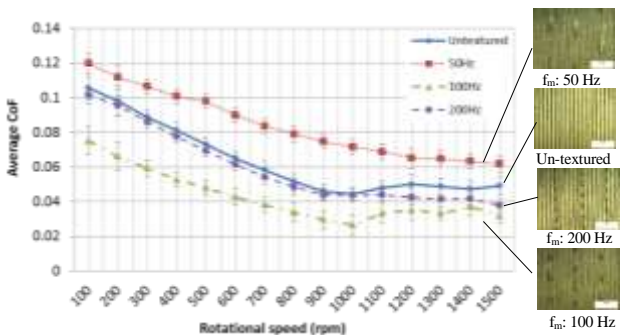


Fig. 6 Average CoF with various frequencies (AISI 1045)

### 5. Conclusions

In conclusion, according to the experimental results, the conclusion can be summarized as follows:

1. The textured surfaces on the cylindrical surface improve the lubrication performance in particular boundary regime as well as in the hydrodynamic regime. The experimental results show the evidence that the textured surfaces reduce the average CoF ranging from 20% to 40% in these trials.
2. Based on the experimental investigation, the micro dimples

which have a depth of 8  $\mu\text{m}$  gives the best performance. The depths lower than 8  $\mu\text{m}$  is also recommended.

3. By using the PTHA, the vibration frequency that is between 100 Hz to 300 Hz is recommended to be used in order to achieve a good lubrication performance. Then, the length of micro dimple in range 200  $\mu\text{m}$  to 60  $\mu\text{m}$  is recommended.

### ACKNOWLEDGEMENT

The author would like to thank to the Basic Science Research Program through the National Research Program through the National Research Foundation of Korea (NRF) funded by the Ministry of Education, Science and Technology (MEST) (Grant No. 2011-0013496) has supported this work.

### REFERENCES

1. Erdemir, A., "Review of engineered tribological interfaces for improved boundary lubrication," Tribology International, Vol. 38, No. 3, pp. 249–256, 2005.
2. Etsion, I., "State of the Art in Laser Surface Texturing," Journal of Tribology, Vol. 127, No. 1, pp. 248–253, 2005.
3. Yu, H., Wang, X., and Zhou, F., "Geometric Shape Effects of Surface Texture on the Generation of Hydrodynamic Pressure Between Conformal Contacting Surfaces," Tribology Letters, Vol. 37, No. 2, pp. 123–130, 2009.
4. Uehara, Y., Wakuda, M., Yamauchi, Y., Kanzaki, S., and Sakaguchi, S., "Tribological properties of dimpled silicon nitride under oil lubrication," Journal of the European Ceramic Society, Vol. 24, No. 2, pp. 369–373, 2004.
5. Kurniawan, R., and Ko, T. J., "A study of surface texturing using piezoelectric tool holder actuator on conventional CNC turning," International Journal of Precision Engineering and Manufacturing, Vol. 14, No. 2, pp. 199–206, 2013.

# Objective Quantification and Subjective Evaluation for the Fastening Force of Seat Belt in a Vehicle Using Seat Belt in a Vehicle Using Force Measurement Robot

Hye-young Cho<sup>#</sup> and Sang-kwon Lee<sup>1</sup>

<sup>1</sup> Acoustics and Vibration Signal Processing, Department of Mechanical Engineering, Inha University, 253 Yonghyun Dong, Nam-gu Incheon, South Korea, 402-752  
# Hye-young Cho / E-mail: aileen73248@naver.com, TEL: +82-32-860-8650

KEYWORDS : Seat Belt, Psychoacoustics, Human Sensibility Enrgonomics, Subjective Evaluation, Seat Belt Fastening Force Metrics

*Currently, researchers could rely on only a subjective evaluation by human sensitivity because there is no distinct standard for measurement or performance evaluation of vehicle seat belt tensioning force. Thus, there are large errors in evaluation test as well as the lack of a clear definition about seat belt fastening feeling and after seat belt performance evaluation of sensitivity test, when improve upon the belt system, it is problem that overall vehicle design and latest mold manufacturing costs. In this paper, an electronic device in the form of a robot for measurable quantitative seat belt fastening feeling was used, and using subjective rating, fastening force analysis with vehicle seat belt fastening force, velocity and angle data measured by robot, fastening feeling by subjective rating developed seat belt sensitivity metrics which is connecting the physical and sensory properties in order to define the sensitivity performance of seat belt fastening force. Using this evaluation system, measurement device and index of vehicle seat belt fastening force, we can get the quality of vehicle seat belt feeling more reasonably and authentically.*

## NOMENCLATURE

$a$  = Acceleration of the moving mass of the seat belt  
 $b$  = Width of the spring trip of retractor  
 $E$  = Modulus of elasticity in tension of retractor spring  
 $F$  = Force acting on the seat belt  
 $F_f$  = Friction force of seat belt  
 $F_h$  = Mean value of the dynamic force in the front half of fastening period  
 $F_i$  = Initial value of fastening force (static force)  
 $F_p$  = Fastening force of seat belt by pulling motion  
 $F_{peak}$  = Peak value of fastening force  
 $F_s$  = Spring force of seat belt retractor  
 $F_v$  = Variation of dynamic fastening force in the fastening period  
 $k$  = Torque spring rate  
 $L$  = Functional spring length of spiral spring of retractor  
 $m$  = Mass of the buckle and moving belt  
 $t$  = Thickness of spiral spring trip of retractor

$Y$  = Estimated subjective rate (value of index)

$\mu$  = Friction coefficient of webbing belt

$\Delta t$  = Seat belt fastening time period

$\Delta x$  = Displacement of buckle

## 1. Introduction

In the past, when design automobile, mainly improve the major performance of vehicle but, nowadays there has been conducted various noise and vibration reduction technology researches and the exterior and interior design for comfort and amenity of automobile is more and more important. In the design of automobile interior, the seat belt fastening quality needs to be research for improve because it also influences on comfort or discomfort of passengers. Up to now, however, the seat belt quality evaluation is only rely on a subjective feeling assessment by the person because there are no specified method criteria or approach for measure and evaluating fastening force of the seat belt system. With these subjective approaches, it is difficult to obtain accurate and reliable results so as the measured

value changes at each assessment, methods, evaluators and evaluation criteria, etc. Therefore, a seat belt fastening force to enhance the performance of a seat belt fastening force is determined on the objective and quantitative indicators of performance are needed. This assignment has the performance sensitivity of the seat belt fastening force are defined, and seat belt fastening force measure device for quantitative measurement of force development, and then the seat belt take-feeling evaluation made by using the apparatus evaluation fastening force is developed. In addition, the performance of the seat belt to define emotional fastening compacts, 4 economic size, 5 full size, 3 premium size and 6 sport utility vehicles(SUV) of various models of the fastening force of the belt on the subjective assessment of the sensitivity. The seat belt fastening elements of the measured quality of objective and the seat belt fastening force index is produced by subjective evaluation results of the correlation between the sensitivity of analysis using multiple linear regression analysis.

**2. Objective Research**

**2.1 Measurement System (Design of Robot)**

Before designing the specific robot for the measurement of fastening force, the professional design engineer tests the moving trajectory of seat belt by fastening the seat belt as shown in Fig. 1 and determines the moving trajectory of a robot. The moving trajectory of driver's arm becomes the trajectory of the robot arm. The robot is designed to move along the trajectory.

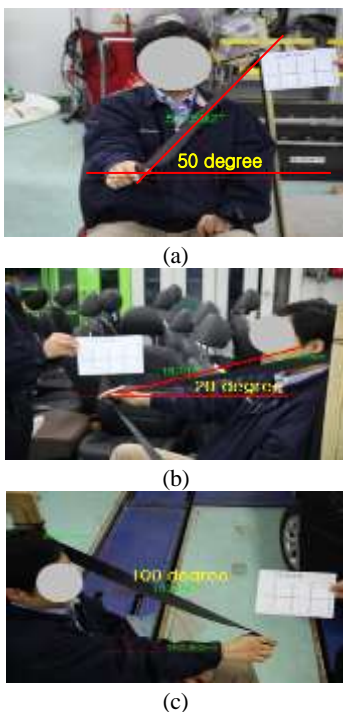


Fig. 1 Moving trajectory of the seat belt when a driver pulls the seat belt

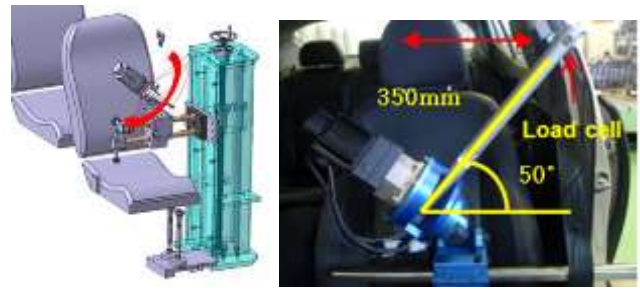


Fig. 2 Virtual drawing of the robot and its moving trajectory when it pulls the seat belt

Fig. 2 shows the robot installed at the car to measure the fastening force and the virtual drawing of robot. When it pulls the seat belt, the load cell, which is attached on the arm of robot, measures the tension force.

**2.2 Experimental Procedures**

The robot is designed to pulls the buckle of a seat belt with constant speed. Before fastening the belt, the initial static force due to the spring of retractor in the seat belt system is measured throughout the load cell as shown in Fig. 3.

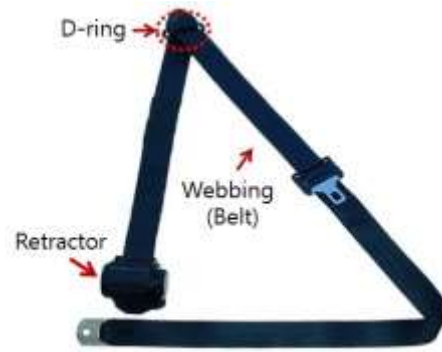


Fig. 3 Seat belt system in a passenger car

During the robot operates and moves along the trajectory with constant speed, the fastening force is changed dynamically depending on the friction force between webbing belt and D-ring and the spring force in the retractor.

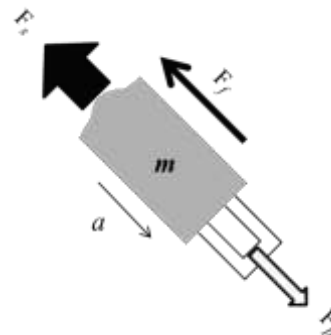


Fig. 4 Free body diagram about the acting force when a seat belt is pulled by a robot.

Fig. 4 shows the free body diagram about the force exciting the seat belt when the buckle of seat belt is pulled by the robot. By utilizing the free body diagram, the dynamic equation for the fastening force is given by

$$\sum F = F_p - F_f - F_s = ma \tag{1}$$

where  $m$  is the mass of the buckle and moving belt. The friction between webbing belt and D-ring yields the friction force  $F_f$  and the spring force  $F_s$  is linearly proportion to the turn of the spring coil of the retractor. The only friction force  $F_f$  and the spring force  $F_s$  influence the fastening force  $F_p$  because the acceleration  $a$  of the moving mass of the seat belt is zero when the moving speed of the robot arm is constant.

### 2.3 Measurement Results

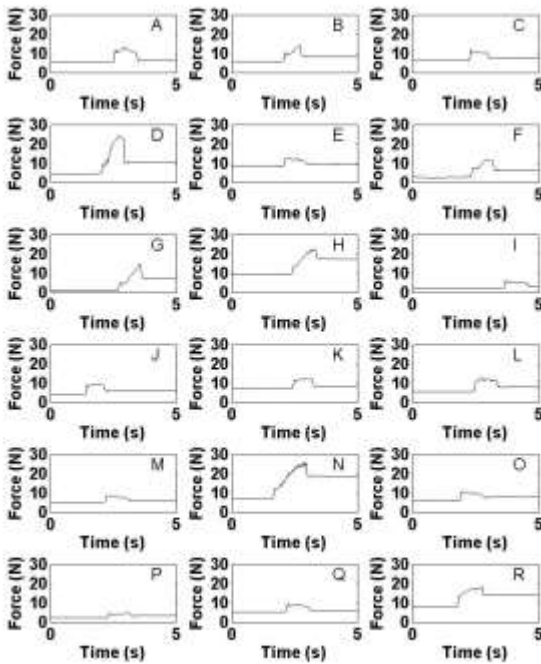


Fig. 5 Time histories of fastening forces measured by the robot when the seat belts are pulled by a robot.

Fig. 5 shows the fastening forces of seat belt measured by the load cell of the robot. The number of test vehicle is eighteen. The seat belts used for this test are the existing seat belts inside of test vehicles. There are 4 types of vehicles such as economic size type, full size type, premium type and SUV type. The fastening forces of 4 economic size passenger cars are plotted as shown Fig. 5 (A) to Fig 5(D), those of 5 full size passenger cars are plotted as shown Fig. 5 (E) to Fig 5(I), those of 3 premium size passenger cars are plotted as shown Fig. 5 (J) to Fig 5(L) and those of 6 SUVs are presented as shown Fig. 5 (M) to Fig 5(R). According to these results, the time histories of fastening forces are different all together. There is no relationship between the shape of time history of fastening force and vehicle type.

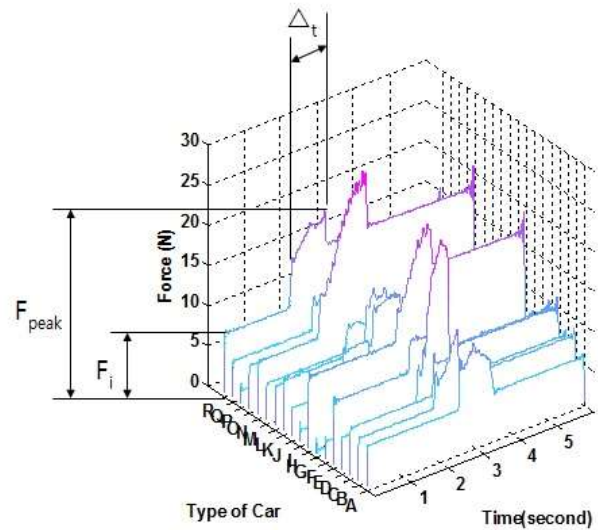


Fig. 6 The waterfall plot for the fastening forces measured from the seat belts of 18 vehicles

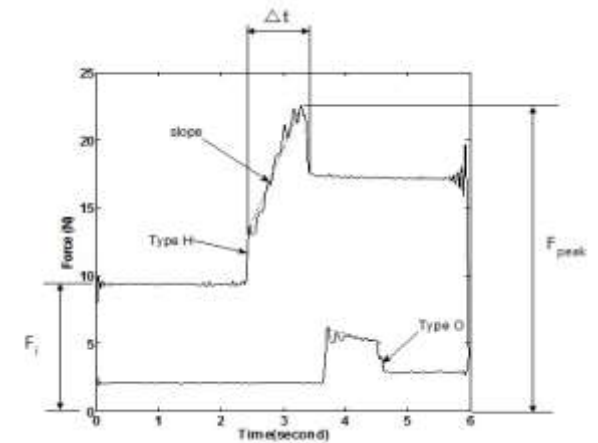


Fig. 7 Four physical quantifications for the fastening forces measured from the seat belts of two sample vehicles

Fig. 6 shows the waterfall plot for the time history of 18 fastening forces. Fig. 7 shows the time history of fastening force for two seat belts as an example. One is the seat belt of type H vehicle and the other one is the seat belt of type O vehicle. The peak value of fastening force  $F_{peak}$ , the initial value of fastening force  $F_i$  of fastening force (static force), the variation of dynamic fastening force  $F_v$  in the region of time period  $\Delta t$  and the mean value of fastening force  $F_h$  of the dynamic force in the front half region of time period  $\Delta t$  are different for 18 fastening forces.

At the start point of the moving belt, the fastening force is the initial vale  $F_i$  of fastening force. This is related to the spring force of retractor. The spring force is related to the turn of spring coil. The turn of the spring coil is changed when the seat belt is pulled by a robot. Therefore, the peak value of the fastening force is also changed. It is inferred that the variation of fastening force in the region of time  $\Delta t$  caused by the change of friction force and the vibration of spring in the retractor. Therefore, the variation  $F_v$  of dynamic fastening force in region of time period  $\Delta t$  is occurred. These four physical quantifications are used for the force metrics to measure the emotional feeling objectively in this paper.

### 3. Subjective Research

**3.1 Participants and Vehicles**

Forty-one healthy subjects, twenty-one males and twenty female participated in the subjective evaluation about emotional feeling of fastening force of the seat belt. Their mean height was 1.65(1.58~1.78) m and their age was 41(25~50) years old. The seat belts of the existing seats from 18 vehicles are used for the subjective evaluation.

**3.2 Set Up**

The test vehicles are parked at the parking area in the wide open place. All participants received a short introduction before the actual test is done to explain what they need to do. It is not allowed for the participant to adjust the seat. All seat belts are tested for approximately 2 hour and participant moves to car by car and seats the car seat of the test vehicles as shown in Fig. 8



Fig. 8 Photography of a participant evaluating the emotional feeling of the fastening force subjectively

Table. 1 Seven step scale anchored at nine opposite attributes

	-3	-2	-1	0	1	2	3	
Uncomfortable	<input type="checkbox"/>	Comfortable						
Cheap	<input type="checkbox"/>	Luxurious						
Rough	<input type="checkbox"/>	Smooth						
Unnatural	<input type="checkbox"/>	Natural						

They pull the seat belt the moving trajectory as shown in Fig. 1. Participants have to rate the emotional feeling for fastening force of seat belts. The four opposite attributes such comfortable, luxurious, smooth, natural are given for the questionnaires about the emotional feeling. Participants also have to rate the emotional feeling for fastening force of seat belt as point scale (for example -3= rough bad, +3= smooth) as listed Table. 1. The information obtained from the questionnaire is tested to find if there is a significant relation between the force metrics measured by the robot and the subjective rating about four questionnaires.

**3.3 Results of Subjective Evaluation**

Fig. 9(a) shows the result of the subjective evaluation about the emotional feeling of the fastening force of seat belt of the economic size vehicles. There is a clear different of the subjective rating in the economic type vehicles. The seat belt of type B car scores high subjective rating. The seat belt of type D scores low subjective rating for 4 questionnaires as shown Fig. 9(a). Form Fig. 5, we find the difference of the time history of fastening force for both type of vehicles. For the full size vehicles, the seat belt of type G car scores high subjective rating as shown in Fig. 9(b). For the luxury car, the seat belt of type J car scores high subjective rating as shown in Fig.

9(c). For the SUV, the seat belt of type P car scores high subjective rating as shown in Fig. 9(d).

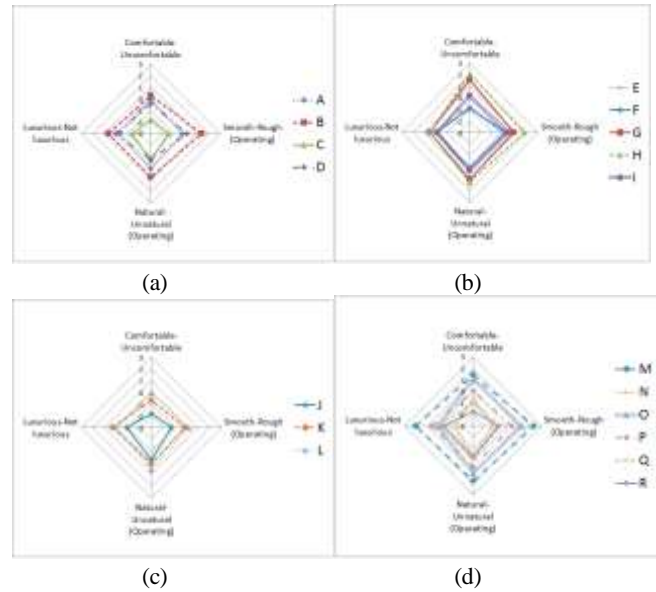


Fig. 9 Radial diagram for the subjective rating of four attributes of emotional feeling for the fastening force of a seat belt

The seat belt with good emotional feeling acquires high scored subjective rating for all 4 attributes. The factor analysis is used to reduce the dimensionality of the data set. Principal component analysis is used to extract the factors. From this factor analysis, one dominant factor is determined. The “Smooth” is selected as the major factor for emotional feeling of the fastening force of the seat belt. The seat belt of G type scores the highest subjective rating for the emotional feeling as shown Fig. 10.

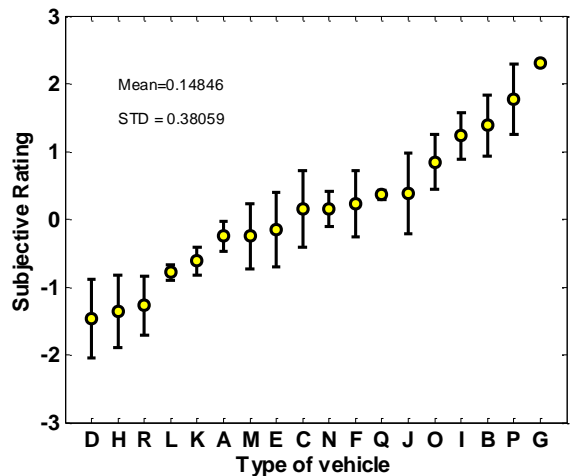


Fig. 10 Subjective rating for the emotional feeling of the fastening forcing of the seat belt of 18 vehicles

The time history of measured fastening force of this seat belt is plotted as shown in Fig. 5. It has almost zero static fastening force at start point.

**4. Development of Fastening Force Index of the Seat Belt**

ISGMA2014-P-D-17

The fastening force of seat belt is measured by using a special robot and the subjective evaluation for the fastening force is performed. This section is studied on the development of fastening force index which is used to estimate the subjective rating about the emotional feeling of the fastening force. This index is made by using four physical quantifications as discussed in section 2.3. Firstly the correlation between four physical quantifications and subjective rating is obtained as shown in Fig. 11.

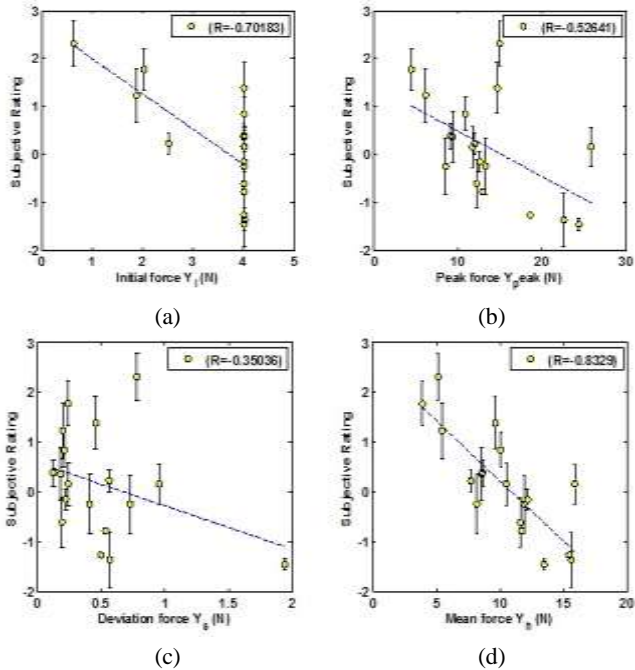


Fig. 11 Correlation between four physical quantifications and subjective rating for the emotional feeling of the fastening forcing of the seat belt of 18 vehicles

The correlation coefficient of initial force with subjective ration is significant as shown in Fig. 11(a). However the subjective rating is scattered at one the initial force of 4N. Peak force and the variation of dynamic fastening force are not correlated with the subjective rating as shown in Fig. 11 (a) and Fig. 11(b). The mean value of the dynamic force is significantly correlated with the subjective rating as shown in Fig. 11 (d). The correlation between four physical quantifications and subjective ratio are listed in the Table 2 and 3 in detail.

Table. 2 Subjective rating value for “smooth-rough” query pair of each vehicle type

Car Type	Classification	Mean Value	Standard Deviation
A	Economic Size	-0.25	0.2242
B		1.38	0.4461
C		0.15	0.5595
D		-1.46	0.5824
E	Full Size	-0.15	0.55
F		0.23	0.4867
G		2.31	0.0216
H		-1.36	0.5316
I		1.23	0.3491
J	Premium Size	0.38	0.5951

K	Sport Utility Vehicle	-0.62	0.203
L		-0.79	0.1197
M		-0.25	0.479
N		0.15	0.2613
O		0.85	0.4099
P		1.77	0.5245
Q		0.36	0.0714
R		-1.27	0.4355

Table.3 Subjective rating for “smooth-rough” query pair and four physical quantifications of fastening force of the seat belt of 18 vehicles

Car Type	Initial Force $F_i$ (N)	Peak Force $F_{peak}$ (N)	Force Variation $F_v$ (N)	Mean Force $F_h$ (N)
A	4.0032	13.32	0.73	11.88
B	4.0061	14.65	0.46	9.63
C	4.0052	11.71	0.24	10.48
D	4.0092	24.44	1.94	13.49
E	4.0079	12.62	0.22	12.17
F	2.5126	11.99	0.56	7.71
G	0.6277	15.00	0.78	5.14
H	4.0187	22.62	0.57	15.58
I	1.8758	6.20	0.20	5.46
J	4.0025	9.11	0.12	8.64
K	4.0058	12.21	0.20	11.59
L	4.0052	12.94	0.54	11.7
M	4.0025	8.53	0.41	12.42
N	4.0206	25.88	0.96	15.9
O	4.0051	10.84	0.21	10.09
P	2.0257	4.41	0.24	3.94
Q	4.0025	9.35	0.18	8.578
R	4.0142	18.57	0.50	15.46
Correlation With Mean Value	R=0.71 p=0.0012	R=0.53 P=0.0248	R=0.35 P=0.1540	R=0.83 P=0.0001

Therefore, the mean force  $F_h$  is selected as the force metric. This force metric is used to development of the fastening force index. By utilizing the linear regress method, the fastening force index is obtained and is given by

$$Y = 2.7987 - 0.2519 \times F_h \tag{2}$$

where  $F_h$  is the mean value of the dynamic force in the front half region of time period  $\Delta t$  as shown in Fig. 7. Fig. 12 shows the correlation between the estimated subjective rating and the subjective rating. The estimated subjective rating is obtained by inserting the value of mean force  $F_h$  into Eq.(2). The correlation is significant ( $R=0.83, p=0$ ).

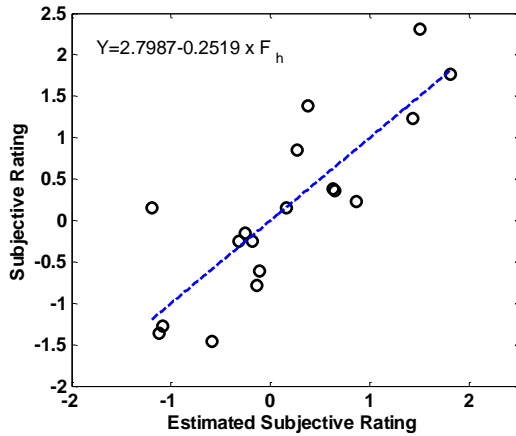


Fig. 12 Correlation between subjective rating and estimated subjective rating of 18 vehicles

### 5. Influence of Seat Belt Components on the Fastening Force of Seat Belt

#### 5.1 Influence of Seat Belt Components

There are four major components in the seat belt such as D-ring, buckle, webbing belt and retractor as shown in Fig. 3. The governing equation for the movement of seat belt is given in Eq.(1). The spring force  $F_s$  is linearly proportion to the displacement of buckle  $\Delta x$  and the spring stiffness  $k$  which is given by

$$F_s = k\Delta x \text{ and } k = \frac{\pi \cdot E \cdot b \cdot t^3}{2160 \cdot L} \quad (3)$$

where  $E$  is Young's modulus of spring material,  $b$  is the width of the spring plate,  $t$  is the thickness of the spring plate and  $L$  is the length of spring plate. The length of spring plate is also related to the turn of the spring coil of the retractor. The friction between webbing belt and D-ring influence the friction force  $F_f$ . The friction coefficient  $\mu$  of the webbing belt changed depending on the materials of webbing belt and the coating method of D-ring.

#### 5.2 Modified of Seat Belt Components



Fig. 13 Seat belt component for 6 seat belt samples used for the improvement test of the emotional feeling about the fastening force of a seat belt

Table.3 Representative Query of Fastening Force; Smooth-Rough

Test No.	D-ring	Number of coils (turns)	Subjective Rating	Standard deviation	Mean force $F_h$ (N)
1	Chrome	18	-1.01	0.58	12.95
2		20	-0.04	0.53	12.71
3		22	-1.30	0.44	14.31
4	Full Metal	18	0.89	0.12	8.16
5		20	0.25	0.20	9.93
6		22	0.17	0.34	10.28

For the improvement of the subjective feeling of the fastening force, the spring force and the friction force should be are modified. In the paper, in order to change the friction force, the coating of D-ring is changed from chrome to metal. The number of turn of the spring coil of retractor is changed for the change of the spring force. The detail modification of the component is listed in the Table.3. Two types of D-ring and three different number of turn of spring coil of the retractor are prepared and their specifications are listed in the table.3. Fig. 13 shows the 6 seat belt with modified component. These samples are applied to the seat belt of M type car.

#### 5.3 Measurement of Fastening Force and Subjective Evaluation for the Modified Components

Total 6 samples are prepared for the improvement test of subjective feeling for the fastening force of seat belt. The fastening forces of 6 samples are also measured by the load cell of the robot. These are measured at the period when the fastening forces of the seat belts of 18 test vehicles are measured. The subject evaluation of the fastening force is also performed at the period when the subjective evaluation of the fastening forces of the seat belts of 18 test vehicles is performed.

#### 5.4 Results

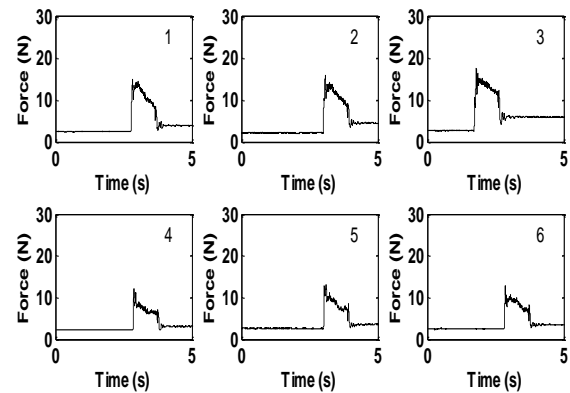


Fig. 14 Time histories for fastening forces of 6 sample seat belts measured by the robot

Fig. 14 shows the measured fastening force when the 6 samples of seat belts are applied to the Type M car. The shapes of dynamic fastening forces are changed. The mean force  $F_h$  of each sample is different one another. The correlation between subject rating and the mean force  $F_h$  is also obtained and plotted as shown in Fig. 15.

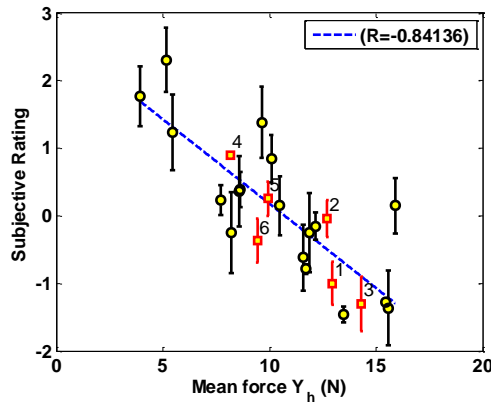


Fig. 15 Correlation between physical quantifications and subjective rating for the emotional feeling of the fastening forcing of the seat belt of 18 vehicles and 6 samples

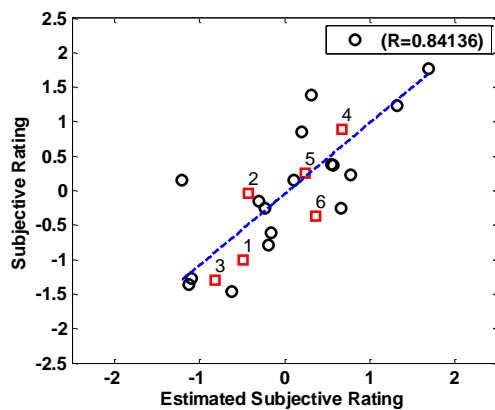


Fig. 16 Correlation between subjective rating and estimated subjective rating of 18 vehicles and 6 samples

The circular marks are related to the 18 test vehicles. The rectangular marks are related to the 6 sample. Fig. 16 shows the correlation between estimated subjective rating and subjective rating. The subjective ratings of the sample No. 4 and No. 5 score higher value than that of the original seat belt attached to the Type M car. The subjective rating sample No. 6 is underestimated because the friction force is reduced by changing the coating material from chrome to metal but the spring force is increased because the turn of spring coil is increased from 18 to 22. Both forces should be trade off.

## 6. Conclusion

In order to development of the objective evaluation method of the emotional feeling of the fastening force of seat belts in the vehicles, the fastening force index is developed. The specific robot designed and manufactured. The robot pulls the seat belt of 18 test vehicles with constant speed. The load cell attached on the robot measured the fastening force. It is found that the mean value of the fastening force is related to the emotional feeling. The subjective evaluation for the emotional feeling of the fastening force of seat belts of 18 test vehicles is performed. Four opposite attributes are used for the questionnaire about emotional feeling. The smooth – rough is selected as a major factor in the paper throughout factor analysis. The subjective rating for the major factor is correlated to the mean value

of the fastening force. The sound index is developed throughout the linear regression for the subjective rating and the mean value of the fastening force. The subjective rating is proportion to the  $1/F_h$ .  $F_h$  is the mean of fastening force. The fastening force depends on the spring force of retractor and the friction force of the seat belt system. The six modified seat belts are prepared for the improvement of the subjective rating. For the change of the friction force, the coating of D-ring is changed from chrome to metal. The turn of spring coil in the retractor is adjusted. The metal coating of D-ring reduces friction force and the low turns of spring coil reduced the spring force. This sample improved the subjective rating of fastening force. The developed index is used for the objective evaluation of the emotional feeling about the fastening force of a seat belt throughout the modification of seat belt components.

## ACKNOWLEDGEMENT

This work was supported by Mid-career Researcher Program through NRF grant funded by the MEST (No. 2010-0014260)

## REFERENCES

1. Sasaki, K., Hosaka, H., Itoh, M., Ishida, K., Ito, A., "A Seat Belt Vibration as a Stimulating Device for Awakening Drivers." IEEE/ASME Transactions on Mechatronics, Vol. 12, No. 5 pp. 511-518, 2007.
2. M. Kolich, N. Seal, S. Taboun, "Automobile Seat Comfort Prediction : Statistical Model vs. Artificial Neural Network" Applied Ergonomics 35, pp.275-284,2004.
3. N. Otto, "Listening Test Methods for Automotive Sound Quality", 103<sup>rd</sup> Audio Engineering Society Convention, 2006.
4. Myers, Raymond H., "Classical and Modern Regression with Applications", Duxbury Resource Center, 1986.

# Effect of $Mg_3AlNi_2$ Content on the Cycling Stability of $Mg_2Ni$ - $Mg_3AlNi_2$ Hydrogen Storage Alloy Electrodes

Sheng-Long Lee<sup>1#</sup>, Yu-Chih Tzeng<sup>1</sup> and Hui-Yun Bor<sup>2</sup>

<sup>1</sup>Depart. of Mech. Eng. & Institute of Materials Sci. and Eng. National Central University, Zhongli, Taiwan  
<sup>2</sup> Materials and Electro-Optics Research Division, Chung-Sheng Institute of Sci. & Tech., Taoyuan, Taiwan  
# Corresponding Author / E-mail:shenglon@cc.ncu.edu.tw, TEL: + 886-3-4267325

KEYWORDS :  $Mg_2Ni$ - $Mg_3AlNi_2$  electrode alloys; Isothermal evaporation casting process; Electrochemical properties

*The new composites  $Mg_2Ni$ - $x$  mol%  $Mg_3AlNi_2$  ( $x = 0, 15, 30, 60, 100$ ) were prepared by means of combining electric resistance melting with isothermal evaporation casting process (IECP). Results show that the cycling stability of the alloy electrode with  $Mg_3AlNi_2$  is superior to that of  $Mg_2Ni$ . XPS analysis revealed that the formation of an Al oxide film during cycling could enhance the anti-corrosion of the surface of the composites. Among the obtained capacity retaining rates,  $Mg_2Ni$ -15 mol%  $Mg_3AlNi_2$  composite had the best anti-corrosion performance. The improvement of the cycling stability of the electrode alloy with 15 mol%  $Mg_3AlNi_2$  can be ascribed to the decrease in the rate of pulverization of the alloy during cycling, leading to retard the corrosion reaction against the alloy surface due to the formation of a dense  $Al_2O_3$  film, which is considered as the factor in the improvement of the cycling discharge-ability of the  $Mg_2Ni$ - $Mg_3AlNi_2$ -based electrode alloys.*

## 1. Introduction

As the negative electrode materials of nickel-metal hydride (Ni-MH) batteries,  $Mg_2Ni$ -based hydride materials have been investigated extensively due to their high theoretical discharge capacity, low cost and light weight [1]. In the recent years, most studies clearly demonstrated that element substitution was regarded as one of the most effective ways to retard the corrosion of Mg in alkaline solution and thus enhance the discharge capacity [2-5]. It was reported that the partial substitution of Al for Mg in  $Mg_2Ni$ -based alloys was able to maintain a high discharge capacity [4-5]. The addition of Al to  $Mg_2Ni$  leads to the formation of  $Al_2O_3$  on the surface of the alloy to prevent the host alloy from the corrosion of alkaline solution. Nevertheless, it was found that the cycling capacity degradation needs still to be improved further to satisfy the practical applications.

Numerous studies have reported an improvement of the cycling stability of composite electrode materials composed of the different metal hydride phases [6-8]. In our previous work, we have studied the effect of  $Mg_3MnNi_2$  on the electrochemical characteristics of  $Mg_2Ni$  alloy and found that the cycling stability of the  $Mg_2Ni$ - $x$  mol%  $Mg_3MnNi_2$  ( $x = 0, 15, 30, 60, 100$ ) was markedly enhanced with the increase of  $Mg_3MnNi_2$  content [9,10]. In addition, the innovative

method could be applied to produce the various proportions of  $Mg_3MnNi_2$  through adding Mn element.

To date, all of these investigations have concentrated only on improving the discharge capacity of  $Mg_2Ni$  alloy through the substitution of Al for Mg [4, 7, 9]. There seems to have been only a few publications on the capacity retardation rate of  $Mg_2Ni$ -based alloys with the appropriate Al content [11]. Consequently, the investigation for clarifying the degradation behavior of the composites  $Mg_2Ni$ - $Mg_3AlNi_2$  is necessary. The effects of  $Mg_3AlNi_2$  content on their structure and electrochemical properties of the composites were investigated. The surface micrographs and chemical compositions of the composites were analyzed by the scanning electron microscopy (SEM) and X-ray photoelectron spectroscopy (XPS).

## 2. Experimental

$Mg_2Ni$ - $x$  mol%  $Mg_3AlNi_2$  ( $x = 0, 15, 30, 60, 100$ ) alloys were synthesized by the method combining electric resistance melting with IECP. The mixture of Mg bulk, Al powder and Ni powder was put into a stainless steel crucible under the protection of argon

atmosphere. The concept and the procedure to prepare the composites have been discussed in [9]. The phase structure and composition of the prepared samples were measured by means of XRD and EPMA analyses. The morphology of the particle surface was observed and compared by SEM. In investigating the surface state of the electrode, XPS measurements were conducted on a Thermo-Sigma type spectrometer at 10<sup>-8</sup> torr using Al K $\alpha$  radiation. In order to study the element distribution profiles on the alloy surface after cycle life testing, XPS depth profiles were examined. The alloy surface was sputtered with Ar<sup>+</sup> ions at 3.0 keV and a rate of ca. 1.0 Ås<sup>-1</sup>.

The charge-discharge measurements were performed with a Neware battery test system as reported in our previous work [9]. The cyclic voltammetry (CV) curves were measured with a CH/600C instrument. The scan rate of CV measurement was 1 mVs<sup>-1</sup> and the scan range was between -1.1 V and -0.35 V.

### 3. Results and Discussion

#### 3.1 The microstructure of the as-cast alloys

The XRD patterns of the composites MAN<sub>x</sub> (*x* represents Mg<sub>3</sub>AlNi<sub>2</sub> content in the composite alloy) are shown in Fig. 1. The result shows that the phase of MAN<sub>0</sub> alloy is Mg<sub>2</sub>Ni with hexagonal structure in Fig. 1(a). The new phase in the MAN<sub>15</sub> alloy is Mg<sub>3</sub>AlNi<sub>2</sub>, which possesses the cubic structure [12]. With increasing Mg<sub>3</sub>AlNi<sub>2</sub> contents, the diffraction peak intensity of the new phase gradually increases. It was found that only single phase Mg<sub>3</sub>AlNi<sub>2</sub> was formed in the MAN<sub>100</sub> alloy according to the multiphase Rietveld analysis [12].

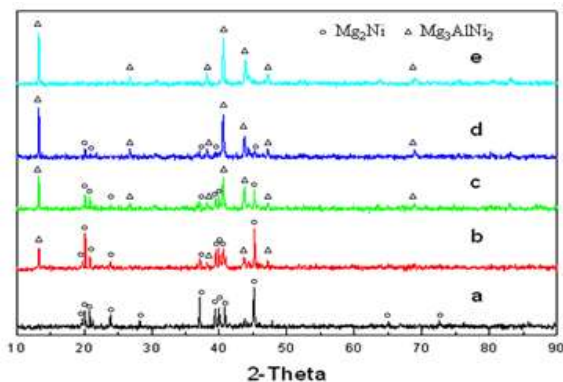


Fig. 1 XRD patterns of the as-cast alloys: (a)MAN<sub>0</sub>, (b)MAN<sub>15</sub>, (c)MAN<sub>30</sub>, (d)MAN<sub>60</sub> and (e)MAN<sub>100</sub>.

Fig. 2 displays the microstructure of the composites MAN<sub>x</sub> by SEM. It can be seen that the MAN<sub>15</sub>, MAN<sub>30</sub> and MAN<sub>60</sub> alloys display Mg<sub>2</sub>Ni phase with a near atomic ratio of 67.1Mg and 32.9Ni, and Mg<sub>3</sub>AlNi<sub>2</sub> phase with a similar atomic ratio of 51.0Mg, 32.2Ni and 16.8Al appears in Fig. 2(a)-(d). The morphology of the MAN<sub>x</sub> alloys consists of phases and deep holes, which mean that the loss of Mg during the IECP. With *x* increasing, the surface morphology of

the Mg<sub>3</sub>AlNi<sub>2</sub> phase turns gradually from fine (*x* = 15, 30) to massive (*x* = 60, 100), and the large shape of Mg<sub>2</sub>Ni phase becomes smaller.

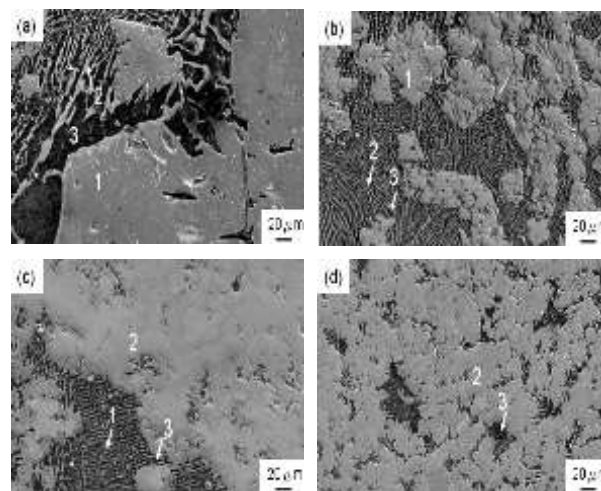


Fig. 2 SEM images of the as-cast alloys: (a)MAN<sub>15</sub>, (b)MAN<sub>30</sub>, (c)MAN<sub>60</sub> and (d)MAN<sub>100</sub>. (1: Mg<sub>2</sub>Ni, 2: Mg<sub>3</sub>AlNi<sub>2</sub>, 3: porosity)

#### 3.2 Discharge performance

Fig. 3 shows discharge capacities at 25 °C as a function of cycle number for MAN<sub>x</sub> electrode alloys. The electrode alloys MAN<sub>x</sub> (0 ≤ *x* ≤ 100) reach their maximum discharge capacity after 1-11 cycles. The discharge capacity of the electrode alloys gradually increases with the rise in Mg<sub>3</sub>AlNi<sub>2</sub> content. When the phase ratio of Mg<sub>3</sub>AlNi<sub>2</sub> reaches *x* = 100, the maximum discharge capacity of the MAN<sub>100</sub> alloy is 110 mAhg<sup>-1</sup>, which is higher than that of the MAN<sub>0</sub> alloy (20 mAhg<sup>-1</sup>). It means that the additional Mg<sub>3</sub>AlNi<sub>2</sub> helped to improve the discharge capacity of the electrode alloys.

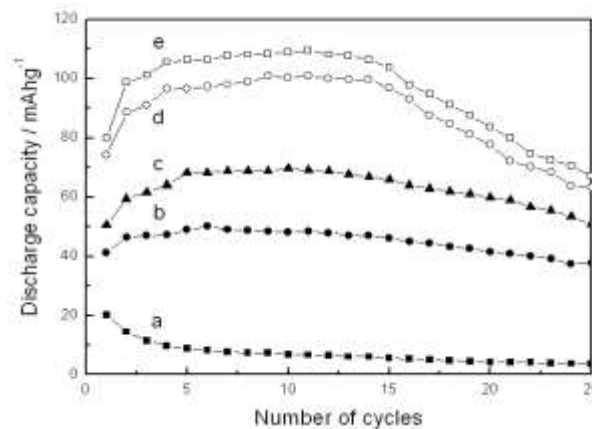


Fig. 3 Discharge capacity as a function of the number of cycles of the as-cast alloys: (a)MAN<sub>0</sub>, (b)MAN<sub>15</sub>, (c)MAN<sub>30</sub>, (d)MAN<sub>60</sub> and (e)MAN<sub>100</sub>.

The cyclic stability of MAN<sub>x</sub> (0 ≤ *x* ≤ 100) alloys can be evaluated by observing the discharge capacity retention rates, C<sub>25</sub>/C<sub>max</sub> × 100%, of the electrode alloys listed in Table 1. In this relationship C<sub>25</sub> represents the discharge capacity at 25th cycle and C<sub>max</sub> represents the maximum discharge capacity. MAN<sub>0</sub> alloy can

ISGMA2014-P-E-10

only maintain about 20% of its maximum discharge capacity (20 mAhg<sup>-1</sup>) at 25th cycle. While the Mg<sub>3</sub>AlNi<sub>2</sub> phase is an addition to the alloys, it causes a rise in the discharge capacity retention rates of the electrode alloys. Among the Mg<sub>3</sub>AlNi<sub>2</sub>-including alloys, MAN100 alloy has a maximum discharge capacity (110 mAhg<sup>-1</sup>), it is keeping about 61% of the storage capacity at 25th cycle. Although MAN15 alloy presents the lower maximum discharge capacity (50 mAhg<sup>-1</sup>), it can still preserve 76% of the storage capacity at 25th cycle. It is obvious that the Mg<sub>3</sub>AlNi<sub>2</sub> phase has an effect upon the rapid degradation of discharge capacity of Mg<sub>2</sub>Ni phase during the charge/discharge cycles. It is generally accepted that the rapid capacity degradation of Mg<sub>2</sub>Ni alloy with cycling in alkaline solution is attributed to the formation of Mg(OH)<sub>2</sub> film on its particle surface to inhibit the hydrogen diffusion and the charge transfer reaction [1-5]. While the presence of Mg<sub>3</sub>AlNi<sub>2</sub> phase in the composite alloys decreases the stability of Mg(OH)<sub>2</sub> formation and improves the hydrogen diffusion reaction, the change in the surface layer of the alloy investigated by XPS is proved that Al<sub>2</sub>O<sub>3</sub> can form a passive film for retarding oxidation reaction of the alloy. However, the appearance causes a progressive decrease in the cycle life with the increment of Mg<sub>3</sub>AlNi<sub>2</sub> phase. The morphologies of the MAN<sub>x</sub> (x = 15, 100) alloys before and after electrochemical charge/discharge cycling are observed by SEM as Fig. 4 shows. It can be seen that the alloy particles are pulverized with cycling due to the cell volume expansion and contraction during hydrogenation and dehydrogenation. The pulverization of the alloy leads to large amount of cracks and the particle surface morphology for each alloy changes from smooth to rough with cycling due to the oxidization of the active components of the alloys. For two alloys after cycling, the particle size of the MAN15 alloy is larger than the MAN100 alloy, which reveals that the partial substitution of Mg<sub>3</sub>AlNi<sub>2</sub> decreases the rate of pulverization. In addition, the white and loose oxides are appeared on the MAN100 alloy surface (Fig. 4(d)), but the gray alloy matrix can be clearly observed for the MAN15 alloy as shown in Fig. 4(b). It is suggested that MAN15 was useful to retard the formation of corrosive reaction against the alloy surface in the alkaline solution and enhance the cyclic discharge stability.

Table1 The cyclic stability of the as-cast MANX (0 ≤ X ≤ 100) alloys

Alloys	C <sub>max</sub> <sup>a</sup> (mAhg <sup>-1</sup> )	C <sub>25</sub> <sup>b</sup> (mAhg <sup>-1</sup> )	C <sub>25</sub> /C <sub>max</sub> (%)
MAN0	20	4	20.0
MAN15	50	38	76.0
MAN30	70	51	72.85
MAN60	101	63	62.37
MAN100	110	67	60.9

a The maximum discharge capacities of the alloy.

b The discharge capacities of the alloy at the 25th cycle.

Fig. 5 exhibits the cyclic voltammograms curves of the MAN<sub>x</sub> electrode alloys in the electrolyte (6M KOH + 1 wt% LiOH) at room temperature. It can be seen from Fig. 5 that the anodic / cathodic peak (-0.85V / -1.0V) current of the electrode alloys gradually increases with the rise of Mg<sub>3</sub>AlNi<sub>2</sub> content. It demonstrated that Mg<sub>3</sub>AlNi<sub>2</sub> promoted the reduction of hydrogen and the absorption of hydrogen on the electrode surface. The surface modification of the electrode alloys gives an obvious increase in the current density and area of the anodic peak. This revealed that Mg<sub>3</sub>AlNi<sub>2</sub> could improve the oxidation activity, which helped to improve the discharge capacity of the electrode alloys.

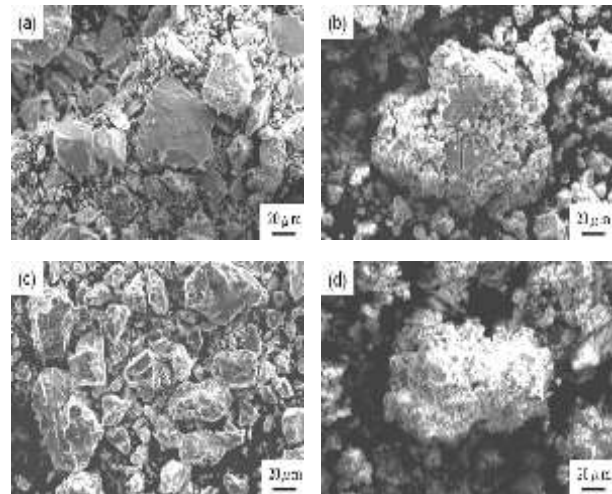


Fig. 4 SEM micrographs of the MAN<sub>x</sub> (x = 15, 100) alloys before and after cycling (x = 15 : (a) as-cast, (b) after 25 cycles ; x = 100 : (c) as-cast, (d) after 25 cycles).

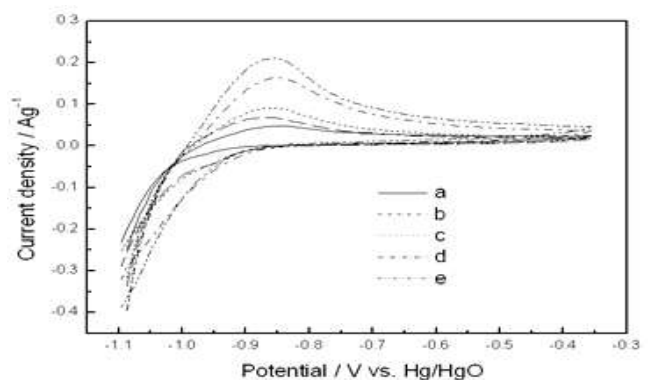


Fig. 5 Cyclic voltammograms curves for the as-cast alloys: (a)MAN0, (b)MAN15, (c)MAN30, (d)MAN60 and (e)MAN100.

### 3.2 Surface analysis

In order to further investigate the effect upon the improvement in the electrochemical characteristics, the distribution of elements in depth of the electrode alloys surface layer during charge-discharge cycles is performed using XPS measurements. Fig. 6 shows depth profiles of constituent distribution of the MAN $x$  ( $x = 0, 100$ ) alloys after 5 charge-discharge cycles. For the alloy with  $x = 0$ , it can be seen that oxygen content is ca. 54 at.% on the alloy surface and constantly starts to reduce until a saturated high content of ca. 38 at.%. The high oxygen content may be ascribed to the thick oxidized layer was formed on the surface of the MAN0 alloy in alkaline solution. It is generally known that the rapid capacity degradation of Mg<sub>2</sub>Ni alloy results from Mg is easily corroded to Mg(OH)<sub>2</sub> by reacting with KOH electrolyte [1-5]. The surface layer oxidized of the MAN100 alloy becomes thinner during charge-discharge cycling as can be seen in Fig. 6(b).

This phenomenon implies that the oxidation of the MAN100 alloy surface is effectively inhibited. To clarify the reason on the surface characteristics of the alloy, XPS spectra of constituent elements of the alloy was carried out before and after cycling. Fig. 7 shows the spectra of Mg<sub>2p</sub>, Al<sub>2p</sub> and Ni<sub>2p</sub> of the MAN100 alloy electrode. It can be judged from the peak position that the elements of Mg and Ni on the surface of the as-cast alloy are in the oxidized state as the result of exposure to the air of the alloy surface. After cycling in the alkaline solution, the Al<sub>2p</sub> peak moves from lower binding energy to higher one, which indicates that Al on the alloy surface is oxidized to form Al<sub>2</sub>O<sub>3</sub>. The binding energy for Mg<sub>2p</sub> decreases, which can be ascribe to that the alloy particles are pulverized owing to the lattice expansion and contraction during charge-discharge cycling that resulted in the binding energy of metallic Mg (49.8 eV) is lower than that of MgO (50.8 eV). This change expects that Al<sub>2</sub>O<sub>3</sub> film should be a factor for the improvement of anti-corrosion performance of the alloy with Mg<sub>3</sub>AlNi<sub>2</sub> phase.

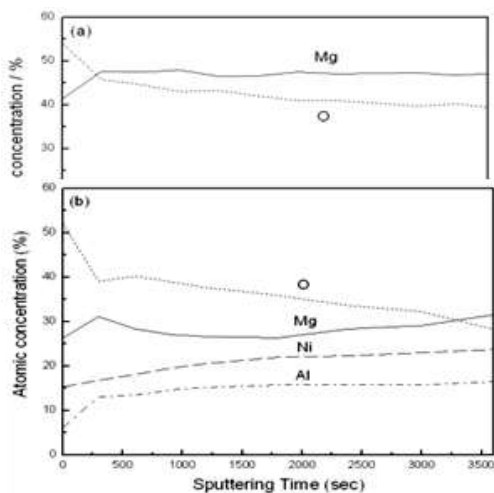


Fig. 6 XPS depth profiles of cycled as-cast alloys: (a)MAN0 and (b)MAN100 after 5 cycles.

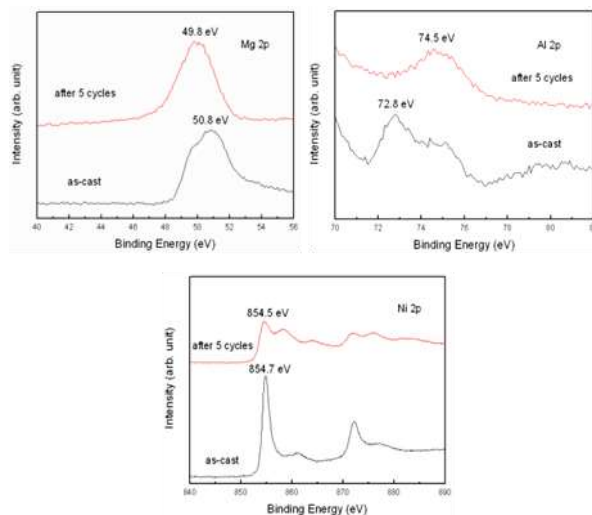


Fig. 7 XPS spectra of Mg<sub>2p</sub>, Al<sub>2p</sub> and Ni<sub>2p</sub> of the MAN100 alloy electrode.

### 4. Conclusion

Mg<sub>2</sub>Ni-  $x$  mol% Mg<sub>3</sub>AlNi<sub>2</sub> ( $x = 0, 15, 30, 60, 100$ ) electrode alloys were synthesized by the method of electric resistance melting and subsequent adoption of IECF technique, and the reason for the improvement of their electrochemical characteristics was investigated. XRD results show that the composites are composed of Mg<sub>2</sub>Ni phases and the new Mg<sub>3</sub>AlNi<sub>2</sub> phases. The addition of Mg<sub>3</sub>AlNi<sub>2</sub> brought about improvement in the discharge capacity and cycle life of the electrode alloys. As the Mg<sub>3</sub>AlNi<sub>2</sub> content increased from  $x = 0$  to  $x = 100$ , the maximum discharge capacity of the alloys increased from 20 mAhg<sup>-1</sup> to 110 mAhg<sup>-1</sup>. This revealed that the Mg<sub>3</sub>AlNi<sub>2</sub> phase could promote the reduction reaction of hydrogen and improve the electrocatalytic activities on the electrode surface according to cyclic voltammetry. XPS depth profiles demonstrated that the surface layer oxidized of the Mg<sub>3</sub>AlNi<sub>2</sub> alloy became thinner and the increase in the anti-corrosion ability due to the formation of an Al<sub>2</sub>O<sub>3</sub> film after 5 charge/discharge cycles. Thus, the cycling stability of the Mg<sub>3</sub>AlNi<sub>2</sub>-including alloy electrodes is improved. Furthermore, with further cycling, the increase in the pulverization of the Mg<sub>3</sub>AlNi<sub>2</sub>-including alloy and an Al<sub>2</sub>O<sub>3</sub> film was gradually formed on the alloy surface, lowering the quantity of active components in the alloy, which leads to that the cycling stability of the MAN15 alloy electrode is noticeable improved as Mg<sub>2</sub>Ni is partially substituted by Mg<sub>3</sub>AlNi<sub>2</sub>.

### REFERENCES

1. H.P. Ren, Y.H. Zhang, B.W. Li, D.L. Zhao, S.H. Guo, X.L. Wang, *Int. J. Hydrogen Energy*, 34, 2009, pp.1429-1436.
2. X. Xiao, L. Chen, Z. Hang, X. Wang, S. Li, C. Chen, Y. Lei, Q. Wang, *Electrochem. Commun.*, 11, 2009, pp.515-518.
3. C. Rongeat, M.-H. Grosjean, S. Ruggeri, M. Dehmas, S. Bourlot, S. Marcotte, L. Roue, *J. Power Sources*, 158, 2006, pp.747-753.
4. M. Jurczyk, L. Smardz, I. Okonska, E. Jankowska, M. Nowak, K. Smardz, *Int. J. Hydrogen Energy*, 33, 2008, pp.374-380.

ISGMA2014-P-E-10

5. M.H. Wang, Y. Zhang, L.Z. Zhang, L.X. Sun, Z.C. Tan, F. Xu, H.T. Yuan, T. Zhang, J. Power Sources, 159, 2006, pp.159-162.
6. L. Xiangdong, H. Lihong, T. Xiao, F. Hongwei, C. Bo, Int. J. Hydrogen Energy, 32, 2007, pp.4939-4942.
7. L.F. Jiao, H.T. Yuan, Y.J. Wang, Y.M. Wang, Int. J. Hydrogen Energy, 34, 2009, pp.1476-1482.
8. Y. Feng, H. Yuan, J. Alloys Comp., 473, 2009, pp.275-279.
9. F.K. Hsu, C.K. Lin, S.L. Lee, C.Y. Lin, H.Y. Bor, J. of Power Sources, 195, 2010, PP.374-379,
10. S.L.Lee, C.Y. Huang, Y.W. Chou, F.-K. Hsu, "Effects of Co and Ti on the electrode properties of Mg<sub>3</sub>MnNi<sub>2</sub> alloy by ball-milling process", Intermetallics, 34 (2013)122-127
11. M. Anik, H. Gasan, S. Topcu, I. Akay, N. Aydinbeyli, Int. J. Hydrogen Energy, 34, 2009, pp.2692-2700.
12. L. Guanglie, C. Linshen, W. Lianbang, Y. Huantang, J. Alloys Comp., 321, 2001, pp.L1-L4.

# Test Planning for a Large Wind Turbine Blade Full Scale Static Test Considering the Test Set-up

Jin Bum Moon<sup>1#</sup>, Hak Gu Lee<sup>1</sup> and Seung-Un Yang<sup>2</sup>

<sup>1</sup> WTRC, 797 Changwondaero, Seongsan-gu, Changwon, Gyeongnam, South Korea, 642-831  
<sup>2</sup> Human Composites, 251 Seohae-ro Gunsan-si, Jeollabuk-do, South Korea, 573-879  
# Corresponding Author / E-mail: jbmoon@kims.re.kr, TEL: +82-55-280-3263, FAX: +82-55-280-3498

KEYWORDS : Carbon Fiber, Cutting Force, Carbon Fiber, Cutting Force

*In the case of the horizontal testing method, the weights of test set-up induce the torsional bending moments on the blade at final deformed state because of the large deflection of blade. This torsional bending moments cause the additional stresses which can increase risk for the static test. Additional force, which has same quantity and opposite direction, should be applied to the loading point to compensate the unwanted torsional bending moments. In this study, this additional force is realized by change the loading direction slightly. Applying additional force will influence on the gravitational bending moment and target bending moment besides reducing the unwanted torsional bending moment. Therefore, the test load planning is revised again by considering the test set-up effect.*

*In this study, the test load calculation procedures considering the above mentioned factors especially the effects of test set-up will be introduced. In addition, a test load planning results for a real blade test is introduced. The considered blade is 3MW class II with 56 m length. The horizontal loading method is employed for a flapwise static test and the vertical loading method is used for an edgewise static test.*

## NOMENCLATURE

$\vec{M}_i$  = calculated test bending moment vector at a point  $i$   
 $\vec{r}_i$  = distance vector between a moment calculation point  $i$   
and a test load applied point  $j$   
 $\vec{F}_j$  = concentrated force applied by winches at a point  $j$   
 $\vec{\lambda}_j$  = direction vector of a winch force at point  $j$   
 $x_i$  = x-axis coordinate of a moment calculation point  $i$   
 $x_j$  = x-axis coordinate of a test load applied point  $j$   
 $z_i$  = z-axis coordinate of a moment calculation point  $i$   
 $z_j$  = z-axis coordinate of a test load applied point  $j$   
 $F$  = winch force for test set-up weight compensation  
 $\phi$  = loading angle for test set-up weight compensation

## 1. Introduction

During development of a large wind turbine rotor blade, full scale blade static test is mandatory for the certification of the blade design [1-3]. The main purpose of the test is to check the survivability of the test blade under design load condition which is an extreme load

condition for whole wind turbine life time. The key technology for the blade static bending test is to realize the test load which is similar to the design load.

In the blade design load, there are six components of the load that composed of three shear forces and three moments. However, it is impossible to apply the six load components simultaneously during the test. Therefore, only the main load component is applied during the test. For example, only the flapwise bending moment is applied for flapwise test. The other load components are unnecessary for the blade certification test. The loading plan shall be established to minimize load component in the other direction.

There are many factors, which should be considered during planning the test load, such as blade deformations, gravity effects, loading directions, test set-up and test layouts. These are frequently ignored for a small wind turbine rotor blade test because the effects to the test results are not severe for the small wind turbine blade. However, with the size of the blade is getting larger, these factors have not been negligible anymore because the effects are not small enough to ignore for the large wind turbine blade. Nowadays, 3MW class blades (about 40 m to 60 m length) are main item in the wind turbine industry. And the 5MW class wind turbines (about 70 m length) are developed and 7MW class (about 90 m length) wind turbines are developing. Recently, a 7MW class wind turbine with

world longest blade (83.5 m length) has been developed by SAMSUNG heavy industry.

Test method significantly influenced on planning of a large wind turbine blade static test considering a test set-up. There are two different test methods for the full scale blade static test (they are classified by the loading direction). The first one is a horizontal test method that pulls a test blade horizontally to the ground. In this test method, the unwanted bending moment terms in the different direction are generated by the gravitational forces and the large deflection of a test blade. Most of the test centers employed the horizontal method. The other is a vertical test method that pulls a test blade vertically up or down. In this test method, the loading direction is same with the direction of the gravity. So it is not necessary to concern about different directional moment. The moment induced by the gravity shall be added or subtracted during the test load calculation.

In this study, a horizontal test with a 56 m length blade and five concentrated forces are considered. With this test object and test set-up, the effects of the real situation of the blade static test are studied.

## 2. Factors influenced on the test loads

### 2.1 Large deflection of a test blade

During the flapwise static test, the test blade is largely deflected as shown in Figure 1. In the Figure 1, the tested blade has 56 m length and the tip deflection is about 12 m.



(a) 0 % of the test loads



(b) 100 % of the test loads

Fig. 1 Blade shape at different load step for full scale blade static test

The large deflection influences on the test bending moments induced by five winches because the large deflection means shortening of moment arm as shown in Figure 2. And also the bending moments induced by gravity are influenced by large deflection of the test blade. Therefore, the test load shall be

compensated by extra load increase during calculation of the test load. Due to this effect, the test bending moments and the gravitational bending moments shall be calculated at the final deflected blade shape.

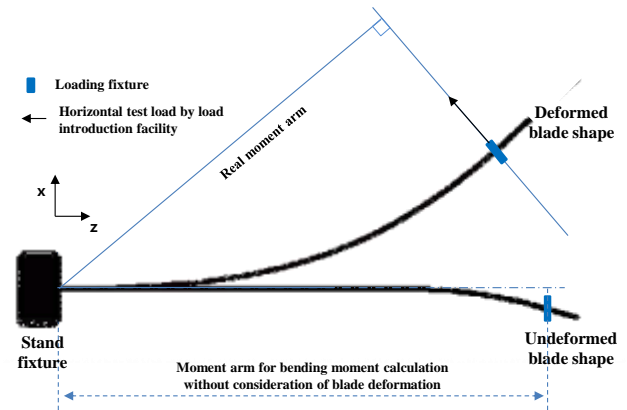


Fig. 2 Schematic diagram of moment arm change with blade deflection

For the edgewise static test, the deflection of the blade is about 3 m which is small compare with the flapwise deflection. It is small enough to ignore the moment arm change. Therefore, the undeflected blade geometry is used for calculating the edgewise test bending moment.

### 2.2 Adverse torsional moment induced by loading fixtures

The adverse torsional moments are induced by the weights of the blade itself and the loading fixtures mounted on the horizontally deformed blade, as shown in Figure 3. The effects by the blade weights are also in the real wind turbine operating situation. However, the weights of the loading fixtures are not in the real situation. Therefore, the weights of loading fixtures should be compensated to reduce an adverse bending moment during static tests.

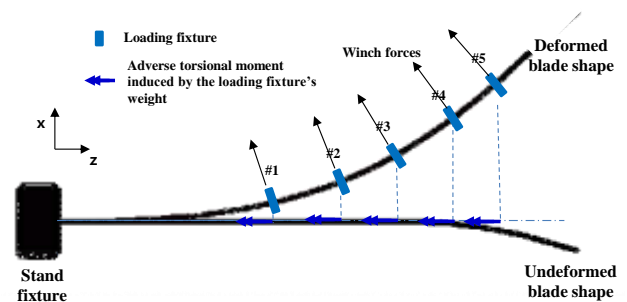


Fig. 3 Adverse torsional moments induced by the loading fixture weights

## 3. Calculation of test bending moment considering the factors

### 3.1 Compensation of large deflection

The test bending moments at each station is calculated using the vector product. With the nomenclature illustrated in Figure 4, the bending moment (at point  $i$ ) induced by concentrated winch forces at

ISGMA2014-P-E-07

point  $j$ , can be expressed as following equation.

$$\vec{M}_i = \sum_{j=1}^n (\vec{r}_{ij} \times \vec{F}_j)$$

The distance vector ( $\vec{r}_{ij}$ ), the load vector ( $\vec{F}_j$ ) and the direction vector ( $\vec{\lambda}_j$ ) are expressed as following equations.

$$\vec{r}_{ij} = (x_j - x_i)\vec{i} + (z_j - z_i)\vec{k}$$

$$\vec{F}_j = F_j \vec{\lambda}_j$$

$$\vec{\lambda}_j = \frac{(z_B - z_A)}{\sqrt{(z_B - z_A)^2 + (x_B - x_A)^2}} \vec{i} - \frac{(x_B - x_A)}{\sqrt{(z_B - z_A)^2 + (x_B - x_A)^2}} \vec{k}$$

Here, the x-axis and z-axis coordinates of the blade deformed shape are used.

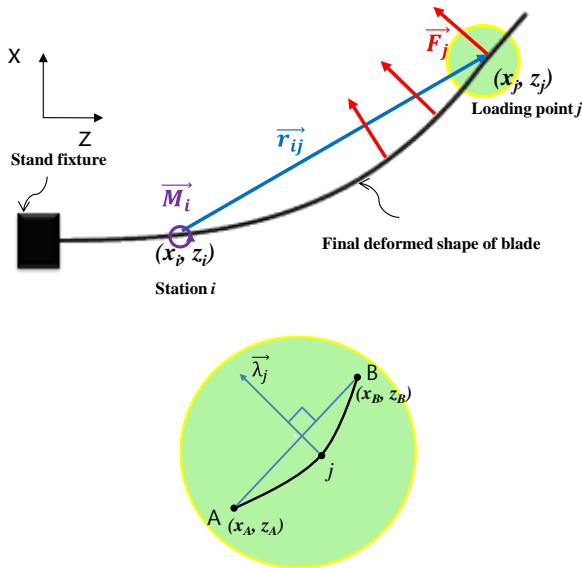
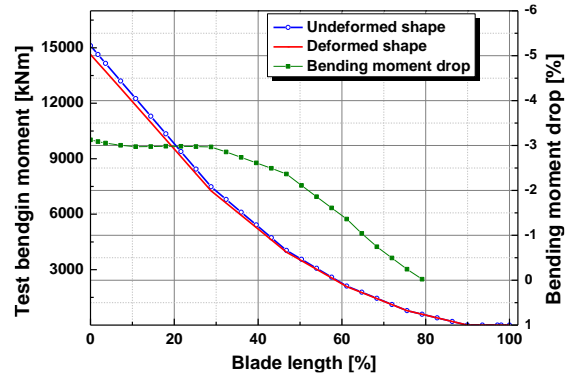


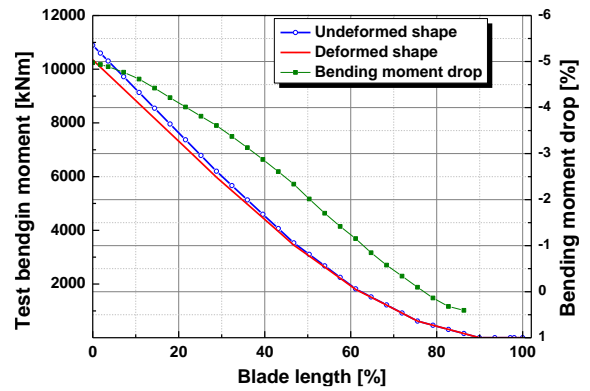
Fig. 4 Nomenclatures of each component at deformed shape

Using the beam model of HC56 blade, the final deformed shape is calculated and the bending moments are calculated with final deformed shape of the test blade. For the blade analysis, the ABAQUS is used for calculation.

With the above calculation method, the calculated test bending moments with same test lay-out (loading position, loading direction and quantity of the winch force) are illustrated in Figure 5. As shown in Figure 5, the calculated test bending moment is reduced by considering the blade deformed shape at the blade root (3 % for maximum flapwise test and 5 % for minimum flapwise test).



(a) Maximum flapwise test



(b) Minimum flapwise test

Fig. 5 Comparison between the test bending moment considering the large deflection and the test bending moment without considering the large deflection.

### 3.2 Compensation of adverse torsional bending moment

The torsional moments induce the adverse stress on the test blade and it can cause unwanted motion of the test blade. In this study, the torsional moments induced by #4 and #5 loading fixtures which are mounted on the out-board are reduced by making additional vertical force on #4 and #5 loading fixture. Because the most of torsional moments are induced by out-board loading fixtures and the inboard winches have no margin to increase the loading angle. The weights of the loading fixtures and the induced torsional moments are listed in Table 1.

Table 1 Adverse torsional moment of loading fixtures

Loading fixture	#1	#2	#3	#4	#5
Location [m]	16	26	34	42	50
Weight [kgf]	2 406	1 393	1 245	1 028	906
x-axis coordinate of deformed shape [m]	0.78	1.68	2.97	5.30	8.85
Torsional moment [kN·m]	18.5	22.9	36.3	53.4	78.7
(portion [%])	(8.8)	(10.9)	(17.3)	(25.5)	(37.5)

The torsional moments are compensated by applying the additional vertical forces to the blade, which have same quantity with

loading fixture's weights. The additional vertical forces are realized by changing of the loading angle of winch force as shown in Figure 6. The force ( $F_x$ ) is determined to make enough test bending moment. The angle ( $\phi$ ) is determined to make same quantity of  $F_y$  with the weight of the loading fixture. Finally, the forces ( $F$ ) applied by the winch #4 and #5 are determined as following equation.

$$F = \frac{F_x}{\cos \phi}$$

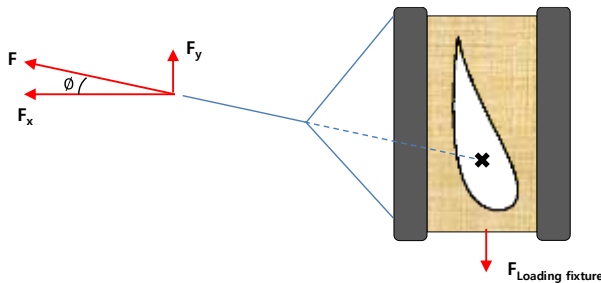


Fig. 6 Schematic diagram of #4 and #5 loading line

According to the above equation, the calculated angles and the forces are listed in Table 3.2. By doing the test with following lay-out, the adverse torsional moment induced by loading fixture is reduced to 63.0 % and much more precise and safe test can be possible.

Table 2 Test loads and the loading angles at each point

Loading fixture	#1	#2	#3	#4	#5
Location [m]	16	26	34	42	50
Winch force [kgf]	11 700	10 000	7 300	7 372	9 394
Loading angle [°]	0	0	0	8.0	5.5

If the required winch height is higher than the maximum height of the winch that the test center has, the smaller angle can be used to reduce the torsional moment. By setting the smaller angle of the test load, the horizontal load factor will be increased slightly but the torsional moment compensation will be decreased slightly. It will not be problem for the certification test because it is more conservative test lay-out.

#### 4. Conclusions

The horizontal test method for the full scale blade static tests has considering factors during calculation of the test loads. The situation and the test set-up should be considered for the precise and safe testing. In this study, the two major factors wear investigated that is test bending moment decrease by a blade large deflection and the compensation of adverse torsional moment by large deflection and gravitational force.

For the calculation of the precise test bending moment and the torsional bending moment, all the moment treated with deflected test blade. As a result, the test bending moment is over-estimated 3 % to

5 % because of the overlooking of the moment arm shortening effect by a large deflection. It is possible to calculate more precise test bending moments to employ the blade deflection during the test load calculation.

For the safer static tests, the adverse side moments should be minimized. To achieve this, the torsional moment induced by the test set-up (loading fixtures) is compensated by changing the loading direction. In this study, about 63.0 % of the adverse torsional moments are compensated. As a result, the static test becomes much safer by considering the test set-up compensation. Also the success rate of the test will be increase.

#### ACKNOWLEDGEMENT

This work was supported by the New & Renewable Energy Core Technology Program of the Korea Institute of Energy Technology Evaluation and Planning(KETEP) granted financial resource from the Ministry of Trade, Industry & Energy, Republic of Korea (No. 2009T00200854 and No. 20133010021750).

#### REFERENCES

1. GL, "Guideline for the Certification of Offshore Wind Turbines," Rules and Guidelines Industrial Services, 2012.
2. IEC, "Full-scale structural testing of rotor blades," IEC TS 61400-23, 2001.
3. DNV, "Design and manufacture of wind turbine blades, offshore and onshore wind turbine," DNV-DS-J102, 2010.

# A Study on the Recycling of Food - Salt Reduction Plan for Compositing of Food Waste

Doo Hee Han

1 Dept. of Architectural Engineering, Chungwoon University, 113, Sukgol-ro, Nam-gu, Incheon, South Korea 402-803 (Zip code)  
# Corresponding Author / E-mail: hanknu@hanmail.net, TEL: +82-10-9352-5404, FAX: +82-32-770-8171

KEYWORDS : Food Waste, Organic Waste, Recycling, Salt

---

*The purpose of this study lies in proposing the method to effectively reduce the salt in order to utilize food waste as the compost. Although 『Fertilizer Control Act』 requires the salt concentration of under 1%, crop cultivation test of specialized research institute requires much lower salt concentration. Although many compositing facilities have been established, a lot of wastes are not utilized due to lack of demand. With the increase in utilization of compost rather than chemical fertilizer due to the preference of environment-friendly farming nowadays, the utilization of food waste full of nutrients as quality compost can be considered as an important task to not only increase the earnings of farm but also resolve the environmental problems.*

---

## 1. Introduction

According to the research by the Ministry of Environment, organic waste occupies 56% of total waste generated in Korea and food waste and vegetables occupy 31.1% of such organic waste. The food waste not only brings about hygienic problems including the high content of moisture, generation of bad odor, and others but also causes contamination of underground water, surface water, and soil due to leachate generated with the reclamation. With the generation of bad odor and harmful gases including  $H_2S$ ,  $NH_3$ , others, it induces secondary contamination. According to the report by Rural Development Administration, about 3,000 microorganisms exist per soil 1g of barren soil and dozens of millions of microorganisms per soil 1g of fertile soil. Such microorganisms proliferate with the intake of nitrogen and phosphorous. When placing compost rich in nitrogen, phosphorous, and others, microorganisms intake them and decomposing them into enzyme, and then the plant intakes such enzyme. Therefore, in case the salt concentration of compost is over 0.1%, microorganisms in the soil are exterminated thus making the soil barren. The crops also are killed as the microorganisms such as bacteria exist in the root of crop and cell of root is destroyed by the salt. Looking into the source of food waste that is food culture of Korea, it is fair to say that it is salt oriented culture seen from Kimchi, soybean paste, food boiled and seasoned with soy sauce, stew, etc. According to the data on salt concentration of food waste investigated and reported by National Institute of Agricultural Science and Technology, as a

result of examining the salinity by randomly collecting the food waste from 50 locations in downtown Seoul, the average salinity of food waste containing 90% moisture was presented to be 4.84%. When the moisture of such food waste is dried or fermented as compost, its volume would reduced to 1/10 and thus at least 10~30% salt would be accumulated in high concentration. When the content of salt is 0.5%, it results in 50% reduction in crop and the damage would be 60 times in case the salt concentration is 30% thus it would bring about catastrophic result. In order to meet such needs, it is necessary to build a foundation to make quality compost by seeking the method to effectively remove salt contained in food waste.

## 2. Establishment of Salt Reduction Process

### 2.1 Damage in crop and desolation of farmland due to excessive salt concentration

Large quantity of microorganisms exists in soil. 3,000 microorganisms exist in 1g of barren soil and dozens of millions microorganisms in fertile soil 1g. When the compost is given to the farmland, microorganisms takes in nitrogen, phosphorous, and organic matters among compost and secretes the enzyme. Then, the plant intakes such enzyme and transfers it to the leaves. Due to chemical reaction including the carbon dioxide assimilation by the sunlight, and others, enzyme assists the formation of big fruits in root or branch. Therefore, as excessive content of salt turns fertile soil into barren soil as it kills the microorganisms. It can be

confirmed that there is 50% decrease in harvest with the salt concentration of 0.3% in over 50% of all crops and there are few crops including rice which presents 50% decrease in harvest with the salt concentration of 0.5% [Table 1]. Among the compositing condition of food waste, the salt concentration of under 1.0% is expected to change into under 0.5% in no time.

## 2.2 Salt Reduction Method for Aerobic Fermentation System

Aerobic fermentation is a type of fermentation which accompanies the oxygen and it can be summarized into below reactions.

Although aerobic treatment is preferred due to relatively abundant nutrients compared to anaerobic treatment, it has weakness in removal of bad odor. In this case, a general method used to reduce salt is to input bulking agent such as sawdust to absorb moisture that generates during the fermentation and it simultaneously reduces the salt concentration. The method to mix 50% of food waste with 50% of sawdust is widely used and remaining salt concentration was examined to be 1.32% as a result of environmental change assessment of soil using such compost .

As an improvement of above method, a technology to add dilution water to dilution agitating tank of flotation type to sort out foreign bodies among food waste and reduce the salinity as the first stage and conduct compositing by dehydrating it to present moisture content of under 70% through crusher and screw dehydrator, mixing it with bulking agent, and then decomposing the organic matters under aerobic condition as the second stage is newly applied [2]. As the salinity removal method, 2.55 tons of dilution water is used per 1 ton of food waste to wash off and remove the salinity. At the moment, removal rate is 86.1% compared to input and it maintains the salt concentration of final compost under 0.2%. With the maintenance of outstanding dehydration efficiency, the amount of consumed sawdust used as bulking agent is about 4% compared to input waste (about 20% for other methods) thus considerable amount of operating cost can be cut and it presents relatively fast organic matter decomposition speed as small quantity of sawdust with relatively slow organic matter decomposition speed compared to the food. Although it has shortcoming in that it presents relatively large amount of leftover water after the treatment, it can be processed in association with sewage treatment plant going through process Bad odor shall be removed with separate installation of bad odor remover.

## 2.3 Salt Reduction Method in Anaerobic Fermentation System

### 1) Treatment Method

A. Use peristaltic high speed fermentation and drying equipment by common anaerobic high speed fermentation and drying method.

B. Use complete sealing treatment method by inner current circulation.

C. Perform treatment only with food waste without other additives for maximum reduction through high concentration fermentation and drying.

### 2) Trait of Treatment Technology

A. It is technology intensive equipment which performs reduction by fermentation and drying in short period of time.

- Reduction is available in short period of time only food waste is treated without use of other additives.

- Origin of leachate problem is removed as treatment is performed without dehydration and cleaning process.

- Generation of bad odor is fundamentally blocked with inner current circulating structure.

- With recirculation of discharged waste heat, the fuel can fully be saved.

B. It was based on principle that food waste is composed of protein, fat, and carbohydrate and it converts into low molecular organic matters as protein is dissolved to amino acid and fat and carbohydrate are dissolved to organic acid during the fermentation. Then, it can be utilized as the source of heat when it is condensed.

In this case, the salt concentration could be reduced to under 0.8% by spraying the water at the input of input and save hopper and at dehydration after the crushing. Table 3 illustrates the content of solids after anaerobic fermentation treatment of food waste[3]. Table 4 shows components after food waste treatment..

Table 1. Components after food waste treatment.

H <sub>2</sub> O(%)	Ash(%)	Organics(%)						Heating Low Value(kcal/kg)
		C	H	N	O	S	Cl	
17.8	10	41.1	7.0	2.51	18.9	0.45	2.24	4,432

## 3. Conclusion

A method to effectively reduce the salt in food waste has been proposed. Salt reduction by water dilution is more effective compared to the mixture of foreign bodies such as sawdust and others. Although many compositing facilities have been established, it is being wasted with the lack of demand. With the increase in utilization of compost rather than chemical fertilizer due to the preference of environment-friendly farming nowadays, the utilization of food waste with abundant nutrients as quality compost can be considered as an important task as it can increase the earnings of farm and resolve environmental problems.

## REFERENCES

1. Ministry of Environment, "Annual Report of Waste", 2002.
2. J. Ahn, "Compost Method of Food Waste", Proceedings of 4<sup>th</sup> New Environmental Technology, 2003
3. B. Min, "Proposal of Food Waste Recycling System", 2009

# Steering Characteristics of AWS(All Wheel Steering) System using Virtual Rigid Axles

Kyung-Ho Moon<sup>1#</sup> and Jai-Kyun Mok<sup>1</sup>

<sup>1</sup> New Transportation Systems Research Center, KRRI, Uiwang 437-757, Korea  
# Corresponding Author / E-mail: khmoon@krii.re.kr, TEL: +82-31-460-5211, FAX: : +82-31-460-5024

KEYWORDS : All Wheel Steering, Virtual Rigid Axles, Bimodal Tram

The bimodal tram is an articulated vehicle with rubber tires. Because the bimodal tram has an extended wheel base and articulated chassis, an AWS (All-Wheel-Steering) system is applied to it to satisfy the required steering performance. There are many methods to control the rear wheels such as front wheel steering angle proportion, steering force feedback, yaw rate feedback and zero side slip angle. The AWS control method using virtual rigid axles is applied to the bimodal tram. The virtual rigid axle is defined as the virtual axle which is not steered at the point where turn center and vehicle body meet perpendicularly. A vehicle with an FWS(front wheel steering) system has a fixed rear axle, whose extended line meets the turn center. In case of an AWS vehicle, the virtual rigid axle is in charge of its role and controls the angles of the rear wheels. In this paper, the steering characteristics of AWS system using virtual rigid axles were analyzed. The simulation and driving test were also performed to evaluate the stability and turning performance of AWS system.

## NOMENCLATURE

$\alpha$  = articulation angle  
 $\delta$  = steering angle  
 $P$  = distance of virtual rigid axle  
 $l$  = wheel base

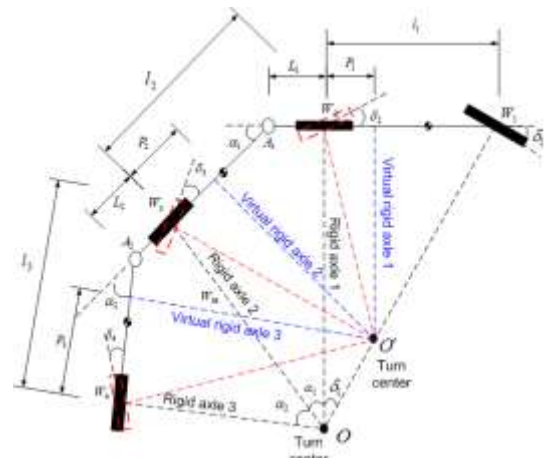
## 1. Introduction

The bimodal tram with a pivoting joint has difficulty in making a sharp turn because of their long body and wheel base. Therefore, the turning radius of the bimodal tram is effectively reduced with AWS(all wheel steering) since all wheels are steered. Various rear wheel control methods for AWS have been developed, but they are generally applied only to four wheel steering cars. The AWS control method using virtual rigid axles is applied to the bimodal tram. The AWS algorithm contains an equation used to control the rear wheels of an articulated vehicle and a method used to set up virtual rigid axles geometrically. In this paper, the steering characteristics of AWS system using virtual rigid axles were analyzed. The simulation and driving test were also performed to evaluate the AWS system.

## 2. Virtual Rigid Axles

The virtual rigid axle is defined as the virtual axle which is not steered at the point where turn center and vehicle body meet perpendicularly as shown in Fig. 1. A vehicle with an FWS system has a fixed rear axle, whose extended line meets the turn center. In case of an AWS vehicle, the virtual rigid axle is in charge of its role and controls the angles of the rear wheels.

Fig. 1 Bicycle model for the articulated vehicle



The equations for rear steering angle can be expressed as shown in equation (1).

$$\delta_{n+1} = -\tan^{-1} \left( \frac{P_n \times \tan \alpha_{n-1}}{(l_n - L_{n-1}) + \frac{L_{n-1} + P_{n-1} - P_n}{\cos \alpha_{n-1}}} \right), \alpha_0 = \delta_1, L_0 = P_0 = 0 \quad (1)$$

Where,  $\delta$  is the steering angle,  $\alpha$  is the articulation angle,  $P$  is the virtual rigid axle,  $l$  is the wheel base,  $L$  is the distance between axle and articulation point.

The virtual rigid axle is geometrically related to the angles of each axle and articulation. An articulation device can be broken easily by compulsory steering. Thus, the virtual rigid axle must be set up according to the angle of articulation, first. Then, the turn center should be made coincident by considering the maximum steering angle of each axle. Assuming that the rear axles are fixed, the value of the virtual rigid axles is zero and turn center is located at O position. But, when the rear axles are steered, turn center moves from O to O' position with the value of the virtual rigid axle, as shown in Fig. 1.

### 3. Performance Evaluation of AWS System

Turning radius, swing-out and swept path width were investigated to determine the turning performance of the AWS system. J-turn(step steering input) simulation was carried out to verify the steering performance of the AWS system. J-turn(step steering input) simulation was carried out for three cases to verify the steering performance of the AWS system:

- Case 1 : AWS without suppression
- Case 2 : AWS with suppression of swing-out
- Case 3 : front wheel steering

The trajectories of the axle center for the three cases are shown in Fig. 2 and Fig. 3. The rear swing-out was measured outside the rear edge, and the swing-out of case 1 was bigger than the others. The swept path width is the difference in paths between the outside front edge and the inside of vehicle side face at the minimum turning radius. The swept path width of case 3 was larger than the others, so a large road width is required in the curve.

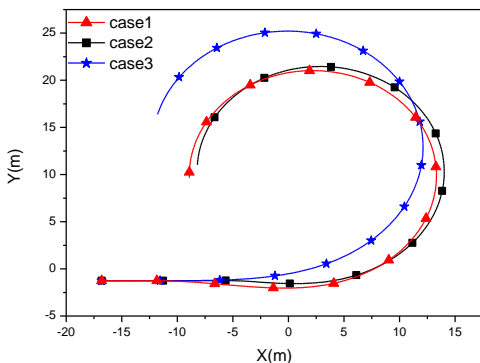


Fig. 2 Comparison of the Swing-out

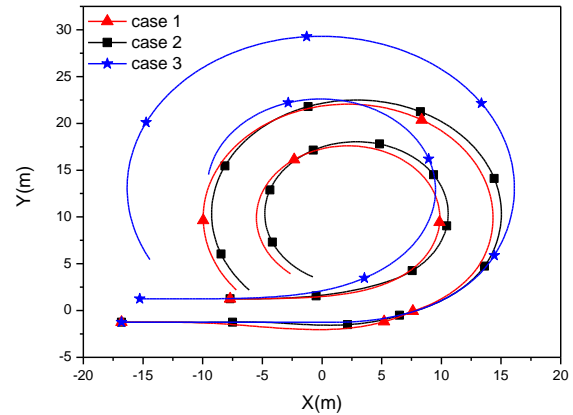


Fig. 3 Comparison of the Swept path width

Table 1 Results of the turning performance

	Turning radius (m)	Off-tracking (m)	Swing-out (m)
Results of field test	11.8	1.09	0.12

The field test of the J-turn of the bimodal tram was also carried out. In the J-turn test, the vehicle velocity was 3km/h at the maximum front steering angle. The turning performance obtained from field test is shown in Table 1. The results are suitable to satisfy EC regulation and the standards of the motor vehicle which restrict swing-out within 0.6m and turning radius within 12m.

### 4. Conclusions

The AWS control algorithm using virtual rigid axles was presented. According to the result of the dynamics simulation, the vehicle with the AWS system turned more smoothly than that with the FWS algorithm, and also had good turning performance. The driving test was performed to evaluate the stability and turning performance of the AWS system. The turning performance obtained from simulation and field test are suitable to satisfy EC regulation and the standards of the motor vehicle which restrict swing-out within 0.6m and turning radius within 12m.

### REFERENCES

1. S. H. Lee, K. H. Moon, T. W. Park, and Y. H. Jeon, (2007). "A Study on the Dynamic Characteristics of the Bi-modal Tram with All-Wheel-Steering System", Journal of the Korean Society for Railway, Vol. 10, No.4, pp 438-443, 2007.
2. K.-H. Moon, et al, "Method for Control of Steering Angles for Articulated Vehicles Using Virtual Rigid Axles", IJAT, Vol. 10 No.4, pp441-449, 2009.

# Analyze the Ride Comfort Characteristics of Railway Vehicles in the Segment of Rail Corrugation

Chan-Woo Lee<sup>1#</sup>

<sup>1</sup>High-Speed Railroad Systems Research Center, Korea Railroad Research Institute, #176, Cheoldo bangmulgwan-ro, Uiwang, Gyeonggi-do, South Korea, 437-757  
# Corresponding Author / E-mail: cwlee@krii.re.kr, TEL: +82-31-460-5204, FAX: +82-31-460-5034

KEYWORDS : Rail Corrugation, High Speed Lines, Ride Comfort, Wheel Set

---

*Rail corrugation wear is one of the most important types of track wear in the railroad infrastructure. In Korea, rail corrugation had not been so serious formerly, but it began to be prevailing in recent years. This paper analyses the possible existence and degree of rail corrugation wear on high speed tracks, and taking into account the dynamic behavior of the KTX train on rail corrugation track. That occurs between R400 and R700 from the size of the curved rail corrugation of the high-speed operating service to the KTX train. KTX train ride was confirmed to be slightly worse than the interval of Rail Corrugation Rail Corrugation. KTX vehicle like if a larger wheel-base was found to be faster processing speed Rail Corrugation. However, the section of Rail Corrugation KTX trains pass through relatively low speed ride quality of the KS R9216 standard was found that the comfortable level.*

---

---

## NOMENCLATURE

$V_t$  = vehicle speed(km/h)

---

## 1. Introduction

Adhesion types of rolling stocks generate noise and vibration running on rail. Vibration is caused by contacting wheel and rail. There are different sizes of noise and vibration which are caused by difference between roughness of rail head and wheel profile. In case of normal abrasion caused by contacting wheel and rail of wheel profile the biggest reason is wheel profile adherence of fine particles and foreign substances which are caused by mutual abrasive effect of wheel and rail. Like the wheel fine cracks occur in contact part of wheel and rail when the trains run under the condition of that some of fine particles or foreign substances adhere to rail head in case of abrasion caused by normal contact wheel and rail. This study does not go over normal abrasion of contacting wheel and rail of rail head, but tries to analyze distinctive features of ride quality caused by vibration in the rail corrugation section which is an abnormal rail abrasion. Most of rail corrugation occurs in curved section. It occurs when trains run faster in the curved section in comparison to curve radius and when trains of bogie which do not have proper curve running performance pass fast. First, this study briefly examines why rail corrugation occurs and its shape. Second, this study analyzes the test

of ride comfort which has strong influence directly on comfort evaluation of passengers. The method of analyzing ride comfort is based on KS R9216. The analysis of ride comfort in the rail corrugation section is based on as followings; the ride comfort is measured and analyzed when KTX train runs on the rail corrugation section which is a type of abnormal rail abrasion and when it runs on normal abrasion section of rail head.

## 2. The Reason of Occurring Rail Corrugation and its Shape

The rail corrugation is caused by torsional vibration of the wheel and axle due to irregular sliding between inside and outside rail when the train runs on the curve section. The vertical contact force between wheel and rail causes cyclic changes of wheel load. Since maximum value of creep force which can occur in contact surface of wheel and rail changes, in case of lessening wheel load it slides due to not occurring horizontal contact force. And when there is wheel load, the sliding disappears. In other words there is a stick-slip vibration because of cyclic changes of wheel load. Since the abrasion loss is proportional to creep force multiplied by slip speed, cyclic abrasion of rail occurs with frequency of changes of wheel load. Here excessive creep means slip with heavy creep force and slip rate is more or less 1%. This abnormal slip rate is frictional characteristic. The self-induced vibration of sound damping generates stick-slip vibration. Since changes of maximum contact surface caused by changes of

vertical contact force is big, the main reason is changes of vertical contact force. Excessive creep does not matter whether it is longitudinal creep or lateral creep. The longitudinal creep is caused by lack of radius difference of wheel rotation at inside and outside track when the trains run on curve rail and the lateral creep is caused by excessive attack angle. Deutsche Bundesbahn(DB) classifies rail corrugations as 8 types according to shape as shown on Fig. 1. ① Band type of rail corrugation : mountain and valley are shining. The edge of inside and outside of shining band is corrugation or it gets out of saw-toothed pattern. ② Non-continuous band type of rail corrugation : the range of rail corrugation is cut by shining band. The valley side looks like dull-finished steel. ③ Disconnected rail corrugation : shining part of peak is parallel to driving direction of the train. ④ Disconnected lateral rail corrugation : On the single track shining part of peak lies at right angles to driving direction of the train and on the double track it has a slope of 105° to driving direction of the train. ⑤ Dot shape of rail corrugation ⑥ Hook shape of rail corrugation : there are various irregularity, but shining part of rail corrugation has various hook shapes. ⑦ Irregular rail corrugation: the size of shining part of rail corrugation is different and there are differences in shape. ⑧ Double track rail corrugation: there are two lines of shining surface side by side. Like Deutsche Bundesbahn(DB) rail corrugation is classified as in detail, but it can be classified as two according to wave length of rail corrugation.

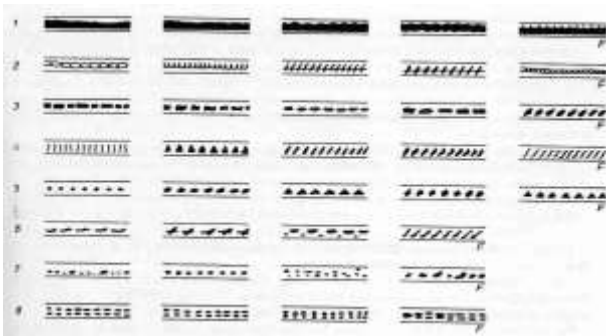


Fig. 1 DB classifies rail corrugations as 8 types

First, a long wave length of rail corrugation occurs in severe curve and wave of abrasion is about 60~2,300mm. The depth of abrasion is 0.5~4mm. The fault on wheel profile is a concavo-convex wave form. One of reasons why a long wave of rail corrugation occurs is that a wheel and an axle are fixed as one and it has a big suspension system with lateral hardness or there is big distance between centers of fixed wheel base and bogie and there is big radius of wheel and when the train runs on curve due to lack of self-handling in lateral direction. Second, short wave length rail corrugation occurs on curve and straight section and the wave is 40~300mm. The reason why there is short wave length rail corrugation is that with dynamic vertical force reduction the stress of wheel/rail contact is getting smaller and slip and taxing occur. Especially on the curve there is difference in electromotive force of inside and outside wheel according to time, but since the wheel is fixed to an axle, on the curve there is vibration of distorted wheel and there are repeated vibration and taxing. The fault of short wave rail corrugation is occasionally

found on inner rail of curve section with small radius. Whenever the wheel and axle repeatedly slip (stick-slip vibration) in lateral, this fault occurs. It is a concavo-convex rail surface with the abrasion depth of 0.1~1.2mm. Mountain and valley parts of wave are shining. In addition to taxing of the wheel, it occurs on the inside rail which has curve radius under R400~R700m.

### 3. Present Condition of Rail Corrugation at Seoul-Pusan High Speed Railway

The rail corrugation in Korea occurs at Geumjeong tunnel of Dongdaegu and Pusan line which began to run in December 2010. The rail corrugation occurs on the curve section which is R400~R600 of Geumjeong tunnel, that is, 409km ~ 415km far from Seoul. This curve section is located in high speed line, but railway is small section with R400~R600 of curve radius. The train speed in this section, R400 which is severe curve section, is 90km/h and current set-up cant amount is 130mm. The KTX trains running in this section is articulated bogie and bogie center distance is 18,700mm which is larger than normal trains. The fixed wheel base of bogie is designed as 3,000mm which is appropriate for high speed trains. When the train runs on the curve section, the bogie does not rotate well. And when the wheel contacts the rail, the rail corrugation occurs due to increasing of lateral creepage by stick-slip. The reason why there is the rail corrugation is that standards of designing and building a connecting line between an existing line and an express line do not fully consider characteristics of KTX trains. Fig. 2 shows that the example of rail corrugation which occurs at Geumjeong tunnel of Seoul-Pusan High Speed Railway.



Fig. 2 Rail Corrugation Shape

### 4. Test and analysis of ride comfort of KTX trains in the section of rail corrugation

The testing ride comfort of KTX trains is carried out at Geumjeong tunnel which is newly built as 2nd plan of Seoul-Pusan High Speed Railway and where occurs rail corrugation. Geumjeong tunnel is one of the weakest sections. Testing section is newly built, but it is connected with an existing line and is a concrete track which is planned and built with comparatively small radius line. The test was carried out at the spot of 409km~415km far from Seoul. The curve radius of the testing section is R400~R600 which is pretty small, but cant amount is 130mm according to minimum cant

ISGMA2014-P-G-07

standard of high speed express. The conditions of measuring and analyzing ride comfort of KTX trains are as followings ;

- Test train : car number #3 of KTX #45 fleet train
- Speed of train : operating speed
- Direction : Downward (T1) Shingyeongju → Pusan  
Upward (T2) Pusan → Shingyeongju
- Object : Ride comfort of up/down and right/left movement of the car
- Method of analysis : According to KS R9216, that is standard of ride comfort, level (dB) of comfort about vibratory acceleration as a unit of 1km is analyzed. Table 1 shows the standard of ride comfort in KS R9216-2000.

Table 1 Ride comfort index in the KS R 9216-2000

Level(A)	Effectiveness value(m/s <sup>2</sup> ) (B)	Index
100dBA > A	0.1 > B	very good comfortable
100dBA ≤ A < 105dBA	0.1 ≤ B < 0.178	good comfortable
105dBA ≤ A < 110dBA	0.178 ≤ B < 0.315	not comfortable
110dBA ≤ A < 115dBA	0.562 ≤ B < 1.0	a little uncomfortable
120dBA ≤ A < 125dBA	1.0 ≤ B < 1.779	very uncomfortable
125dBA ≤ A	1.779 ≤ B	extremely uncomfortable

Fig. 3 and Fig. 4 are the result of testing ride comfort. The value of ride comfort is as follows; in case of T2 (upward) the value of right and left is 88dB~94dB and in case of T1 (downward) the value of right and left is 88dB~92dB. They are in very good level according to standards of ride comfort by KS R 9216-2000. The comfort value of vertical direction is as follows; in case of T2 (upward) the value is 96dB~100 dB, in case of T1 (downward) the value is 95dB~100dB. Like the ride comfort of right and left direction, they are in very good level according to standards of ride comfort by KS R 9216-2000.

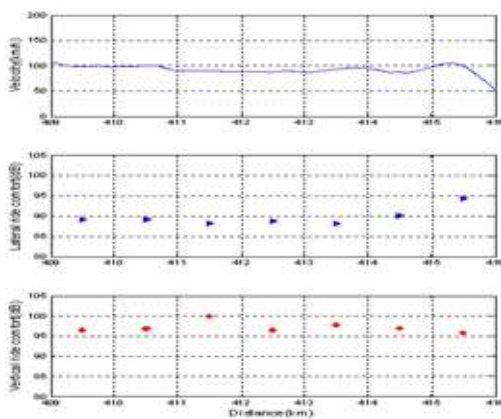


Fig. 3 Experimental value of ride comfort at KTX train ; up line(T2)

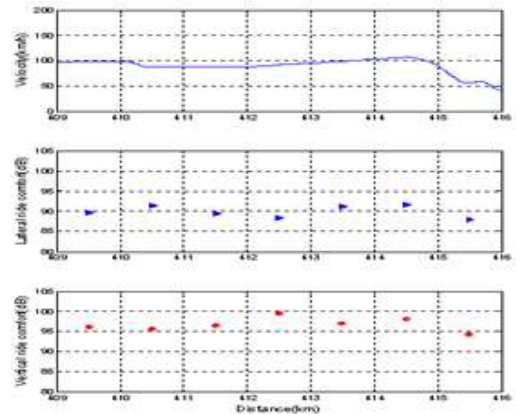


Fig. 4 Experimental value of ride comfort at KTX train ; down line(T1)

### 5. Conclusions

This study analyzes characteristics of ride comfort which decide comfort of passengers when Korea high speed train, KTX, runs on the section of rail corrugation. It is known that when KTX trains run on the curve section, bogie center distance is big and the fixed wheel base within bogie is long, thus performance of passing curve section is not good. The result of testing ride comfort at the section of rail corrugation is as follows; the level of ride comfort which speaks of vibratory characteristics is very high according to standards of KS R9216, although there is rail corrugation. When the train runs on the section of rail corrugation, noise inside of trains increase 2~3dB due to abnormal contact of wheel and rail. It is found out that the study on reducing noise rather than reducing vibration for better comfort which affect the comfort of passengers when the high speed trains run slowly with curve radius of R400~R600 is necessary for the future.

### REFERENCES

1. Kim, D.S., Lee, C.W., et al., 2011, "Development of Interface Technology on Catenary/Pantograph and Vehicle/Track to Speed up High-Speed Train," KRRI Report 2011-045, pp. 90~100.
2. P. Ding, M.Dittrich, 1996, "Roughness on Dutch railway wheels and rails", Journal of sound and vibration 193, pp 103-112.

# Investigation of the Effect of Tool Wear and Surface Roughness in Ultrasonic-assisted Milling

Chang Ping Li<sup>1</sup>, Min Yeop Kim<sup>1</sup>, Tae Jo Ko<sup>#</sup> and Jong Kweon Park<sup>2</sup>

<sup>1</sup> School of Mechanical Engineering, 214-1, Yeungnam University, Gyeongsan-si, Gyeongsangbuk-do, South Korea, 712-719

<sup>2</sup> High-precision mechanical system Laboratory, Korea Institute of Machinery & Materials, Daejeon, South Korea, 305-343

# Corresponding Author / E-mail: tjko@yu.ac.kr, TEL: +82-53-810-3836, FAX: +82-53-810-4627

KEYWORDS : Hybrid Machining Process, Ultrasonic-assisted Milling, Tool Wear, Surface Roughness

*Tool wear plays a vital role in influencing the ease of cutting, the quality of the resultant machined surface, and machining costs. In this paper, a new hybrid machining process (HMP) is proposed. The system has a milling spindle with ultrasonic vibration for the sake of the HMP system. In this system, the core technology is to design an ultrasonic vibration horn for the spindle using finite element method (FEM) and impact testing method. After the assembly of the HMP system, the final goal that is to reduce tool wear and to improve the surface roughness was investigated. Contrast to the conventional cutting systems that has large tool wear to the SM45C HRC28 steel workpiece, the tool wear as well as surface roughness has been greatly improved by the HMP. The machining cost and burr has also been reduced efficiently.*

## 1. Introduction

Nowadays manufacturing industry is facing challenges from advanced difficult-to-machine materials (tough super alloys, ceramics, and composites), stringent design requirements (high precision, complex shapes, high surface quality), and machining costs [1]. The reasons for developing a hybrid machining process (HMP) is to make use of the combined or mutually enhanced advantages, and to avoid or to reduce some adverse effects of the constituent processes produce when they are applied individually [2].

In recent years, there has been a rapid increase in the demand for micro-parts in many industries. However, the micro-parts are very sensitive to ultrasonic vibration. Vibration-assisted machining (VAM) combines precision machining with small-amplitude of tool vibration to improve the fabrication process. The VAM was first used in the late 1950s for traditional macro scale metal-cutting applications. These VAM experiments of the glass, steel, and brittle ceramics confirmed that the tool life could be extended and allow economic machining of such materials; improvements in the surface roughness and ductile cutting compared to conventional machining were also demonstrated [3]. The VAM has been applied to a number of processes from turning to drilling as well as grinding

Ultrasonic vibration assisted micro-drilling (UVAD) process can reduce the exit cracks of micro hole and increase the tool life [4], and improve the quality of the machined surface [5]. Jin et al. found that ultrasonic vibration cutting (UVC) could be carried out for a workpiece with high hardness and the tool life could also be increased

[6]. Zhou et al. found that surface roughness of the aluminum-based metal matrix composite became better in ultrasonic vibration assisted turning [7]. The UVC is an effective method to obtain better cutting performance, and this combined machining technology has been widely used in successful turning and drilling. However, very less data is recorded in case of ultrasonic-assisted milling (UAM).

The purpose of this research is to investigate the effects of machining length on tool wear and surface roughness in UAM and CM of steel SM45C HRC28. The research was done through many experiments to compare the difference between UAM and CM.

## 2. Hybrid Processing Machine

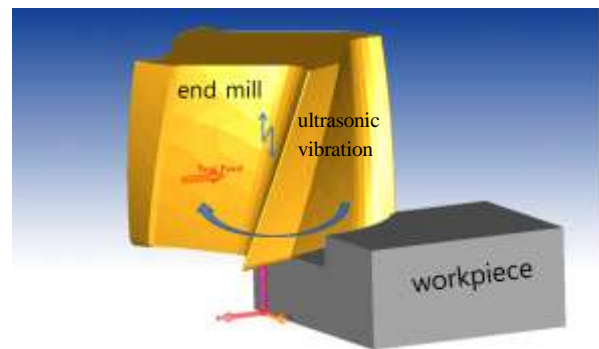


Fig. 1 Ultrasonic-assisted milling machining mechanism

The HMP system mechanism and setup are shown in the Fig.1 and Fig. 2. The capability of the system allows us to perform various hybrid machining experiments. Two or more different processing methods can be combined, for instance, EDM-Milling, US-Milling, or EDM-US-Milling, etc. Maximum spindle speed is 9600 rpm. We designed an ultrasonic vibration horn for the spindle using FEM and impact testing method, and the horn has been manufactured and tested. The resonance frequency of the transducer is 40 kHz and for cooling of spindle, air is used as coolant.

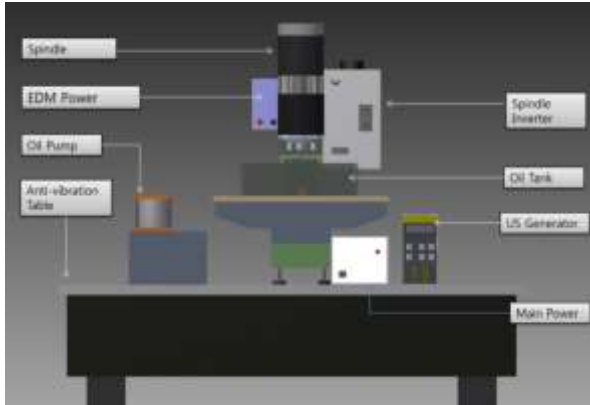


Fig. 2 Hybrid machining setup

### 3. Experiment

#### 3.1 Design of Experiments

The conditions of experiment are shown in Table 1. The variables of the experimental conditions are machining length and ultrasonic displacement. In this experiment, the workpiece (SM45C H<sub>R</sub>C28) was used. In order to prevent the tool fracture, the high-speed 9,000 rpm and slow feed rate were used.

The purpose of the experiment is to observe the tool wear and the surface roughness to compare performance UAM and CM.

Table 1 Experimental Parameters

<b>Fluid</b>	Kerosene
<b>Tool diameter</b>	1 mm
<b>Tool type</b>	Two-flute end mill
<b>Tool material</b>	Tungsten carbide
<b>Workpiece material</b>	Steel SM45C H <sub>R</sub> C28
<b>Feed rate</b>	0.002 mm/tooth
<b>Spindle speed</b>	9000 rpm
<b>Ultrasonic displacement</b>	0 , 1.50 μm
<b>Machining length</b>	500, 1000, 1500, 2000, 2500, 3000 mm

#### 3.2. Experimental results and discussion

CM and UAM experiments were completed in the same CNC machine tools (Hyper-15). Tool wear and the surface roughness results are shown in Fig.4 and Fig. 5, respectively. As shown in the Fig. 4, UAM improves the tool wear in comparison with CM by 34.9% on average. Fig. 3 shows microscopic images of tool condition after performing 3000 mm machining length on SM45C H<sub>R</sub>C28 by

UAM and CM. From this figure, the tool wear of the CM is very obvious than UAM. This results in rapid increase in workpiece roughness as shown in Fig 5. By using UAM, the surface roughness is reduced up to 61.5% compared to CM. The variation of surface of the workpiece (SW45C H<sub>R</sub>C28) after different machining method is shown in Fig. 6.

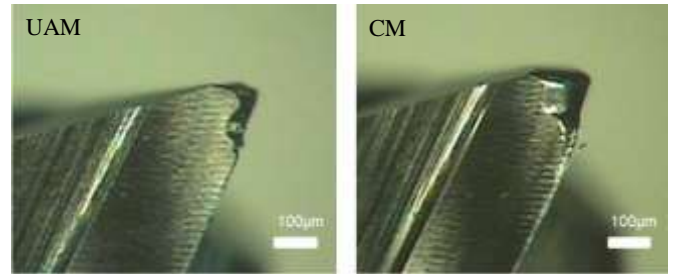


Fig. 3 Microscopic images of tool condition after (a) UAM and (b) CM the workpiece of SM45C H<sub>R</sub>C28 for 3000 mm

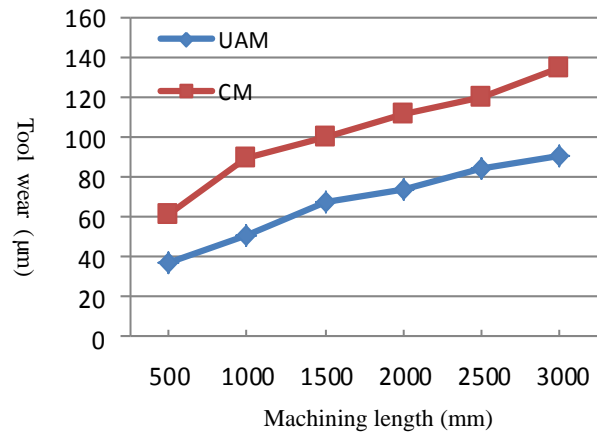


Fig. 4 Variation of the flank wear of the tool with the distance in machining SW45C H<sub>R</sub>C28 of UAM and CM

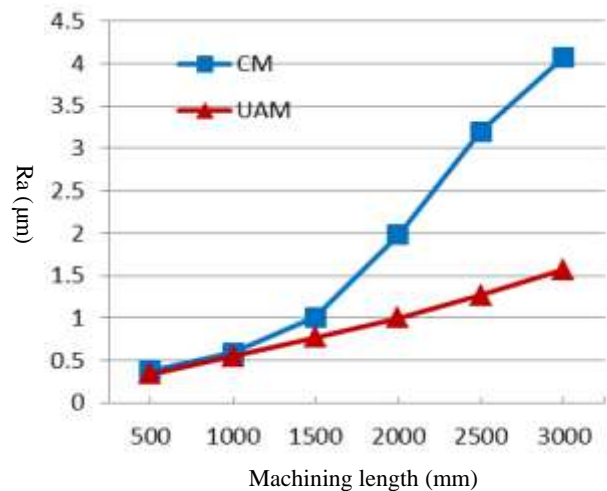


Fig. 5 Variation of roughness of the workpiece of SW45C H<sub>R</sub>C28 with the distance in CM and UAM

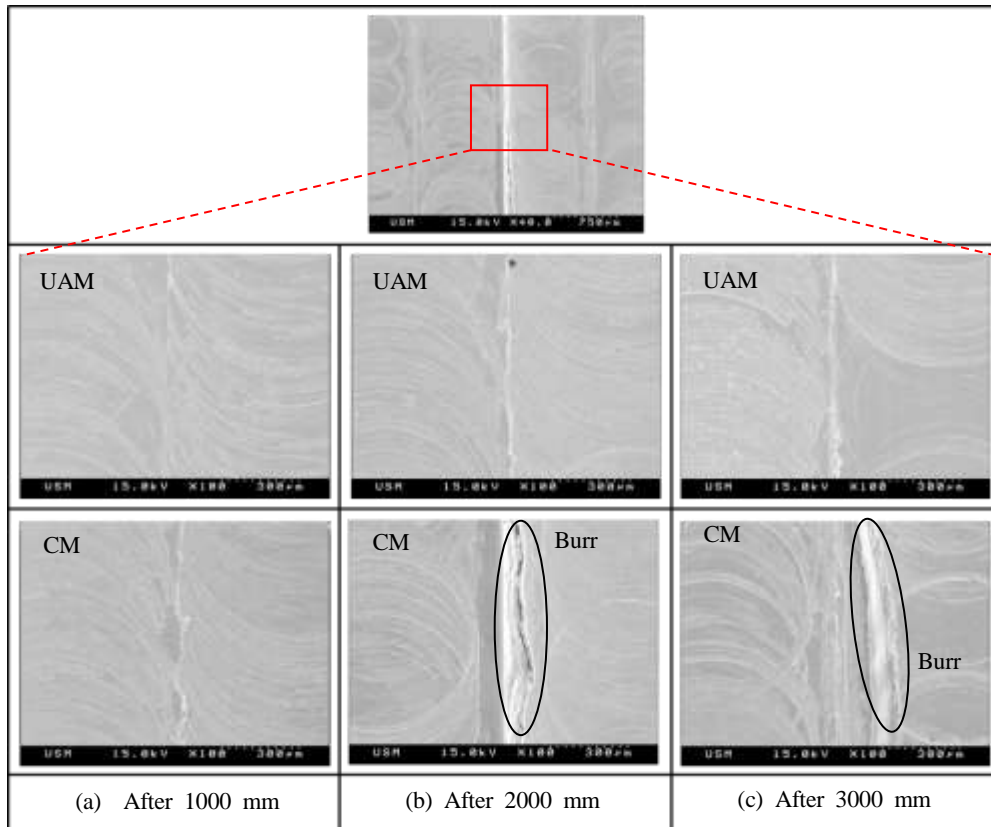


Fig. 6 Variation of surface of the workpiece of SW45C HRC28 with the distance (a) after 1000 mm (b) after 2000 mm (c) after 3000 mm in UAM and CM

#### 4. Conclusions

Experiments were carried out to study the tool wear and surface finish during CM and UAM of SW45C HRC28. Milling machining of difficult-to-cut materials generates concentrated thermal/frictional damage at the cutting edge of the tool and rapidly decreases the tool life. The tool wear is reduced up to 34.9% by using UAM.

The tool wear can lead to rough machined surface. From the Fig. 5, experimental results show that the UAM can significantly reduce the surface roughness and burr.

Our experimental investigations revealed that ultrasonic vibration enhances the abrasive resistance of the cutting tool and produces better surface finish in our developed hybrid machining. This result could be due to accelerated heat transfer by ultrasonic vibration.

#### ACKNOWLEDGEMENT

This research was supported by Ministry of Knowledge Economy (MKE) of the Korea Government proceeded as a part of next generation new technology development project.

#### REFERENCES

1. Yadava, V., Jain, V. K., Dixit, P. M., "Temperature distribution during electro discharge abrasive grinding," *Machining Science and Technology-An International Journal* 6(1), pp. 97–127, 2002.
2. Rajurkar, K. P., Zhu, D. J., McGeough, A., "New Developments in Electro-Chemical Machining," *Annals of the CIRP*, vol.48/2, pp.569-579, 1999.
3. Brehl, D. E., and Dow, T. A., "Review of vibration-assisted machining," *J. Precision Engng*, 32, 153–172, 2007.
4. Liu, J.W., Jin, J., Ko, Tae. Jo., "Micro-hole Machining for Ceramic using Ultrasonic Machining," *KSPE*, pp. 267~268, 2011.
5. Chern, G. L., H. J., "Using workpiece vibration cutting for micro-drilling," *Journal of Materials Processing Technology*, 27(7~8), pp. 688-692, 2006.
6. Jin, M., Murakawa, M., "Development of a practical ultrasonic vibration cutting tool system," *J Mater Process Technol* 113:342–347, 2001.
7. Zhong, Z.W., Lin, G., "Ultrasonic assisted turning of an aluminium-based metal matrix composite reinforced with SiC particles," *Int J Adv Manuf Technol* 27:1077–1081, 2006.

# Supercapacitor Based on Polypyrrole and TEMPO-oxidized Bacterial Cellulose Nanofibers (TOBCN) Nanocomposite Films

Fan Wang<sup>1</sup>, Jong Yun Kim<sup>1</sup>, Deok-Hyu Lee<sup>1</sup> and Chang-Doo Kee<sup>1#</sup>

<sup>1</sup> School of Mechanical Systems Engineering, Chonnam National University, 77 Yongbong-ro, Buk-gu, Gwangju, South Korea, 500-757  
# Corresponding Author / E-mail: cdkee@chonnam.ac.kr, TEL: +82-62-530-1667, FAX: +82-62-530-1689

KEYWORDS : Bacterial Cellulose, Polypyrrole, Polymer Electrolyte, Supercapacitor

*The novel supercapacitor cell has been developed based on polypyrrole(PPy) and TEMPO-oxidized bacterial cellulose nanofibers (TOBCN) films. Flexible nanocomposite films of PPy/TOBCN are synthesized by the chemical oxidative polymerization of pyrrole with TOBCN. Resulting composite films are characterized by Fourier transform infrared spectroscopy, x-ray diffraction, scanning electron microscope and thermogravimetric analysis. The polymer electrolyte based on electrospun PVdF fiber is prepared by immersing PVdF film into 1-Ethyl-3-methylimidazolium tetrafluoroborate (EMIMBF<sub>4</sub>) solution. The electrochemical performances of the supercapacitor cell are measured through cyclic voltammetry (CV) and charge-discharge tests. It's found that the supercapacitor cell demonstrates a mass-specific capacitance of 133 F/g at the current density of 0.2 A/g. With high specific capacitance and excellent cycle life, this supercapacitor indicates the exciting potential for high-performances energy storage applications.*

## 1. Introduction

Recently, the supercapacitor has received much attention due to its high power density and long cycle life.<sup>1</sup> Conducting polymers could be employed as adaptable energy storage devices because of their inherent fast redox switching, mechanical flexibility, low weight and high conductivity.<sup>2</sup> Among the conductive polymers, polypyrrole (PPy) has drawn much attention, owing to its high conductivity, flexibility, thermal and environmental stability. However, the poor mechanical properties and process-ability of PPy have limited their applications.

In our study, for the first time, a flexible TEMPO-mediated oxidized bacterial cellulose nanofibers (TOBCN)/PPy composite was synthesized by the chemical oxidative polymerization of pyrrole on the surface of cellulose nanofibers. TOBCN can be obtained through the treatment of BC using 2,2,6,6-tetramethylpyperidine-1-oxyl radical (TEMPO)-mediated oxidation.<sup>3</sup> The advantage of using TOBCN is clearly because of the presence of hydroxyl (OH) and carboxylate (COOH/COO<sup>-</sup>Na<sup>+</sup>) moieties on the surface of TOBCN.<sup>4</sup> In the present work, we investigate the possibilities of using these materials for energy storage in supercapacitor.

## 2. Experimental Section

The PPy/TOBCN composite films were prepared by dispersing 0.45 g of TOBCN in the distilled water (100 ml). A solution of 1 g of FeCl<sub>3</sub> was added to the TOBCN solution. After the mixture solution was stirred for 40 min, 1 ml pyrrole and 2 ml HCl were added to the PPy/TOBCN solution. The polymerization time was allowed to react for 1 h at room temperature. Finally, the resulting structure was collected on a filter paper and air-dried to a constant mass on a Petri dish.

## 3. Results and Discussion

To investigate the surface morphologies of TOBCN, PPy and PPy/TOBCN films, SEM micrographs were examined, as shown in Fig. 1. Fig. 1(a) shows a typical morphological structure of TOBCN composed of individual nanofibers with a diameter of about 10 nm. SEM of PPy/TOBCN exhibits that the PPy nanoparticles were entangled in the TOCN network and uniformly coated on the surface of TOBCN surface, as shown in Fig. 1(c and d).

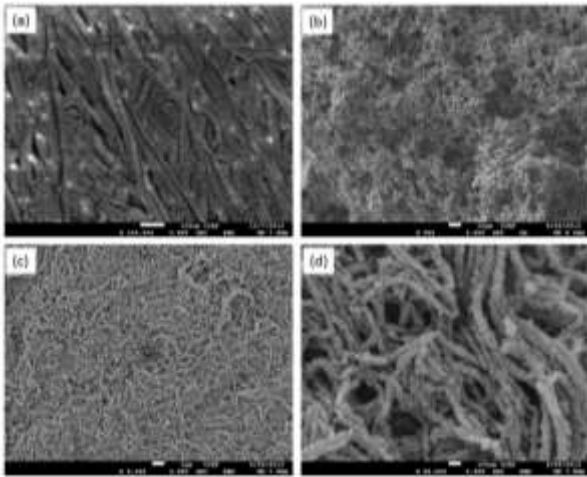


Fig. 1 SEM images: (a) TOBCN (5K $\times$ ), (b) PPy (500 $\times$ ), (c) TOBCN (5K $\times$ ), and (d) TOBCN (50K $\times$ )

Electrochemical behavior of the supercapacitor cell was investigated by galvanostatic charge/discharge, as shown in Fig. 2. Two pieces of PPy/TOBCN films were used as the electrodes and PVdF-EMIMBF<sub>4</sub> was used as the electrolyte, which was prepared by immersing electrospun membrane into EMIMBF<sub>4</sub> solution. The mass specific capacitance was carried out using the equation  $C_m = (I \times \Delta t) / (\Delta V \times m)$ , where  $\Delta t$  is the discharge,  $\Delta V = 1$  V, and  $m$  is the total mass (~40 mg). The value of  $C_m$  as high as 134 F/g was gained for the supercapacitor based on PPy/TOBCN and PVdF-EMIMBF<sub>4</sub> electrolyte at the current density of 0.2 A/g. The high  $C_m$  may be due to the good dispersion of PPy coated around TOBCN, which could provide a good electrolyte-accessible surface area to enhance utilization of PPy nanoparticles for redox reactions.<sup>5</sup>

The presented PPy/TOBCN composite material is high conductive, light-weight and flexible. It can be molded into various shapes. In addition, the thin sheets of PPy/TOBCN can be rolled to prepare compact energy storage devices. Also, the novel supercapacitor based on PPy/TOBCN composite material and PVdF-EMIMBF<sub>4</sub> electrolyte has a potential application in high-performance, wearable/stretchable and flexible, light-weight and environmentally friendly energy-storage devices.

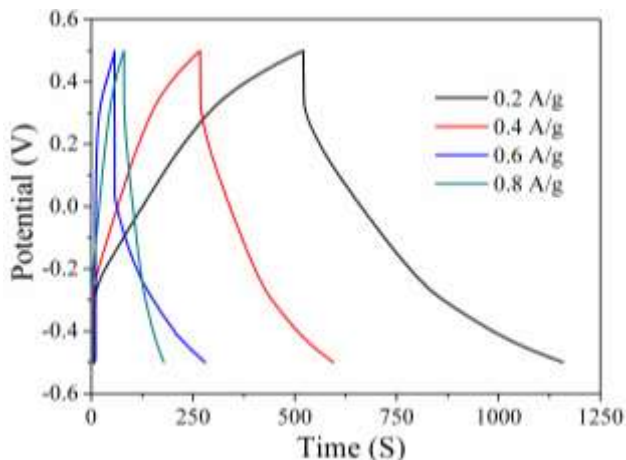


Fig. 2 Charge/discharge curves of the supercapacitor cell

## 4. Conclusion

In summary, a novel supercapacitor based on PPy/TOBCN and PVdF-EMIMBF<sub>4</sub> electrolyte was developed. The conductive PPy/TOBCN film was successfully synthesized by oxidative polymerization of pyrrole with iron (III) chloride as an oxidant and TOBCN as reinforcement agent. Our results demonstrated a flexible, stable and conductive composite film because of PPy nanoparticles well coated the surface of TOBCN network. The supercapacitor showing a mass-specific capacitance of 134 F/g at the current density of 0.2 A/g paves the way toward promising applications in future high-performance and flexible energy storage devices.

## ACKNOWLEDGEMENT

This work was supported by International Collaborative R&D Program through KIAT grant funded by the MOTIE (N0000894).

## REFERENCES

1. Nishide, H. and Oyaizu K., "Toward Flexible Batteries," *Science*, Vol. 319, No. 5864, pp. 737-738, 2008.
2. Schultze, J. W. and Karabulut. H., "Application Potential of Conducting Polymers," *Electrochimica Acta*, Vol. 50, No. 7, pp. 1739-1745, 2005.
3. Isogai, A., Saito, T. and Fukuzumi, H., "TEMPO-oxidized Cellulose Nanofibers," *Nanoscale*, Vol. 3, pp. 71-85, 2011.
4. Jradi, K., Bideau, B., Chabot, B. and Daneault, C., "Characterization of Conductive Composite Films Based on TEMPO-oxidized Cellulose Nanofibers and Polypyrrole," *J. Mater. Sci.*, Vol.47, pp. 3752-3762, 2012.
5. Nystrom, G., Razaq, A., Strømme, M., Nyholm, L. and Mihranyan, A., "Ultrafast All-Polymer Paper-Based Batteries," *Nano. Lett.*, Vol. 9, No. 10, pp. 3635-3639, 2009.

# Development of an Advanced Suturing Mechanism for an Endoscopic Surgery Using Successive Suturing Device

Byung Gon Kim<sup>1</sup>, Kyung Tae Jun<sup>1</sup>, Kyungnam Kim<sup>1</sup> and Daehie Hong<sup>1#</sup>

<sup>1</sup> Division of Mechanical Engineering, Korea University, Anam-dong, Seongbuk-gu, Seoul, Korea, 136-701  
# Corresponding Author / E-mail: dhong@korea.ac.kr, TEL: +82-2-3290-3369, FAX: +82-2-926-9290

KEYWORDS : Endoscope, Suture, Stitch, Bead, Successive Suturing Device

*A successive suturing device (SSD) has been developed for continuous suture operation using an endoscope. It is a device developed to make continuous suture operation to be performed using a bead and suction cap. In this paper, a basic mechanism of SSD is explained and its limitation is discussed. While a suction cap can effectively fix a stomach wall during suturing is being performed, it has a problem of interrupting a sight of operator and of increasing a difficulty of control of an endoscope. However, There is a risk that a problem which stitching fiber is cut because of a friction force of a stitch fiber and bead in the process of tightening the fiber tightly. In this paper, a new suturing method and several assistance tools to resolve the limitations of SSD will be introduced. It is a reversed needle tool to pull a stomach wall instead of a suction cap and a protection cap positioning a stomach wall and preventing unintentional wound. Due to this, some limitations of SSD have been overcome and a result has been proved through an in-vitro experiment.*

## 1. Introduction

Due to reduced recovery time, difficulty of operation and beauty, minimally invasive surgery has widely developed.<sup>1,2</sup> Many suturing devices using endoscope including T-tag, Eagle Claws, endoscopic staplers, endostitches, over-the-scope-clip system(OTSC) and successive suturing device (SSD), have already widely developed.<sup>3-12</sup> Few of them are verified for their feasibility and safety, but others have disadvantages on successive suturing operation since they do not allow consecutive suturing. In addition, some of them need additional equipment installation other than endoscope and suturing devices which make relatively difficult to pass through patients' throat. Most of equipment are not convenient and safe enough to be commercialized. Many researches on these issues have been continued.

We have been developed SSD.<sup>13</sup> It is a full thickness suturing device which sutures both muscular coat and mucous layer by using anchoring beads. Full thickness suturing has an advantage of recovery speed and safety compared with only suturing mucous layer. Currently, SSD can consecutively suture up to 6 times and also only using channel of conventional endoscope without any additional equipment attached. The better suture strength was proved in comparison with conventional endoscopic clip and hand suturing by a

specialist.<sup>14</sup>

SSD has relatively simple mechanism and good suture capacity, but there are some limitation to be solved before going on to clinical stage. In this paper, those limitations are discussed, and explain suturing process and development of a new equipment. Thus, through

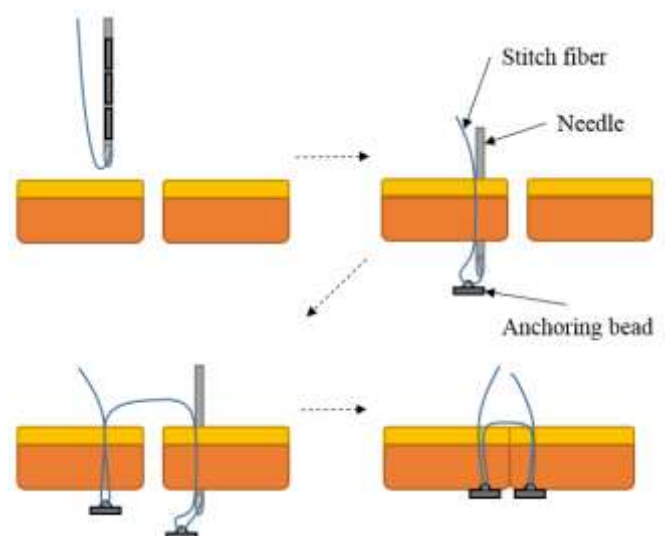


Fig. 1 Basic mechanism of SSD

in-vitro animal testing, increased work stability and suture efficiency are proven.

## 2. SSD

### 2.1 Basic mechanism

Basically SSD can perform suture operation by using a needle, a bead, and an anchoring bead. In previous research, its suture capacity has been proven.<sup>14</sup> The basic process of the device is Shown Fig. 1. Firstly, a suction cap approaches to the target position in the stomach and pulls a part of tissue to be sutured. Then, a needle from one of endoscope channel pierces through stomach wall and anchoring beads are discharged from the needle. A stitching fiber goes through the anchoring bead and comes back to inside of the stomach. The bead, then, is positioned on the opposite side of the stomach and holds the stitching fiber. The incision part used in previous experiment was a wound made by 18mm balloon for endoscope, and to suture this, six suturing operation was performed. To confirm its suture capacity, endoscopic clip and specialist's direct suture method were compared. Front suction cap was used to perform the experiment and thus, anchoring bead was placed on outer side of the stomach.

### 2.2 Limitation of SSD

#### 2.2.1 Suction cap

Two suction caps were used in previous research stage. One was normal endoscopic front suction cap, and the other one was side suction cap (Fig. 2).

In case of front suction cap, it does not block the view of endoscopic camera so that it allows accurate suction operation in relatively desired position. However, the main downside of it is the needle which pierce through from inside stomach to outside stomach so that can make unintended wound on organs outside stomach, as shown in Fig. 3(a). In previous experiment, such suction cap was used since it was only for proving suture capacity on extracted stomach. In animal test or clinical test, this method cannot be used.



Fig. 2 Front suction cap and side suction cap



(a) Front suction cap



(b) Side suction cap

Fig. 3 Suction and piercing through by needle

To overcome such difficulties of front suction cap, side suction cap has been developed. The side suction cap is designed to approach to tissues on stomach wall at right angle to suction direction. After the needle passes through tissues, it allows to discharge a bead inside stomach (Fig. 3 (b)). With this, it removes the possibility of damaging organ outside stomach and allows to perform in-vivo test. However, it has a limitation blocking the view of endoscopic camera, which gives inconvenient environment to an operator. Also the suction direction is fixed so that it is difficult to perform suture operation accurately. In addition, for thin tissue suction, 8mm\*7mm suction area is required while larger area is needed when practicing thicker tissue in muscular coat suction. The suction area is more than required area for 18mm incision part suture for NOTES and therefore performing precise suture operation in small part is difficult. This issue will be discussed in following section.

#### 2.2.2 Bead and stitching fiber

A system using a bead and a stitching fiber is one of methods that allows to perform suture operation overcoming limitation of endoscope which the task should be fulfilled on only one side of stomach wall. However, there are some limitations discovered in previous experiment. This device used a titanium bead and nylon stitching fiber. Six times suture operation results in very complicatedly tangled structure and frictional force on six points on a hook of the bead. When tightening stitching fiber tensely, frictional force on each point of contact increases and when over-tightened, it may be cut.

Also in the process of suture operation, bead and stitching fiber might disturb suction cap's work. When a bead is in the area of suction near incision site, they might be pulled up together and if a needle pierce through in this case, then a situation like fiber being cut or bead blocked inside a needle might happen. As successive suture operation is practiced, there are more beads and the fibers to be avoided in suction work and with the side suction cap's vision problem, it gets harder to operate.

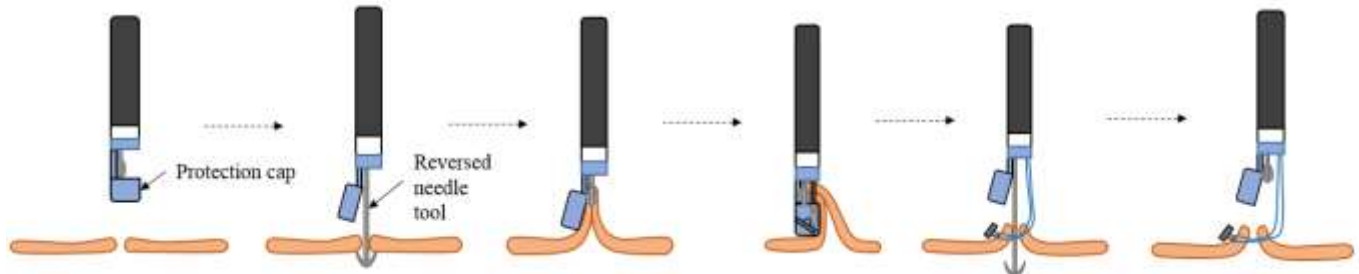


Fig. 4 Procedure of stitch using protection cap and reversed needle tool

**3. New suturing mechanism**

New suturing mechanism including reversed needle tool and protection cap was developed to overcome limitations of current equipment mentioned above. The reversed needle tool is designed to pull tissues replacing suction cap. The protection cap prevent needle from making unintended wounds while positioning stomach wall in the center of front endoscope so that the needle can pierce through stably. Using this, above mentioned limitations of SSD could be overcome and due to half-reduced number of process and beads needed for suture, operation time was reduced greatly. Also the part where blocking the view of endoscope was lessened providing more convenience to an operator, and with decrease in the number of beads needed the cut of stitching fiber due to friction between beads and the fiber can be solved. The procedure of stitch is shown in Fig. 4

**3.1 Reversed needle tool**

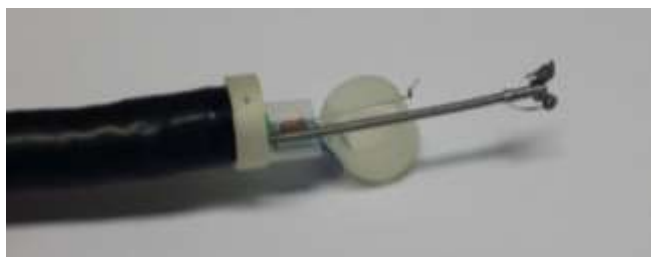
In case of using suction cap, all the parts of that except suction area should be sealed so it is inevitable to block the view of endoscope. Endoscope, though, should approach close to the incision part for suction. To overcome this, a new tool to bring stomach tissue to the front of endoscope instead of suction cap was developed. This equipment uses one of two endoscope channels so to perform suturing operation, two channel endoscope is needed. Two channel endoscope (GIF-2T 240, Olympus) was used in the development of this equipment. This tool, like a fish hook, the needle is hooked opposite to the direction of an endoscope and can be opened and folded as necessary (Fig. 5). The work process is as follows. To avoid making unintended wound, the folded needle goes through an incision part to outside of the stomach and opens up reversed needle. At that point, the needle faces toward the stomach wall from outside stomach and since there is no sharp part facing outside the stomach, it does not make any damage on outer organ. The reversed needle in opened position hooks the stomach wall from outside of the incision part and brings it to the front of an endoscope. Later, suturing process



(a) Endoscope head equipped with reversed needle tool



(b) Extrude the tool and open reversed needles

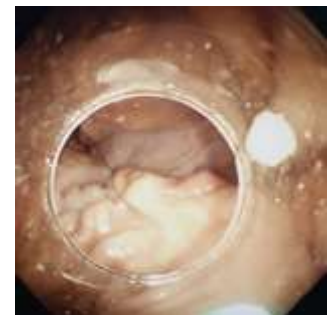


(c) Fold reversed needles to grab tissue

Fig. 5 Reversed needle tool



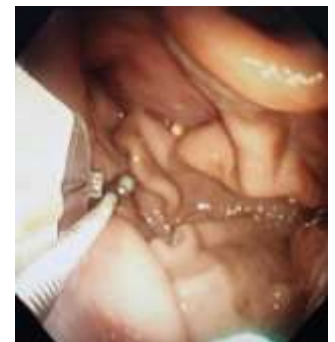
(a) Side suction cap



(b) Front suction cap



(c) Protection cap



(d) Extruding reversed needle tool

Fig. 6 Views of each caps

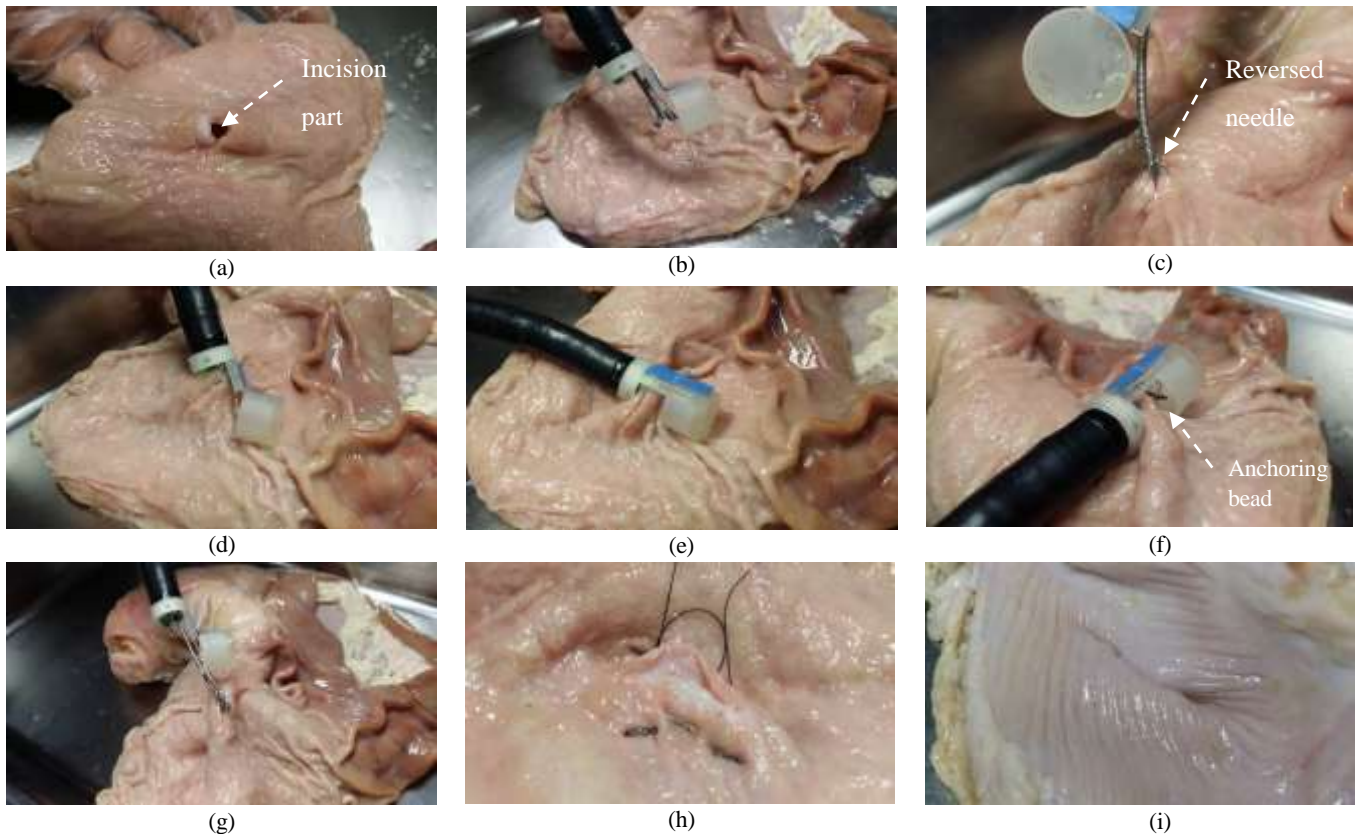


Fig. 7 Sequence of suture operation using new method. (a)Incision part is made on stomach wall. (b) An endoscope is controlled to aim incision part. (c) A Reversed needle tool grabs tissue. (d) Stomach wall is pulled at front of endoscope. (e) A Protection cap is fold to position incision part. (f) An anchoring bead is extruded. (g) A protection cap opens and reversed needle tool is took out from stomach wall. (h) A result of suture on inner side of stomach wall. (i) A result of suture on outside of stomach wall

is performed, and the reversed needle tool is removed from the stomach wall and is folded to come back into the stomach. This gives several advantages over suction cap, which provides clear view and decreases the limitation to approaching direction toward incision site on stomach wall. Unlike the case of side suction cap, with the reversed needle tool, an endoscope can face the incision part at front, which gives more convenience to an operator. Also both side of the incision parts are positioned in front of the needle at the same time which allows the needle to pierce through two layers of the stomach wall at once. As a result, number of beads needed for one stitch is reduced to one from two.

### 3.2 Protection cap

In addition to application of the reverse needle mentioned above, a new cap to improve suture safety and convenience was developed. The role of this cap is to prevent inadvertent wound when the needle pierces as well as positioning stomach wall so that the needle can pierce two layers of the wall at once. Not to block the view of an endoscope, this cap was installed opened to outside by torsion spring and can be closed using wire when necessary. The views of each caps is shown in Fig.6

First the reverse needle tool explained earlier moves forward to drag tissues in the incision part which to be sutured toward the front of an endoscope. Then, both sides of the incision part will be positioned to the front of the channel where the needle is installed as

closing the cap by pulling the wires connected to it. Then when the needle pierces the stomach wall, both side of incision parts will also be pierced, and at that point, the needle does not damage any other parts by the protection cap positioned at opposite side. After a bead is discharged, the needle is retrieved. Such task gives convenience compared to previous method since an endoscope is looking at the incision site from the front directly while operation is performed. Also less area is needed when pulling tissues compared to suction cap, relatively precise suture operation can be performed, and with one pierce and one bead the same result can be obtained as two performance of the former method.

### 3.3 Result of suture operation

If suture operation is performed using previously mentioned tool, the final suture form is shown in fig. 8. Three beads are used and three stitch works were performed. It is equivalent to six beads and six stitch works by previous method. As a result, the number of operation performed was halved, and also the frictional force on bead and stitching fiber when tightening the fiber was also halved.

## 4. Experiment

To verify the feasibility of the equipment, in-vitro test was conducted. A stomach similar to humans was extracted from a pig which

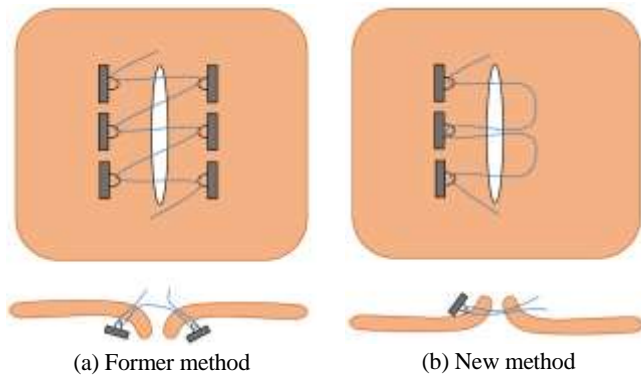


Fig. 8 Result of suture operation

often used for endoscope experiment was used. Whole stomachs were acquired from a local butcher shop immediately after sacrifice, and the specimens were tested as soon as they were obtained. The sequence of suture operation using new method is shown in Fig. 7. To compare with previous equipment, 3 stitching were performed, and time taken was compared. The reverse needle has 5mm of length and 15mm when opened maximum. This was long enough to cover both sides of incision part but sometimes, it could not drag both sides of incision part or only stitching muscular coat except mucous layer. Depending on the size of incision part, adjusting the length of the reverse needle should be improved. For protective cap, it positioned stomach wall effectively and prevented damaging unintended parts. However, there is a situation that a bead is discharged cannot be seen at all as it is covered with a stomach wall.

A process of tightening a suture after completing suturing has clearly improved compared to the past. A suture could be tightened relatively smoothly and a condition of a stomach wall after completing suturing can be seen in Fig. 8. It is similar with a result of suturing of existing SSD. It also expected that suturing strength would be also similar but it needs to be verified by an additory experiment.

## 5. Conclusion and discussion

There are few limitations to be solved for current SSD before clinical test stage. In this paper, the new stitching method to overcome the limitation and the tool to realize this was introduced. Those can be simply installed on a conventional endoscope and keep having strong points of SSD which are simple structure and mechanism and ability to practice successive suturing operation, they give more convenient operation with shorter working hour. The short working hour and the convenient operation will give less fatigability in surgery environment and avoid medical accidents, which is imperative in application of the clinical test. This is a prerequisite for an endoscopic suture device to be commercialized other than effective suture capacity.

There are several problems to be resolved. First, even though a reversed needle tool was effective to grip and pull a stomach wall, a case that the tool cannot be collected as a reverse needle and stitching fiber became entangled in the process of releasing a stomach wall.

Also, this is too big at present so it is not easy to install and remove from an endoscope. A study on a miniaturization method is necessary. Because this mechanism has a structure that a worker cannot see a process of a bead being discharged, a function which can guarantee discharge of a bead should be added to a protective cap. There is a possibility that suturing strength became weakened because a number of beads used for suturing is reduced compared to an existing method. An additional study comparing suturing strength is also necessary.

Suture device introduced in this paper needs less number of beads compared to previous one, but since the number of stitches for suture are the same so the suture strength is expected to be similar. This is a part where it needs further investigation in other research.

## ACKNOWLEDGEMENT

This research was supported by Basic Science Research Program through the National Research Foundation of Korea (NRF) funded by the Ministry of Science, ICT & Future Planning (MSIP) (No. 2007-0056094). And this work was supported by the Human Resources Program in Energy Technology of the Korea Institute of Energy Technology Evaluation and Planning (KETEP) grant financial resource from the Ministry of Trade, Industry & Energy, Republic of Korea. (No. 20124010203250)

## REFERENCES

1. Wagh, M. S., Merrifield, B. F. and Thompson, C. C., "Endoscopic transgastric abdominal exploration and organ resection: initial experience in a porcine model," *Clinical Gastroenterology and Hepatology*, Vol. 3, No. 9, pp. 892-896, 2005.
2. Giday, S. A., Kantsevov, S. V. and Kalloo, A. N., "Principle and history of natural orifice transluminal endoscopic surgery (NOTES)," *Minimally Invasive Therapy & Allied Technologies*, Vol. 15, No. 9, pp. 373-377, 2006.
3. Azadani, A., Bergstrom, M., Dot, J., Abu-Suboh-Abadia, M., Armengol-Miro, J. R. and Park, P., "A new in vivo method for testing closures of gastric NOTES incisions using leak of the closure or gastric yield as endpoints," *Journal of Laparoendoscopic & Advanced Surgical Techniques*, Vol. 22, No. 1, pp. 46-50, 2011.
4. Austin, R. C. P., Mosse, C. A. and Swain, P., "A novel use of T-tag sutures for the safe creation and closure of the NOTES gastrotomy using a hybrid technique," *Surgical Endoscopy*, Vol. 23, No. 12, pp. 2827-2830, 2009.
5. Chiu, P. W., Lau, J. Y., Ng, E. K., Lam, C. C., Hui, M., To, K. F., Sung, J. J. and Chung, S. S., "Closure of a gastrotomy after transgastric tubal ligation by using the Eagle Claw VII: a survival experiment in a porcine model (with video)," *Gastrointestinal Endoscopy*, Vol. 68, No. 3, pp. 554-559, 2008.

6. Ryou, M., Fong, D. G., Pai, R. F., Rattner, F. W and Thompson, C. C., "Transluminal closure for NOTES: an ex vivo study comparing leak pressures of various gastrotomy and colotomy closure modalities," *Endoscopy*, Vol. 40, No. 5, pp. 432-436, 2007.
7. Sodergren, M. H., Comber, R., Clark, J., Karimyan, V., Athanasiou, T., Teare, J., Yang, G. Z. and Darzi, A., "What are the elements of safe gastrotomy closure in NOTES? A Systematic Review," *Surgical innovation*, Vol. 17, No. 4, pp. 318-331, 2010.
8. Schurr, M. O., Arezzo, A., Ho, C. N., Anhoeck, G., Buess, G and Lorenzo, N. D., "The OTSC clip for endoscopic organ closure in NOTES: device and technique," *Minimally Invasive Therapy & Allied Technologies*, Vol. 17, No. 4, pp. 262-266, 2008.
9. Meireles, O. R., Kantsevov, S. V., Assumpcao, L. R., Magno, P., Dray, X., Giday, S. A., Kalloo, A. N., Hanly, E. J. and Marohn, M. R., "Reliable gastric closure after natural orifice transluminal endoscopic surgery (NOTES) using a novel automated flexible stapling device," *Surgical Endoscopy*, Vol. 22, No. 7, pp. 1609-1613, 2005.
10. Renteln, D. V., Vassiliou, M. C. and Rothstein, R. I., "Randomized controlled trial comparing endoscopic clips and over-the-scope clips for closure of natural orifice transluminal endoscopic surgery gastrotomies," *Endoscopy*, Vol. 41, No. 12, pp. 1056-1061, 2009.
11. Arezzo, A. and Morino, M., "Endoscopic closure of gastric access in perspective NOTES: an update on techniques and technologies," *Surgical Endoscopy*, Vol. 24, No. 2, pp. 298-303, 2010.
12. Banerjee, S, Barth, B. A., Bhat, Y. M., Desilets, D. J., Gottlieb, K. T., Maple, J. T., Pfau, P. R., Pleskow, D. K., Siddiqui, U. D., Tokar, J. L., Wang, A. and Rodriguez, S. A., "Endoscopic closure devices," *Gastrointestinal Endoscopy*, Vol. 76, No. 2, pp. 244-251, 2012.
13. Bae, K., Jung, K., Chu, B., Hong, D., Chun, H., Kim, Y. and Keum, B., "Development of a novel successive suturing instrument for an endoscope using beads and a side suction cap," *International Journal of Precision Engineering and Manufacturing*, Vol. 10, No. 2, pp. 97-103, 2009.
14. Song, Y., Choi, H. S., Kim, K., Kim, Y., Kim, B. G., Hong, D., Keum, B. and Chun, H. J., "A simple novel endoscopic successive suture device: a validation study for closure strength and reproducibility," *Endoscopy*, Vol. 45, No. 8, pp. 655-660, 2013

# An Experimental Study on the Multiple Layer Perforated Panel Sound Absorbing System for Railroad Noise Reduction

Yoon-Sang Yang<sup>1</sup>, Du-San Baek<sup>2</sup>, Dong-Hoon Lee<sup>2#</sup>, Jae-Chul Kim<sup>3</sup> and Choon-Keun Park<sup>4</sup>

<sup>1</sup> Department of Energy System Engineering, Seoul National University of Science and Technology

<sup>2</sup> Department of Mechanical and Automotive Engineering, Seoul National University of Science and Technology

<sup>3</sup> High Speed Railroad Systems Research Center, Korea Railroad Research Institute

<sup>4</sup> Taechang Nikkei CO.,LTD

# Corresponding Author / E-mail: ldh@seoultech.ac.kr, TEL: +82-2-970-6331, FAX: +82-2-979-7331

KEYWORDS : Environment Noise, Panel Sound Absorbing System, Railroad Noise, Sound Absorption Coefficient, Sound Absorbing Material

*Passengers in subway train are exposed to a worse noise environment when they are in the tunnel than in the open field. Many of research on the noise reduction techniques such as the attachment of the sound absorbing materials on the tunnel wall or rail ballast, rail coating and rail grinding have been progressed for the improvement of the noise environment in subway train. From the previous study on the proposed noise reduction techniques, it is shown that the bulk reacting type sound absorbing materials such as the polyester, light weight concrete block with air pocket and polyurethane foam have a good sound absorbing performance, but they have some disadvantages like corrosion by moisture, dust scattering, malfunction of absorbing performance by repetitive wind pressure, difficulty with water cleaning and fire problems. In order to overcome these problems, thus, an locally reacting type sound absorbing system which consisted of the dimensions such as thickness, hole diameter and porosity, the depth of airspace and the number of the perforated panels is proposed as an alternative for the improvement of the noise environment in a cabin by the reduction of tunnel noise.*

*The objective of this study is to investigate design parameters on the multiple layer perforated panel sound absorbing system for the reduction of the tunnel noise in the subway. Multiple layer perforated panel sound absorbing system composed of the perforated panel with sub-millimeter holes and the airspace backed a rigid wall or between panels. The experiment is performed through the change of number of perforated panel, cross sectional area and the depth of airspace of the perforated panel absorbing system under the conditions of the normal and random incidence sound, respectively.*

*From the experimental result, it is shown that the acoustic resonance frequency at which acoustic absorption becomes maximal is well consistent with the number of perforated panel for multiple layer perforated panel system. This acoustic resonance frequency can be controlled by the adjustment of the number of perforated panel, cross sectional area and the depth of airspace. It is found that it has better absorption performance at lower frequency band to increase the number of perforated panel.*

## 1. Introduction

Passengers in subway train are exposed to a worse noise environment when they are in the tunnel than in the open field. The reason is that the sound intensity of the acoustic field in the tunnel significantly increases by reflected waves occurred in the closed space. Many of research on the noise reduction techniques such as the attachment of the sound absorbing materials on the tunnel wall or rail ballast, rail coating and rail grinding have been progressed for the improvement of the noise environment in subway train. The noise reduction effects of sound absorbing material showed

2~3dB(A) and rail coating and rail grinding showed 2dB(A).<sup>(1)</sup>

From the previous study on the proposed noise reduction techniques, it is shown that the bulk reacting type sound absorbing materials such as the polyester, light weight concrete block with air pocket and polyurethane foam have a good sound absorbing performance, but they have some disadvantages like corrosion by moisture, dust scattering, malfunction of absorbing performance by repetitive wind pressure, difficulty with water cleaning and fire problems. In order to overcome these problems, thus, an locally reacting type sound absorbing system which consisted of the dimensions such as thickness, hole diameter and porosity, the depth of airspace and the number of the perforated panels is proposed as an alternative for the

improvement of the noise environment in a cabin by the reduction of tunnel noise.<sup>(2)</sup>

The objective of this study is to investigate design parameters on the multiple layer perforated panel sound absorbing system for the reduction of the tunnel noise in the subway.

**2. Experimental theory**

Fig. 1 schematically shows an impedance tube having no flow of plane sound field with two microphones used to obtain acoustic characteristics at one end of the tube.

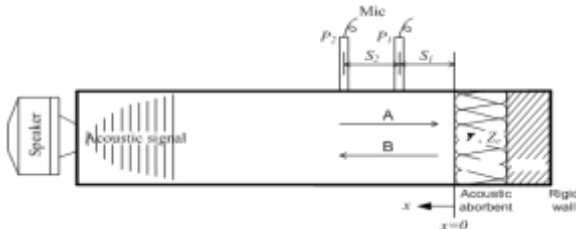


Fig . 1 Schematic of an acoustic impedance tube

The acoustic pressures at  $p_1$  and  $p_2$  are Eq.(1) and Eq.(2), respectively.

$$p_1 = Ae^{j(\omega t + ks_1)} + Be^{j(\omega t - ks_2)} \tag{1}$$

$$p_2 = Ae^{j(\omega t + k(s_1 + s_2))} + Be^{j(\omega t - k(s_1 + s_2))} \tag{2}$$

The transfer function was defined by  $H_{12} = p_1 / p_2$  as follows

$$H_{12} = \frac{Ae^{+jks_1} + Be^{-jks_2}}{Ae^{+jk(s_1+s_2)} + Be^{-jk(s_1+s_2)}} \tag{3}$$

The reflection coefficient can be calculated by measuring only the transfer function as follows <sup>(3)</sup>

$$R = \frac{H_{12} \times e^{+jk(s_1+s_2)} - e^{+jks_1}}{e^{-jks_1} - H_{12} \times e^{-jk(s_1+s_2)}} \tag{4}$$

By substituting Eq. (4) into Eq. (5), the normal incidence sound absorption coefficients of multiple layer perforated plate systems are obtained.

$$\alpha_n = 1 - |R|^2 \tag{5}$$

**3. Experimental setup**

Fig. 2 shows the experimental setup for measuring the normal incidence sound absorption coefficients of multiple layer perforated panel sound absorbing systems. The impedance tube is a

rectangular acrylic pipe of 35mm × 35mm cross-section, 900mm in length, and 10mm in thickness. Two microphones are mounted flush with the inner surface of the impedance tube. Microphones used in this experiment are 1/4inch pressure type. A loudspeaker is located at one end of the impedance tube, and the multiple layer perforated panel sound absorbing system is attached at the other end. A random sound generator provides sound signal through an amplifier to the loudspeaker. The frequency range of the frequency analyzer is up to 4,000Hz and the resolution is set to 8Hz.

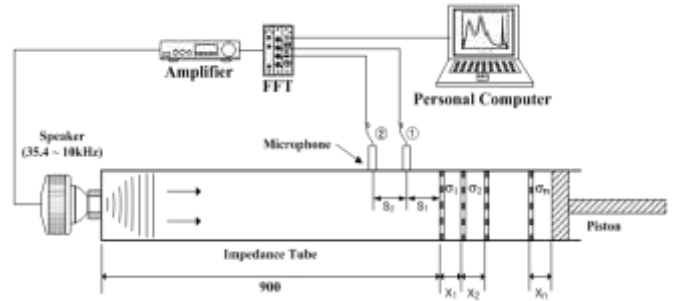


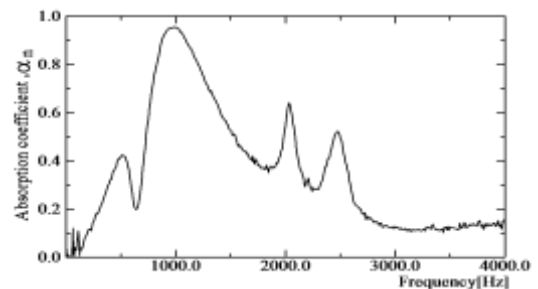
Fig. 2 Experimental setup for sound absorption coefficient measurement

A sound transfer function is measured using two microphones mounted at two locations of the tube. Where  $s_1$ (=80mm) is the distance between the first microphone and perforated plate and  $s_2$ (=40mm) is the distance between two microphones.

**3. Results and discussion**

For studying the effect of the number of perforated panel on the normal sound absorption coefficient of the multiple layer perforated panel system, the measured absorption coefficients with increasing the number of perforated panel are compared in Fig. 2. Here the symbol n in the figures indicates the number of perforated panel. The length of airspace is 30mm and the porosity of perforated plate is  $\sigma = 1\%$ . From the results shown in Fig. 3, it can see that increasing the number of perforated panel has better absorption coefficient at lower frequency bands and more broadband absorption ranges.

(a) n=1



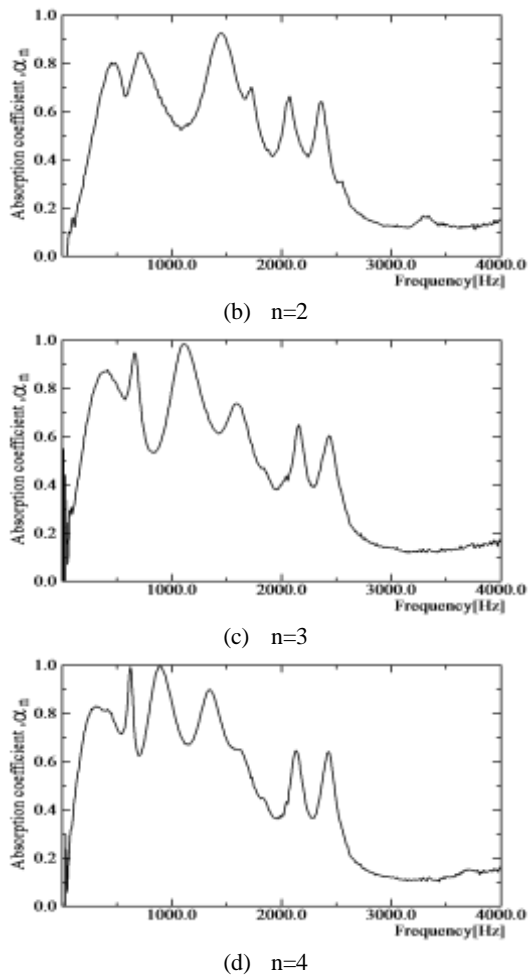


Fig. 3 Effect of the number of perforated panel on the normal sound absorption coefficients

#### 4. Conclusion

The acoustic resonance frequencies can be controlled by adjustment of porosity and length of airspace. Multiple layer perforated panel has better absorption performance than single layer perforated panel at lower frequency bands and more broadband absorption ranges.

#### ACKNOWLEDGEMENT

This subject is supported by the Korea Ministry of Environment as “Advanced Industrial Technology Development”

#### REFERENCES

1. C. K. Hong, R. T. Jeong and B. H. Kim, “A Study on an Analysis of Noise Reduction Effects using the tentatively Installed Sound-absorbing Materials in Metro Tunnel”, Proceedings of the Korean Society for Railway annual autumn conference, pp.125-131, 2008.
2. D. H. Lee and Y. P. Kwon, “Estimation of the absorption performance of multiple layer perforated panel system by transfer matrix method”, JSV, Vol.278, pp. 847-860, 2004.

3. J. Y. Chung and D. A. Blaser, “Transfer Function Method of Measuring in-Duct Acoustic Properties. Theory, II Experiment”, J. Acoust. Soc. Am., Vol. 68, No. 3, pp. 907-921, 1980.

# Complete Recycling Method for Lungfishes Waste

Doo Hee Han

1 Dept. of Architectural Engineering, Chungwoon University, 113, Sukgol-ro, Nam-gu, Incheon, South Korea 402-803 (Zip code)  
# Corresponding Author / E-mail: hanknu@hanmail.net, TEL: +82-10-9352-5404, FAX: +82-32-770-8171

KEYWORDS : Sea fish waste, Organic Waste, Recycling

---

*Abstract In this paper, a method for drying a variety of untreated fish waste, and carbonizing the dried material under a reduced pressure, thereby achieving a more stable and economical treatment for the waste materials, and an apparatus for performing the method were discussed. We proposed updated speedy dryer which have continuous input and screw conveyor. If we use updated speedy dryer, fish waste can be changed to useful feed and liquid composts. With the method and apparatus, it is possible to separate condensate water from a high-temperature and high-humidity air stream and discharge the condensate water having passed through a purifying operation, while utilizing the residual air stream as burning air required for drying and carbonization of waste material. This has the effects of preventing from generation of contaminants and environmental pollution while reducing fuel costs, and a carbide, obtained via the drying and carbonization of the waste material, is available into solid fuel having superior burning efficiency. The condensate water can be used to deodorants.*

---

## 1. Introduction

In general, the reclamation, fermentation & drying, drying, combustion, and others are used for waste treatment. With the contamination surrounding the landfill, generation of leachate, bad odor, and others, the allowance of reclamation among them is very limited thus it does not function as fundamental resolution for waste treatment. Also, considerable amount of time and effort are required for the utilization of it as compost using fermentation treatment and there is difficult of resolving environmental contamination as large quantity of harmful gas or bad odor is generated during the fermentation & drying process. Also, it is improper to be directly utilized due to high content of salt within compost and particularly it has shortcomings in that there is only limited numbers of waste types to which fermentation & drying treatment can be conducted among non-treated waste available for such fermentation & drying process. Moreover, although the drying methods include hot-air drying, floating air input drying, rotary kiln type drying, micron spraying type drying, and others, all of these mixes outer air and puts inside and presents high ratio of exhaust in inner current thus it spreads the exhaust related contamination with the difficulty of disposing the exhaust, brings about fuel loss due to the direct outer exhaust during the treatment, and present very low combustion rate as solid fuel because drying substance cannot adhere to floating inner current due to supply of outer air in drying process. Moreover, as it performs the drying operation with the use of separate heat source from the outside, it is uneconomical as it requires high fuel cost, difficult to recycle as

there is imbalance in property even in case of substance completed of drying treatment, and recognized as unpleasant facility as environment contaminants generated during the drying treatment deteriorates surrounding environment. The purpose of this study lies in introducing complete recycling method to conduct distilled drying of fish waste rich in fat and protein using, utilize the solids as livestock feed, and utilize the condensate water as deodorant and external source of carbon for sewage treatment plant using continuous dryer[1].

## 2. Continuous High Speed Dryer

### 2.1 Design

Continuous high speed dryer is composed of transmission and agitating device with L-shaped wing, heating device, heat exchanger, condensate water producing device, inner current circulator, and others. In regards to the agitating device, it was devised so that screw with L-shaped wing performs not only the rotation but also drying function of lungfishes by the heat. Weighing feeder adjusts and supplies adequate amount of waste to be circulated inside the dryer. Heat exchanger and condensate water producing device induces the congelation by quenching at the moment gas with high temperature and moisture passes through. Then, it discharges the condensate water outside and circulates dry gas once again with high temperature to assist the heating. When such process is repeated, solids are dried. Inner heating temperature shall maintain at 80~100°C.

## 2.2 Production of Testing Equipment

For the testing equipment, facility of 10 ton/day was manufactured based on daily treatment capacity. L-shaped spiral screw for transmission and drying was made to perform smooth agitation and prevent the foreign bodies from adhering to the inner wall. In regards to condensate water producing device, dryer and heat exchanger were installed outside to increase the efficiency of drying. The efficiency of drying process enabled 1 ton of lungfishes to dry with water content of under 5% in 8 hours. Fig 1 illustrates the example of installation.



Fig. 1 Sample(Speedy dryer)

Drying process can be briefly summarized as below [3].

- 1) Input and seal the lungfishes and intestines of fish to storage hopper of collection vehicle for temporary storage.
- 2) Crush the waste input to storage hopper.
- 3) Transfer food waste within crusher to weighing feeder through sealed transporter.
- 4) Produce solids and condensate water by continuous drying process.
- 5) Adjust the speed so that water content of dried matters is under 5%.
- 6) Transport to sorting machine through an outlet for automatic sorting and separation.

## 3. Sampling and Component Analysis

### 3.1. Test Operation

Only lungfishes and intestines of fish except those with hard shell including clams, conches, and others were used for test operation. In case of drying the lungfishes only, the drying was unsuccessful with the formation of mass during the drying process caused by large quantity of fatty substances. 1 ton of marine waste could be dried within 5 hours when the drying is conducted together with foliage powder rich in fiber.

### 3.2. Manufacturing of Test Feed

Dried matters were temporarily stored after removing foreign bodies with vibrating screen. Location with great ventilation was necessary as it solidifies under high moisture atmosphere. Fig. 2 illustrates the property of dried marine waste.



Fig. 2. Dried sea waste

### 3.3. Test Application of Feed

Feed was applied to nearby duck farm. As a result of 1 month use, there was no problem with the growth of duck under naked-eyes. We showed the components of lungfishes waste after drying, also heating low value is 5200kcal/kg. Location with great ventilation was required as it solidifies under high moisture atmosphere.

Table 1. Components of lungfishes waste after drying.

Organics(%)							Heating Low Value
C	H	N	O	S	Cl	Ash	
41.1	7.1	3.32	33.0	0.45	2.24	13.2	5200kcal/kg

## 4. Conclusion

Although relatively large amount was used as the compost in regards to the recycling of organic waste such as food waste, it is high time for development of new substitute feed with the increase in feed price. When waste fish and shellfish are effectively dried and utilized as quality feed to meet such demand, simultaneous performance of waste treatment and recycling becomes available. Although petroleum was generally used for heat source of dryer in the past, it is inadequate with the increase in oil price thus the drying with relatively inexpensive nighttime electricity or steam boiler which uses the waste heat of incinerator is beneficial. We have succeeded in effectively making dry powder by adding external fiber material to marine waste and using sealed high speed dryer. Above method could fundamentally prevent the generation of bad odor during the drying process and presented potential for effective feed production through standardized packaging. As a

result of test feeding on poultry, no distinctive impediment was detected and growth status was similar compared to using previous feed. Condensate water can be utilized for deodorant, external carbon source of sewage treatment plant, and others. Therefore, complete recycling of marine waste can be accomplished when using solid/liquid separator method by evaporation with sealed type high speed dryer.

## REFERENCES

1. D. Han, "Development of food waste recycling method", Final report of CNETDC, 2007
2. D. Han, "Perfect recycling of sea fish waste by speedy dryer", J. of Environmental and Thermal Engineering, 2010
3. D. Han, "A study on the recycling method of food waste burning energy", Final report of Sanhakfund, 2008

# A New Energy Efficiency Index for the German Manufacturing Sector

Jörg Mandel<sup>1#</sup> and Alexander Sauer<sup>2</sup>

<sup>1</sup> Institute for Energy Efficiency in Production, University of Stuttgart, Nobelstr. 12, 70569 Stuttgart, Germany  
<sup>2</sup> Laboratory of Applied Manufacturing Technology, Munich University of Applied Sciences, Lothstr. 64, D-80335 Munich, Germany  
 # Jörg Mandel/ E-mail: joerg.mandel@eep.uni-stuttgart.de, TEL: +49-711-970-1980, FAX: +49-711-970-1002

KEYWORDS : Energy-Efficiency-Index, German Industry Sector, leading Index, Energy Savings, Energy Efficiency Investment, Importance of Energy Efficiency

*Reliable measurements of energy efficiency relevant developments are of increasing importance to decision makers on various levels. In order to effectively assess the current situation as well as future advancements in the field of energy efficiency, index concepts are inevitable. The paper briefly reviews existing energy efficiency figures applied in Germany followed by the description of the concept and implications of a new leading energy efficiency indicator that is tailored towards the manufacturing industry, the new Energy-Efficiency-Index (EEI) for the German manufacturing sector. Its ascertainment-based concept is related to the ifo-economic climate index, detecting the overall rating of the importance of energy efficiency for German companies, investments into energy efficiency measures and achieved energy savings. The index takes into account both assumptions of future development of energy efficiency relevant aspects of the companies and their achievements in the recent past. The Energy-Efficiency-Index is composed of several sub-indices structured in three categories – the importance of energy efficiency to the companies, the investment in energy efficiency means and the energy savings. The Energy-Efficiency-Index climaxes in a top index figure representing the energy efficiency climate in the German manufacturing sector.*

## 1. Index calculation and Energy Efficiency Indices

### 1.1 Theoretical background of index figures

Indices, or index numbers, are ratios that can be classified into elementary indices, growth indicators, and composite indices (Cramer et al. 2008). Before creating an energy efficiency index of the German manufacturing sector, the differences of the three terms will be briefly explained.

Elementary indices are expressed as the quotient of two measured values, using time series to track the trend of the measured values. For the denominator of this quotient, a fixed reference value is defined, while the numerator indicates the measured values of the reporting period. Examples for elementary indices are the prices quoted for bonds. For instance, the price for a Unitymedia GmbH (WKN A1CRZ6) bond on 11.02.2013 was quoted as 109.85% of its face value. This shows that the current market value always relates to the face value.

Index	Calculation	Notes
Elementary index	$I_{k,t} = \frac{x_t}{x_k}$	$k \in \{0, \dots, s\}$ $x_t, t \in \{0, \dots, s\}$ $x_k$ Fixed date Reporting value Base value
Growth indicator	$w_t = \frac{x_t}{x_{t-1}}$	$x_t, t \in \{1, \dots, s\}$ $x_{t-1}$ Reporting value Reporting value of the previous period
Laspeyres price index	$P^L_{0,t} = \frac{\sum_{j=1}^n p^t_j q^0_j}{\sum_{j=1}^n p^0_j q^0_j}$	$q^k_1 \dots q^k_n$ mit $k \in \{0, t\}$ Items under consideration at base date ( $k = 0$ ) and reporting date ( $k = 1$ )
Laspeyres quantity index	$Q^L_{0,t} = \frac{\sum_{j=1}^n p^0_j q^t_j}{\sum_{j=1}^n p^0_j q^0_j}$	
Paasche price index	$P^P_{0,t} = \frac{\sum_{j=1}^n p^t_j q^t_j}{\sum_{j=1}^n p^0_j q^t_j}$	$p^k_1 \dots p^k_n$ mit $k \in \{0, t\}$ Prices for items under consideration at base date ( $k = 0$ ) and reporting date ( $k = 1$ )
Paasche quantity index	$Q^P_{0,t} = \frac{\sum_{j=1}^n p^t_j q^t_j}{\sum_{j=1}^n p^t_j q^0_j}$	
Fisher price index	$P^F_{0,t} = \sqrt{P^L_{0,t} \cdot P^P_{0,t}}$	
Fisher quantity index	$Q^F_{0,t} = \sqrt{Q^L_{0,t} \cdot Q^P_{0,t}}$	

Fig. 1: Selected rules for calculating index numbers

Growth indicators, unlike elementary indices, have no fixed reference value but instead use the measured value of the preceding reporting

period as the denominator. The ratio is therefore expressed as a quotient of the measured values of the reporting period and the immediately preceding period.

Growth indicators can be used, for example, to point out the population growth. The Federal Statistical Office, for instance, projected an overall population growth in Germany of 0.1% for 2011 (Destatis 2013a).

While elementary indices and growth indicators provide a ratio for a single item, composite indices can be used to produce a ratio for groups of items (e.g. baskets of goods) as quantity, price or sales indices. To calculate them, the methods of Paasche, Laspeyres and Fisher are applied (Cramer et al. 2008). A sales index is an elementary index, while price and volume indices require a more detailed description. A price index compares the current price of an item to its price in a base period, weighting the resulting ratio for all items considered, whereas a quantity index compares and weights the quantities for all items considered.

The methods of Paasche and Laspeyres differ in how they apply weighting. With Paasche, the price index uses the quantities of the reporting period and the base prices, while the quantity index uses the prices of the reporting period and the base quantities. For each reporting period, the weighting is adjusted accordingly. By contrast, the Laspeyres price index uses the quantities of the base period, while the quantity index uses the prices of the base period. Thus, the weighting remains constant across all reporting periods. Applying Fisher's method for calculating an index means to take the geometric mean from the Paasche and the Laspeyres results (Cramer et al. 2008). The stock market index DAX 30 exemplifies how to calculate an index according to the Laspeyres price index. The reported stock prices reflect the prices of the analyzed objects (i.e. stocks). The relevant numbers of stocks used for calculating the index are subject to regular reviews and are adapted, if necessary. Correction factors are used to take account of the fact that the DAX 30 is not a price index but a performance index (Stankov 2008).

## 1.2 The Ifo Business Climate Index

The Ifo Business Climate is a leading indicator for economic development in Germany (Ifo 2013). It is based on about 7,000 monthly survey responses of firms in manufacturing, construction, wholesaling and retailing. Companies are asked to give their assessments of the current business situation and their expectations for the next six months. The assessment differentiates three categories for the current situation: good, satisfactorily and poor. The expectations for the upcoming six month are divided into: more favourable, unchanged and more unfavourable. The replies are weighted according to the importance of the industry and aggregated. As a first step of the calculation of the index balance values of the current business situation and the expectations are quantified as the difference of the percentages of the responses "good" and "poor" and the difference of the percentages of the responses "more favourable" and "more unfavourable". The business climate is subsequently

calculated as a mean of the balances of the business situation and the expectations as follows:

$$\text{Business Climate Balance} = \sqrt{(\text{situation} + 200) \cdot (\text{expectations} + 200)} - 200$$

The Ifo Business Climate balances can thus fluctuate between extreme values of -100 and +100. The negative value of -100 is realized when all responding firms appraise their situation as poor or expect business to become worse. The positive value of +100 visualizes the situation if all responding firms assessed their situation as good or expect an improvement in their business. For calculating the index values the business climate balance under review is normalized to the average business climate balances of a base year. Both nominator and denominator are increased by 200. The index value is thus calculated by:

$$\text{Index value} = \frac{\text{Business Climate Balance} + 200}{\text{Average Business Climate Balance in the base year} + 200} \cdot 100$$

## 1.3 Energy Efficiency Indices

Pérez-Lombard et al. (2013) review some energy efficiency fundamental topics by addressing the problem of measuring energy efficiency both in qualitative and quantitative terms and discussing main methodological problems of the construction of energy efficiency indicators including the links between energy efficiency and energy savings. Their work focuses on the precise measurement of efficiency ratios. The recent development of energy efficiency indicators in Germany follows a different approach. Subsequently, four main indices applied in Germany are highlighted.

DENA publishes the quarterly German Energy Turnaround Index (*Deutscher Energiewendeindex, DEX*) in cooperation with Ernst & Young (Edelmann, Kohler 2013). The aim being to contribute to an objective discussion of the consequences and requirements of the 'Energiewende' or energy transition, the DEX tries to fully capture the mood of the stakeholders and all that are concerned. To this end, about 2000 executives and directors from different sectors are surveyed in writing. The DEX gives an impression of the sentiments at every stage of the value chain in the energy sector and the energy supply industry, as well as among consumers and investors. It also collects data from politics and organizations as a reference but this data is not included in the overall index. On a scale from 0 (very negative) to 200 (very positive), the respondents are asked to rate their current situation as well as the past three and the next 12 months. The effects of the energy transition are then estimated with reference to the energy triangle. So far, the energy transition has been rated positively only in terms of environmental objectives, receiving more negative scores on efficiency and on supply security.

With a focus on the electricity sector, McKinsey examines the present state of energy transition in its *Energiewende-Index Deutschland 2020* (Vahlenkamp & Gohl 2013). Along the three dimensions of the energy trilemma, its aim is to provide a quarterly analysis of the achievement of energy policy objectives up to the year 2020. Five relevant indicators are assigned to each dimension, e.g. failure of power supply as an indicator of supply security. Based on the

ISGMA2014-P-N-07

reference year 2008, each indicator is related to an initial value and a target value for 2020, in line with the objectives set out by the Federal Government. Assessments are marked on a scale from 0 to 100. For indicators where continuity in the development between start and finish is needed, target values are defined for a year or quarter by linear interpolation. For indicators with annual targets defined by the Federal Government, interpolation is performed on a quarterly basis. In addition, a maximum permissible deviation from the target value is defined for each indicator, which should neither be exceeded nor underachieved. This way, the success of the energy transition is measured at regular intervals and appropriate adjustment measures are identified.

The *Energiewende-Kosten-Index EKK* (Energy Transformation costs Index ETCX) is published by the Oeko-Institut (Institute for Applied Ecology) and focuses on the costs of the “*Energiewende*” (Matthes et al. 2012). As a control and assessment indicator, this index allows attributing important cost items in the power supply system. The EKK confines itself not to a single price-increasing element in the mix of energy and climate policy instruments. Instead, it captures the overall context of price-increasing and price-decreasing tendencies as well as the underlying objectives. The EKK has different parts: The electricity price index, defined as the sum of wholesale prices and the full apportionment of costs under EEG & KWKG regulation (German Renewable Energy Act & Combined Heat and Power Act); fuel market effects; redistributive effects of the EEG; and the contribution of CO<sub>2</sub> costs. The EKK is displayed as a time series from 2003 onwards, because sufficiently reliable and comprehensive data weren't available for the liberalized electricity market before that time. To sufficiently differentiate between the causes leading to a reduction in electricity prices regarding intensified competition and merit-order effects, a correction factor for adjusting electricity prices was introduced in the reference year 2003. The electricity price is thus reduced to a level that corresponds with the cost of fuel in the EKK model.

	Deutscher Energiewende Index (DEX)	Energiewende-Index Deutschland 2020	Energiewende-Kosten-Index (EKK)
Published by	DENA, Ernst & Young	McKinsey	Oeko-Institut
Objective	Captures overall sentiment to contribute to an objective discussion of the consequences of energy transition and the necessary actions	Tracks and shows current trends and contributes to public debate by an objective analysis based on facts	Creates an objective measure for the changes in electricity prices => Balanced view of price-increasing and price-decreasing effects
Subject of analysis	- Environment - Supply Security - Efficiency	- Climate and environmental protection - Supply security - Efficiency	Cost items in the power supply system; changes in electricity prices including price-modifying effects
Scaling	0 bis 200	0 bis 100	---
Basis of index	Business survey; Assessment of current situation; assessment of past three months; expectations for the next 12 months	Defines targets for 2020 for each of the 15 indicators => analysis of target achievement and development based on statistics	Wholesale prices, EEG&KWKG apportionment of costs; fuel market effects; redistributive effects of EEG; contribution of CO <sub>2</sub> costs
Focus on energy efficiency	Yes, direct focus	Yes, indirect focus	---

Fig. 2: Comparison of indices

The *Energiewende-Navigator* (energy transition navigator) also aims to analyze the present state of energy transition (Bundesverband der Deutschen Industrie 2012). This annually updated index is published

by the Federation of German Industries (Bundesverband der Deutschen Industrie BDI) and adds the dimensions of acceptance and innovation to the energy trilemma. It resorts to 42 differently weighted indicators, such as overall greenhouse gas emissions or investment in energy efficiency, to numerically evaluate these five dimensions. In addition, by looking back on the history of each indicator in the last two years it helps to estimate future developments. For some areas, target values were defined on a scale from 0 to 100, which are in line with the ‘Energy Concept’.

In general, energy efficiency is only at the focus of attention in the *DEX index* and the *Energiewende-Navigator*. Indirectly, McKinsey touches on the subject in the *Energiewende-Index* but does not deal with it in detail. Besides, it examines energy efficiency measures mainly for companies that are directly related to the energy industry. So far, a targeted energy efficiency analysis, presented as an index for industry as a whole and especially the manufacturing sector, has not been undertaken (Fig.2).

## 2. Concept of an energy efficiency index for the German industry sector

As explained above, a number of different indices on the subject of energy transition already exist. However, none of these indicator systems is tailored to the manufacturing industry in Germany and takes into account both the evaluation of the current state and future prospects. The new Energy Efficiency Index (EEI) is designed to fill this gap. The EEI has three major objectives: Based on regular surveys, it is to continually provide benchmarking data for manufacturing companies. Another goal of the EEI is to provide regular feedback to policymakers on the situation of the German manufacturing industry. Last but not least, the index data and the trends they display can be used to point out the need for action and the challenges for research. The EEI is not meant to precisely calculate a ratio between any energy service and the amount of required energy input but to aggregate both quantitative figures and climate factors. This is realized by three sub-indices that address the importance of energy efficiency (EBI), the amount of investment into energy efficiency measures (EII) and the development of energy intensity (ESI). The top indicator, the Energy Efficiency Index (EEI), is computed from the geometric mean of all three sub-indices as follows:

$$EEI = \sqrt[3]{EII \cdot ESI \cdot EBI}$$

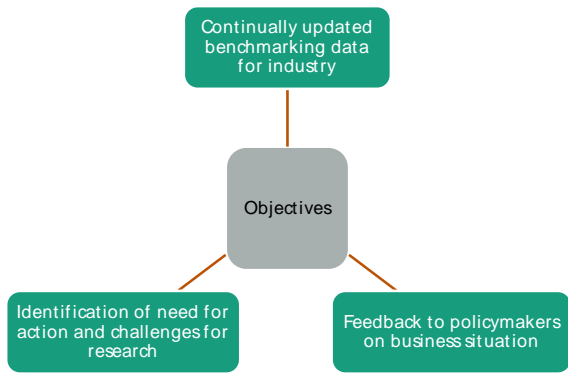


Fig. 3: Objectives of the Energy Efficiency Index

**2.1 Data collection**

The collection of index data follows the survey system of the Ifo Business Climate Index. Field data are collected and evaluated in regular surveys twice a year. As with the Ifo Business Climate Index, data on the current situation and on expectations are collected to provide an outlook on the near future. The data collected by the EEI survey refer to three sub-categories:

- current and future importance of energy efficiency
- completed and planned investment in energy efficiency
- achieved and planned energy intensity

Each sub-category represents a particular intention (Fig. 4). While the evaluation of the current and future importance of energy efficiency by the interviewee gives an impression of the overall attitude of manufacturing companies towards energy efficiency improvements. With other words, what do companies think about the criticality of energy efficiency to their businesses?

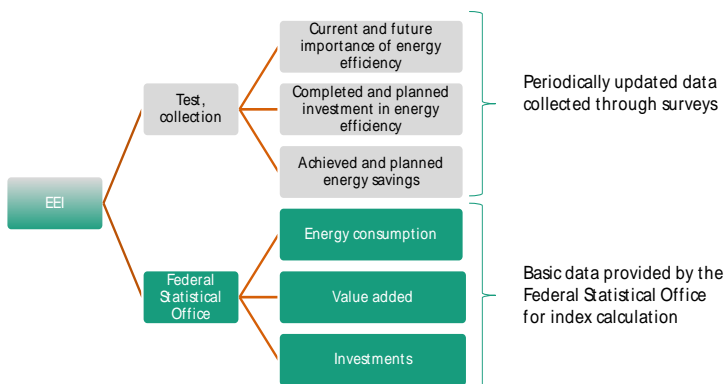


Fig. 4: Design and collection of the Energy Efficiency Index

The assessment of completed and planned investment in energy efficiency is meant to give an impression on future energy intensity. The underlying hypothesis is decreasing energy intensity by increased investment in energy efficiency measures. Like in many macroeconomic models the amount of investments is used as a leading indicator for the development of energy intensity in the future. Furthermore the amount of investment can be correlated with the

overall importance of energy efficiency. Consistent behavior of companies most probably will lead to a correlation between the importance of energy efficiency and the investment into energy efficiency measures. A third logical verification of the consistency is assured by the third sub-category of the index - achieved and planned energy savings. Increasing importance of energy efficiency and increasing investments in energy efficiency measures should also lead to an increase in planned energy savings.

Subsequently the EEI is composed of the three sub-indices EBI (importance of energy efficiency), EII (investment in energy efficiency), and ESI (trend in energy intensity) (Fig.5). The three sub-indices can be aggregated for each of the 28 business sectors in the manufacturing industry defined by the Federal Statistical Office of Germany. This methodology allows for the calculation of separate energy efficiency indices for each business sector. If aggregated across all sectors to allow for an integrated index for the manufacturing industry as a whole, the collected data of each sector is weighted by a parameter relevant to the three sub-indices. The data used for this refer to energy consumption, investment, and gross value added in this sector.

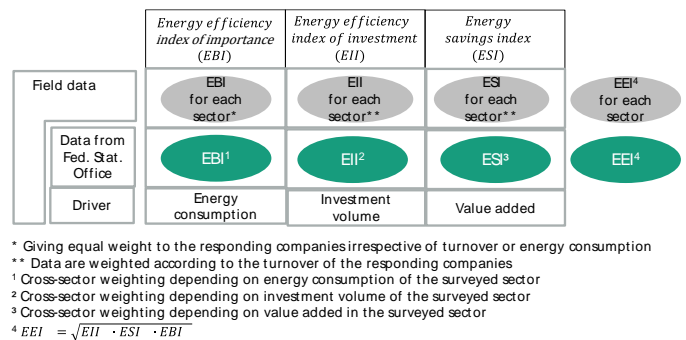


Fig. 5: Sector-specific and cross-sector evaluation methods of the EEI

Table 1 shows the population of companies in Germany that shall be covered by the EEI. The “WZ08-xy” codes are representing the different business sectors corresponding to the statistical data of the Federal Statistical Office of Germany. In total about 36,000 companies shall be covered with total turnover of 1,659,955 million Euros, a gross value added of 473,558 million Euro, Energy consumption with a value of 37.709 million Euro and an investment volume of 45.768 million Euro. These basic data is used for the normalization of the comprehensive sub-indices.

Table 1: Basis for calculating the EBI sub-index

Table 1: Business sectors of Germany and main characteristics for the Energy Efficiency Index (Destatis 2013b)					
Period under review: 2010	Companies	Turnover 1,000 EUR	Gross value added 1,000 EUR	Energy Consumption 1,000 EUR	Investment 1,000 EUR
Business Sector					
WZ08-05	6	3.921.379	1.062.536	220.910	
WZ08-06	4	2.762.103	1.217.492	66.880	
WZ08-08	346	4.626.287	1.644.668	429.625	
WZ08-09	14	419.976	189.449	10.062	34.144
WZ08-10	4.643	134.877.372	25.780.201	3.376.947	3.345.648
WZ08-11	483	18.495.352	6.368.061	536.556	844.498
WZ08-12	21	16.955.937	12.526.254	50.573	193.739
WZ08-13	647	10.942.924	3.263.168	407.083	253.034
WZ08-14	281	7.602.930	2.043.285	45.675	93.851
WZ08-15	131	2.391.540	615.879	21.592	129.092
WZ08-16	953	17.116.171	3.978.356	635.712	505.507
WZ08-17	785	38.667.811	9.170.282	2.565.822	1.201.643
WZ08-18	1.374	16.497.628	5.691.888	396.644	694.157
WZ08-19	44	120.370.589	38.853.895	967.545	885.205
WZ08-20	1.151	147.033.945	36.713.891	7.112.982	4.335.022
WZ08-21	240	39.793.209	15.706.696	518.966	1.460.657
WZ08-22	2.643	67.264.889	20.782.400	1.824.594	2.219.789
WZ08-23	1.461	36.294.857	11.742.621	2.664.244	1.494.376
WZ08-24	898	91.753.357	17.364.221	6.621.059	2.271.909
WZ08-25	6.486	92.102.049	33.801.418	2.057.932	2.954.714
WZ08-26	1.535	63.841.910	21.040.713	643.202	2.844.452
WZ08-27	1.837	102.311.976	35.872.943	927.825	2.529.933
WZ08-28	5.094	199.423.836	66.754.469	2.018.473	4.647.896
WZ08-29	1.020	322.454.607	67.880.767	2.592.248	10.442.422
WZ08-30	251	32.812.417	9.256.020	258.959	676.443
WZ08-31	945	16.348.653	5.353.045	246.534	383.072
WZ08-32	1.385	22.934.763	9.164.820	255.248	912.466
WZ08-33	1.364	29.936.222	9.718.828	234.748	414.019

**2.2 Calculation of the sub-index EBI – importance of energy efficiency**

For the EBI companies are asked for their assessment concerning the importance energy efficiency for their business. The assessment differentiates three categories for the current situation (relatively small, comparable to other factors, relatively high) and three categories for the expectations (decreasing, more or less constant, increasing).

First, the assessments given by the companies on the importance of energy efficiency are accumulated and mapped for each sector before being normalized to all responses that were taken into account. In line with the ifo Business Climate Index, neutral responses are not included and a geometric mean of the assessments of the business situation and the expectations is calculated before being normalized to the sub-index EBI for each sector.

To calculate the EBI (Fig.6) across all sectors, the balances of assessments on the situation and the expectations concerning energy consumption are weighted for each sector. Energy consumption here means the energy consumption of the sector expressed in Euro in a base period defined by the Federal Statistical Office. The creation of the sub-index EBI for all sectors is performed correspondingly to the above procedure. The sub-index can assume values between 0.33 and 3. The value of the EBI is calculated as follows:

Calculation step	Notes
$EBSC_{cur,l,j} = \frac{\sum_{i=1}^n number\ high_{cur,l,i} - number\ low_{cur,l,i}}{\sum_{i=1}^n number_{i,l}} \cdot 100$	Data on high and low importance of energy efficiency is balanced for each sector with a view to the current situation
$EBSC_{exp,l,j} = \frac{\sum_{i=1}^n number\ high_{exp,l,i} - number\ low_{exp,l,i}}{\sum_{i=1}^n number_{i,l}} \cdot 100$	Data on high and low importance of energy efficiency is balanced for each sector with a view to expectations
$EBSC_{s,l,j} = \sqrt{(EBSC_{cur,l,j} + 200) \cdot (EBSC_{exp,l,j} + 200)} - 200$	Geometric mean is calculated from the balances of current situation $EBSC_{cur,l,j}$ and expectations $EBSC_{exp,l,j}$
$EBIS_{i,j} = \frac{EBSC_{s,l,j} + 200}{EBSC_{0,j} + 200}$	Geometric mean index is calculated for the base period of a specific sector
$EB_{cur,i} = \frac{\sum_{j=1}^n EBSC_{cur,l,j} \cdot ESC_{0,j}}{\sum_{j=1}^n ESC_{0,j}}$	Balance of current situation in a sector $EBSC_{cur,l,j}$ is weighted regarding energy consumption $ESC_{0,j}$
$EB_{exp,i} = \frac{\sum_{j=1}^n EBSC_{exp,l,j} \cdot ESC_{0,j}}{\sum_{j=1}^n ESC_{0,j}}$	Balance of expectations in a sector $EBSC_{exp,l,j}$ is weighted regarding energy consumption $ESC_{0,j}$
$EB_{S_i} = \sqrt{(EB_{cur,i} + 200) \cdot (EB_{exp,i} + 200)} - 200$	Geometric mean index of the weighted balances of current situation and expectations is calculated across all sectors
$EBI = \frac{EB_{S_i} + 200}{EB_{S_0} + 200}$	The cross-sector geometric mean index of a base period is calculated
$EBSC_{k,l,j}$ $EBIS_{i,j}$ $EB_{k,i}$ $EB_{S_i}$ $ESC_{i,j}$	$k \in \{cur, exp\}$ $l \in \{0,1\}$ $l=1$ : reporting period, $l=0$ : base period $j \in \{1, \dots, n\}$ sectors surveyed (SC) $i \in \{1, \dots, m\}$ companies surveyed

Fig. 6: Basis for calculating the EBI sub-index

**2.3 Calculation of the sub-index EII – investment in energy efficiency measures**

For the EII companies are asked for their assessment concerning the ratio of the investment into energy efficiency measures in relation to their overall investment activities during the last 12 month and for their expectation for the upcoming 12 month. The replies can be given on a cardinal scale with ten units. The lowest value possible is “<1%” and the highest value that can be declared is “>20%”.

The first step for the calculation of the EII is to weight the collected data that indicate the investment in energy efficiency measures relative to the total investment. The weighting for a specific sector is based on the turnover of the surveyed company and applies to the values concerning current situation and expectations. The subsequent calculation of the geometric mean creates a balance of situation and expectation values. The relationship between the balances of the reporting period and the base period allows producing a sub-index EII for each sector.

To calculate the sub-index EII across all sectors, the weighted percentages of investment for the current situation and for the expectations of each sector are weighted based on the investment volume of the individual sector. Corresponding to the above procedure, a balance is calculated from the geometric mean of the weighted investment percentage for the current situation and for the expectations. The relation of this balance for the reporting period to

the base period produces the sub-index EII across all sectors. The minimum value of the sub-index is zero. From a mathematical point of view, a limitation in the positive direction is not given, so a suitable base period should be selected as a starting point. The value of the EII is calculated as follows:

Calculation step	Notes
$IASC_{cur,1,j} = \frac{\sum_{i=1}^n IA_{cur,1,i} \cdot U_{1,i}}{\sum_{i=1}^n U_{1,i}}$	The current share of investment $IA_{cur,1,i}$ in energy efficiency measures is weighted, based on the turnover $U_{1,i}$ of the companies surveyed in a specific sector
$IASC_{exp,1,j} = \frac{\sum_{i=1}^n IA_{exp,1,i} \cdot U_{1,i}}{\sum_{i=1}^n U_{1,i}}$	The expected share of investment $IA_{exp,1,i}$ in energy efficiency measures is weighted, based on the turnover $U_{1,i}$ of the companies surveyed in a specific sector
$EISSC_{1,j} = \sqrt{(IASC_{cur,1,j}) \cdot (IASC_{exp,1,j})}$	The geometric mean creates a balance of the current situation $IASC_{cur,1,j}$ and the expectations $IASC_{exp,1,j}$ regarding the share of investment in energy efficiency measures for each sector
$EIISC_j = \frac{EISSC_{1,j}}{EISSC_{0,j}}$	The geometric mean index $EIISC_j$ is calculated for a base period for a specific sector
$IAG_{1st,1} = \frac{\sum_{j=1}^n IASC_{1st,1,j} \cdot ISC_{0,j}}{\sum_{j=1}^n ISC_{0,j}}$	The current share of investment $IASC_{cur,1,j}$ for a specific sector is weighted, based on its investment volume $ISC_{0,j}$ in the base period
$IAG_{exp,1} = \frac{\sum_{j=1}^n IASC_{exp,1,j} \cdot ISC_{0,j}}{\sum_{j=1}^n ISC_{0,j}}$	The expected share of investment $IASC_{exp,1,j}$ for a specific sector is weighted, based on its investment volume $ISC_{0,j}$ in the base period
$EIS_1 = \sqrt{(IAG_{cur,1}) \cdot (IAG_{exp,1})}$	The geometric mean creates a balance of the current situation and the expectation values regarding the share of investment in energy efficiency measures across all sectors
$EII = \frac{EIS_1}{EIS_0}$	The cross-sector geometric mean index of a base period is calculated
$IAW_{SC,l,j}$ $U_{1,i}$ $EIISC_j$ $ISC_{1,j}$	$IA_{k,l,i}$ $EISSC_{1,j}$ $IAG_{k,l}$ $EIS_l$ $k \in \{cur, exp\}$ $l \in \{0,1\}$ $l=1$ : reporting period, $l=0$ : base period $j \in \{1, \dots, n\}$ sectors surveyed (SC) $i \in \{1, \dots, m\}$ companies surveyed

Fig. 7: Basis for calculating the EII sub-index

**2.4 Calculation of the sub-index ESI – energy intensity**

For the ESI companies are asked for their assessment concerning the energy intensity. The current situation is given by a free value with the dimension megawatt-hours per thousand Euro of turn-over. The assessment of the upcoming future in terms of the next 12 month is derived by a cardinal scale with eleven units. The lowest value possible is “<1%” and the highest value that can be declared is “>10%”.

The third sub-index calculation of the ESI follows similar rules. The expectations and the current situation with a view to the energy intensity (energy consumption in proportion to value added) of the surveyed companies are at first weighted separately for each sector. The calculation of the geometric mean for the current situation and for the expectations serves to create a balance for the energy intensity in each sector. The sub-index ESI for a separate sector is derived from the reciprocal value of the relation of the balance of the energy intensity in the reporting period and the base period for a sector. The reciprocal value is necessary at this point, since an increase in the sub-index is meant to signify a reduction in energy intensity.

The aggregation of the weighted energy intensities of the individual sector follows the creation of a price index according to Laspeyres.

Energy intensity is here understood as price. The value creation within a sector can be interpreted as quantity. Since an increase in the index here is meant to signify a reduction in energy intensity, the reciprocal Laspeyres price index is defined as an index for the energy intensity across all sectors both referring to the current situation and to the expectations. The sub-index ESI across all sectors is calculated as a geometric mean of the indices for the expected energy intensity and the energy intensity of the current situation. From a mathematical point of view, the sub-index for energy intensity ESI can take any positive value. The basis of the sub-index should therefore be reviewed regularly. The value of the ESI is calculated as follows:

Calculation step	Notes
$EISC_{cur,1,j} = \frac{\sum_{i=1}^n EI_{cur,1,i} \cdot U_{1,i}}{\sum_{i=1}^n U_{1,i}}$	The current energy intensity $EI_{cur,1,i}$ is weighted, based on the turnover $U_{1,i}$ of the companies surveyed in a specific sector
$EISC_{exp,1,j} = \frac{\sum_{i=1}^n EI_{exp,1,i} \cdot U_{1,i}}{\sum_{i=1}^n U_{1,i}}$	The expected energy intensity $EI_{exp,1,i}$ is weighted, based on the turnover $U_{1,i}$ of the companies surveyed in a specific sector
$ESSSC_{1,j} = \sqrt{EISC_{cur,1,j} \cdot EISC_{exp,1,j}}$	The geometric mean creates a balance of the current situation and the expectations regarding energy intensity for each sector
$ESISC_j = \frac{ESSSC_{1,j}}{ESSSC_{0,j}}$	The geometric mean index is calculated from the reciprocal value of the relation of the balance of energy intensity in the reporting period $ESSSC_{1,j}$ and the base period $ESSSC_{0,j}$ for a specific sector
$\frac{1}{ESS_{cur}} = \frac{\sum_{j=1}^n EISC_{cur,1,j} \cdot VSC_{0,j}}{\sum_{j=1}^n EISC_{cur,0,j} \cdot VSC_{0,j}}$	The geometric mean index for the current situation of all sectors is calculated from the reciprocal value of a Laspeyres price index from energy intensity $EISC_{cur,1,j}$ (price) and value added $VSC_{0,j}$ (quantity) for each sector
$\frac{1}{ESS_{exp}} = \frac{\sum_{j=1}^n EISC_{exp,1,j} \cdot VSC_{0,j}}{\sum_{j=1}^n EISC_{cur,0,j} \cdot VSC_{0,j}}$	The geometric mean index for the expectations of all sectors is calculated from the reciprocal value of a Laspeyres price index from energy intensity $EISC_{exp,1,j}$ (price) and value added $VSC_{0,j}$ (quantity) for each sector
$ESI = \sqrt{ESISC_{cur} \cdot ESISC_{exp}}$	The cross-sector geometric mean of the ESI index is calculated from current situation and expectations regarding energy intensity
$EISC_{k,l,j}$ $EU_{k,1,i}$ $U_{1,i}$ $ESS_k$	$ESSSC_{1,j}$ $ESISC_j$ $WSC_{l,j}$ $k \in \{cur, exp\}$ $l \in \{0,1\}$ $l=1$ : reporting period, $l=0$ : base period $j \in \{1, \dots, n\}$ sectors surveyed (SC) $i \in \{1, \dots, m\}$ companies surveyed

Fig. 8: Basis for calculating the ESI sub-index

**3. Sensitivity analysis of the EEI**

To understand and interpret the complex index figures sensitivity analyses of the three sub-indices and the interdependency with the top indicator have been performed.

The following chart (Fig. 9) shows an increase in the current importance of energy efficiency. The abscissa indicates the proportion of respondents assessing the importance of energy efficiency for their businesses as “relatively high” ( $EB_{AS-15,1}$ ). The ordinate shows the value of the sub-index EBI and the index EEI. The trends of the sub-index EBI and the EEI rise in a proportional manner.

ISGMA2014-P-N-07

$EB_{As-Is,1}$  rises from 25 to 75 while  $EB_{Exp,1}$  stays constant at a level of 25 and  $EBS_0 = 25$ . This represents an increase of 200% of the base value. The sub-index EBI ascends about 10.6% and the EEI about 5.1%.

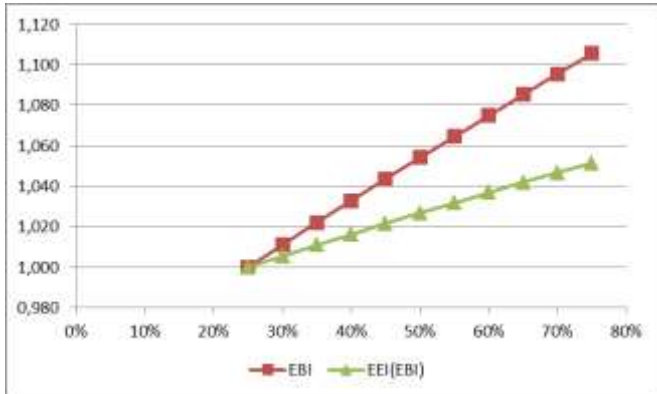


Fig. 9: Increase in the current importance of energy efficiency

The Fig. 10 shows an increase in the investment into energy efficiency measures. The abscissa indicates the proportion of the investment of the respondents into energy efficiency compared to the overall investments ( $IAG_{As-Is,1}$ ). The ordinate shows the value of the sub-index EII and the index EEI. The trends of the sub-index EII and the EEI rise in a proportional manner.  $IAG_{As-Is,1}$  rises from 2.5% to 3.0% while  $IAG_{Exp,1}$  stays constant at a level of 2.5% and  $EIS_0 = 2.5\%$ . This represents an increase of 20% of the base value. The sub-index EII ascends about 9.5% and the EEI about 4.7%.

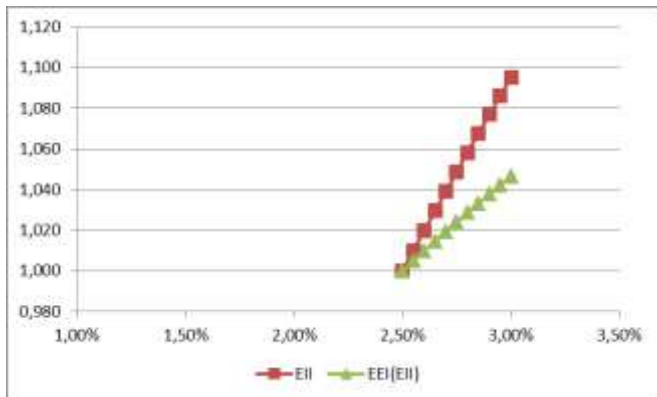


Fig. 10: Increase in the investment into energy efficiency measures

The lower chart (Fig. 11) shows a decrease of energy intensity. The abscissa indicates the energy intensity index of all business sectors ( $\frac{1}{ESS_{Ist}}$ ). The ordinate shows the value of the sub-index ESI and the index EEI. The trends of the sub-index ESI and the EEI rise in a proportional manner.  $\frac{1}{ESS_{Ist}}$  rises from 1.00 to 1.11 while  $\frac{1}{ESS_{erw}}$  stays constant at a level of 1. This represents an increase of 11% of the base value. The sub-index ESI ascends about 5.4% and the EEI about 2.7%.

The sensitivity analysis shows the sensitivity of the sub-indices and the EEI. Even having serious deviations within one single basic value the amplitude of the sub-indices and the EEI is absorbed by the other basic values at constant levels.

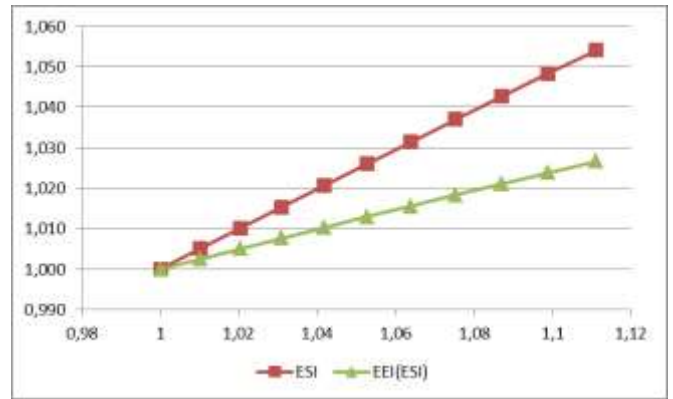


Fig. 11: Decrease of energy intensity

#### 4. Summary

The paper presents the theoretical background of index figures to highlight the differences between the basic concepts followed by a brief description of existing energy efficiency related indices in Germany. The presented new Energy Efficiency Index is designed as a leading indicator for the trend of energy efficiency in the German manufacturing industry. It collects information on the business situation and the expectations with regard to the importance of energy efficiency, to investments, to increase energy efficiency and to the trend in energy intensity. In combination with the basic value of the Federal Statistical Office of Germany, it is possible to draw conclusions on the current situation and on the expectations for a single sector as well across all relevant business sectors. The quality of the conclusions depends very much on the number, the turnover, the energy consumption and the investment intensity of the responding companies, and how evenly they are spread across the different sectors.

#### REFERENCES

1. Cramer, E. & Kamps, U. (2008). *Grundlagen der Wahrscheinlichkeitsrechnung und Statistik*. zweite, überarbeitete Auflage. Berlin: Springer.
2. DESTATIS (2013). Population by area % changes on the previous year. [https://www.destatis.de/EN/FactsFigures/Indicators/LongTermSeries/Population/Irbev03.html?cms\\_gtp=150348\\_list%253D2&https=1](https://www.destatis.de/EN/FactsFigures/Indicators/LongTermSeries/Population/Irbev03.html?cms_gtp=150348_list%253D2&https=1). Accessed 16 June 2013.
3. DESTATIS (2013b). Genesis online Datenbank. [https://www-genesis.destatis.de/genesis/online/data.jsessionid=E2225EB93A48D1FBBF0B4A1505BEB21F.tomcat\\_GO\\_2\\_2?operation=statistikenVerzeichnisNextStep&levelindex=0&levelid=1371419695149&index=3&structurelevel=3](https://www-genesis.destatis.de/genesis/online/data.jsessionid=E2225EB93A48D1FBBF0B4A1505BEB21F.tomcat_GO_2_2?operation=statistikenVerzeichnisNextStep&levelindex=0&levelid=1371419695149&index=3&structurelevel=3), Accessed 16 June 2013.
4. Edelmann, H. & Kohler, S. (2013). Deutscher Energiewende-Index (Energy Transition Index – DEX), 4th quarter 2012. [http://www.dena.de/fileadmin/user\\_upload/Publikationen/Energie-systeme/Dokumente/DEX\\_4\\_Quartal\\_Ergebnisse\\_Englisch.pdf](http://www.dena.de/fileadmin/user_upload/Publikationen/Energie-systeme/Dokumente/DEX_4_Quartal_Ergebnisse_Englisch.pdf). Accessed 16 June 2013.
5. Ifo (2013): Calculating the Ifo Business Climate, <http://www.cesifo-group.de/ifoHome/facts/Survey->

- Results/Business-Climate/Calculating-the-Ifo-Business-Climate.html. Accessed 16 June 2013.
6. Matthes, F. et al. (2012). Strompreisentwicklungen im Spannungsfeld von Energiewende, Energiemärkten und Industriepolitik. <http://www.oeko.de/files/forschungsergebnisse/application/octet-stream/download.php?id=1587>. Accessed 16 June 2013.
  7. Pérez-Lombard, L., Ortiz, J., Velázquez, D. (2013). Revisiting energy efficiency fundamentals. *Journal of Energy Efficiency*. DOI 10.1007/s12053-012-9180-8.
  8. Stankov, D. (2008). *Die Kapitalverflechtungen hinter dem DAX 30*. Dissertation. FU Berlin.
  9. Vahlenkamp, T. & Gohl, M. (2013). Energiewende-Index Deutschland 2020., *Energiewirtschaftliche Tagesfragen*. 63 (6), 33-35.
  10. Bundesverband der Deutschen Industrie (2012). Energiewende-Navigator 2012 des BDI. <http://www.energiwende-richtig.de/download/file/fid/232>. Accessed 16. June 2013.

# Overview of Mechanical and Electrical Products Low Carbon Design

Zhifeng Liu, Mengdi Gao<sup>#</sup>, Huanbo Cheng, Qingyang Wang and Xuan Zhou

School of Mechanical and Automotive Engineering, Hefei University of Technology, Hefei, China, 230009  
<sup>#</sup> Corresponding Author / E-mail: haohaoxuexi-9999@163.com, TEL: +86-15156218446, FAX: +86-0551-290-1775

KEYWORDS : Low-carbon Design; Eco-design; Lightweight; Modular; Carbon Footprint

---

*With the enormous challenges of global warming and the transformation of development, the concept mechanical and electrical products low-carbon design had been highly valued by the research institutions in the world. Low-carbon design is a design approach which aims to reduce greenhouse gas emissions in each period of the whole life cycle including designing, manufacturing, transporting, using, recycling etc. This review stated briefly the recent progress of the mechanical and electrical products low carbon design. Implementation of low-carbon design study was discussed from the eco-design for energy saving, lightweight design, modular design etc. The following aspects of carbon footprint calculation and evaluation for low carbon design were summarized. The future development trend of mechanical and electrical products low carbon design were discussed to clarify the key points and research direction of low carbon design.*

---

## 1. Introduction

With the global economy making astounding advances and products quickly updating process, resources shortage, ecological unbalance and environmental degradation have become one of the most serious challenges for human beings in the new century. Under the background of global climate warming, "low carbon economy" based on low energy consumption and low pollution has attracted the world's attention, meanwhile low carbon development has become an inevitable trend of social development.

Low carbon refers to lower or less greenhouse gas (mostly CO<sub>2</sub>) emissions. Low-carbon design is a design approach aimed to reduce emissions of greenhouse. Mechanical and electrical products (MEPs) refer to all the mechanical and electrical equipment. With the progress of science and technology, the traditional MEPs have been highly developed with abundant kinds, involving all aspects of people's life, so low carbon design of MEPs is of great significance to the development of economy and environment. MEPs low-carbon design is a design approach which aims to reduce greenhouse gas emissions in each period of the whole life cycle including designing, manufacturing, transporting, using and recycling etc. Due to the products carbon emissions related to all aspects of the life cycle and many impact factors as well as the complex carbon emissions distribution, so low-carbon product design is a very complex process.

Some methods such as energy saving, emission reduction, lightweight and modular methods are used in MEPs low carbon design and manufacture process, which provide more opportunities

for products to win the market. But due to the extension of products life cycle and the incorporation of environmental factors, product development, manufacturing and processing technology are facing more challenges. For example, with products low carbon performance improving, the cost of the product manufacturing may be increased as well, resulting that the market competitiveness of products is reduced. Meanwhile MEPs low-carbon performance is associated with multiple factors, such as carbon footprint evaluation,<sup>1</sup> disassembly and recycling, structural module reuse, maintainability<sup>2</sup> and the evaluation of environmental friendliness. From low carbon design and manufacturing proposed come so far, there is no carbon footprint evaluation method which is widely and consistently accepted, the basic concept, connotation, framework, criterion as well as design guidelines and methodology of low carbon design are urgently need to be formed.<sup>3</sup> Focusing on the particular stage of products life cycle, the relative theory and methods have been put forward including the green design and manufacturing which are used in the early stage of design,<sup>4,5</sup> and the component disassembly and recycling,<sup>6-8</sup> key parts remanufacturing,<sup>9,10</sup> maintenance repair design, green supply chain<sup>11-12</sup> and product LCA<sup>13</sup> which are performed at the end of life.

## 2. MEPs Low Carbon Design Method

MEPs low carbon design process is a complex system decision-making process involving multi-disciplinary, multi-field knowledge. Scholars in the world have studied on different aspects of MEPs low carbon design on the whole life cycle of producing, manufacturing and using etc. Implementation of MEPs low-carbon design study was discussed from the eco-design for energy saving, lightweight design and modular design in this paper.

## 2.1 Eco-design for Energy Saving

Eco-design means environmental factors are taken into consideration in the whole life cycle including product designing, using, maintaining and recycling. Eco-design is not only satisfying the people's needs, but also paying attention to environmental protection and sustainable development principle. Eco-design for energy saving is a modern design method considering the carbon emissions and energy efficient synthetically without reducing product proper function, quality and service life.<sup>14</sup> At present, some related work can be summarized into two aspects, one is the analysis of product energy design factor, the other is the optimization and improvement of energy saving design.

Gutowski T. et al. used a thermodynamic framework to characterize the material and energy resources used in manufacturing processes, and studied the energy consumption of machine tool model under different processing strategies, proposed that the necessity and feasibility of thermodynamic analysis on the machining process.<sup>15</sup> A generalized model of a manufacturing system is depicted as shown in Fig 1.<sup>16</sup> A. Hassanpour et al. studied on the influence factor of energy consumption on motor in order to optimize and improve the efficiency of it.<sup>17</sup> ElFerik S. and Belhadj C.A. et al. analyzed the relationship between environment temperature with humidity and air conditioning energy consumption, and established air conditioning product energy consumption model based on neural network, stochastic Markov chain method respectively.<sup>18-20</sup> Liu Z.F. et al. used dishwasher as the model to analyze the energy consumption during use stage and to extract the energy design factor.<sup>21</sup> The energy-consuming framework of product system and the product life-cycle energy model is set up based on the analysis of energy-consuming characteristic of mechanic products, the dynamic characteristic of the energy property is expounded by Qi Y.H. et al.<sup>22</sup> NC machine energy consumption model in use stage was established, and the conception of EDF which reflected the control mechanism and elements of product's energy property was introduced EDF decomposition of coupling mechanism was established by Zhou D. et al.<sup>23</sup> Zhang H.C. et al. integrated the axiomatic design and modularity design theories with energy factor, presented a mathematic energy model based on energy factor to calculate the total energy consumption within entire product lifecycle.<sup>24</sup> All the overview above is focused on MEPs energy design factor analysis.

Researchers have carried out a lot of research from different aspects on energy saving design optimization and improvement. Kim H.G described the optimization problem of energy saving design process, studied reusing, remanufacturing and recycling of product from the point of energy saving.<sup>25</sup> The energy relation in several aspects are analyzed and quantized by QI Y.H. et al., such as the

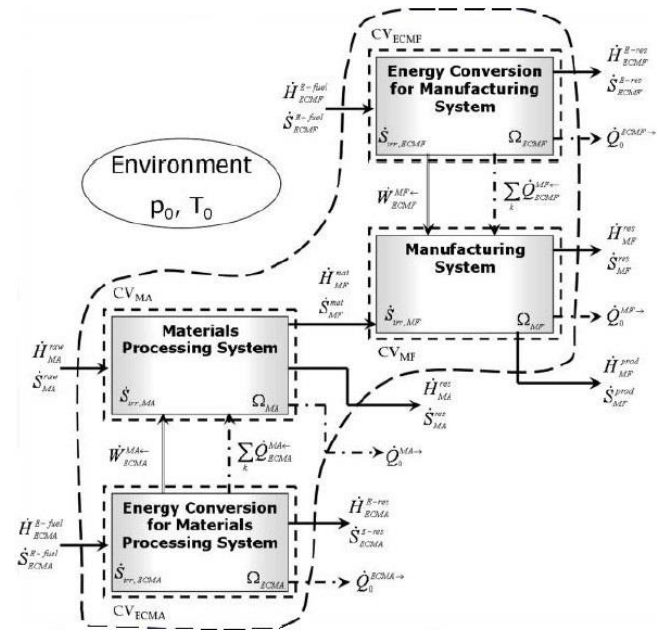


Fig1. Diagram of a manufacturing system (modified and redrawn from reference 16)

materials compatibility, the assembly and disassembly, the energy transmission in the use stage, the part life and EOL. Then a low carbon product structure combination design method from the perspective of energy clustering optimization was proposed.<sup>26</sup> Wakui T. and Cipollone R. et.al. did some energy-saving research on some kinds of electric vehicle through use the model to optimal the fuel cell system.<sup>27-28</sup> T.A. and Minav et al. studied opportunities of utilizing electric servo drives in the control of hydraulic lifting systems directly by an electric-servomotor-driven hydraulic machine and enabling energy recovery in them.<sup>29</sup> Zeng X. et al. proposed that hybrid technology was a new energy saving method for wheel loaders. Currently, several energy management strategies (EMSs) have been applied to hybrid electric wheel loaders (HEWLs).<sup>30</sup> Hsu, Y. L and Saidur, R. et.al. researched on energy-saving strategies for motor in any mechatronic system.<sup>31,32</sup> Hu S.H. and Avram. O. I. et.al monitored the machine tools system to measure and evaluate the energy consumption in use stage then divided the energy requirements of a machine-tool system into two parts, i.e. constant energy consumption and variable energy consumption in order to enhance energy efficiency of machine tools.<sup>33,34</sup>

Eco-design for energy saving emphasize on reducing MEPs energy consumption in use stage, which could reduce greenhouse gas emissions directly, so it is an important way of low carbon design. Additionally, eco-design also includes sustainable design,<sup>35</sup> and life-cycle assessment<sup>36</sup> etc, with emphasis on reducing the degree of the impact on the environment in product whole life cycle. It contains disassembly and recyclability after scraped and life cycle analysis, which can be subdivided into disassemblable structure unit map for products,<sup>37</sup> disassembly sequence planning<sup>38,39</sup> and evaluation<sup>40,41</sup> etc. Recyclability design emphasizes on recycling technology research<sup>42,43</sup> and recycling management and recycling schemes evaluation<sup>44,45</sup>, etc. Green design was expanded to the whole life cycle in the research of Pan Y.H.<sup>46</sup> and Li F.Y.'s<sup>47</sup>, of which the essence is that the environmental factors are taken into consideration in the whole life cycle from the beginning of design and manufacturing. Vinodh, S.,<sup>35</sup>

Yang, C. J.,<sup>48</sup> Chou J. R.,<sup>49</sup> and Victor Pondelet<sup>50</sup>.et.al applied TRIZ method to the product life cycle assessment, studied on the integration methods which can benefit for achieving ecologicalization, and provided a method reference for the future research.

## 2.2 Lightweight Design

MEPs light weight method is mainly to use the higher strength material to substitute the lower strength material, or use structure optimization to improve the material utilization rate, in order to reduce weight, its essence is that lightweight design concept is considered in optimization design to satisfy low carbon design requirement, which is particularly important in large MEPs design.

Some theory on lightweight was studied by Liu X.L.et al. who divided the machinery processing low carbon manufacturing technology system structure into product low carbon design, low carbon production process, low carbon energy development and so on. The paper involved low carbon manufacturing technology such as lightweight, modular and ecological design method, summarized the importance of product structure optimization in low carbon design, and pointed out the basic direction of low carbon operation.<sup>51</sup> Robert A. and Erik T.et al proposed while meeting the requirements of lightweight design may cause an increasing in manufacturing costs, and the results indicated that weight reduction will not always lead to improved environmental performance. Materials offering high weight savings such as carbon fibres and magnesium have been shown to give limited or negative environmental benefits over their life cycles due to increased environmental burdens associated with their production. Thus it needs to consider the conflict between lightweight and other aspects in the design process.<sup>52,53</sup> A breakeven analysis determined at which stage in the vehicle's life the lighter weight components would yield a cost benefit. The results of this analysis are shown in Fig2. The first of the lightweight scenarios to breakeven is SMC, which has the lowest materials and manufacturing costs after steel and benefits were achieved after only 17,200 km. The carbon fibre component had the lowest weight of all scenarios, but had the highest materials and manufacturing costs, resulting in benefits obtained relatively late in the vehicle's life at 121,000 km.<sup>52</sup>

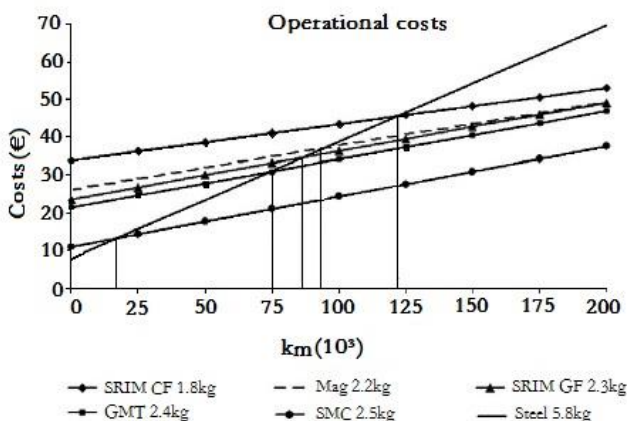


Fig2 Breakeven analysis results(modified and redrawn from reference52)

The typical lightweight design of MEPs will be illustrated as follows. Guo L. and J. J. Zulaika have studied on machine tool structure optimization and achieved the lightweight goal.<sup>54,55</sup> Cao H.J. applied the lightweight design and remanufacturing design to reduce fixed carbon emissions in the machine tool carbon emissions process.<sup>56</sup> Shi G.H.,<sup>57</sup> Zhao H.,<sup>58</sup> Li Y.P.,<sup>59</sup> Peng Y.,<sup>60</sup> Zheng S.L.<sup>61</sup> and Clain B.<sup>62</sup> all focused on the vehicle structure optimization to achieve automobile body and engine lightweight under the conditions of satisfying its functional and performance. Li Y.,<sup>63</sup> Yan Z.<sup>64</sup> used new materials to achieve the lightweight of MEPs. Lightweight optimization design of press frame structure is made through parametric finite element analysis by Zhao H., in the premise of not reducing the stiffness, it is showed that body weight was reduced by 20.3%, the maximum stress is reduced by 16.1%, the angular distortion is decreased by 13.8%.<sup>65</sup> The lightweight and stiffness of upper beam of hydraulic press is optimized by Li Y.C., the size of different parts of upper beam is distributed reasonably, the stiffness of upper beam is increased by 5% and its mass is decreased by 10% in comparison to the original design.<sup>66,67</sup> The structure and matched equipment of aircraft is lightweight operated by Tan H.F.<sup>68</sup> and Yang H.,<sup>69</sup> then the aim of aircraft lightweight is obtained. The mass of industrial robot is decreased by 10% through topological optimization of its structure and control system by Albert Albers.<sup>70</sup>

There is a larger optimization space in MEPs Lightweight design with satisfying the functionality, performance and quality conditions, which plays an important role in reducing equivalent carbon emissions in materials processing and carbon emissions in manufacturing process, so the MEPs lightweight design itself is a low-carbon design.

## 2.3 Modular Design

The concept of modular design was put forward in 1950s,<sup>71</sup> modular design is defined as a design method that “on the basis of function analysis of different function or same function with different performance, different specifications of products in a certain range, a series of functional modules were established and designed, then different module is selected and combined to make up various products which can meet different needs of the market”. Module identification and division,<sup>72</sup> module evaluation and decoupling design,<sup>73</sup> module interface design,<sup>74,75</sup> module reuse degree evaluation,<sup>76,77</sup> module modeling<sup>78,79</sup> and generalized modular design<sup>80</sup> etc. are gradually developed on this basis. At present, environmental factors were taken into account in modular design, green modular design,<sup>81</sup> low carbon technology based on modular design<sup>82</sup> and modular design for life cycle<sup>83</sup> are gradually came into being.

Modularity can increase the number of standard component of products, achieve rapid configuration of products and improve disassembly of products. These advantages can reduce the direct or indirect carbon emission in various aspects of product life cycle. With the rapid development of modular theory and application, the aim of series steps of green modular disassembling operation of structure, disassembly sequence generation and concrete disassembly methods was achieved based on the methods of standardized module structure,

module standard interface, module reusability and module disassembly and recyclability,<sup>84,85</sup> which will indicate the direction of structure low carbon operation as well as structure combination technology.

### 3. Carbon Footprint Analysis and Evaluation

Product carbon footprint analysis and evaluation is one of the criteria and constraints in product design. Low carbon is short for low "carbon emissions" or "carbon footprint". The term "carbon emissions" or "carbon footprint" originates from ecological footprint proposed by Wackemagel and Rees which is often used as environment performance indicators to measure the product property.<sup>86,87,88</sup> The scholars have different understanding on the definition of low carbon footprint which is used as an important scientific basis for design.

#### 3.1 Carbon Footprint Analysis

Scholars in the world have carried out the exploratory research on the analysis carbon footprint. Some researchers focused on the analysis of components carbon footprint, for example, Zhang X.F. et al.<sup>89</sup> analyzed the parts connection characteristics, the GHG emissions of connection units are calculated by the proposed recursive distribution approach of connection units' carbon footprint based on analytic hierarchy process (AHP) method. Song J S. proposed a low-carbon product design system in the entire life cycle based on BOM using the embedded GHG emissions data of the parts.<sup>90</sup>

And some other researchers focused on specific MEPs, Toby et al. put forward the heuristic method of telecommunications and electronics products carbon footprint.<sup>91</sup> Jeong I T. et al. proposed an assessment method for eco-design improvement options using global warming and economic performance indicators.<sup>92</sup> The external cost which converts the external effect of global warming into a monetary value was chosen as the global warming performance indicator in order to measure the performance of the GHG reduction of the product, and this assessment method was applied to the liquid crystal display (LCD) panel for a case study. G.Lucchetta et al. addresses the multi-objective problem of minimizing the overall environmental impact by incorporating the numerical simulation of the process and the structural analysis of the part in a CAD-based shape optimization environment.<sup>93</sup> Cao H.J. et al. introduced a method for assessing the carbon emissions of machine tools lifecycle according to the analysis of product structure and life cycle characteristic of machine tools, based on the principle of LCA.<sup>94</sup> Yin J. analyzed the dynamic characteristics of carbon flow for mechanical manufacturing system, proposed a dynamic modeling method of carbon flow based on extended first-order hybrid Petri nets, simulated and optimized the time domain characteristics of the energy flow and material flow, and calculated the corresponding carbon emissions.<sup>95</sup>

These carbon footprint calculation methods were studied from different aspects and different levels, the factors involved are more and more comprehensive, which provides a good reference for the future carbon footprint calculation integration at the manufacturing stage.

#### 3.2 Carbon Footprint Evaluation

Based on the carbon footprint analysis, scholars in the world have carried out carbon footprint evaluation from different perspectives, such as manufacturing system, craft process, material preparation and energy production.

Narita Hirohisa et al proposed to build a future manufacturing system based on LCA, which can calculate the carbon footprint according to the exact processing information including machine tool unit, the condition of tool, the quantity of coolant and lubricating oil and workpieces.<sup>96</sup> Through the supply chain modeling and linear programming method, the function between resource utilization and related variables during low carbon manufacturing process is described by S.Trdech at the workshop level and extension process chain level.<sup>97,98</sup> Sun L.F. et al. built the library of basic components by tracking the carbon emissions in production of each parts and describing them by their manufacture process. The hierarchical model for carbon emissions of complex equipment products was constructed from bottom to top by constructing the structure and drawing the information of carbon emissions layer by layer.<sup>99</sup> The UK transport carbon model is built by Christian Brand in order to explain the calculation method of carbon footprint external cost. And the carbon emission prediction and evaluation method was proposed through researching energy circulation mechanism in system based on the model of technology, economy and energy system (such as MARKAL model and DFT model).<sup>100</sup> Venkatesh A. built uncertainty evaluation model of greenhouse gas emissions during fossil fuel life cycle by employing process framework and statistical modeling method.<sup>101</sup> Yoshioka Takuyuki proposed a method of energy balance analysis and calculation of CO<sub>2</sub> emissions by LCA, and a way of reducing CO<sub>2</sub> emissions by using biomass energy.<sup>102</sup> The process of quantify energy efficiency by LCA is proposed by Portha Jean-Francois, and the relationship between elements in the process and the environment are considered. The aim is to build the function between carbon dioxide emissions and the related thermodynamic quantities based on thermodynamic functions, which can calculate carbon dioxide emissions.<sup>103</sup> Streamlined life cycle assessment is first proposed by Riffa Gianluc, and these studies were used to evaluate three types of carbon footprint.<sup>104</sup> In Japan, in order to facilitate the boundary division and specific calculation, 45 kinds of product category rules were set in the calculation of carbon emissions by Inaba Atsushi, and the low carbon products were developed at the same time.<sup>105</sup>

Although the methods of carbon footprint evaluation are not the same, the same target of evaluation is to obtain the product strategy which is low-carbon and the function, quality as well as performance could meet the demand.

### 4. Conclusions and Prospect

This paper reviews the research status of MEPs low carbon design, the study was discussed from the eco-design for energy saving, lightweight design and modular design etc. Carbon footprint calculation and evaluation for low carbon design were summarized in

this paper. In the view of research status in the world, the specific operation of MEPs low carbon design started earlier and has been relative mature. However, the analysis and evaluation of MEPs low carbon design starts later. Systematic approach system has not been established and it is still in initial stage.

#### 4.1 Conclusions of MEPs low carbon design method

MEPs lightweight design is an efficient method to reduce the direct and indirect carbon dioxide emission, but justly focusing on weight reduction will not always lead to improve environmental performance. So it is important to consider the conflict between lightweight and other aspects in the design process.

Ecology mainly reflects the concept of the harmony between human and nature as well as sustainable development, but MEPs eco-design in purely energy saving perspective is not comprehensive. The environment impact should be considered from each stage of the life cycle which is from producing to recycling, and the impact level should be measured by certain standards.

Additionally there are some problems need to be solved on modular design: ①Module can reduce carbon emissions under non-modular operation, and achieve modular or group calculation of carbon emissions, but at the same time of module standardized operation ,module internal scalability will be weaken; ②Problems of the combination sequence in sub module combination process, sub module selection scheme, auxiliary unit transformation after sub module changing are still need to be solved; ③Performance parameters coupled calculation model of combined module is also a problem.

Carbon footprint analysis method is a new perspective to calculate and evaluate carbon emissions, which plays an important role in evaluating the greenhouse effect. But in engineering machinery field the carbon footprint database of parts information has not been completely established. The current carbon footprint calculation is obtained by a rough calculation rather than experiment. In addition, the carbon footprint is affected by working environment, artificial operation as well as the calculation deviation, and corresponding function models of the influence factors has not been established. In order to calculate the complex product carbon footprint, the systematically logic system need to be established. In life cycle design process, evaluation standard of carbon footprint in each link has not been formulated, therefore the carbon footprint detection and evaluation will be a little subjective. Thus, when one or several links carbon emission exceeds the standard, but the whole carbon emissions is below the standard, how to distinguish low carbon products from high carbon ones become the key point, which need to give the bounds of each link in the comprehensive evaluation system based on establishment of each link evaluation and the whole life cycle evaluation system.

#### 4.2 Prospect of MEPs Low Carbon Design

In the method of MEPs low carbon design, only taking the carbon footprint as an indicator is not enough to judge whether each step of structure design fit the requirements. One of the effective methods to

achieve product low carbonization is considering multi-factors including carbon footprint, optimization of cost and structure property, and establishing the reasonable feedback mechanism, which is also one of the difficulties in research.

The methods of carbon footprint calculation need to be further improved, such as calculation boundary, data selection and carbon emission coefficient in process analysis method. Taking Carbon footprint as a target condition and combining mature algorithm in the process of carbon footprint calculation. In the specific carbon emissions calculation at different stage, various methods should be considered to calculate product carbon footprint. These calculating process highlight the analysis of the relationship between emissions of carbon footprint and other factors of product, as well as the influence to other stage of whole life cycle while optimizing carbon footprint of each phase, then corresponding decoupling model and the influence equation will be built. In this context of carbon footprint optimization, improving the competitiveness of products effectively is the decisive factor to ensure the effective implementation of the low carbon products design.

Carbon footprint evaluation method application should be strengthen in the field of engineering, especially the application in concept design, process design and recycling design. The product carbon footprint evaluation range and corresponding evaluation system should be established, part satisfy the principle and whole satisfy the principle of the various stages of the product life cycle carbon footprint evaluation should be confirmed.

#### ACKNOWLEDGEMENT

The work is financially supported by National Natural Science Foundation of China (NSFC).

Thanks to the support of NSFC, item: 51135004.

#### REFERENCES

1. Laurent A., Olsen S. I. and Hauschild M. Z., "Carbon footprint as environmental performance indicator for the manufacturing industry," *CIRP Annals Manufacturing Technology*, Vol. 59, No.1, pp.37-40, 2010.
2. Ajukumar, V. N. and O. P. Gandhi., "Evaluation of green maintenance initiatives in design and development of mechanical systems using an integrated approach," *Journal of Cleaner Production*, Vol.51,pp. 34-46, 2013.
3. Herrmanni T. and Hauschild M. Z., "Effects of globalization on carbon footprints of products," *CIRP Annals Manufacturing Technology*, Vol.58, No.1, pp.13-16, 2009.
4. Liu Fei, Li Congbo and Cao Huajun, "Green manufacturing technology connotation and system framework based on product life cycle," *Journal of Mechanical Engineering*, Vol. 45, No. 12,pp. 115-120, 2009.
5. Russo, D. and C. Rizzi, "Structural optimization strategies to design green products," *Computers in Industry* , Vol. 65, No. 3,pp.

- 470-479, 2014.
6. Gerne S., Kobeissi A. and David B., "Integrated approach for disassembly processes generation and recycling evaluation of an end-of-life product," *International Journal of Production Research*, Vol. 43, No. 1, pp. 195-222, 2005.
  7. Kim H. J., Ciupek M. and Buchholz A., "Adaptive disassembly sequence control by using product and system information," *Robotics and Computer Integrated Manufacturing*, Vol. 22, No. 3, pp. 267-278, 2006.
  8. Liu Zhifeng, Li Xinyu and Zhang Hongchao, "Research on design methods of products based on ADSM," *Journal of Mechanical Engineering*, Vol. 45, No. 10, pp. 192-197, 2009.
  9. Wang Xiang and Chen Ming, "Implementing extended producer responsibility: vehicle remanufacturing in China," *Journal of Cleaner Production*, Vol. 19, No. 6/7, pp. 192-197, 2011.
  10. Xu Binshi, Liu Shican and Shi Peijing, "The frontier issues of development and industrialization of remanufacturing engineer," *China Surface Engineering*, Vol. 21, No. 1, pp. 1-5, 2008.
  11. Tjiparo Z. and Thompson G., "Review of maintainability design principles and their application to conceptual design," *Journal of Process Mechanical Engineers*, Vol. 218, No. E2, pp. 103-113, 2004.
  12. Gabbar Hossam A., "Engineering design of green hybrid energy production and supply chains," *Environmental Modelling & Software*, Vol. 24, No. 3, pp. 423-435, 2009.
  13. Liu Hongqi and Chen Shixing, "Comprehensive evaluation model and method system of product greenness," *China Mechanical Engineering*, Vol. 11, No. 9, pp. 1013-1016, 2000.
  14. Chinese Mechanical Engineering Society, "Technology roadmaps of Chinese mechanical engineer," Beijing: China Science and Technology Press, 2011.
  15. Gutowski T., "Thermodynamic Analysis of Resources Used in Manufacturing Processes," *Environmental Science and Technology*, Vol. 43, pp. 1584-1590, 2009.
  16. Branham M.; Gutowski T. and Sekulic D., "A thermodynamic framework for analyzing and improving manufacturing processes," *Proc. of IEEE International Symposium on Electronics and the Environment*, 2008.
  17. A. Hassanpour Isfahani and H. Lesani, "Design Optimization of Linear Induction Motor for Improved Efficiency and Power Factor," *Proc. of IEEE Electric Machines & Drives Conference*, Vol. 2, pp. 988 - 991, 2007.
  18. El Ferik S. and Belhadj CA., "Neural network modeling of temperature and humidity effects on residential air conditioner load," *Proc. of The 4th IASTED International Conference on Power and Energy System*, pp. 557-562, 2004.
  19. El Ferik S. and Belhadj CA., "Predicting AC power consumption using a stochastic Markov chain simulating weather conditions," *Proc. of the 14th IASTED International Conference on Applied Simulation and Modelling*, pp. 247-52, 2005.
  20. Belhadj, C.A. and El Ferik, S., "Segregated residential air conditioner load model behavior with temperature and humidity," *Proc. of the 5th IASTED International Conference on Power and Energy Systems*, Vol. 13, pp. 2-7, 2005.
  21. Liu Zhifeng, Jiang Yun and Gao Yang, "Study of energy design method for dishwasher," *Journal of Hefei University of Technology (Natural Science)*, Vol. 34, No. 9, pp. 1281-1285, 2011.
  22. Qi Yunhui, Huang Haihong, Liu Cuangfu and Liu Zhifeng, "Energy analysis method based on dynamic life cycle," *China Mechanical Engineering*, Vol. 43, No. 8, pp. 129-134, 2007.
  23. Zhou Dan, Liu Guangfu and He Ping, "Study on extracting method of energy design factors for NC machines," *China Mechanical Engineering*, Vol. 22, No. 3, pp. 351-355, 2011.
  24. H.C. Zhang and H. Li, "An energy factor based systematic approach to energy-saving product design," *Annals of the CIRP*, Vol. 59, pp. 183-186, 2010.
  25. Kim H.G. "Stress analysis and design strategy for lightweight car seat frame," *Proc. of the 5th International Conference on Fracture and Strength of Solids (FEOFS2003): Second International Conference on Physics and Chemistry*, pp. 597-602, 2004.
  26. Qi Yunhui, Wang Shuwang and Liu Guangfu, "Product Structure Element Clustering Design for Energy Optimization," *China Mechanical Engineering*, Vol. 44, No. 1, pp. 161-167, 2008.
  27. Wakui, T., "Energy-saving effect of a residential polymer electrolyte fuel cell cogeneration system combined with a plug-in hybrid electric vehicle," *Energy Conversion and Management*, Vol. 77, pp. 40-51, 2014.
  28. Cipollone, R., "Model based Design and Optimization of a Fuel Cell Electric Vehicle," *Energy Procedia*, Vol. 45, pp. 71-80, 2014.
  29. Minav, T. A., "Analysis of electro-hydraulic lifting system's energy efficiency with direct electric drive pump control," *Automation in Construction*, Vol. 30, pp. 144-150, 2013.
  30. Zeng, X., "Research on energy saving control strategy of parallel hybrid loader," *Automation in Construction*, Vol. 38, pp. 100-108, 2014.
  31. Hsu, Y. L., "Energy-saving trajectory planning for a toggle mechanism driven by a PMSM," *Mechatronics*, Vol. 24, No. 1, pp. 23-31, 2014.
  32. Saidur, R., "Applications of variable speed drive (VSD) in electrical motors energy savings," *Renewable and Sustainable Energy Reviews*, Vol. 16, No. 1, pp. 543-550, 2012.
  33. Shaohua Hu, Fei Liu and Tang Hu, "An on-line approach for energy efficiency monitoring of machine tools," *Journal of Cleaner Production*, Vol. 27, pp. 133-140, 2012.
  34. Avram, O. I. and P. Xirouchakis, "Evaluating the use phase energy requirements of a machine tool system," *Journal of Cleaner Production*, Vol. 19, No. 6-7, pp. 699-711, 2011.
  35. Vinodh, S., "Integration of ECQFD, TRIZ, and AHP for innovative and sustainable product development," *Applied Mathematical Modelling*, 2013.
  36. Song, Q., "Life cycle assessment of TV sets in China: a case study of the impacts of CRT monitors," *Waste Manag.*, Vol. 32, No. 10, pp. 1926-1936, 2012.
  37. Zhang Xiufen, Zhang Shuyou and Yi Guodong, "Construction and evolution of disassemblable structure unit map for products," *Journal of Mechanical Engineering*, Vol. 47, No. 3, pp. 95-102, 2011.

38. Smith, S., "Disassembly sequence structure graphs: An optimal approach for multiple-target selective disassembly sequence planning," *Advanced Engineering Informatics*, Vol. 26, No. 2, pp.306-316, 2012.
39. Jiang Jibin, Xu Mingsan, Zeng Shoujin and Su Fa. "Disassembly Path Planning Method of Waste Electromechanical Products in Remanufacturing," *Transactions of the Chinese Society for Agricultural Machinery*, Vol. 40, No. 10, pp.203-206, 2009.
40. Zhang Ling, Wang Zhengxiao and Pan Xiaohong, "Generation and evaluation of disassembly sequences in green design," *Transactions of the Chinese Society for Agricultural Machinery*, Vol. 41, No. 10, pp.199-207, 2010.
41. Cao Yicong, Feng Yixiong and "Tan Jianrong. Dynamic characteristics of multi-stage planetary gears of shield tunnelling machine based on planet mesh phasing analysis" *Journal of Mechanical Engineering*, Vol.47, No. 23, pp.144-152, 2011.
42. Colledani, M. and T. Tolio, "Integrated process and system modelling for the design of material recycling systems," *CIRP Annals - Manufacturing Technology*, Vol. 62, No. 1, pp. 447-452, 2013.
43. Russo, D. and C. Rizzi, "Structural optimization strategies to design green products," *Computers in Industry*, Vol. 65, No. 3, pp. 470-479, 2014.
44. Nagalingam, S. V., "Performance measurement of product returns with recovery for sustainable manufacturing," *Robotics and Computer-Integrated Manufacturing*, Vol. 29, No.6, pp. 473-483, 2013.
45. Sun Youchao, Huang Jinyong and Wang Wei, "Quantitative evaluation method of product disassembly based on parts failure rate and disassembly time," *Journal of Mechanical Engineering*, Vol. 46, No. 13, pp.147-154, 2010.
46. Pan Yunhe, Sun Shouqian and Bao Enwei, "The current developing situation and tend of computer aided industrial design technology" *Journal of Computer-Aided Design & Computer Graphics*, Vol. 11, No.3, pp. 248-252, 1999.
47. LI Fangyi, Duan Guanghong and Wang Jinsong, "Green product design assessment," *Journal of Tsinghua University: Science and Technology*, Vol. 42, No. 6, pp. 783-786, 2002.
48. Yang, C. J. and J. L. Chen, "Forecasting the design of eco-products by integrating TRIZ evolution patterns with CBR and Simple LCA methods," *Expert Systems with Applications*, Vol. 39, No. 3, pp. 2884-2892, 2012.
49. Chou, J. R., "An ARIZ-based life cycle engineering model for eco-design," *Journal of Cleaner Production*, Vol. 66, pp. 210-223, 2014.
50. Victor Poudelet, Julie-Anne Chayer and Manuele Margni, "A process-based approach to operationalize life cycle assessment through the development of an eco-design decision-support system," *Journal of Cleaner Production*, Vol. 33, pp.192-201, 2012.
51. Liu Xianli and Chen Tao, "Theory and technology of low-carbon manufacturing in machinery manufacturing" *Journal of Harbin University of Science And Technology*, Vol. 16, No. 1, pp. 1-8, 2011.
52. Witik, R. A., et al., "Assessing the life cycle costs and environmental performance of lightweight materials in automobile applications," *Composites Part A: Applied Science and Manufacturing*, Vol. 42, No. 11, pp. 1694 – 1709, 2011.
53. Erik Tempelman, "Fundamentals of Materials and Design," *Materials Experience* Vol.27, No. 1, pp. 64–68, 2006.
54. Guo Lei, Zhang Hui and Duan Guanghong, et al., "Light weight design of a machine tool based on sensitivity analysis," *Journal of Tsinghua University: Science and Technology*, Vol. 51, No. 6, pp. 846-850, 2011.
55. Zulaika J. J., Campa F. J., Lopez De Lacalle L. N., "An integrated process- machine approach for designing productive and lightweight milling machines," *International Journal of Machine Tools & Manufacture*, Vol. 51, No. 7/8, pp. 591-604, 2011.
56. Huajun Cao and Hong Cheng Li, "A carbon efficiency approach for life-cycle carbon emission characteristics of machine tools," *Journal of Cleaner Production*, Vol. 37, pp. 19-28, 2012.
57. Shi Guohong, Chen Yong and Yang Yuze, et al, "BIW architecture multidisciplinary light weight optimization design," *Journal of Mechanical Engineering*, Vol. 48, No. 4, pp. 110-114, 2012.
58. Zhao Han and Qian Demeng, "Research on lightweight design of automobile structure based on ANSYS," *Transactions of the Chinese Society for Agricultural Machinery*, Vol.36, No.6, pp. 12-15, 2005.
59. LI Yanping, Liu Haijiang and Tong Ronghui, "Lightweight scheme selection for car-body based on multi-objective satisfaction," *Computer Integrated Manufacturing Systems*, Vol. 17, No. 1, pp.37-44, 2011.
60. Peng Yu and Hao Zhiyong, "Virtual-prototype-based dynamic lightening design," *Journal of Zhejiang University: Engineering Science*, Vol. 42, No. 6, pp. 984-988, 2008.
61. Zheng Songlin and Wang Yansheng, "Weight-reduction Design of Auto Structures Based on Strength Features," *Journal of Mechanical Engineering*, Vol. 02, pp. 129-133, 2008.
62. Clain B., "Lightweight design: calculation basis and compound structure," Beijing: China Machine Press, 2010.
63. Li, Y., "Experimental study of glass-fiber mat thermoplastic material impact properties and lightweight automobile body analysis," *Materials & Design*, Vol. 25, No.7, pp. 579-585, 2004.
64. Yan Zhang, "Lightweight design of automobile component using high strength steel based on dent resistance," *Materials & Design*, Vol. 27, No. 1, pp. 64–68, 2006.
65. Zhao Han and Chen Xingyu, "Research on Lightweight Design of Press Frame Structure Based on Parametric FEA," *Journal of Engineering Graphics*, Vol. 1, No. 1, pp.20-25, 2010.
66. LI Yancong and Zhang Lianhong, "Multi-objective Optimization Design of Heavy Forge Framed Hydraulic Press Driven by Stiffness and Mass," *Journal of Mechanical Engineering*, Vol. 46, No. 1, pp. 140-146, 2010.
67. Li Yancong and Zhang Lianhong, "Lightweight and Stiffness Optimization of a Hydraulic Press's Upper Beam Based on

- Neural Networks and Genetic Algorithms,” *Mechanical Science and Technology for Aerospace Engineering*, Vol. 29, No. 2, pp. 164-169, 2010.
68. Tan Huifeng, Wang Chao and Wang Changguo, “Progress of new type stratospheric airships for realization of lightweight,” *Acta Aeronautica et Astronautica Sinica*, Vol. 31, No. 2, pp. 257-264, 2010.
  69. Yang He, Li Heng and Zhang Zhiyong, “Advance and trends on tube bending forming technologies,” *Chinese Journal of Aeronautics*, Vol. 1, pp. 1-12, 2012.
  70. Albers A, Ottnad J., “Integrated structural and controller optimization for lightweight robot design,” *Proc. of 9th IEEE-RAS International Conference on Humanoid Robots*, pp.93-98, 2009.
  71. Erixon G, Yxkull V A. and Arnstrom A., “Modularity the basis for product and factory reengineering,” *CIRP Annals-Manufacturing Technology*, Vol. 45, No. 1, pp. 1-4, 1996.
  72. Umeda Y., Fukushige S., “Product modularity for life cycle design,” *CIRP Annals-Manufacturing Technology*, Vol. 57, pp. 1-13, 2008.
  73. Umeda Y., Fukushige S., “Evaluation of scenario-based modularization for life cycle design,” *CIRP Annals Manufacturing Technology*, Vol. 58, No. 1, pp. 1-4, 2009.
  74. Wulfsberg, J. P., et al. “A function integrated and intelligent mechanical interface for small modular machine tools,” *Precision Engineering*, Vol. 38, No. 1, pp. 109-115, 2014.
  75. Umeda Y., Fukushige S. and Tonoike K., “Product modularization for lifecycle design,” *CIRP Annals- Manufacturing Technology*, Vol. 57, No. 1, pp. 13-16, 2008.
  76. Umeda Y., Fukushige S. and Tonoike K., “Evaluation of scenario-based modularization for lifecycle design,” *CIRP Annals-Manufacturing Technology*, Vol. 58, No. 1, pp. 1-4, 2009.
  77. Ameta G, Mani M. and Rachuri S., “Carbon weight analysis for machining operation and allocation for redesign,” *International Journal of Sustainable Engineering*, Vol. 2, No. 4, pp. 241-251, 2009.
  78. Li Jiang, Zhong Shisheng and Liu Jin, “Research on modular design methods based on extension theory,” *Computer Integrated Manufacturing Systems*, Vol. 12, No. 5, pp. 641-648, 2006.
  79. Li Guoxi, Wu Jianzhong and Zhang Meng, “Approach to product modular design based on FPBS,” *Journal of National University of Defense Technology*, Vol. 31, No. 5, pp. 75-81, 2009.
  80. Gao Weiguo, Xu Yanshen and Chen Yongliang, “Theory and methodology of generalized modular design,” *Chinese Journal of Mechanical Engineering*, Vol. 43, No. 6, pp. 48-54, 2007.
  81. Shana S. and Yen C C., “Green product design through product modularization using atomic theory,” *Robotics and Computer-Integrated Manufacturing*, Vol. 26, No. 6, pp. 790-798, 2010.
  82. Tang Tao, Liu Zhifeng and Liu Guangfu, “Research on the methodology of green modular design,” *Journal of Mechanical Engineering*, Vol. 39, No. 11, pp. 199-204, 2009.
  83. Ji, Y., “Green modular design for material efficiency: a leader-follower joint optimization model,” *Journal of Cleaner Production*, Vol. 41, pp. 187-201, 2013.
  84. Qi, Y., X. B. and Wu , “Low-carbon Technologies Integrated Innovation Strategy Based on Modular Design,” *Energy Procedia*, Vol. 5, pp. 2509-2515, 2011.
  85. Umeda, Y., “Product modularity for life cycle design,” *CIRP Annals-Manufacturing Technology*, Vol. 57, No. 1, pp. 13-16, 2008.
  86. Johnson E., “Disagreement over carbon footprints: A comparison of electric and LPG for knives,” *Energy Policy*, Vol. 36, No. 4, pp. 1569-1573, 2008.
  87. Foo D C Y., Tan R R. and Ng D K S., “Carbon and footprint-constrained energy planning using cascade analysis technique,” *Energy*, Vol. 33, No. 10, pp. 1480-1488, 2008.
  88. Qi Yunhui ,Wang Shuwang and Liu Guangfu, “Product Structure Element Clustering Design for Energy Optimization,” *Journal of Mechanical Engineering*, Vol. 44, No. 1, pp. 161-167, 2008.
  89. Xiu Fen, Zhang Shu, You Zhang and Zhi Yong Hu., “Identification of connection units with high GHG emissions for low-carbon product structure design,” *Journal of Cleaner Production*, Vol. 27, pp. 118-125, 2012.
  90. Song JS. and Lee KM., “Development of a low-carbon product design system based on embedded GHG emissions,” *Resources Conservation and Recycling*, Vol. 54, No. 9, pp. 547-556, 2010.
  91. Toby J. and Okrasinski T A., Schaeffer W., “Estimating the carbon footprint of telecommunications products: a heuristic approach,” *Journal of Mechanical Design, Transactions of the ASME*, Vol. 132, No. 9, pp. 0945021 -0945024, 2010.
  92. Jeong I. T. and Lee K.M., “Assessment of the ecodesign improvement options using the global warming and economic performance indicators,” *Journal of Cleaner Production*, Vol. 17, No. 13, pp. 1206-1213, 2009.
  93. G.Lucchetta, P.F.Bariani., “Sustainable design of injection moulded parts by material intensity reduction ,” *Annals of the CIRP*, Vol. 59, pp. 33-36, 2010.
  94. Cao Huajun, Li Hongcheng and Song Shengli, “Evaluation method and application for carbon emissions of machine tool based on life cycle assessment,” *Computer Integrated Manufacturing Systems*, Vol. 17, No. 11, pp. 2432-2437, 2011.
  95. Yin Jiu, Cao Huajun and Du Yanbin, “Dynamic Modeling of Carbon Flow for Mechanical Manufacturing System Based on Extended First-order Hybrid Petri Nets,” *Journal of Mechanical Engineering*, Vol. 47, No. 23, pp. 152-160, 2011.
  96. Narita Hirohisa and Kawamura Hiroshi, “Development of prediction system for environmental burden for machine tool operation (1st report, proposal of calculation method for environmental burden),” *Proc. of JSME International Journal, Series C: Mechanical Systems, Machine Elements and Manufacturing*, Vol. 49, No. 4, pp. 1188-1195, 2007.
  97. S. Tridech and K. Cheng, “Low Carbon Manufacturing: Characterization,” *Proc. of The 6th International Conference on Manufacturing Research*, pp. 403-402, 2008.
  98. S. Tridech and K. Cheng, “An investigation on the framework for EREE-based low carbon manufacturing,” *Proc. of the 5th International Conference on Responsive Manufacturing-Green Manufacturing*, pp. 257-267, 2010.

99. Sun Liangfeng, Qiu Lemiao, Zhang Shuyou and Wu Xiaorong, "Hierarchical model for carbon emissions of complex equipment for low-carbon design," *Computer Integrated Manufacturing Systems*, Vol. 18, No. 11, pp. 2381-2390, 2012.
100. Christian Brand, Martino Tran and Jillian Anable, "The UK transport carbon model: An integrated life cycle approach to explore low carbon futures," *Energy Policy*, Vol. 8, pp. 1-17, 2010.
101. Venkatesh A., Griffin W. M. And Jaramillo P., "Uncertainty analysis of life cycle greenhouse gas emissions from petroleum-based fuels and impacts on low carbon fuel policies," *Environ. Sci. Technol.*, Vol. 45, No. 1, pp. 125-131, 2010.
102. Yoshioka Takuyuki, Aruga, Kazuhiro, Nitami Toshio, Kobayashi Hiroshi, Sakai and Hideo, "Energy and carbon dioxide (CO<sub>2</sub>) balance of logging residues as alternative energy resources: System analysis based on the method of a life cycle inventory (LCI) analysis," *Journal of Forest Research*, Vol. 10, No. 2, pp. 125-134, 2005.
103. Portha Jean-Francois, Jaubert Jean-Noel, Louret Sylvain, Pons and Marie-Noelle, "Definition of a thermodynamic parameter to calculate carbon dioxide emissions in a catalytic reforming process," *International Journal of Thermodynamics*, Vol. 11, No. 2, pp. 81-89, 2008.
104. Griffa Gianluca, Radice Lorenzo, Bianco Claudio, Andrae Anders, Bin Zhu, Dong Han, Gemma Paolo and Shudong Luo, "Carbon footprint of next generation fixed networks," *Proc. of the 32nd International Telecommunications Energy Conference*, 2010.
105. Inaba Atsushi, "Carbon footprint of products," *Nihon Enerugi Gakkaishi Journal of the Japan Institute of Energy*, Vol. 89, No. 7, pp. 623-631, 2010.

# Standardized Hazardous Materials Management for Global Environmental Compliance in Industrial Enterprises

Markus Hornberger<sup>1</sup>, Robert Mieke<sup>1,#</sup> and Thomas Bauernhansl<sup>1</sup>

<sup>1</sup> Fraunhofer Institute for Manufacturing Engineering and Automation (IPA), Nobelstrasse 12, 70569 Stuttgart, Germany  
# Corresponding Author / E-mail: Robert.Mieke@ipa.fraunhofer.de, TEL: +49(0)711-970-1424, FAX: +49(0)711-970-1002

KEYWORDS: Process Engineering, Hazardous Substances, Environmental Compliance

*Enhanced global trade forces companies to comply with a variety of environmental legislations each being subject to continuous modifications. Apart from various maximum permissible values of certain substances and different requirements, e.g. for registration or authorization, latest developments in the field conflict minerals constrain enterprises to adjust internal processes. This puts high pressure especially on global players with multiple thousand active suppliers and hundreds of global sales regions. For OEMs global environmental compliance requires involvement of the entire supply chain and multiple internal business units. Additionally, law enforcement agencies expand activities while competitors may easily take misconduct to court and thus may temporarily refuse market access. This may induce dramatic costs for companies. In order to reduce risk and prevent undesired obsolescence of their products, companies seek a standardized process to guarantee global environmental compliance.*

*Recently, scientific improvements in this area have been rare. In this paper we introduce a highly applicable approach that has been tested successfully in over 70 companies in Germany. We divide efforts in five categories (1. targets; 2. actual company status; 3. risk assessment 4. required actions; 5. long term validation) and 14 steps towards global environmental compliance. Thereby, we identify affected divisions and define distinct methods to effectively map legal requirements, evaluate suppliers and rate a company's material stock. Hereupon, we combine supplier and material rating in order to evaluate a company's general risk and name a number of distinct actions for supplier communication. We come up with solutions to adjust internal processes such as data processing and IT as well as recommendations for detailed work procedures and audit plans to effectively ensure long term global environmental compliance.*

*Although integral risk validation might not be possible, our paper shows a high demand in industries for future research in the field standardizing environmental compliance processes by applying unique algorithms. Additionally, current environmental risk assessment methods leave room for interpretation. We identify possible approaches for improvements as well as solutions for current methods.*

## 1. Introduction

Green manufacturing is one of today's major challenges to industries.<sup>1</sup> Besides the reduction of material and energy use, policies seek to prevent consumers and the environment from certain hazardous substances. Most governments have realized their obligation to remove these substances from consumer products and have introduced appropriate legislations. Most relevant legislations in the field of hazardous materials in consumer products within the European Union (EU) are ELV, WEEE, RoHS, and REACH.<sup>2-5</sup> Other countries and regions will or have introduce(d) similar regulations with slightly different requirements. Differing specifications essentially cover scope of application, maximum permissible values,

exception, exemptions and documentation requirements. Since 2003 global legislations and requirements in this field thus have increased exponentially as displayed in figure 1.<sup>6</sup>

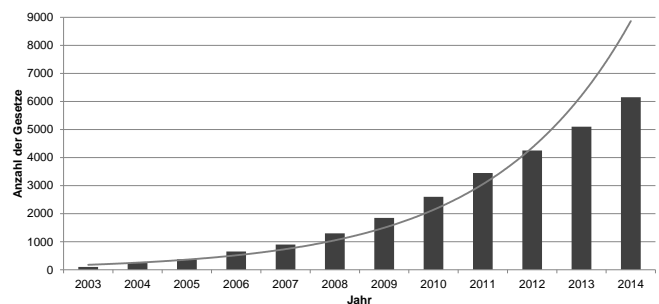


Figure 1 Amount of global environmental legislations<sup>6</sup>

On a long term, the amount of global legislations and requirements are expected to continuously increase. Enhanced global trade due to globalization hence forces companies to comply with a variety of environmental legislations each being subject to continuous modifications. Companies generally have to ensure legal compliance over their entire supply chain. This eventually increases complexity of business and puts high pressure especially on global players with multiple thousand active suppliers and hundreds of global sales regions.

Non-compliance may significantly affect profit, sales figures and reputation. In 2013, the use of a banned cooling agent by regulation (EC) No 842/2006 in Daimler vehicles forced the French government to refuse market access.<sup>7</sup> Although concrete numbers were not published by Daimler, estimations account for 4500 vehicles not being sold in France.<sup>8</sup> Substantial monetary losses and reputation damage remain as results of this case.

In this context, three sources of risk are predominant: [1] law enforcement, [2] competitors and [3] obsolescence of products. Over the past couple of years, law enforcement agencies have expanded activities. Furthermore, competitors may easily take misconduct to court and thus may temporarily refuse market access. A temporary loss of market access may induce dramatic costs for companies. Most important for industrial enterprises is, however, the avoidance of undesired obsolescence of their products. Generally, governments grant exemptions if appropriate technologies for certain applications do not exist. These exemptions are limited to the date of a novel technology being introduced. If a company is not able to follow technological development and adjust products this leads to rapid undesired obsolescence. This especially represents a major challenge to those companies that have long development periods and apply batch production.

Companies thus face a wide variety of challenges in order to guarantee global environmental compliance. We identify five problem areas.

[1] Decision makers lack in *explicit knowledge* about relevant legislations and methods of risk assessment. Furthermore, legislative amendments are not being followed properly.

[2] The *product spectrum* is source of further complexity. Following the current trend towards individualization, companies often manufacture a wide variety of products, each being subject to other legislations and exemptions. Also commonly modules from predecessor generation that might not fulfill requirements of today's legislations are integrated into new products.

[3] The *exposure to master data* represents another source of concern. The value-added process of industrial companies requires the application of different data bases, e.g. for design (CAx) and resource planning (ERP). In order to guarantee global environmental compliance, up to date information about prohibited substances have to be present at each level of business, especially R&D, procurement, sales as well as quality, project and environmental management. This again requires an interface data base that commonly does not exist or is poorly managed. Additionally, often imprecise definition of materials and other attributes makes it difficult to overlook the entire

material spectrum.

[4] *Procurement and distribution* in terms of high numbers of suppliers and sales regions with low levels of informational connection additionally increase complexity.

[5] *Responsibilities* concerning hazardous material management within industrial enterprises are dubious. It often is not clear who documents legislative amendments, calculates business risk, releases materials, etc.

Considering the information above, two main problems for further research occur:

1. What elements are essential for a hazardous materials management system (HMMS)?
2. How can companies effectively introduce and live HMMS?

Recently, scientific improvements in this area have been rare. In this paper we introduce a highly applicable approach that has been tested successfully in over 70 companies in Germany.

## 2. Basics and boundaries

Although many authors have aimed at defining the term *business process* its understanding remains universal.<sup>9-11</sup> In the following, we refer to the most common definition from Davenport and Short (1990). A business process is a “[...] set of logically related tasks performed to achieve a defined business outcome”.<sup>9</sup>

Generally, industrial companies seek standardization of administrative processes as they do not directly add value to final products. Many authors have highlighted benefits from business process standardization.<sup>11,12</sup> These are essentially improving operational performance, reducing processing costs, increasing consumer satisfaction and enabling compliance with regulations.<sup>13</sup>

In this context, a variety of management systems have been discussed in literature and successfully implemented in industries. On this basis standards have been developed and legislations have been introduced, including quality (International Organization for Standardization 2005), environment<sup>15</sup> and energy<sup>16</sup> as well as EMAS (acronym for Eco- Management and Audit Scheme)<sup>17</sup> and compliance management<sup>18</sup>. None of these involve concrete instructions for hazardous materials management in companies.

The implementation of HMMS is essential for global compliance in the field of environmental law and might be linked to a compliance management system as described in<sup>18</sup>. While formerly being related to finance and health care, the term *compliance* today refers to the general adherence of all relevant legislations.<sup>19-21</sup> A distinct focus on substances in industrial products was not found in any of these sources.

Nevertheless, companies have to face a certain risk of not being compliant. This might either be caused by lack of external (e.g. relevant requirements) or internal information (substances in applied materials). Both, the term risk as well as concepts for risk management have been discussed in literature excessively.<sup>22-26</sup> According to the International Organization for Standardization, the term risk describes the “effect of uncertainty on objectives”.<sup>27</sup> In the context of HMMS risk is understood as the probability of being non-compliant. Thereby, HMMS essentially follows recommendations from ISO 31000 as displayed in figure 2.<sup>28</sup>

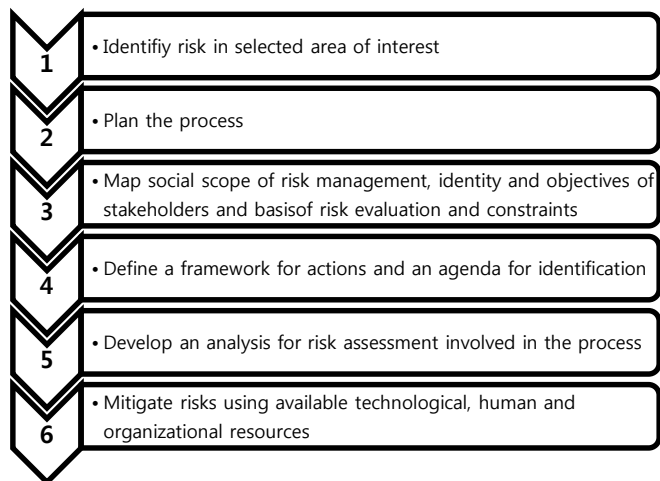


Figure 2 ISO 31000 risk management implementation<sup>28</sup>

### 3. Legal requirements

In the following we illustrate the introduction of HMMS using the example of RoHS, REACH and Conflict Minerals for the EEE industry. Therefore, the following paragraphs present essential legal requirements that arise from these three legislations.

The RoHS2 directive (2011/65/EU) is specifically designed for the EEE industry.<sup>4</sup> It restricts the use of certain hazardous substances, i.e. the heavy metals lead (Pb), mercury (Hg), cadmium (Cd) and chromium IV (Cr6) as well as the flame retardants polychlorinated biphenyls (PBB) and polybrominated diphenyl ethers (PBDE). These substances are permitted to certain maximum permissible values (0.01 % w/w for cadmium, 0.1 % w/w for the rest) related to the homogeneous material. The European directive currently grants 41 exemptions for applications where these substances are not easily substituted. In summary, the European RoHS2-Directive essentially requires the compliance with its maximum permissible values as well as a technical documentation. Similar legislations are found in many other countries and regions, including China, Japan, Korea, the Eurasian Economic Community customs union, etc., each having slightly deviating requirements.

The regulation (EC) No 1907/2006 concerning the Registration, Evaluation, Authorization and Restriction of Chemicals (REACH) is a centerpiece of European chemical law and its efforts to harmonize jurisdiction.<sup>5</sup> Based on the principle of direct industrial responsibility it targets all chemical substances that are placed on the EU market

(scope of REACH). Apart from its multiple specifications, its requirements may essentially be summarized as: [1] registration (“no data, no market” – all chemical substances), [2] information requirements (article 33), [3] authorized substance use (annex XIV) and [4] restriction (annex XVII). While the RoHS directive sets a uniform reference value (homogenous material), REACH currently has a variety of reference values leaving each affected country space for law enforcement interpretation. This leads to ambiguity even within the EU. Similar legislations have been introduced in many other countries and regions, including parts of the USA, Turkey, Japan, the Eurasian Economic Community customs union, etc., again each having slightly deviating requirements.

Conflict minerals may not be defined as hazardous substances. Latest developments and requirements in this area however justify a consideration within HMMS. Conflict minerals are referred to as minerals mined in conditions of armed conflict and human rights abuses. In the USA section 1502 of the Dodd–Frank Wall Street Reform and Consumer Protection Act (Dodd-Frank Act) forces several, mainly U.S. companies to report if these minerals are applied to their products.<sup>29</sup> Currently, the section 1502 of the Dodd-Frank Act focusses on eastern provinces of the Democratic Republic of the Congo. Affected minerals are cassiterite (tin), wolframite (tungsten), coltan (tantalite), and gold, each predominantly being applied to EEE products. Compliance is requested over the entire supply chain. Since companies being traded at US stock exchange generally have multiple thousand suppliers, section 1502 of the Dodd-Frank Act affects organization globally. Requirements for companies may essentially be summarized as: [1] information, [2] documentation, [3] audit and [4] due diligence requirements. The EU is planning to implement a slightly different approach based on voluntary participation in 2014.<sup>30,31</sup> Figure 3 summarizes requirements for companies from the EEE industry from RoHS, REACH and Conflict Minerals.

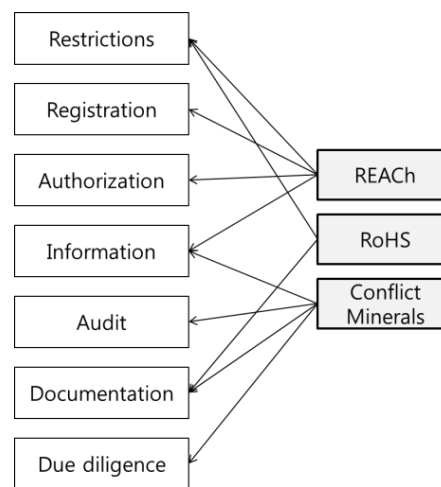


Figure 3 Summary of legal requirements from REACH, RoHS and Conflict Minerals

### 4. An approach towards standardized hazardous materials management

In the following we introduce basic elements of HMMS. We distinguish between five superior categories: [1] targets, [2] actual company status, [3] risk assessment, [4] required actions and [5] long term validation as illustrated in figure 4.



Figure 4 HMMS five step, closed loop approach

The five categories are furthermore divided into 14 steps of concrete actions as displayed in table 1.

Table 1 HMMS - 14 steps towards global environmental compliance

Step	Action	Category
1.	Identification of legal requirements	<i>Targets (external)</i>
2.	Identification of customer requirements	
3.	Identification of documentation requirements	
4.	Clarification of affected products	<i>Actual company status</i>
5.	Evaluation of status quo of supplier / manufacturer communication / rating	
6.	Evaluation of status quo of material classification	<i>(internal)</i>
7.	Risk and impact assessment	<i>Risk assessment</i>
8.	Initiation of actions - communication, control, analysis	<i>Required actions</i>
9.	Re-evaluation of suppliers, manufacturers and material	
10.	Development and continuous improvement of supplier and manufacturer audits	
11.	Overall process development, integration and continuous improvement	<i>Long term validation</i>
12.	Development and continuous improvement of instructions for design, purchase, sales, control and analysis	
13.	IT integration and support	
14.	Documentation and allocation of responsibilities	

The following subsections discuss each aspect of HMMS in detail.

### 4.1 Identification of legal requirements

First, a company has to identify relevant legislations in each distribution country. Two approaches are common: [1] the acquisition of country warrants of apprehension from a specialized service provider. These services are generally expensive and limited to a single product. [2] A self-employed documentation of relevant legislations is by far less expensive and data sources are manifold.<sup>32-34</sup>

### 4.2 Identification of customer requirements

Additional customer requirements, e.g. aluminum free, may significantly affect product development. Generally, these requirements should be clear before design and manufacturing, e.g. from contracts, terms and conditions, etc. In certain industries, e.g. consumer electronics or industries with long development periods, additional customer requirements might occur after sales start. In certain cases a company thus is forced to re-design a product which decreases earnings per unit significantly. Customer requirements have to be documented similar to legal requirements.

In both cases, we propose a two-step approach: [1] the construction of a requirement matrix as displayed in table 2 followed by [2] a detailed description of legislation specific requirements.

Table 2 Requirement matrix

Countries of distribution	Legal requirements				Consumer requirements	Summary of requirements
	REACH	RoHS	Conflict Minerals	...		
EU	x	x	X	...	-	X
USA	x	-	X	...	x	X
China	x	x	-	...	-	X
.....	...	...	...	...	...	...

This matrix guarantees a comparatively effective overview of relevant legislations and enables a company to develop its distinct definition of a certain legal group according to relevant sales regions (e.g. EU-RoHS + Korea-RoHS + China-RoHS).

### 4.3 Identification of documentation requirements

According to article 7 (b) of 2011/65/EU (EU-RoHS2) manufacturers are required to draw up a “[...] technical documentation and carry out the internal production control procedure in line with module A of Annex II to Decision No 768/2008/EC [...]”<sup>4,35</sup> Decision No 768/2008/EC regulates fundamentals of CE labeling according to article 30 of Regulation No 765/2008.<sup>36</sup> With the CE label a manufacturer declares compliance with all relevant EU regulations and requirements. For EEE products RoHS2 compliance thus is a basis for the CE labeling. Decision No 768/2008/EC essentially demands for internal manufacturing controls and technical documentation. EEE product specific documentation requirements are normed within EN 50581.<sup>37</sup> Required contents of a technical

documentation according to EN 50581 are: [1] a general description of the product, [2] documents covering applied materials, components and assembly groups, [3] information regarding connection of previously described documents as well as [4] a list of standards and technical specification and norms that have been applied. A manufacturer is obliged to determine, collect and evaluate relevant information as well as secure validation. Approved documents are standards, supplier / manufacturer / material declaration and analytical results.

Currently, EN 50581 does not exhibit validity for conflict minerals and REACH. Project experience has however shown sound compatibility.

**4.4 Clarification of affected products**

As the first step of internal status-quo analysis a clarification of affected products has to be conducted, in this case according to REACH, RoHS and Conflict Minerals. REACH targets all products. A separate REACH specific clarification thus is not needed. Since most companies are also not directly affected by conflict minerals but indirectly as supply chain member, the clarification of affected products occurs within customer / supply chain communication. A product however has to fulfill a variety of specifics to be affected by RoHS. According to article Q1.7 of the RoHS-FAQs the chronology of decisions is illustrated in figure 5.<sup>38</sup>

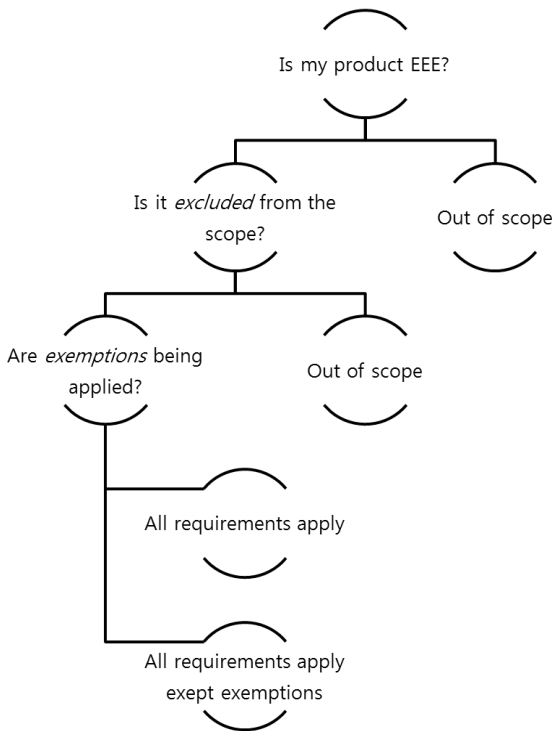


Figure 5 RoHS specific decision tree<sup>38</sup>

According to figure 5 a tabular form as illustrated in annex 1 has shown to be most effective.

**4.5 Evaluation of status quo of supplier / manufacturer**

**communication**

After the clarification of affected products, status-quo information of supplier and manufacturer communication / rating is gathered. Within this step two major topics should be analyzed: [1] fundamentals of supplier communication and [2] methods of supplier rating.

First, supplier communication should cover all relevant legislations. Many companies claim compliance of supplier goods with relevant legislations but assure themselves inadequately. The development of standardized supplier / manufacturer communication letters has shown to be most effective. In this context, phrasing should be legally harmonized. Furthermore, written and signed letters are the only acceptable form of communication and legal references should be updated frequently.

Depending on size, companies generally have implemented a system of supplier rating. General methods of supplier rating have been described in detail.<sup>39</sup> Common measures are supplier quality, constancy and branch codes. Since suppliers may be spread globally, another measure of credibility may be appropriate according to EN 50581.<sup>37</sup> Information from various countries have been shown to not be equally reliable. The corruption perception index, annually released by Transparency International, provides a sound measure for supplier information credibility and is widely accepted by enforcement agencies.<sup>40</sup> In addition, it is easily implemented and combinable with other measures due to its simple scale (0 – 100). In summary, supplier rating may be carried out as displayed in table 3. Thereby, measure grading is autonomously selectable by a company.

Table 3 Supplier measures and rating example

Measure	Rating
CPI	100
Supplier quality	80
Supplier constancy	50
...	...
Summary	230

Each supplier has to be rated according to the previously defined measures. This enables a company to define risk categories with respect to its ratio.

**4.6 Evaluation of status quo of material classification**

Material evaluation also follows the idea of risk categorization. A wide variety of materials exist in industrial companies, e.g. standard materials, drawing parts, and components. We developed a systematic approach for material evaluation that is displayed in annex 2 based on material and component categories of IEC 62474 and IEC 62321-2.<sup>41,42</sup> According to willingness, we differ between two common approaches: [1] the simple material evaluation and [2] the integral material evaluation. The simple method is entirely based on analytical experience, e.g. from IEC 62321-2. Thereby the risk is calculated on a material category level. This approach is rather fast and offers a sound start for companies that have not applied HMMS before. On a long

term, it however reveals great weaknesses since it does not respond to specifics within a material category and additional requirements from other legislations are not easily transferred. In contrast, the integral material evaluation allows a by far superior risk calculation. Thereby, each material and component that is affected within a company is analyzed in detail and apportioned in chemical components. Accepted methods for identification of chemical composition are technical standards, material declarations being linked to specific material data sheets and analytical test results (e.g. X-ray fluorescence or wet chemistry analysis). This method is associated with great efforts but allows complete coverage of all relevant legislations and allows long term validity due to its overall transparency.

Against the background of the discussed exponential increase of environmental legislations only an integral material evaluation facilitates long term validation. Essentially following the described approach above, a variety of enterprises have developed solutions in terms of compliance tools.<sup>43-46</sup> In many cases these tools are of great help, although mostly providing an environment but leaving the user with maintenance issues.

A reasonable approach for risk classification is based on the probability that a prohibited substance may appear. Common risk categories are low (L), medium (M) and high (H).

#### 4.7 Risk and impact assessment

Risk assessment is an integral part of HMMS as it displays the current level of compliance and allows the deviation of urgent actions. Various methods of risk assessment in industrial enterprises have been discussed in literature and successfully implemented.<sup>47</sup> As described in section 2, risk refers to the probability of failing to be compliant. In terms of HMMS it is dominated by two attributes: [1] material risk and [2] supplier / manufacturer risk.

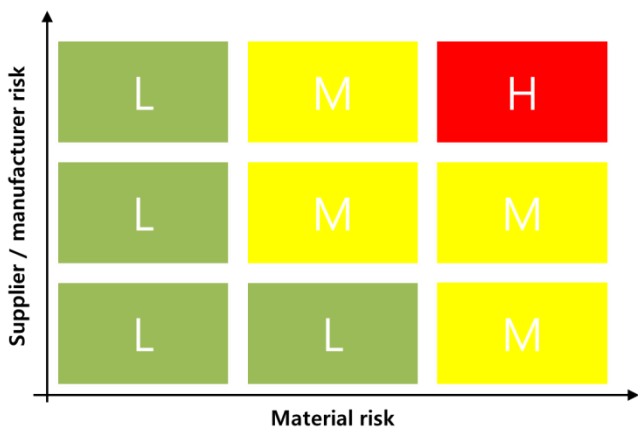


Figure 6 Risk matrix

Although not exposing each case of risk consistently, the implementation of a risk matrix has been shown to be most applicable in practice. It allows an application for both single materials and entire products. Figure 6 illustrates an example of a risk matrix. Previously defined supplier and material risk span a nine field matrix in which three categories of risk are differed: low (L), medium (M)

and high (H).

#### 4.8 Initiation of actions - communication, control, analysis

In a next step specific actions are allocated to each of the categories. While for materials from low risk categories a single supplier / manufacturer declaration is satisfactory, additional control sample analysis (e.g. XRF) are appropriate. Continuous analytical testing is advisable for materials and components from high risk categories. On a long term high risk categories should be substituted. Table 4 exemplifies the initiation of actions according to categories from previously defined risk matrix.

Table 4 Initiation of actions according to risk category

L	Supplier / manufacturer declaration
M	Additional control sample analysis
H	Additional continuous analytical testing

#### 4.9 Re-evaluation of suppliers, manufacturers and materials

All actions have to be conducted frequently and results have to be integrated in the continuous risk assessment of materials and suppliers. Generally, a company is free to determine intervals of re-evaluation. Against the background of continuous legal modifications, practice has however shown that periods of six to twelve months are most effective.

#### 4.10 Development and continuous improvement of supplier and manufacturer audits

Supplier and manufacturer audits are common for company and product specific qualification and an essential element of many quality and environmental management system. In the context of HMMS supplier and manufacturer audits are to be conducted for medium and high risk suppliers that might not easily be substituted or strategically relevant.

#### 4.11 Overall process development, integration and continuous improvement

The first step of long term HMMS validation is the development of an appropriate overall process. The process is the centerpiece of HMMS. It has to cover all essential steps of compliance management, responsibilities and has to be practical. After its integration a system of continuous improvement is required in order to guarantee compliance while regulations may be amended. An example for an appropriate HMMS process covering all essential steps is found in annex 3.

#### 4.12 Development and continuous improvement of instructions for design, purchase, sales, control, and

## analysis

Work instructions are present in nearly every industrial company in order to guarantee standardized operational procedures. Affected divisions are essentially R&D, purchase, sales as well as project, quality, and environmental management. A variety of urgent questions have to be answered within this step, e.g.:

- At what point does the developer need to be informed about the legal applicability of certain materials?
- Who is responsible for material and component clearance? How shall compliance be guaranteed and documented before material and component clearance?
- How shall procedural methods of incoming inspection be extended in order to fulfill previously defined requirements of control and analysis?
- Etc.

HMMS specific work instructions have to be subject to continuous improvement.

### 4.13 IT integration and support

IT integration and support is essential for long term compliance. From stage one of product development legal compliance has to be assured. Developer, purchase and sales employee have to have access to accurate information at the right time. A developer needs to know what materials he can use for a legally compliant design. A purchaser needs to know what documents and analytical test he needs to run for a certain material. In this sense, a company's IT structure has to represent the previously defined process and work instructions. A sound IT environment thus demands for an adequate interface between data bases. As discussed above, a variety of enterprises have developed IT solutions for environmental compliance interfaces.<sup>43-46</sup> A serious discussion of pro and cons of different concepts has to be abandoned at this point.

### 4.14 Documentation and allocation of responsibilities

According to documentation requirements, defined in step three, long term validation closes with the compilation and continuous actualization of the technical documentation. Besides its external purpose, the assurance of compliance against law enforcement agencies, it has to serve as a tool for knowledge transfer within an organization. Due to increasing fluctuation, companies are forced to effectively pass knowledge from one employee to another. Since hazardous materials management represents an expansive field and knowledge goes along with experience, a technical documentation is essential for knowledge transfer.

## 5. Discussion and critical review

The 14 steps of HMMS cover all legal requirements, in this case

of REACH, RoHS, and Conflict Minerals. The approach currently however exhibits flaws in certain range areas. These areas are essentially limited to risk assessment where the matrix approach leaves space for interpretation. Since material and supplier are equally rated, the approval via supplier declaration would eventually lead to a downgrading of a risk material. This is not in the interest of the authors. We thus propose a disparate quantitation of supplier and material risk, with a stronger focus on materials (e.g. 60:40). Other methods of risk assessment, e.g. FMEA, are also possible, have been shown to be too complex in practice. A holistic approach of hazardous materials risk calculation has not yet been developed.

Although complete elimination of risk might not be possible, HMMS comprises all essential elements of legal environmental compliance in the field of hazardous materials.

## 6. Summary and forecast

A variety of management systems have been discussed in literature and successfully implemented in industries, as discussed in section two. Nevertheless, none of these have been able to fulfill essential requirements of hazardous materials management. In this paper we presented a highly applicable approach referred to as HMMS that has been successfully tested in over 70 companies in Germany and is expected to be universally transferable to industrial companies globally. HMMS is divided in 14 steps covering five superior categories: [1] targets, [2] actual company status, [3] risk assessment, [4] required actions and [5] long term validation.

On a long term, against the background of the dramatically increasing global amount of environmental legislations, the implementation of a standardized hazardous materials management system as proposed in this paper is essential for nearly every industrial company. In turn, governments and law enforcement agencies are requested to adjust activities and find interfaces in order to reduce complexity of business. A fair balance of legal requirements and industrial expenses has to be realized in order to guarantee success of environmental policies.

Additionally, extended research is needed on a downstream basis in order to provide governments with accurate information on the status of implementation of different legislations. Traditionally, communication between governments and industries is poorly distinctive and circular. Novel methods are needed, e.g. for quantification of obsolescence potentials of certain substances and technologies.

## ACKNOWLEDGEMENT

We appreciate continuous support from and valuable discussions with Dr. Joerg Mandel and Sylvia Wahren at Fraunhofer IPA as well as our numerous industrial partners in Germany and worldwide.

## REFERENCES

1. OECD. Sustainable Manufacturing Toolkit - Seven Steps To

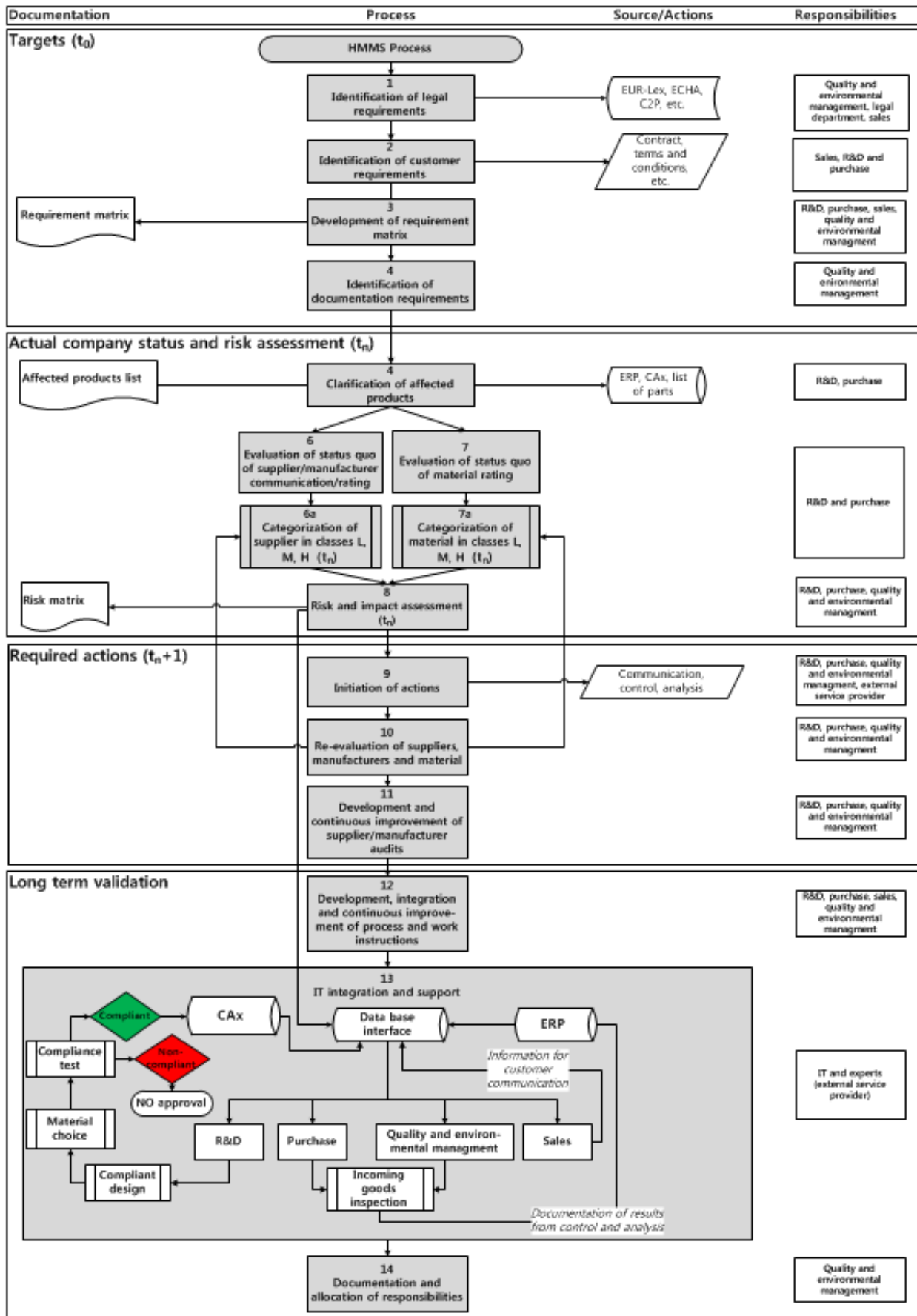
- Environmental Excellence.; 2011. Available at: <http://www.oecd.org/innovation/green/toolkit/48661768.pdf>.
2. European Union. DIRECTIVE 2000/53/EC OF THE EUROPEAN PARLIAMENT AND OF THE COUNCIL of 18 September 2000.; 2000.
  3. European Union. RICHTLINIE 2002/96/EG DES EUROPÄISCHEN PARLAMENTS UND DES RATES vom 27. Januar 2003 über Elektro- und Elektronik-Altgeräte.; 2003.
  4. European Union. DIRECTIVE 2011/65/EU OF THE EUROPEAN PARLIAMENT AND OF THE COUNCIL of 8 June 2011 on the restriction of the use of certain hazardous substances in electrical and electronic equipment.; 2011.
  5. European Union. REGULATION (EC) No 1907/2006 OF THE EUROPEAN PARLIAMENT AND OF THE COUNCIL of 18 December 2006 concerning the Registration, Evaluation, Authorisation and Restriction of Chemicals (REACH), establishing a European Chemicals Agency, amending Directive 1999/4.; 2006.
  6. Compliance and Risk. C2P Global Regulations By Subject Area (Entered Into Force 2003-2010). 2011.
  7. European Union. REGULATION (EC) No 842/2006 OF THE EUROPEAN PARLIAMENT AND OF THE COUNCIL of 17 May 2006 on certain fluorinated greenhouse gases.; 2006.
  8. Handelsblatt. Kältemittel-Streit: Freie Fahrt für Daimler in Frankreich. 2013.
  9. Davenport TH, Short JE. The New Industrial Engineering: Information Technology and Business Process Redesign. MIT Sloan Manag. Rev. 1990. Available at: <http://sloanreview.mit.edu/article/the-new-industrial-engineering-information-technology-and-business-process-redesign/>. Accessed April 12, 2014.
  10. Scheer A-W, Nüttgens M. ARIS Architecture and Reference Models for Business Process Management. Lect. Notes Comput. Sci. 2000;1806:376–389.
  11. Münstermann B, Eckhardt A, Weitzel T. The performance impact of business process standardization: An empirical evaluation of the recruitment process. Bus. Process Manag. J. 2010;16(1):29 – 56.
  12. Muenstermann B, von Stetten A, Laumer S, Eckhardt A. The performance impact of business process standardization: HR case study insights. Manag. Res. Rev. 2010;33(9):924 – 939.
  13. Beimborn D, Gleisner F, Joachim N, Hackethal A. The Role of Process Standardization in Achieving IT Business Value. In: Proceedings of the 42nd Hawaii International Conference on System Sciences - 2009.; 2009:1–10.
  14. International Organization for Standardization. ISO 9000 - Quality management. 2005.
  15. International Organization for Standardization. ISO 14000 - Environmental management. 2009.
  16. International Organization for Standardization. ISO 50001 - Energy management. 2011.
  17. European Union. REGULATION (EC) No 1221/2009 OF THE EUROPEAN PARLIAMENT AND OF THE COUNCIL of 25 November 2009 on the voluntary participation by organisations in a Community eco-management and audit scheme (EMAS), repealing Regulation (EC) No 761/2001 and Commission Deci. 2009.
  18. Torp J. Compliance Management System. AlexInformation; 2004.
  19. Klaus Moosmayer. Compliance -Praxisleitfaden für Unternehmen. C.H. Beck; 2010.
  20. Görling H, Inderst C, Bannenberg B. Compliance – Aufbau, Management, Risikobereiche.. C.F. Müller; 2010.
  21. Wieland J, Steinmeyer R, Grüninger S. Handbuch Compliance-Management - Konzeptionelle Grundlagen, praktische Erfolgsfaktoren, globale Herausforderungen. Erich Schmidt Verlag; 2010.
  22. Knight FH. Risk, Uncertainty and Profit. Houghton Mifflin Company; 1921.
  23. Rescher N. A Philosophical Introduction to the Theory of Risk Evaluation and Measurement. University Press of America; 1983.
  24. Drake RA. Decision making and risk taking: Neurological manipulation with a proposed consistency mediation. Contemp. Soc. Psychol. 1985;11:149–152.
  25. Holton GA. Defining Risk. Financ. Anal. J. 2004;60(6):19–25.
  26. Hillson D. Practical Project Risk Management: The Atom Methodology. Management Concepts.; 2007.
  27. International Organization for Standardization. ISO 31000 - Risk management. 2009.
  28. International Organization for Standardization. ISO/DIS 31000 - Risk management — Principles and guidelines on implementation. 2009.
  29. U.S. Government. DODD-FRANK WALL STREET REFORM AND CONSUMER PROTECTION ACT - PUBLIC LAW 111–203—JULY 21, 2010.; 2010.
  30. European Commission. JOINT COMMUNICATION TO THE EUROPEAN PARLIAMENT AND THE COUNCIL Responsible sourcing of minerals originating in conflict-affected and high-risk areas Towards an integrated EU approach. 2014.
  31. European Commission. Proposal for a REGULATION OF THE EUROPEAN PARLIAMENT AND OF THE COUNCIL setting up a Union system for supply chain due diligence self-certification of responsible importers of tin, tantalum and tungsten, their ores, and gold originating in conflict-affected areas. 2014.
  32. EUR-Lex. Der Zugang zum EU-Recht. 2014. Available at: <http://eur-lex.europa.eu/homepage.html?locale=de>. Accessed April 12, 2014.
  33. ECHA. European Chemicals Agency. 2014. Available at: <http://echa.europa.eu/de/>. Accessed April 10, 2014.
  34. Compliance and Risk. C2P. 2014. Available at: <http://www.complianceandrisk.com/services/c2p/>. Accessed February 10, 2014.
  35. European Union. DECISION No 768/2008/EC OF THE EUROPEAN PARLIAMENT AND OF THE COUNCIL of 9 July 2008 on a common framework for the marketing of products, and repealing Council Decision 93/465/EEC. 2008.
  36. European Union. REGULATION (EC) No 765/2008 OF THE EUROPEAN PARLIAMENT AND OF THE COUNCIL of 9 July 2008 setting out the requirements for accreditation and market surveillance relating to the marketing of products and repealing Regulation (EEC) No 339/93.; 2008.
  37. British Standard. BS EN 50581:2012 - Technical documentation for the assessment of electrical and electronic products with respect to the restriction of hazardous substances. 2012.
  38. European Commission. RoHS 2 FAQ. 2012. Available at: [http://ec.europa.eu/environment/waste/rohs\\_eee/pdf/faq.pdf](http://ec.europa.eu/environment/waste/rohs_eee/pdf/faq.pdf). Accessed April 10, 2014.
  39. Beucker S. Ein Verfahren zur Bewertung von Lieferanten auf der Grundlage von Umweltwirkungen unter Berücksichtigung von Prozesskosten.; 2005. Available at: [http://elib.uni-stuttgart.de/opus/volltexte/2006/2461/pdf/Diss\\_Beucker\\_hs.pdf](http://elib.uni-stuttgart.de/opus/volltexte/2006/2461/pdf/Diss_Beucker_hs.pdf).
  40. Transparency International. Corruption Perceptions Index - Overview. 2014. Available at: [www.transparency.org/research/cpi/overview](http://www.transparency.org/research/cpi/overview). Accessed April 11, 2014.
  41. International Electrotechnical Commission. IEC 62321:2008 - Electrotechnical products - Determination of levels of six

- regulated substances (lead, mercury, cadmium, hexavalent chromium, polybrominated biphenyls, polybrominated diphenyl ethers). 2008.
42. International Electrotechnical Commission. IEC 62474 - Material Declaration for Products of and for the Electrotechnical Industry. 2012.
  43. SAP. SAP Product and REACH Compliance 2.0. 2014. Available at: <http://help.sap.com/reach20>. Accessed February 11, 2014.
  44. SAP. SAP Product Stewardship Network. 2014. Available at: <http://www.sap.com/pc/tech/cloud/software/product-stewardship-network/overview/index.html>. Accessed April 11, 2014.
  45. Hewlett-Packard. HP Compliance Data Exchange (CDX). 2014. Available at: <http://www8.hp.com/de/de/business-solutions/solution.html?compURI=1330154#.U1YTTxAXsQA>. Accessed April 11, 2014.
  46. PTC. PTC Materials Compliance Solution. 2014. Available at: <http://de.ptc.com/solutions/materials-compliance/>. Accessed April 10, 2014.
  47. Hua AH, Hsu C-W, Kuo T-C, Wu W-C. Risk evaluation of green components to hazardous substance using FMEA and FAHP. *Expert Syst. Appl.* 2009;36(3):7142–7147.





Annex 3 – HMMS process



# High Income Return and Safe Investments through Financing of Energy Efficient Measures in the Industry

Robert Kasprowicz<sup>1#</sup>, Siegfried Stender<sup>2</sup> and Thomas Bauernhansl<sup>2</sup>

<sup>1</sup> Fraunhofer Institute for Manufacturing Engineering and Automation, Nobelstrasse 12, 70569 Stuttgart  
<sup>2</sup> Fraunhofer Institute for Manufacturing Engineering and Automation, Nobelstrasse 12, 70569 Stuttgart  
#Corresponding Author / E-mail: Robert.Kasprowicz@ipa.fraunhofer.de, TEL: +49-(0)7119701908

KEYWORDS : Energy Efficiency, Green Investment Funds, Contracting, Financing of Energy Efficiency Measures

---

*Energy-efficient technologies may induce large energy and monetary savings in various industries. Based on our study, investigating the German industry by covering over 250 publications, we show that investments of merely 5 billion euro may generate cash-positive savings of about 20 billion euro until 2020. Until 2030 the savings are increasing up to over 60 billion euro. However, plenty of commonly identified potential in industries remains unrealized due to comparatively short requested payback periods in order to minimize a company's investment risk. According to our last survey of industrial enterprises it can be seen that usual payback periods for energy efficient machines shall not exceed 3 years. Energy efficient measures with higher payback periods often remain unused, but regardless can generate a payback rate of over 20% over its entire lifetime.*

*Against this background we compare different methods for industrial energy efficiency investment evaluation and come up with effective recommendations for operators to realize more energy savings and reduce energy costs. Recent studies show that enterprises are realizing more energy efficiency measures while using a total cost approach as a basis for an investment decision than enterprises which concentrate only on short-term profit maximization.*

*Furthermore, new funding models for efficiency measures could be an alternative to take full advantage of specific monetary potentials. In times of low market rates investors gain less interest rate income as years before. 2009 fixed-period interest rates dropped to 0,5% and today they are partially still under the inflation rate. As a result the demand for classical asset management with mutual funds dropped steadily in recent years and investors are looking for alternative investments. Using private capital to invest in energy efficiency will solve two problems at once:*

*Capital assets in energy efficiency may significantly improve portfolio compositions of investors while simultaneously provide required financial resources for efficient technologies. As a result investors gain high income returns and enterprises are able to reduce their overall CO<sub>2</sub> emissions. Furthermore, through the use of different funding models the payback period for enterprises can be considerably shortened. In this paper we discuss several funding and business models and show the specific impacts on cost-effectiveness, payback-periods and common requirements.*

---

## 1. Introduction

### 1.1 Importance of energy efficiency

Due to continuing risks of climate change, increasing scarcity of resources and rising energy and resource prices, sustainability today influences more than ever decisions in business, politics, science, and also private behavior<sup>1,2</sup>. In order to be able to exist in the marketplace and to be competitive in the future, therefore energy-efficient production of goods and services is essential for manufacturing enterprises to reduce energy costs. This situation is reflected on the energy costs and trends. For example, electricity prices in the industry

increased dramatically in the last 13 years: between 2000 and 2013 the price for a kWh electricity in Germany rose by an average of 140%. Additionally the average electricity price in 2013 for the German industry was about 10.6 euro cents/kWh. The vast majority of the EU have considerably lower prices: Sweden (5.5 cent/kWh), France (6.6 cent/kWh), Spain (6.9 cent/kWh) are only 3 of 25 countries in the EU with lower energy prices than Germany<sup>3</sup>. Based on this, German industry is operating under a high competitive pressure.

Besides the economic impact on the industry, there are also environmental reasons for energy efficiency. With a share of more than 40% of total electricity consumption the German industry has a great impact on the national CO<sub>2</sub> footprint of Germany<sup>4</sup>. In addition to the climate goals within the EU, Germany also intends to reduce its primary energy consumption by 20% by the year 2020<sup>5</sup> compared to 2008 and additionally double its energy productivity<sup>6</sup> compared with 1990, which corresponds to an increase of 2.1% per year until the year 2050.<sup>7</sup> Based on the latest developments, national objectives will be jeopardized if actions are not taken with respect to an intensified energy efficiency in the industry: the industrial energy consumption increased since 1992 by 0.1% p.a. Simultaneously the industrial energy productivity increased by an annual average of 1.7% between 1995 and 2008.<sup>8</sup> Based on this development an increasing energy productivity of 3 to 3.7 is necessary for the remaining period until 2020<sup>9,10</sup>. Thus, due to a continuation of actual developments, the current diffusion of energy efficiency is not sufficient to achieve national goals<sup>11</sup>.

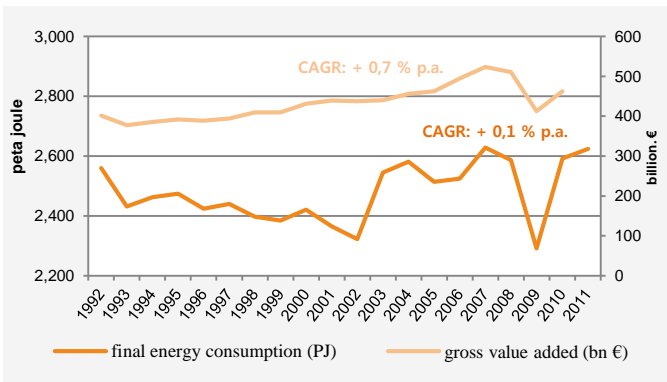


Fig. 1: final energy consumption in the industry<sup>12</sup>

In the past periods, the German industry has already achieved significant energy savings through efficiency measures. Final energy savings of more than 500 PJ were realized.<sup>13</sup> However, a larger part of Energy savings were therefore neutralized by economic growth, which increased in the past 20 years by 0.7% p.a.

### 1.2 Efficiency potentials in German industries

As a part of our latest meta-study of energy efficiency potentials, over 250 publications were reviewed and analyzed with respect to the type and amount of existing potentials. These potentials vary depending on technology, branch and assumptions for the future.

Based on our study, the following illustration Figure2 summarizes both electrical and thermal energy saving potentials. The electrical potential consists of individual potentials of common cross-sectional technologies<sup>14</sup>, which have a share of 87% of the electrical saving potential in the German industry<sup>15</sup>. Potentials based on thermal energy are mainly induced by branch- and process-specific

technologies and are summarized from individual saving potentials of energy-intensive industries. These aggregated potential-categories hereinafter are compared to the specific saving objectives of the industry by 2020.

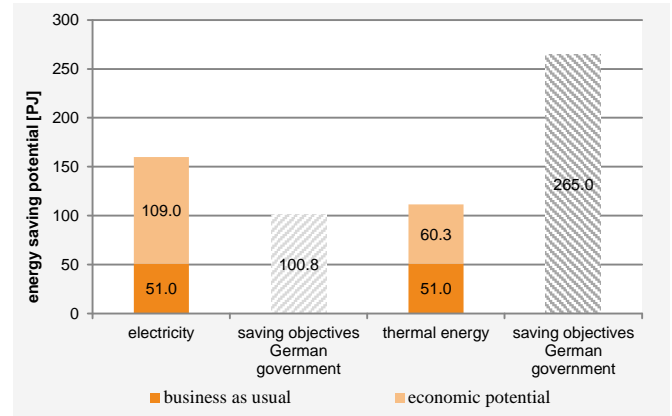


Fig. 2: energy saving potential of German industry<sup>16</sup>

At the same time the specific potentials are classified according to their level of realization: the market potential is based on a business as usual scenario. This is generated by 2020 based on the actual diffusion of technologies and efforts and has a value of 51 PJ each, considering electrical and thermal saving potentials. However, the overall possible saving potential which can be economically tapped is much larger and has a value of 160 PJ. Thus current efforts need to be tripled to tap the full economical electricity potential. To meet energy saving objectives (100 PJ) current efforts in the areas of energy efficiency still need to be doubled. The economical viable thermal potential has a value of 111 PJ. Based on this, current efforts must be doubled to achieve the energy saving goals in the area of thermal energy<sup>16</sup>. However, these economical potentials might induce high monetary savings. An incremental investment of roughly 5 billion Euros would return nearly four times as much – 20 billion euros by 2020.

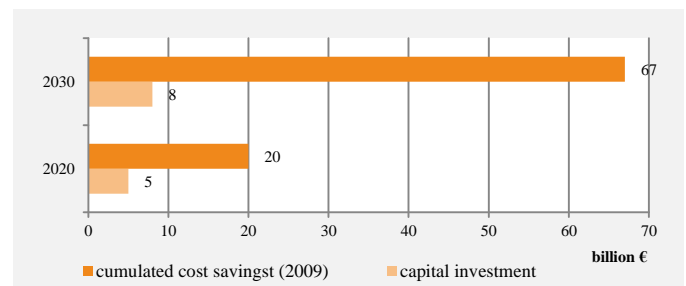


Fig. 3: monetary savings through energy efficiency by 2030<sup>15</sup>

The longer the observation period is chosen, the more saving effects manifest themselves through reduced energy costs. Figure3 shows the development of both necessary investment and corresponding monetary savings. Other studies anticipate that investments of 24 billion euros may indicate a return of 100 billion euros by 2050<sup>17</sup>. In summary, it can be concluded that huge economical saving potentials still exist for the German industry with high profitability.

<sup>5</sup> and 50% by the year 2050

<sup>6</sup> Energy productivity is defined as the ration between energy consumption and gross domestic product

<sup>7</sup> Energy productivity is defined as the ration between energy consumption and gross domestic product

<sup>14</sup> such as pumps, electric motors, fans, compressed air and lighting

### 1.3 Common obstacles

The current situation especially in German industry seems paradoxical: As a leader in the global market for environmental and efficient technologies Germany has a share of 15% and therefore an absolute international leading position. Whereas the current global market volume for environmental and efficient technology in 2011 was about 2,000 billion euros and is intended to rise to more than 4400 billion euros by 2025.<sup>18</sup> Despite these impressive development forecasts Germany itself has still many unused saving potentials, particularly in the industrial sector<sup>19</sup>.

Despite the high quantified monetary saving effects, a major part of existing energy saving potentials is left unused. For the non-realization of efficiency potentials a variety of factors can be mentioned that make implementation of efficiency measures difficult. Apart from well-known non-monetary reasons, such as lack of transparency, corporate-culture, organizational framework conditions, two reasons are considered to be the main cause of unused economical saving potentials: lack of knowledge about the existing potentials and insufficient financial resources<sup>20</sup>. Furthermore even if companies have sufficient financial capital, strict assessment standards will cut investment opportunities. This is reflected in recent surveys on primary criteria guiding any investment decision: 80% of companies surveyed based their investment decisions only on the payback-period.<sup>15</sup> According to our latest survey of industrial enterprises the generally accepted period for efficiency measures typically shall not exceed 3 years.<sup>20</sup> Depending on the technology, field of application and branch the acceptance-range may vary.

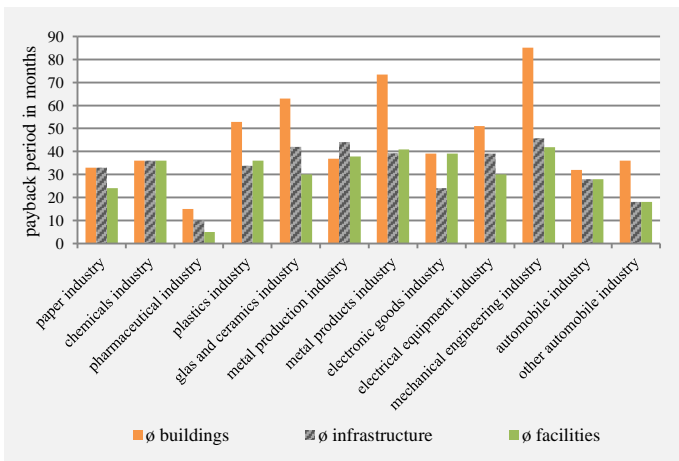


Fig. 4: accepted payback-period industry<sup>20</sup>

Figure 4 shows that companies accepting longer payback-periods in the area of efficiency measures for buildings rather than in the area of machinery, infrastructure, and process measures.

However, a decision based on a payback period does not give any indication of the economic viability of specific measures. Furthermore most of energy efficiency measures have a significantly longer technical lifetime referring to the payback-periods and a high profitability across their entire lifecycle. Due to the required short payback periods many high profitable efficiency projects are left

unused or will not be realized. This connection is best reflected by the following table, which shows the internal interest rate of an efficiency measure for selected lifetime ranges in dependence on the payback period time. For example, an investment with a payback period of 2 years and an overall lifetime of 3 years generates an internal interest rate of 24%. Additionally a lifetime of 4 years will generate an interest rate of 35%. Assuming that no investments are made within a payback period that exceeds 3 years, internal interest rates between 24% and 11% depending on the plant lifetime are left unused.

Table 1: Interest rates and payback periods<sup>16</sup>

Pay-back period	Internal interest rates							
	Plant lifetime							
	3	4	5	6	7	8	12	15
2	24%	35%	41%	45%	47%	49%	49%	50%
3	0%	13%	20%	25%	27%	31%	32%	33%
4		0%	8%	13%	17%	22%	23%	24%
5			0%	6%	10%	16%	17%	19%
6				0%	4%	11%	13%	15%
8					0%	5%	7%	9%
	Not-realized measures							

In summary, it must be emphasized that there is a huge unused economical potential in the German industry which partly can be realized through an approach which neutralizes on the one hand the difficulties of insufficient funds and on the other hand the required short payback-periods.

## 2 Performance Contracting

Energy efficiency measures often require both high organizational and financial efforts. New territories are being entered and thus new experiences had to be made. In order to reduce complexity, areas of competence are outsourced by providing the necessary services through an external partner or service provider, called contractor.

The contractor creates or optimizes an energy efficient technology for the customer on his own account. The customer enterprise neither owns nor runs this technology. Therefore the customer is saving the investment costs for specific technologies to increase energy efficiency. The final payment for the provided technology and service will be calculated and charged by the amount of working hours or produced pieces. Therefore the contractor takes the entrepreneurial risk while the customer only pays per use. The overall advantage derives from the reduced complexity and monetary risk on the user's side<sup>22</sup>. The contractor commonly focusses on specific areas, such as lighting or pump contractors, and is therefore able to bundle expertise, synergies and economic advantages<sup>23</sup>.

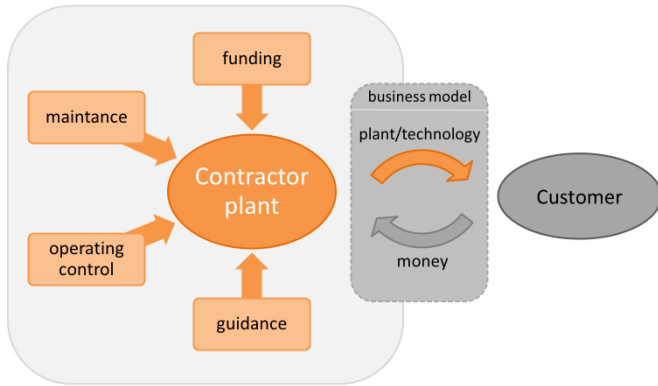


Fig. 5: scope of supply and services within contracting<sup>24</sup>

Additionally the company is able to focus on its core business, while the contractor can expand his business and sales. Overall, there is a variety of specific contracting models, which are differentiated by rules of ownership as well as rights and obligations. The so-called delivery-contracting found a broad acceptance in the last few years<sup>24</sup>. Due to the growing need to minimize complexity of non-core business activities, common technologies and business models used within contracting have traditionally nothing to do with the company's main business. Therefore a lot of contracting business models in the industry focus on building services, power generation, and equipment as well as on cross-sectional technologies.

In contrast, contracting models based on branch- and process specific technologies, which are dominating the thermal energy saving potential in Germany, are uncommon and did not prove feasible yet. Due to the missing knowledge about process- and product-specific framework conditions within a company, possible process-based solutions are too complex and diverse. Resulting benefits of a contracting model would be lost with a high degree of probability. Therefore common contracting approaches are not able to solve the problem of unused thermal saving potentials in the industry.

**2.1. New approach: investment fund models**

Based on the specified disadvantages of contracting models, a new approach to finance unused efficiency potentials was developed. Within this new approach industrial companies should be motivated to realize previously unrecognized energy efficiency measures.

This approach is based on the assumption that more than ever investors are looking for attractive investment opportunities with appropriate profits. One of the most influential developments over the past five years has probably been the way in which the inflation and effective interest rate has been infiltrated. Since the second half of 2009, effective interest rates with a term between at least one year and more than three years, is remaining below the inflation rate. This development is shown in figure 6.

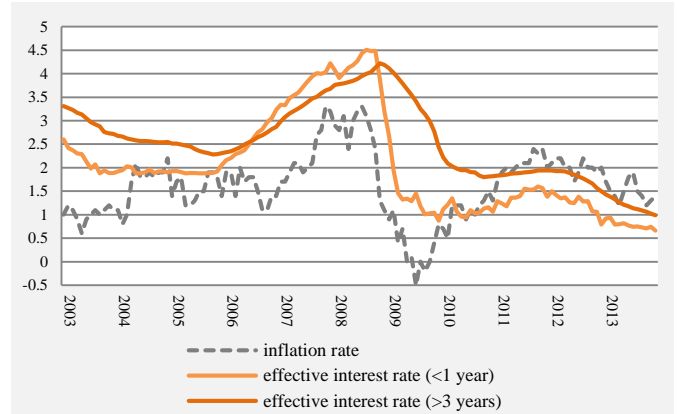


Fig. 6: inflation and interest rate in Germany<sup>25</sup>

Based on the development of the interest market, the value of saved money calculated on the basis of the nominal rate is gradually eroded by inflation. As a result, both private as well as commercial investors are investing in material assets. Combining the need for investment opportunities and at the same time the need in the industry for capital to finance efficiency measures might be a win-win solution.

To exploit unused energy saving potentials in the industry within the new approach, necessary financial capital is provided by an investment fund. Therefore an investor will generally purchase shares in the fund directly from the fund itself. Simultaneously an independent authority or agency is mandated by a customer enterprise to deliver a technical evaluation of possible enterprise-specific measures and quantifies the potential. This agency possibly provides specific efficiency technology itself or uses an adequate distributor network to ensure and supervise the implementation.

It is also likewise conceivable that industrial enterprises already analyzed their specific efficiency potentials and requests the fund-organization for financial support. The main difference to a common contracting business model is that the technology provider and the financial capital provider are fully independent from each other. But as long as there is no expert appraisal confirming, the investment fund will not be disbursed. If the technical rating is successful, the recommended technology will be supported. The generated cost savings through the efficiency measures will be divided between the customer enterprise and the investment fund. Within the fund the insurance agency takes a share of the returns as well.

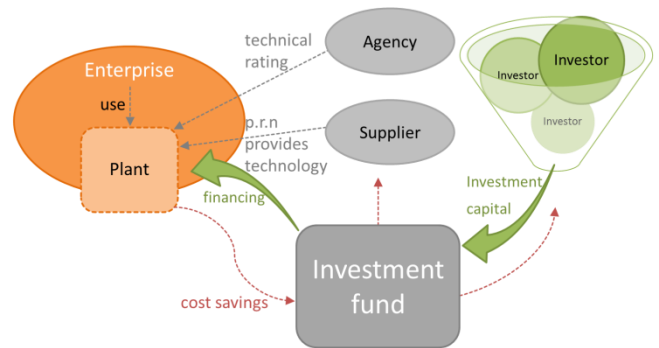


Fig. 7: new investment fund approach

This three-way partnership creates a triple-win situation: investors benefit from stable returns and make a contribution to environmental protection. The company realizes energy and financial savings without using their own capital. And last but not least, the technology partners also benefit from increased orders and reputation. Furthermore, Due to the realized returns, further efficiency measures can be financed and unused energy potentials can be exploited. In the following, the investment fund approach will be explained and quantified based on a developed decision making tool using the example of a typical energy efficiency investment.

**2.2.1 Baseline scenario**

The following example will serve as a basis for the following explanations. For a better understanding, the original example has been simplified in order to provide an initial impression of how the funding approach creates benefits. The starting point of this baseline-scenario is an energy efficient plant which has aggregated investment costs of 10.000 euro and provides a cost reduction of 2.500 euro p.a.<sup>26</sup> Additionally, the entire period of use of the facility is 15 years and the market interest rate is 10%. Within this baseline scenario, it is assumed that 100% of the necessary investment is going to be financed from the company's financial resources.

Due to an assumed initial period of 1 year, the usual payback period is 5 years.<sup>27</sup> The resulting cash flow and net present value (NPV) of the investment is shown in the following figure 8. Based on that scenario, the annual cash flow (CF) of the investment is 2.500 euro and the total net present value of this efficiency measure after 15 years is 9.015 euro.

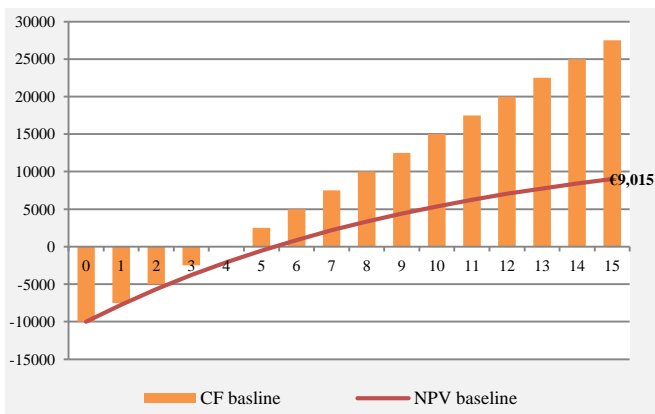


Fig. 8: cash flow and NPV baseline scenario

<sup>26</sup> In the original calculation tool the costs are sub-divided into: personal costs, energy costs, other resources costs, installation and disposal costs, and maintenance costs. Furthermore a dynamic development of production and energy consumption as well as a volatile production output is implemented to support a realistic development of possible cost reductions.

<sup>27</sup> Assuming that time within the initial period is needed for start-up, adjustment, learning effects, and manifestation of cost reduction effects

**2.2.2 Investment fund scenario 1**

The first business model assumes that the necessary investment of 10.000 euro is partly financed through the participation of the investment fund. The basic conditions for this scenario are: the fund lifetime is also 15 years, the required rate of return within the fund is 20%, and the share of the investment costs is 75%. However, this share is not fixed and only serves as an example.<sup>28</sup> Furthermore it is assumed, that the participating private investors within the fund accept a long-term periods to receive the 20% rate of return.<sup>29</sup> The enterprise share of the total investment is 2.500 euro, while the investment fund covers costs of 7.500 euro. Due to the required interest rate of 20% of the fund, the annual return is reduced to 896 euro for the enterprise (CF fund model), which has also an impact on the net present value. Based on the defined cost and return ratio, the company's specific payback period changes as well. The following figure 9 summarizes the changed framework conditions and compares it with the baseline scenario. Within this scenario, the payback period has been shortened to 3 years from the company's point of view. However, the investment is still profitable for the enterprise. Despite being shortened by over 50%, the investment has a net present value of 4.314 euro from the company's point of view, while the fund interest rate of 20% has been completely fulfilled.

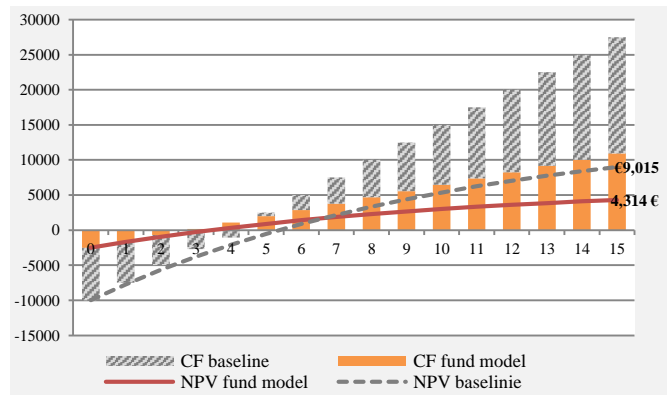


Fig. 9: cash flow and NPV fund model 1

Against the background of required payback periods of at least 3 years, this scenario shows a method to exploit unused potential and simultaneously ensures an economic incentive for companies. It also enhances the attractiveness of investments for efficiency measures. As shown in figure 7, the fund finances the investor and the insurance company by dividing the realized interest rate.

**2.2.3 Investment fund scenario 2**

This second scenario quantifies the impact on the first scenario, if the funding contract is shorter than the facility's entire period of use. Within this scenario it is assumed, that the facility's use period is still 15 years, but the duration of the fund is limited to 9 years.

<sup>28</sup> The share can be optimized within the required return of the participating enterprise

<sup>29</sup> Therefore this fund can also be seen as a bond fund.

Furthermore it is assumed, that the fund covers 100% of the investment costs for the facility. Conversely, this means the efficiency technology and the corresponding energy and CO<sub>2</sub> emission savings are provided free of charge for the enterprise. To achieve the required 20% rate of return, the investment fund takes the complete returned cash flow until the contract expires after 9 years. From year 9 onwards, the facility remains with the company. From that moment the ownership and cost savings are transferred to the company. The following figure summarizes this scenario and compares it to the baseline scenario.

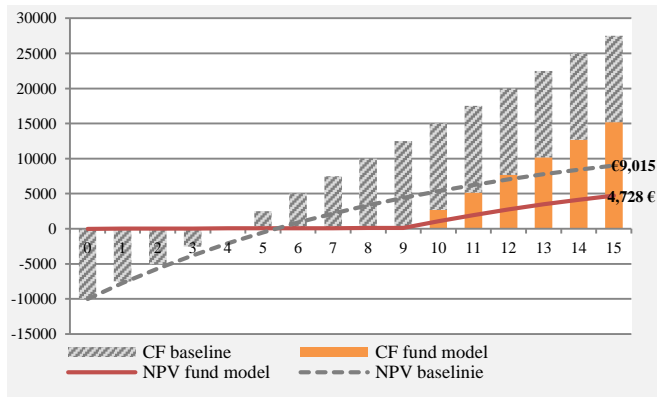


Fig. 10: cash flow and NPV fund model 2

Due to the assumption, that 100% of the costs born directly by the investment fund, the payback period of the efficiency measure is from the company's point of view zero. Furthermore a higher the net present value can be realized compared to scenario 1. Within 15 years the investment has a NPV of 4728 euro. The big advantage of this scenario derives from the company's possibility to avoid investment costs and simultaneously take advantage of the opportunity to reduce energy consumption and CO<sub>2</sub> emissions. Furthermore an even higher net present value can be realized compared to scenario 1 due to the shortened fund duration.

#### 2.2.4 Investment fund scenario 3

The third scenario is an extended version of scenario 2. It is again assumed, that the fund covers 100% of the investment costs for the facility. The fund duration is assumed to be 15 years, as well as in scenario 1. The main difference to scenario 2 derives from the assumption, that the investment fund pays expected future cost savings already in the first period to the company. Except for the first payment, the investment fund keeps all future savings. In contrast to the baseline scenario and scenario 1, where the company has to pay fully or partly for the facility, the participating enterprise receives the cumulated cash flow in the beginning.

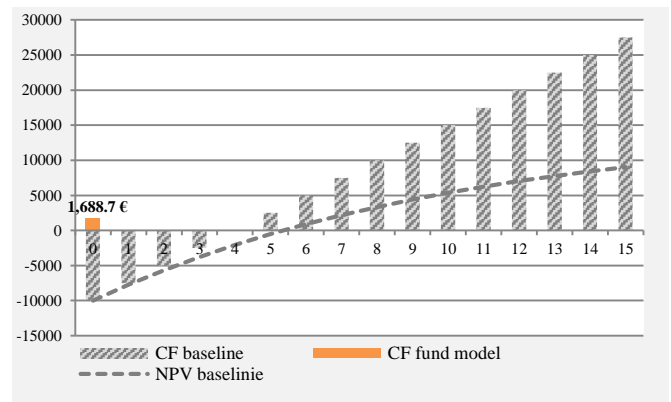


Fig. 11: cash flow and NPV fund model 3

As well as scenario 2, this scenario enables the enterprise to release itself from investment and other costs, such as maintenance or disposal costs. The customer completely outsources the necessary facility and every financial and organizational part of it. Every organizational necessity to monitor energy and cost savings is the responsibility of the investment fund. Therefore, the advantage compared to scenario 2 is the lower necessary organizational and coordination effort between customer and fund operator. Additionally the customer enterprise receives a financial incentive in the beginning, depending on the specific efficiency measure. Simultaneously energy- and CO<sub>2</sub> savings are realized. In summary, this scenario provides the possibility to realize energy saving potentials without any necessary financial investment for the enterprise.

### 3. Conclusions

Energy efficiency is the key technology to achieve both reducing national greenhouse gas emissions and ensure global competitiveness of the German industry. However, an essential part of the existing saving potentials are unused due to reservations towards high investment costs and long payback periods. In order to address this issue, common approaches, such as contracting models, are focusing only on cross-sectional technologies to increase energy efficiency of companies. Therefore, a considerably high share of energy saving potential remains unused.

Using private capital to invest in energy efficiency will solve two problems at once: Capital assets in energy efficiency may significantly improve portfolio compositions of investors while simultaneously provide required financial resources for efficient technologies. As a result investors gain equally distributed high income returns (assumption: 20%). Simultaneously a large number of individual funding projects can be aggregated in one fund in order to ensure a risk diversification and minimize the risk of default<sup>30</sup>. The investment fund raises on the one hand capital from investors, on the other hand the fund identifies, finances, and supervises projects. Additionally customer enterprises are able to reduce their overall energy consumption and CO<sub>2</sub> emissions and are benefiting from an enhanced image. Furthermore, through the use of different funding models the payback period for enterprises can be considerably

shortened. Depending on the technology, risk affinity and knowhow of the involved participants, shares and contract term as well as obligations can be adapted.

However, a complete exploitation of existing saving potentials is not exclusively necessary for German industries in future periods. Recent studies show, however, that it cannot be assumed that the energy consumption is significantly lowered in the future: The international agency assumes that the final energy demand of EU is rising until 2035. Both in the CPS and NPS the main objective, reduction of energy consumption by 20% by 2020, will not be met.<sup>8</sup> Based on the NPS the reduction will be only 14% by 2020. Only in the so called 450 Scenario, which assumes that the atmospheric CO<sub>2</sub>-emission concentration is limited to 450 ppm, slightly decreasing final energy consumption is approximately achieved<sup>31</sup>.

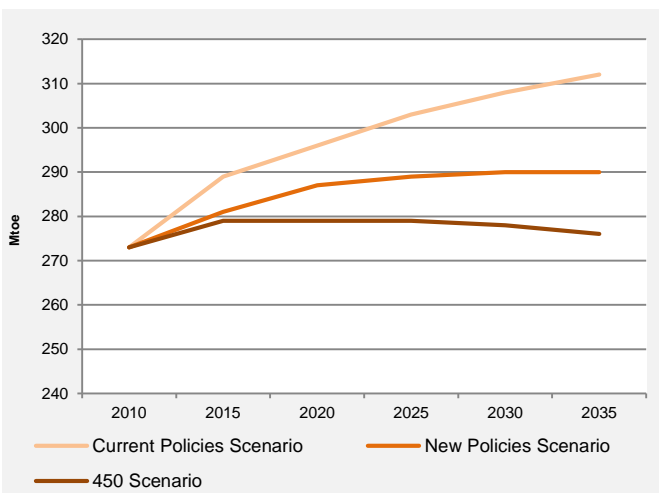


Fig. 12: final energy consumption in the European industry by 2035<sup>31</sup>

However all scenarios are based on a full development of existing efficiency potentials. In case of any partial potential development, the energy consumption would be even higher. Therefore, the presented funding models could be an important instrument to ensure ecologic and economic objectives. Without incentives and promoting of energy-efficient technologies, cost-effective energy efficiency measures will be left unused and environmental objectives will be missed.

## REFERENCES

- 1 Commission of the European Communities, Communication from the Commission to the European Parliament, the Council and the Committee of the Regions on the Sustainable Consumption and Production and Sustainable Industrial Policy Action Plan, 2008.
- 2 Finkbeiner, M. et al., "Towards Life Cycle Sustainability Assessment", pp. 3309-3322, 2010.
- 3 Feld, L. et al., "Neustart in der Energiepolitik jetzt", Kronberger Kreis, pp. 14-20, 2014.
- 4 Umweltbundesamt [ed.], "Entwicklung der Treibhausgasemissionen in Deutschland nach Sektoren", 2011.
- 5 Arbeitsgemeinschaft Energiebilanzen [ed.], "Ausgewählte Effizienzindikatoren zur Energiebilanz Deutschland, Daten für die Jahre 1990 bis 2011", 2012.
- 6 Sauerborn, K. et al., "Innovationspotenziale für Umwelt und Klimaschutz in Europäischen Förderprogrammen Nordrhein-Westfalens", 2010.
- 7 Hüttl, R., "Energiewende: Sichere Energieversorgung – heute und morgen", 2012.
- 8 Statistisches Bundesamt [ed.], "Nachhaltige Entwicklung in Deutschland – Indikatorenbericht.", pp. 6-20, 2012
- 9 Umweltbundesamt [ed.], "Energieeffizienz in Zahlen – Endbericht", pp.104-149, 2011
- 10 Prognos AG [ed.], "Energieeffizienz in der Industrie - Eine makroskopische Analyse der Effizienzentwicklung unter besonderer Berücksichtigung der Rolle des Maschinen und Anlagenbaus", 2009.
- 11 Pehnt, M. et al., "Endbericht – Energieeffizienz – Potenziale, volkswirtschaftliche Effekte und innovative Handlungs- und Förderfelder für die Nationale Klimaschutzinitiative", 2011.
- 12 Bauernhansl, T., et al.: "Management Summary - Energieeffizienz in Deutschland – Ausgewählte Ergebnisse einer Analyse von mehr als 250 Veröffentlichungen", pp. 5-17, 2013.
- 13 Roland Berger Strategy Consultants [ed.], "Effizienzsteigerung in stromintensiven Industrien - Ausblick und Handlungsstrategien bis 2050", 2011.
- 14 Umweltbundesamt [ed.], "Energieproduktivität und Energieintensität", 2012.
- 15 Deutsche Bundestiftung Umwelt [ed.] "Energie effizient – Klimaschutz in Industrie und Gewerbe", 2008.
- 16 Institut für Energieeffizienz in der Produktion [ed.], "Energieeffizienz-Index der deutschen Industrie – 1. Auswertung zum 20.12.2013", 2013
- 17 Hirzel, S., Sontag, B., Rohde, B., "Betriebliches Energiemanagement in der industriellen Produktion.", 2013

<sup>8</sup> Based on the assumption that both current policies and development are retained (current policies scenario - CPS) and already planned and new measures are enabled (new policies scenario – NPS) the final energy consumption increases

- 18 Hirschner, J., Hahr, H., Kleinschrot K., „Facility Management im Hochbau“ pp. 128-137, 2013
- 19 Dudda, C., Radgen, P. and Smid, J., “Contracting Finanzierung Betreibermodelle”, Druckluft effizient, pp. 7-12, 2004
- 20 EnergieAgentur.NRW, Ministerium für Wirtschaft, „NRW spart Energie. Contracting: Energieeffizienztechnologien ermöglichen“, pp. 8-12, 2007
- 21 Deutsche Bundesbank [ed.], Effektivzinssätze, 2013.
- 22 Reichmuth, T. et al., “Die Finanzierung der Energiewende in der Schweiz”, pp.235-312, 2014.
- 23 International Energy Agency [ed.], “World Energy Outlook 2012 – Zusammenfassung”, 2012.

# ISGMA 2014 PROCEEDINGS

**Editor | Won-Shik Chu (Seoul National University)**

ISGMA Secretariat | Byeong Kwon Lee (secretariat@isgma.org)

Tel. +82-2-518-0722 / Fax. +82-2-518-2937

The Korean Society for Precision Engineering  
(100-808) SKY1004 Building 12F, 50-1 Junglim-ro, Jung-gu, Seoul, Korea